Numerical and Experimental Investigation of the Structural Behavior during Aircraft Emergency Landing on Water

A thesis accepted by the Faculty of Aerospace Engineering and Geodesy of the University Stuttgart in partial fulfilment of the requirements for the degree of Doctor of Engineering Sciences (Dr.-Ing.)

by

MARTIN HANS SIEMANN

born in Blankenburg (Harz), Germany

Main referee: Prof. Dr.-Ing. Heinz Voggenreiter
Co-referee: Prof. Dr.-Ing. habil. Stefan Hiermaier
Date of defence: July 4$^{\text{th}}$, 2016

Institute of Aircraft Design
University of Stuttgart
2016

Acknowledgments

The research leading to the present work was conducted at the German Aerospace Center (DLR), Institute of Structures and Design in Stuttgart. I would like to acknowledge those, who especially contributed to the success of this thesis as well as my work.

I would like to thank my adviser, Prof. Dr. Heinz Voggenreiter (Director DLR Institute of Structures and Design and Professor at the University Stuttgart), for his scientific advice and for his confidence in my work. His guidance during all the time of my research as well as the writing of this thesis helped me staying on track. Furthermore, I would like to thank Prof. Dr. Stefan Hiermaier (Director Fraunhofer Institute for High-Speed Dynamics and Professor at the University Freiburg) for his interest in my research work and his examination as co-referee.

I am particularly thankful to Dr. Nathalie Toso and Christof Kindervater, current and former heads of the Department of Structural Integrity, for giving me the opportunity to work at DLR and also for supporting my desire to pursue this thesis in parallel to my project work. Special thanks go to Nathalie, who raised my interest in the topic of fluid-structure interaction and finally made me decide to accept the job at DLR.

I offer my profound gratitude to my technical adviser and colleague, Dieter Kohlgrüber. Dieter, thank you for your all-around-support from the very first minute of my work, for all our valuable discussions, and for your thorough review of the thesis.

Also, I am deeply grateful to Dr. Paul Groenenboom (ESI Group, Delft) for his dedication to the continuous development of the simulation software used. Paul contributed to the successful outcome of this thesis through countless discussions, software updates, and his patience to answer all my SPH-related questions with impressive clarity.

I express my sincere thanks to Dr. Alessandro Iafrati and his team (CNR-INSEAN, Rome), who managed the design, the manufacturing, and the installation of the test facility, and who finally conducted the guided ditching experiments, on which my research builds upon. Moreover, Alessandro helped my understanding of involved hydrodynamics and contributed to my knowledge through numerous discussions.

My thanks also go to my colleagues at DLR, who provided a pleasant working environment and valuable support at all times. Thanks for letting me be part of the team.

Last but certainly not least, I would like to thank my family. With their advice and their confidence in my abilities, my parents always supported me, which finally led me to this point.

Finally, I am extremely thankful to my wife for her ability of renunciation of time and her tremendous support. From my heart I thank you, África, for your motivation and constant encouragement, so to say for being my cheerleader, which helped me especially through the tough moments of the thesis. In return for your support, I promise to become fluent in Spanish. ¡Ahora! Para agradecer todo ese apoyo a mi encantadora esposa, prometo hablar fluido en español.

Stuttgart, July 2016

Martin Siemann

Contents

Nomenclature

Acronym	Meaning
ALE	Arbitrary Lagrangian-Eulerian
APDL	*ANSYS* Parametric Design Language
CAAC	Civil Aviation Administration of China
CEL	Coupled Eulerian-Lagrangian
CIRA	Italian Aerospace Research Center
CNR-INSEAN	Consiglio nazionale delle ricerche - Istituto Nazionale per Studi ed Esperienze di Architettura Navale
CPU	Central processing unit
CS	Certification Specifications
DOF	Degree of freedom
EASA	European Aviation Safety Agency
EC	European Commission
EOS	Equation of state
EWVT	Extended Weighted Voronoi Tessellation
FAA	Federal Aviation Administration
FAR	Federal Aviation Regulations
FE	Finite Element
FSI	Fluid-structure interaction
ID	Identifier code for guided ditching test cases
ISPH	Incompressible SPH
MLM	Modified Logvinovich Model
NACA	National Advisory Committee for Aeronautics
NTSB	National Transportation Safety Board
PLINK	Point link
SMAES	SMart Aircraft in Emergency Situations (EC-funded research project, 7th Framework Program, 2011–2014)
SPH	Smoothed Particle Hydrodynamics
TAD	Translating active domain
TPBC	Translating periodic boundary condition
VPS	*Virtual Performance Solution* (formerly *PAM-CRASH*)

Acronym	Meaning
WCSPH	Weakly compressible SPH
WVT	Weighted Voronoi Tessellation
XSPH	EXtended SPH

Abstract

Although occurring infrequent, the emergency landing of aircraft on water constitutes a crucial facet within aviation safety and, hence, it engages aircraft manufacturers within design and certification processes. Currently employed methods to analyze ditching comprise experimental testing, comparison with already ditching-certified aircraft designs, and semi-analytical as well as uncoupled numerical simulations. Since these means comprise several drawbacks and limitations, there is the motivation to employ advanced, coupled numerical methods to enhance the analysis capabilities of the structural behavior under ditching loads. Moreover, there is no fundamental understanding of the occurring hydrodynamic phenomena, the detailed fluid-structure interaction and the dynamic structural response in ditching. The subject is of particular interest as aforementioned methods do not consider effects due to structural deformations, which limits their validity. It is claimed by the author that structural deformations significantly affect the hydrodynamic loads acting during a ditching, as they modify the boundary conditions the fluid is facing; therefore, they should be taken into account for an accurate assessment of the structural behavior through coupled simulation approaches.

In this context, the present thesis investigates the structural behavior under representative impact conditions by means of an evaluation of experimental data as well as numerical simulations. In particular, it is investigated how and to what extent structural deformations affect the hydrodynamic loading during water impact at high horizontal velocity.

For that purpose, first the state of the art of methods for ditching analysis is reviewed with particular focus on advanced numerical simulation approaches. A more detailed insight is given into the coupled approach of Smoothed Particle Hydrodynamics (SPH) and Finite Element (FE) method, as it is adopted in this thesis.

Comprehensive experimental data of novel, unique guided ditching experiments conducted by CNR-INSEAN during the research project SMAES are evaluated. Based thereon fundamental knowledge about determining factors and key physical effects involved in the hydrodynamic loading and the corresponding structural response under ditching conditions is established. Starting with a characterization of the hydrodynamics, the structural behavior, and their interaction, the effects of impact conditions (combination of pitch angle and horizontal impact velocity), panel curvature, and structural deformations on hydrodynamic loads, resulting forces, and local strains are described.

Most interestingly, hydrodynamic loads are found to increase considerably as soon as structural deformations occur, which supports the above thesis. The assessment of the results of this evaluation establishes the basis for the subsequent development and validation of the numerical model.

Based on these findings, a numerical simulation model of the guided ditching experiments is developed adopting the coupled SPH-FE approach. Particular focus is put on enhancements of the fluid modeling, which previously did not permit such simulations at high forward velocity. Due to the application of state-of-the-art numerical techniques, the developed simulation model is robust and efficient, which for the first time enables profound numerical analyses.

Finally, results of comprehensive parameter studies are presented. These permit validating the developed SPH-FE simulation model based on extensive comparison with experimental data for a broad range of test cases. The regarded parameters are horizontal impact velocity, pitch angle, lateral panel curvature, and panel type (combination of material and thickness). Panels made of aluminum and composite materials with thicknesses between 15 and 0.8 mm are considered. Subsequently, the validated simulation model is employed to explore and to assess in detail the structural response of highly deformable structures under hydrodynamic loading. The mechanisms that were experimentally identified to affect the hydrodynamic loading of deformable structures are further investigated in order to assess their importance. Consequently, the findings of this numerical investigation corroborate the thesis that structural deformations should be taken into account in the analysis of the structural behavior through coupled simulation approaches.

Overall, the attained knowledge in this thesis contributes to a deeper comprehension of the behavior of aeronautical structures under hydrodynamic loading.

Kurzfassung

Obwohl Flugzeugnotwasserungen nur selten vorkommen, bilden sie einen kritischen Teilaspekt der Flugsicherheit und beschäftigen daher Flugzeughersteller im Rahmen von Auslegungs- und Zertifizierungs-Prozessen. Derzeit eingesetzte Verfahren zur Analyse von Notwasserung umfassen experimentelle Tests, Vergleiche mit bereits für Notwasserung zertifizierten Flugzeugmustern, und semi-analytische sowie ungekoppelte numerische Simulationen. Da die genannten Verfahren verschiedene Nachteile und Einschränkungen aufweisen, besteht die Motivation höherwertige, gekoppelte numerische Methoden zu verwenden, um die Analysefähigkeiten des Strukturverhaltens unter Notwasserungslasten zu verbessern. Darüber hinaus gibt es kein grundlegendes Verständnis der bei einer Notwasserung auftretenden hydrodynamischen Phänomene, der detaillierten Fluid-Struktur-Interaktion und der dynamischen Strukturantwort. Das Thema ist besonders von Interesse, da die oben genannten Verfahren die Auswirkungen von strukturellen Verformungen derzeit nicht berücksichtigen, was deren Aussagekraft einschränkt. Der Autor stellt die These auf, dass strukturelle Verformungen die hydrodynamischen Lasten während der Notwasserung erheblich beeinflussen, da sie die Fluid-Randbedingungen ändern. Für eine präzise Analyse des Strukturverhaltens sollten sie daher durch den Einsatz von gekoppelten Simulationsansätzen mit einbezogen werden.

In diesem Zusammenhang untersucht die vorliegende Arbeit das strukturelle Verhalten unter repräsentativen Aufprallbedingungen anhand einer Auswertung experimenteller Daten sowie anhand von numerischen Simulationen. Insbesondere wird untersucht, wie und in welchem Umfang strukturelle Deformationen die hydrodynamischen Lasten beim Wasseraufprall mit hoher Vorwärtsgeschwindigkeit beeinflussen.

Dazu wird zunächst der Stand der Technik der Methoden zur Analyse von Notwasserungen aufgezeigt, wobei der Fokus speziell auf den höherwertigen numerischen Simulationsansätzen liegt. Ferner wird ein detaillierter Einblick in den gekoppelten Ansatz aus Smoothed Particle Hydrodynamics (SPH) und Finite Elemente (FE) Methode gegeben, da dieser im Rahmen der Arbeit eingesetzt wird.

Umfangreiche Messdaten neuer, einzigartiger Notwasserungs-Experimente, die im Rahmen des Forschungsprojekts SMAES von CNR-INSEAN durchgeführt wurden, werden ausgewertet. Darauf basierend wird ein grundlegendes Verständnis der Einflussgrößen und der wichtigsten physikalischen Effekte, die die hydrodynamischen Lasten und die resultierende Strukturantwort bestimmen, erarbeitet. Beginnend mit einer Charakterisierung

der Hydrodynamik, des Strukturverhaltens und deren Zusammenspiel werden die Effekte der Aufprallbedingungen (Kombination aus Anstellwinkel und horizontaler Aufprallgeschwindigkeit), der Krümmung der Paneele und der strukturellen Verformungen auf die hydrodynamischen Lasten, die resultierenden Kräfte und die lokalen Dehnungen beschrieben. Interessanterweise wird festgestellt, dass hydrodynamische Lasten deutlich ansteigen sobald strukturelle Deformationen auftreten, was die obige These stützt. Die Bewertung der Ergebnisse dieser Auswertung bildet die Grundlage für die nachfolgende Entwicklung und Validierung des numerischen Modells.

Anhand dieser Ergebnisse wird ein numerisches Simulationsmodell der Notwasserungs-Experimente basierend auf dem gekoppelten SPH-FE Ansatz entwickelt. Ein besonderer Fokus liegt dabei auf Verbesserungen der Fluid-Modellierung, die derartige Simulationen bei hoher Vorwärtsgeschwindigkeit zuvor nicht zuließ. Durch die Anwendung moderner numerischer Techniken ist das entwickelte Simulationsmodell robust und effizient, was erstmalig tiefgreifende numerische Analysen ermöglicht.

Abschließend werden Ergebnisse umfangreicher Parameterstudien vorgestellt. Diese erlauben es, das entwickelte SPH-FE Simulationsmodell anhand umfangreicher Vergleiche mit experimentellen Daten für eine Vielzahl von Testfällen zu validieren. Darin betrachtete Parameter sind: horizontale Aufprallgeschwindigkeit, Anstellwinkel, Paneel-Krümmung in Querrichtung und Paneel-Typ (Kombination aus Material und Dicke). Es werden Aluminium- sowie Faserverbund-Paneele mit Dicken zwischen 15 und 0.8 mm betrachtet. Anschließend wird das validierte Simulationsmodell dazu verwendet, das Strukturverhalten hochdeformierbarer Strukturen unter hydrodynamischen Lasten im Detail zu erforschen und zu bewerten. Die zuvor anhand der experimentellen Auswertung identifizierten Mechanismen, die die hydrodynamischen Lasten auf deformierbaren Strukturen beeinflussen, werden weiter untersucht, um deren Einfluss zu bewerten. Die Ergebnisse dieser numerischen Untersuchung erhärten die These, dass strukturelle Verformungen die hydrodynamischen Lasten während der Notwasserung erheblich beeinflussen, und dass diese daher bei Analyse des Strukturverhaltens durch den Einsatz gekoppelter Simulationsansätze berücksichtigt werden sollten.

Insgesamt trägt das in dieser Arbeit erlangte Wissen zu einem tieferen Verständnis des Verhaltens von Luftfahrtstrukturen unter hydrodynamischen Lasten bei.

1 Introduction

Crashworthiness with emphasis on increasing passenger safety under dynamic loading is a central topic in aircraft design pursued by both aircraft manufacturers as well as research institutions. In the majority of cases, the structural behavior during impact on solid ground is analyzed and thus comprehensive knowledge has been generated[1]. The emergency landing on water, however, still challenges engineers due to the additional burden to account for the complex impact environment and the involved fluid-structure interaction (FSI). This chapter presents the background and motivation for the present work on fixed-wing aircraft emergency landing on water. Moreover, it defines the thesis and outlines the objectives of the work. Finally, the structure of the dissertation is given.

1.1 Background and Motivation

The topic of aircraft ditching has attracted large attention in public media in recent years through the successful emergency landing on the Hudson river near Weehawken, New Jersey, USA, on January 15, 2009. The Airbus A320-214 aircraft experienced multiple bird strikes just after take-off from New York's LaGuardia Airport leading to a loss of thrust on both engines, hence forcing the crew to pursue an emergency landing on the nearby Hudson. It is worth to note that with approximately 3.8 m/s (12.5 ft/s) the aircraft impacted at a much higher sink rate as specified by the airworthiness authorities under aircraft ditching regulations. Hence, this accident is considered a crash on water (cf. Section 2.1). However, all 155 occupants of flight US1549 survived with only five being reported as seriously injured. [5, 40, 66, 114]

More recently, on April 13, 2013, a Boeing 737-800NG aircraft operated by Lion Air (flight JT904) undershot the runway of Ngurah Rai International Airport (Denpasar, Bali, Indonesia) and crashed into the water surrounding this airport. According to flight data and cockpit voice recorders, the aircraft descended too early, leaving it about 1850 m short of the touchdown zone. Although the aircraft fuselage broke behind the center wing box, the airframe remained essentially intact. All 101 passengers and seven crew members survived—among them, only four passengers received serious injuries. [68]

Fortunately emergency landings on water, comprising ditching and crash on water, do not occur frequently as it was reported by Toso [156] who assessed water related civil jet

---

[1]Consult e.g. Waimer [161] for a comprehensive review of crashworthiness research.

Figure 1.1: Examples of two successful water emergency landings: 2009 US Airways accident
on Hudson River, New Jersey, USA (left, image from [120])), and 2013 Lion Air
accident near Ngurah Rai International Airport, Denpasar, Bali, Indonesia (right,
image from [68]).

transport aircraft accidents between 1959 and 2006. Most of today's air traffic, however,
operates over water and the majority of airports—approximately 76%—is located such
that approaches and near-airport operations, i.e. takeoff, final approach, landing, and go-
around, are above significant bodies of water [121]. According to Johnson [84], 60% of all
types of accidents of the worldwide jet fleet between 1959 and 1979 occurred during these
operations. This exposure highlights the importance to aviation safety and, therefore, the
need to analyze ditching as part of the aircraft design and certification process.

The overall objective of aircraft ditching analyses is to increase the survivability for
passengers and crew in terms of minimizing the risk of immediate injuries and allowing for
safe evacuation. This is directly linked to the overall structural integrity of the fuselage as
well as the separation or large distortion of interior parts [92]. Aforementioned accidents
emphasize the importance of structural integrity for the successful outcome of a ditching
event. In fact, water impact accidents generally appear to be survivable if structural
damages remain minor. This is attributed to lower decelerations and better floatation
characteristics allowing for proper evacuation if the structure remains intact [121]. Also,
early experimental findings support this claim; for instance, Fisher and Hoffman [43]
concluded, "Most airplanes could be ditched with relative safety if extensive damage to
the fuselage could be avoided; therefore, the strength of the fuselage bottom is probably
the most important parameter influencing ditching behavior."

In order to quantify the structural capacity of aircraft structures under hydrodynamic
loading, the prediction of global and local structural loads and resulting deformations
is of fundamental importance. The analysis, however, is very challenging as ditching is
a time-dependent, highly nonlinear multiphysics problem with different length and time
scales resulting in complex loading conditions and coupled fluid-structure interaction.

Therefore, the analysis of ditching has been widely based on experimental testing of
sub-scale models in order to evaluate the probable aircraft motion under various impact
conditions with the objective to demonstrate that the aircraft can make a safe landing.
However, effects related to the structural integrity are rarely regarded in recent experi-
mental campaigns because of the immense financial as well as temporal effort associated.

Also, such experiments require costly prototypes, limiting the number of designs to be investigated, and they only allow for a certain number of probes, which results in comparatively little insight into involved physical phenomena. Finally, quasi-rigid aircraft models are commonly used, which do not permit analyzing the structural response.

With growing availability of powerful computers in recent years, simulations are increasingly employed to analyze the structural behavior under ditching conditions. Current analyses are based on uncoupled approaches due to significant challenges associated with coupled approaches. Therein hydrodynamic loads are first established experimentally based on sub-scale model testing or computationally using simple (semi-)analytical approaches. Both means are rather inaccurate; for instance, sub-scale experimental testing suffers from inevitable scale effects and also available (semi-)analytical approaches rely on a list of assumptions and simplifications that lead to a lack of accuracy. Regardless of the method, hydrodynamic loads are derived based on rigid structures thus not accounting for effects of structural deformations. In a subsequent step, interpolated pressure loads are applied to finite element models with explicit time integration as they are used within conventional crash studies. Occurring structural deformations, which significantly modify the boundary conditions describing the FSI, are not taken into account because the two steps are not coupled. Consequently, current approaches do not account for inherent changes of hydrodynamic loads due to related structural deformations. In fact, it is not known how and to what extent structural deformations affect hydrodynamic loads. Nevertheless, the author claims:

Structural deformations significantly affect the hydrodynamic loads acting during a ditching, as they modify the boundary conditions the fluid is facing, and should be taken into account for an accurate assessment of the structural behavior through coupled simulation approaches.

The development of suitable numerical simulation tools employing coupled approaches offers great potential to improve the design and certification processes of novel aircraft. The considerably increased flexibility associated with numerical simulations could reduce development costs as well as time to market. In addition, the necessity for extensive experimental test campaigns could be significantly reduced, not only through partial substitution by simulations (virtual testing), but through improved design of experiments based on predictive pre-test simulations. Enhanced numerical tools will furthermore provide the means to assess the structural capacity of novel structural designs, for example, those that use hybrid materials or unconventional structural shapes. This potentially allows for increased structural performance in terms of robustness and vulnerability under hydrodynamic loading through vast amounts of studies possible with such numerical tools, as they allow a deeper insight beyond experimental measurements. In the future, this could eventually lead to a predominantly simulation-based design and certification.

1.2 Objectives and Structure

The objective of this thesis is to investigate how aeronautical structures behave under hydrodynamic loading as experienced during impact on water at high forward velocity in order to advance the fundamental understanding as well as to enhance the predictive capabilities of numerical simulations for the structural analysis within aircraft design and certification. The intended contribution to the state of the art comprises two main components:

(1) First, involved physical phenomena and determining factors are to be identified based on experimental data of a novel and unique experimental campaign of guided ditching tests. The influence of fundamental impact parameters and the relevance of structural deformations shall be evaluated in order to determine effects to be taken into account for the numerical modeling.

(2) Based on the attained knowledge, a coupled numerical modeling approach comprising the Smoothed Particle Hydrodynamics (SPH) and the Finite Element (FE) method is to be developed, validated, and assessed in terms of its predictive capabilities as well as its limitations. The numerical model should be able to adequately and efficiently reproduce the determining mechanisms and involved phenomena identified in the experimental evaluation, in order to investigate and to quantify the structural behavior under representative hydrodynamic loading.

The resulting structure of this thesis is given subsequently.

Chapter 2 provides fundamentals about fixed-wing aircraft emergency landing on water as well as its importance within the aircraft design and certification process. An insight into state-of-the-art certification procedures is followed by an overview of methods employed to investigate ditching. Particular focus is put on the SPH-FE approach that will be adopted within this thesis. The chapter concludes with a summary of identified challenges and open questions, which serve to define the detailed objectives of this thesis.

An experimental campaign of guided ditching tests under realistic full-scale impact conditions is presented in **Chapter 3**. The experimental setup is described and results are exploited in order to identify the determining factors involved in the FSI. Furthermore, the evaluation of experimental results presents the effects of impact conditions, panel curvature, and structural deformations on the test results. A summary and a discussion of experimental findings serve as basis for the subsequent development of the numerical simulation model.

Chapter 4 describes the development of the numerical model. Modeling aspects of the structural and the fluid model are presented. Furthermore, results of sensitivity studies are shown to illustrate and to assess the effectiveness of various modeling features.

In order to validate the simulation model comprehensive parameter studies covering different impact conditions and panel types are shown in **Chapter 5**. Moreover, the structural response is evaluated in detail to advance the understanding of the structural behavior under ditching loads. Achieved results are assessed and the capabilities and limitations of the developed numerical model are discussed.

Finally, **Chapter 6** summarizes the contributions and derived conclusions of this thesis. Encountered limitations throughout this work are addressed and possible directions for future research are presented.

2 Fundamentals and State of the Art

This chapter presents the fundamentals of the present work on fixed-wing aircraft emergency landing on water. After a distinction between ditching and crash on water, the characteristic phases as well as an insight into typical structural damages of real aircraft structures are presented. This is followed by a brief summary of relevant certification requirements and state-of-the-art procedures. In addition, an overview of relevant analysis methods with particular emphasis on structural analysis is presented. The SPH-FE approach adopted in this thesis as well as the fundamentals of the SPH method are briefly reviewed in order to provide the necessary basis for succeeding developments. Based on the review, current analysis methods are assessed with respect to their advantages and disadvantages, which finally leads to a summary of identified open questions and the formulation of detailed objectives of this thesis.

2.1 Ditching and Crash on Water

Fixed-wing aircraft emergency landings on water are classified into two basic categories: ditching and crash on water[1]. Ditching refers to a planned emergency landing on water. It is considered a planned event when prior to the water impact the aircraft structure is intact, the pilot has sufficient control of the aircraft, and there is enough time to prepare the aircraft as well as the passengers for the upcoming emergency situation. Ditching is to be distinguished from a crash on water, which may be either unplanned or which may occur under impact conditions other than those defined by the airworthiness authorities. This is, for instance, with a descent rate exceeding the design limit of typically 1.5 m/s (5 ft/s) or with loads outside the design limits specified in the certification regulations. [30, 84, 121]

Four consecutive phases of ditching are typically distinguished in literature [11, 92][2]: (1) approach, (2) impact, (3) landing, and (4) floatation as shown in Fig. 2.1. Below a comprehensive summary of each phase along with key aspects crucial for survivability is provided.

Phase 1: Approach Assuming that the pilot has sufficient control of the aircraft (flight controls and essential systems operative, except engines) and there is sufficient time for

---

[1]Crash on water is also referred to as unplanned ditching [30].
[2]Some authors regard impact and landing as one phase [22], but here they are considered separately.
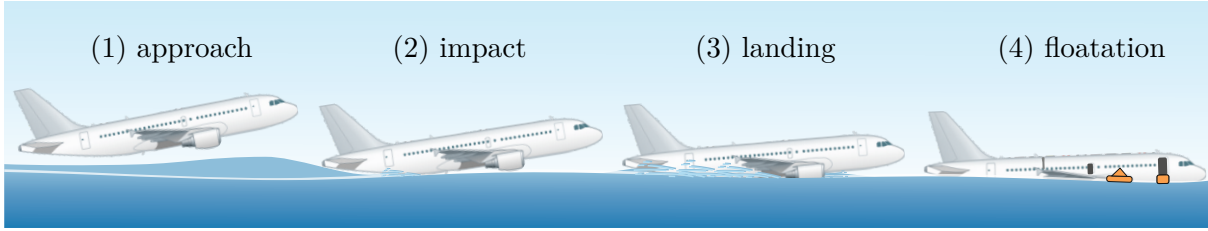
Figure 2.1: Illustration of consecutive phases of aircraft ditching.

preparation, the aircraft configuration is optimized to that one predetermined during certification in order to maximize the probability of occupant survival. In general, ditching aims at low approach velocities and corresponding nose-up attitude with the aircraft impacting in level position. Following a flare at the end of the approach phase to reach a minimal vertical velocity as recommended by the manufacturer, the aircraft should decent with the smallest possible rate, i.e. typically less than 1.5 m/s. In order to achieve these flight conditions, flaps are typically set to their maximum position to lower the impact velocity, fuel is jettisoned to reduce the weight and hence the landing speed, external ports and openings are shut, and the landing gear should be retracted [121]. However, in the case of a loss of engine thrust or limited controls, it is difficult to achieve the design ditching conditions, which consequently contributes to the severity of the impact.

Furthermore, the approach should be performed in accordance with the direction of wind and waves: in low sea state, ditching in the direction of the wind may allow for a lower impact velocity resulting in reduced loads making this approach safest. Ditching into pronounced waves, however, may be catastrophic, because the aircraft may tend to dive into the wave front causing fatal decelerations and significantly more structural damage. Therefore, in higher sea states with the presence of distinct waves, the approach should be made parallel to the wave crests, i.e. orthogonal to the wave direction. In the latter scenario, stronger crosswind with potential gusts may, however, endanger a landing in level position, which is essential.

Moreover, the crew informs and prepares the passengers for the upcoming emergency (e.g. wear life vests, prepare life rafts, and explain emergency exits as well as evacuation procedure) and the situation is communicated to the flight control in order to initiate rescue efforts.

Phase 2: Impact The subsequent impact phase, which starts with the first contact of the bottom rear fuselage to the water, is of highest interest for the structural analysis as the structure is subject to extreme loading conditions evoked by the hydrodynamic pressure acting on the skin. The pressure is characterized by sharp gradients in time and space with pressure peaks rapidly moving along the immersing structure. These high impact pressures typically cause large local deformations with membrane stresses in the fuselage skin. In the vicinity of stiffer structural parts such as stringers and frames, the

skin additionally carries very local bending stresses. This loading condition is significantly different compared to that in an impact on solid ground, where loads are directly transmitted into reinforcing structural parts such as stringers and frames, which are designed to absorb the impact energy. Furthermore, structural loads during water impact are generally lower but act longer compared to those of an impact on hard ground under similar impact conditions [6, 48]. Consequently, structural energy absorbers are typically not effective when impacting on water and the energy is only partially absorbed by structural deformation of the skin [81]. Thus, the impact energy during a water impact is primarily dissipated by momentum transfer to the water. The structural integrity of the fuselage skin is therefore of great importance because it has to transfer the water pressure loads to the supporting structure. Hence, the hydrodynamic loads depend on the structural integrity, which defines the boundary conditions for the FSI, and they will be significantly affected if the structure deforms or even fails. This poses a design challenge for crashworthy structures that should be effective for impact on both ground and water as discussed by Hughes et al. [72, 73]. The authors demonstrated the different failure mechanisms between ground and water impact for a helicopter subfloor structure under pure vertical impact conditions.

The damage to the aircraft during the impact phase usually covers buckling of the skin together with severe deformations of the bottom fuselage, potentially accompanied by rupture (see Fig. 2.2). Resulting openings in the skin immediately lead to loading and subsequent distortion of internal structures, endangering the structural integrity and possibly affecting the global aircraft kinematic behavior. Furthermore, the dynamic loading of internal structures can cause severe decelerations, which endanger human survival. In addition, openings will adversely affect the later floatation capability and are therefore not desirable. Inside the cabin, the passenger floor may undergo significant displacement
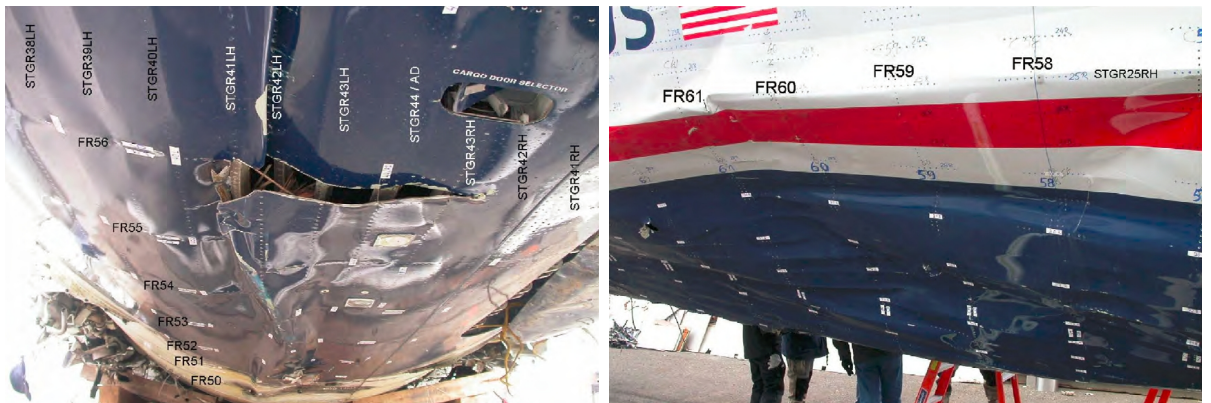

Figure 2.2: Exemplary damage to aircraft bottom fuselage. View on bottom rear fuselage (left) and side view on rear fuselage (right). Indications FR and STGR denote frame and stringer positions, respectively. Images refer to the 2009 US Airways accident on the Hudson River (cf. Section 1.1) and are taken from [112].

potentially leading to fracture of floor beams, dislocation of seats and items in the cabin, and jamming of exit doors. This puts the success of the subsequent evacuation at risk and may even directly cause fatalities. Generally, the larger the accelerations from the impact, the larger will be the extent of the damage. [73, 121, 156]

Phase 3: Landing   The subsequent landing phase starts with the immersion of the structure into the water and lasts until just before the aircraft comes to rest, i.e. when it starts floating. During the landing phase, hydrodynamic phenomena such as suction, overpressure, cavitation, air cushioning, air entrapment, and ventilation may occur. These are caused by the highly dynamic flow conditions involving water, air, and their mixture, as well as the resulting pressure acting along the structure in contact with water. Hydrodynamic phenomena affect the fluid-structure interaction and their occurrence may therefore influence the global aircraft motion during the landing phase leading either to a successful ditching or to the catastrophic failure of the aircraft accompanied by a higher risk of fatalities. In order to give an understanding of possible hydrodynamic phenomena, they are briefly summarized below[3]:

- Suction and overpressure: Due to the convex longitudinal curvature of a typical transport aircraft bottom fuselage and the large forward velocity of the aircraft relative to the water, the fluid flow undergoes an acceleration while the fuselage immerses. Consequently, the static pressure of the fluid decreases according to Bernoulli's principle. The reduced pressure may cause the rear fuselage to be sucked into the water, which affects the global aircraft motion as it was observed in numerous experiments (see Section 2.3.2). The occurrence of suction may be beneficial for the aircraft motion as it reduces the loads associated with the impact of the forward bottom fuselage. However, if the effect is too strong, it can result in skipping with uncontrolled subsequent impacts and typically severe consequences. In contrast, wetted areas near the root of the generated water jet and those ahead of the curved fuselage portion experience an overpressure, which acts opposed to the suction force.[4] This overpressure is essentially responsible for the local structural loading.

- Cavitation: In general, the phenomena of cavitation refers to the phase change of a fluid from liquid to vapor state, which is initiated by a local pressure drop below the fluid's corresponding vapor pressure. Thus, cavitation occurs in conjunction with the suction effect that is responsible for the required decrease of the pressure. Yet, cavitation provides a natural limitation to the suction forces as it restricts the

---

[3]Further information on possible hydrodynamic phenomena is given in various literature, e.g. [11, 22, 64, 74, 92, 124, 156, 165].

[4]Assuming typical aircraft fuselage designs, suction and overpressure zones are both located well behind the center of gravity.

minimum fluid pressure. The formation of cavities near the fluid-structure interface results in a decrease of mean density in the surrounding fluid, which may lower the hydrodynamic loads, and locally affects the acting pressure.

- Air cushioning: This effect refers to the compression of the air layer between the approaching structure and the water surface, which may deform the free surface prior to impact and form an air pocket. The resulting downward motion of the free surface reduces the hydrodynamic load during the early stage of the impact. The effect is the stronger, the more the air is prevented from escaping from underneath the structure. That is, for instance, due to small angles of incidence between structure and water as well as due to high impact velocities. Therefore, air cushioning is assumed to be more relevant for aircraft with flat and concave bottom fuselage shapes.

- Air entrapment and ventilation (also aeration): Air can get entrapped under the immersing structure resulting in air bubbles after the collapse of the air cavity. In addition, ventilation results from the reduced pressure in the impact zone due to the suction effect and describes additional air that is sucked under the immersed fuselage structure. Both phenomena aerate the water [39], which generally leads to a density reduction of the air-water mixture and reduces the magnitude of peak impact pressures [20, 97].

In addition to damages described for the impact phase, engines and nacelles, control surfaces, high-lift devices, and fairings may be torn off during the landing phase. In case that the structural integrity is lost during the impact phase, it may initiate global failure such as breaking of the fuselage. Some accident reports document fracture and separation of the fuselage[5], which typically occurs near sections of different stiffness such as near the wing box or behind the cockpit section.

Phase 4: Floatation After the aircraft has significantly slowed down, it should float for sufficient time to safely evacuate all passengers and crew. The structural damages experienced by the aircraft determine the amount of water ingress and thus the floatation capability. Additionally, structural damages may impede a rapid evacuation. Due to the presence of structural damages encountered during water accidents, the floatation phase typically ends with the aircraft sinking.

Fundamentally, the design of the aircraft may provide features with a positive contribution to its floatation capabilities such as a low-wing configuration and a large wing area. Also, the light weight of an aircraft due to empty fuel tanks is beneficial for the floatation.

---

[5]Cf. ditching of Lion Air Boeing 737 shown in Fig. 1.1 (right) or water landing of hijacked Boeing 767 in 1996 off Comoros Islands [93].

Overall, the survivability of a water emergency landing *ab initio* depends on the given emergency scenario. This comprises human factors such as crew experience and performance, available time to prepare passengers and aircraft for the impact, obeying instructions by passengers (belt up, brace position, ...), and other given conditions like distance to shore and time to rescue. Moreover, present environmental conditions, which are beyond control, such as sea state, water temperature, wind and wave direction, visibility and light conditions, and ambient temperature determine the survivability.

The above insight into the phases of a controlled water landing highlights the important role played by the structural integrity. In general, a crashworthy aircraft structure contributes to the survivability, which is directly linked to the amount of experienced structural damages [84]. Therefore, ditching and in particular the structural capacity under hydrodynamic loading must be investigated during aircraft structural design and certification in order to demonstrate compliance of the design with specific regulations as explained in the following section.

2.2 Ditching Certification

2.2.1 Requirements

Aircraft ditching must be considered during certification when an aircraft is designed for extended overwater operations[6]. Therefore, it is required for the majority of today's commercial jet transport aircraft. Just as for regular certification, specific airworthiness regulations contain the applicable requirements to be demonstrated by the manufacturer. The information given below is based on the *Certification Specifications CS-25: Large Aeroplanes* [31] issued by the European Aviation Safety Agency (EASA), but they are in accordance with similar regulations of the Federal Aviation Administration (FAA) and the Civil Aviation Administration of China (CAAC)[7]. Generally speaking, aircraft must meet the requirements of paragraphs §563 Structural ditching provisions, §801 Ditching, §807(i) Ditching emergency exits for passengers, §1411 General (Safety Equipment), and §1415 Ditching equipment. Among these, §801 contains the main ditching certification requirements for transport-category aircraft. The content may be summarized as follows:

- The design must minimize the probability of immediate occupant injury, e.g. structures must withstand loads such that passengers are not injured by their failure.

- The aircraft must provide and maintain appropriate means for evacuation, i.e. doors and emergency exits must be operative.

---

[6]According to the EC regulation 859/2008, OPS 1.060 Ditching [38], this applies to aircraft with a seating capacity of more than 30 passengers operating with a distance to the nearest shoreline greater than 400 nautical miles (approx. 740 km) or 120 minutes at cruise speed, whichever is the smaller.

[7]The CAAC regulations are in Chinese, yet their similarity is stated in [165].

- The probable aircraft behavior in a water landing must be shown by means of model tests or comparison with aircraft of similar configuration for which the ditching characteristics are known.

- The aircraft must float under probable water conditions for sufficient time and in appropriate trim allowing for evacuation of all passengers and crew into life rafts.

It is interesting to note that §801(c) explicitly prescribes means to demonstrate the probable aircraft behavior, i.e. model tests or comparison. In practice, manufacturers must determine and demonstrate optimum flight conditions allowing for safe ditching, which are to be included in the flight manual. From a structural design point of view, §563 requests that ditching provisions must meet structural strength considerations as under §801 (e), which states that structures must withstand probable maximum local pressures. Here, sufficient structural integrity comprising the global as well as the local structural capacity under hydrodynamic loading must be substantiated. The structural analysis enables an assessment of the amount of water ingress based on the predicted structural damages. This, in turn, has to be taken into account for the proof of floatability in terms of floatation time and attitude, both allowing for safe and rapid evacuation.

EASA currently reviews ditching regulations in order to provide further guidance [30, 162]. Based on a recent Certification Review Item [30], EASA presented its opinion: manufacturers should establish the optimum ditching conditions with respect to parameters such as aircraft weight, horizontal and vertical velocity, attitude, and flap setting upon initial contact in order to demonstrate compliance with the airworthiness regulations. Moreover, investigations shall assume the aircraft weight to be not less than the maximum design landing weight, the vertical impact velocity shall be not less than 1.5 m/s (5 ft/s), and the wing lift may be assumed to be equal to the aircraft weight upon impact. Finally, safe ditching characteristics shall be demonstrated for reasonable variations of key parameters such as horizontal impact velocity (+10% of established optimum) and attitude ($\pm 1°$). This shows that authorities request robust sizing to account for likely deviations.

Also, investigations of the 2009 accident on the Hudson river conducted by the National Transportation Safety Board (NTSB) led to several recommendations to EASA and FAA, who shall request aircraft manufacturers applying for ditching certification to demonstrate that their specific ditching conditions can be attained [66].

In summary, the objective of ditching certification is to increase the chances of survival of the occupants, whereas the loss of the aircraft is acceptable. Manufacturers typically substantiate ditching characteristics by a combination of comparison with previous designs, by sub-scale model tests, and, more recently, also by supportive numerical analysis. The following section provides an insight into state-of-the-art ditching certification procedures.

2.2.2 Procedures

Within the focus of this work, the following insight into state-of-the-art ditching certification procedures addresses means employed to evaluate the structural capacity and to some extent the global motion of the aircraft. Procedures used to investigate and prove floatation capabilities are not covered[8].

Design and certification procedures rely to a large extent on experimental testing of sub-scale models as well as on comparison with aircraft of similar design that have been proven to satisfy ditching regulations. For instance, according to Pilorget [126] the ditching certification of the Dassault Falcon 50, a medium size business jet, was achieved in 1979 by means of argumentation based on reports from the National Advisory Committee for Aeronautics (NACA) [43, 103] and by comparison with previous sub-scale model experiments conducted on Mystere 20, Falcon 10, and Mercure aircraft [52]. Furthermore, the ditching certification of the Airbus A320 in 1988 was based on the same NACA reports [43, 103] as well as on comparison with more than 200 experiments on sub-scale models of Airbus A300 B2 and Dassault Mercure aircraft [52] considering their similar geometries compared to the A320 [5, 40, 66]. Also the ditching certification activities for the Mitsubishi Regional Jet, a twin-engine regional airplane with a capacity of up to 90 passengers designed in Japan, comprised sub-scale experiments [101].

Recently, the analysis of ditching capabilities tends more and more toward the supportive use of numerical simulation tools as exemplary sketched in Fig. 2.3. For instance, Climent et al. [22] report about using a combination of 112 sub-scale model tests (1:8) and advanced numerical simulation techniques for the ditching certification of the EADS CASA CN-235-300M, a medium size military transport aircraft, accomplished in 2006. Their numerical approach was to apply interpolated, scaled experimental pressures on the bottom rear fuselage area of a deformable finite element full aircraft model using the explicit FE software package *PAM-CRASH* (today called *Virtual Performance Solution, VPS*). Accounting for the absence of deformation in the sub-scale experiments, the applied pressures were corrected by a factor of 0.58, which was estimated based on numerical investigations of vertical impacts of the same aircraft model onto a pure finite element water model. This technique was repeated for a set of critical cases accompanied by sensitivity studies. Within this nonlinear structural analysis, the aircraft was able to withstand hydrodynamic loads and thus its structural integrity was demonstrated [125]. Although this uncoupled approach gave insight into the amount of deformation and potential rupture of the structure, it relies on several simplifications and assumptions to take into account the effects of structural deformation. Moreover, it does not account for the coupled FSI, where the structural response interacts with the fluid flow responsible for the pressure distribution and the associated hydrodynamic loading.

---

[8]For floatation analysis procedures consult for instance [22, 121].
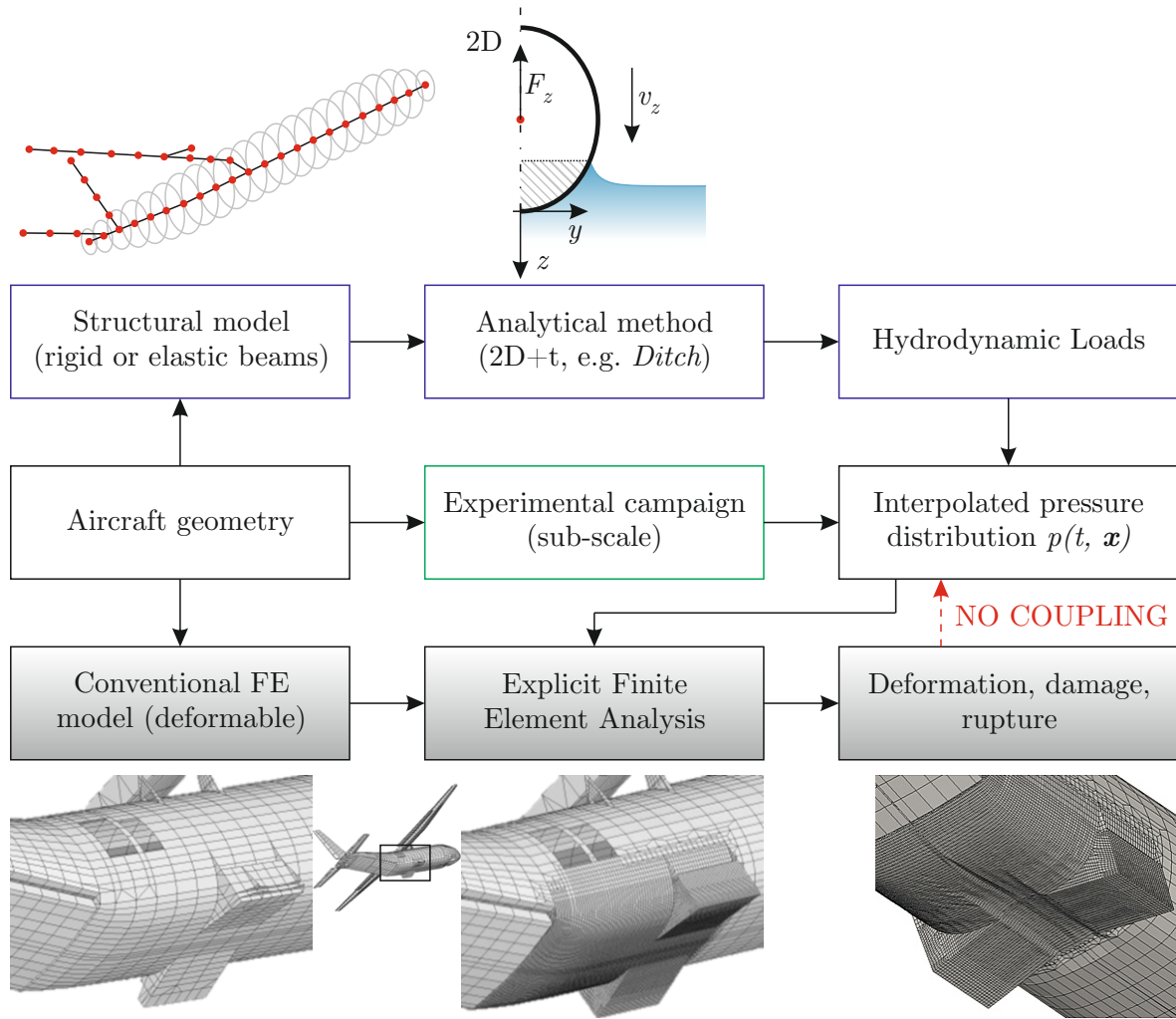
Figure 2.3: Scheme of uncoupled approaches for structural analysis using either experimentally or computationally established pressure distributions to load the finite element structural model. Images of aircraft FE model taken from [22, 125].

Novel aircraft, such as the Airbus A350 with approx. 50% of the structure in composite design, may no longer allow for comparison with similarly designed aircraft. Therefore, the A350 ditching certification was achieved by numerical analysis (see Fig. 2.3, top branch). The semi-analytical *Ditch* tool (see Section 2.3.3) was used to assess the global aircraft behavior for a variety of impact conditions. In order to investigate the structural capacity of the novel composite fuselage design under hydrodynamic loading, analytical pressure time histories derived using *Ditch* were mapped onto a detailed finite element crash model used within subsequent explicit finite element analyses with the FE software *Abaqus*. The same analysis approach yet with an alternative FE solver has been employed for the certification of the Airbus A380 with its unconventional design and size without the additional need for experimental testing. Overall, this approach, which does not take into account the coupled FSI, allowed to get an understanding of the extent of possible structural damages and it was accepted by the airworthiness authorities to substantiate the structural capacity under ditching loads.

To conclude, currently used means to prove the structural capacity in the aircraft design and certification process comprise experimental testing of sub-scale models, comparison with aircraft of similar design that have been demonstrated to satisfy ditching regulations, and, more recently, uncoupled numerical approaches. The above insight indicates that there is a strong request from aircraft industry for numerical tools due to their advantages[9]. However, currently employed numerical tools are on the one hand based on gross assumptions with respect to effects of structural deformation and failure, as rigid body aircraft are commonly used to establish the acting hydrodynamic loads. And on the other hand, they do not couple the hydrodynamics with the resulting structural deformation, for which the effects have not yet been investigated.

The limitations and drawbacks mentioned point out the necessity to incorporate advanced simulation tools using coupled numerical approaches into the process of analyzing ditching capabilities. Nevertheless, the application of coupled approaches within industrial processes requires significant enhancements as well as extensive validation in order to establish acceptance by the authorities. This thesis attempts to contribute to both.

2.3 Methods for Ditching Analysis

This section provides an insight into relevant methods for ditching analysis. In particular, methods employed for the analysis of the structural behavior under ditching loads as well as related effects due to structural damages are presented. Fundamental aspects of underlying theories and background information are included as required in order to facilitate the understanding as a whole. Yet, not every method is described in detail as this would exceed the focus of this work. Methods employed in the course of this thesis are presented in adequate depth. The purpose is to describe previous efforts to analyze the structural response due to hydrodynamic loading and to outline the state of the art.

Overall, there are several excellent reviews on the fundamentals of water entry and related applications. These are not repeated here, yet relevant information is briefly provided for completeness. A comprehensive review of work related to water entry was published by Seddon and Moatamedi [130] in 2006. The authors covered early analytical developments and experimental work starting in 1929 and completed their review with analytical, experimental as well as numerical work done until 2003 including several applications involving aeronautical structures (Apollo command module, Space Shuttle orbiter, solid rocket boosters). Most interesting for the present work, they concluded with an outlook on future work, which according to their findings "will almost certainly utilize numerical modeling techniques" [130]. However, they indicated the large amount of validation work required and also the need for a deeper understanding of the involved phenomena. Both issues will be addressed in this thesis.

---

[9]Refer to Tab. 2.2 in Section 2.3.4.

Hughes and Campbell [71] extended Seddon's review [130] dealing exclusively with helicopter water impact and related crashworthiness aspects in their review paper published in 2008. This work pointed out the significant advances in the field of numerical methods and in particular the coupled SPH-FE approach (cf. Section 2.4). Furthermore, a review paper by Abrate [4] on the superordinate topic of hull slamming featured a broad overview of related analytical models, experiments, computational techniques, as well as many applications in various fields, one of them being aircraft ditching.

In the remainder of this section, methods presented comprise accident investigations, experimental testing, and computational methods including (semi-)analytical, hybrid, and advanced numerical methods in the order mentioned. These three main methods are also referred to as the *triangle of aircraft ditching investigation methods* as proposed by Lindenau and Rung [92, 93]. Respective capabilities and achievements are discussed, and advantages as well as disadvantages are summarized at the end of each section.

2.3.1 Accident Investigations

A comprehensive review of available accident data on fixed-wing emergency landings on water may be found in [156]. Therein, an assessment of the type of water impact accident and its extent with respect to fatalities is presented, and four ditching accidents are described in more detail.

Furthermore, detailed investigations of accidents with the focus on ditching analysis have been published by Lindenau and Rung [93], who conducted a review of large transport jet aircraft ditching accidents between 1963 and 2009. Despite the low number of ditching accidents, their analysis provides interesting insight into the emergency scenarios and reveals valuable information on the structural damages as well as on the survivability.

In addition, specific accident reports[10] are issued by national agencies after investigations are completed. Such reports typically comprise highly detailed information on aspects of the emergency scenario. Photographs of the recovered structure, such as the ones shown in Fig. 2.2, allow assessing types and extent of structural damages.

In summary, investigations of accident data allow mainly for reconstruction of global kinematics based on data collected by flight data recorders assuming that they were recovered after the accident. However, their data acquisition rate is relatively low, which largely limits the insight into the physics of ditching [93]. Since ditchings occur infrequently, accident investigations are restricted to individual accidents (aircraft type, circumstances), which does not allow for general conclusions. With respect to structural analysis, accident investigations provide a view on the amount and types of structural damage after the accident, although damages may be falsified during recovery, which restricts the validity. A detailed analysis of the local structural behavior is not meaningful.

---

[10]See for instance [66, 112, 113].

2.3.2 Ditching Experiments

There is a wide range of experimental water impact tests available in the literature. Here the focus is put on experiments with relevance for fixed-wing aircraft ditching and in particular on investigations including the analysis of structural behavior and damages.

In general, ditching-relevant experiments can be classified according to the tested structure: simple geometrical shapes, sub-scale aircraft models, and full-scale aircraft. These groups are identified by increasing complexity as well as related financial and temporal efforts while decreasing the flexibility in terms of design changes and parameter studies. An insight into each group is provided in the following.

Simple Geometrical Shapes   Water impact experiments involving simple geometrical shapes were conducted in order to increase the knowledge about hydrodynamics and in particular the pressures acting on the bottom of seaplanes starting in the 1950s. Quasi-rigid structures in guided motion experiments were usually tested, which provided well-defined boundary conditions. Note that here solely oblique impact experiments are considered, whereas planing[11] experiments are not covered. Documented test series available in the literature include structures with flat [137], convex [32], convex-concave[12] [33], V-shape [35], and inverted V-shape [34] cross-sections. Although these experiments were performed at lower impact velocities than those expected during a transport aircraft ditching, they enabled a basic understanding of the hydrodynamic behavior.

One of the most renowned reports is that of Smiley [137], who conducted an extensive experimental campaign of guided impact experiments using an 18 mm thick, rectangular steel profile with a flat bottom surface measuring 1.5 m in length and 0.3 m in width. The author investigated pressure distributions occurring during impacts at different pitch angles (6–45°), horizontal velocities (7–26 m/s), vertical velocities (0.7–2.8 m/s), and with two different impacting masses (533 kg and 987 kg), which led to a total of 25 documented test runs. Measurements comprised time histories of vertical velocity and acceleration, pressures at 19 locations, draft, and wetted length[13]. As the focus was on pressure measurements and the structure was quasi-rigid, which prevented noticeable deformation, no strain data were recorded. Based on the experimental data acquired, Smiley comprehensively described the pressure distribution over the structure. The author not only demonstrated the presence of strong, characteristic pressure gradients in longitudinal direction, but also that these become sharper and very localized for smaller pitch angle cases and that the spatial pressure distribution becomes more voluminous when increasing the pitch angle[14].

---

[11]Planing is characterized by purely horizontal, steady motion, i.e. no vertical velocity component.

[12]The central part was convex, but the deadrise angle smoothly reduced toward the sides resulting in a locally concave curvature.

[13]Longitudinal distance of that part of the structure in contact with water.

[14]See for instance Fig. 6–9 in [137].

Although Smiley's work represents a valuable contribution to the field of oblique water impact, his findings must be treated with care as the available equipment in the 1950s was of low precision compared to today's standards. The author himself reported that the size of the pressure gauges relative to the area over which the peak pressure acts may have introduced significant errors. Also, the frequency response characteristics of the gauges may have had an effect, which could not be estimated. Similar findings were described by Smith et al. [138], who found that the maximum pressure measured in experiments depends on the size of the sensible element of the pressure gauge. This points out the difficulties of experimental pressure measurement under given impact conditions.

To summarize, there have been no relevant impact experiments at high horizontal velocity including simple deformable structures. Due to the lack of such experimental data, the effects of structural deformations on hydrodynamic loads under typical ditching conditions are still unknown.

Sub-scale Models   Experimental testing of sub-scale aircraft models is frequently utilized to demonstrate compliance for ditching certification as it is one means accredited by the airworthiness authorities (see Section 2.2.1). Such experiments allow exploring the ditching performance of corresponding full-scale aircraft based on comprehensive test series covering key parameters such as impact velocities, attitude, weight, position of center of gravity, flap setting, gear position, and sea state, but also unconventional design aspects such as external components. Measurements typically comprise attitude, accelerations, as well as pressures along the bottom fuselage, and they are usually supported by high-speed video recordings. Based on experimental observations, procedures for safe ditching are derived. In addition, experimental pressure measurements are used to analyze the structural capacity of the airframe as delineated in Section 2.2.2.

Scale model tests commonly assume reduced similarity with respect to geometry and kinematics, thus covering dominating effects during the regarded impact phase. This results in applying Froude scaling[15] based on constant Froude numbers $Fr = v/\sqrt{gl}$ between sub- and full-scale aircraft with velocity v, gravitation acceleration g, and characteristic length l. As it is not possible to scale all involved physics, there are inevitable scale effects. Nevertheless, as full-scale testing is practically impossible due to the exorbitant costs, sub-scale testing is widely used.

Starting in the 1940s, NACA researchers significantly investigated the ditching performance for a range of transport [42, 152, 153] and military [145] aircraft as well as the space shuttle orbiter [151] using dynamically similar sub-scale models. Typical model scales were between 1:10 to 1:30, which resulted in model sizes of up to 2.5 m in length and wingspan. Models were accelerated along a guide rail and subsequently released so that they glide freely onto the water.

---

[15]A comprehensive description of scaling laws can be found in [142].

Investigations covered effects of several design parameters such as the rear fuselage shape [103], external wing tanks [102], engine installations [153], and landing gear position [154, 155]. Frequently, flight conditions such as attitude, velocities, and weight as well as calm and rough sea states were considered [42, 152, 154, 155]. Also, specific ditching aids, i.e. additional structural components such as hydrofoils or hydroflaps, were tested in order to improve the ditching behavior [145]. Fisher and Hoffman [43] reviewed tests done by NACA until 1956 including a tabular summary of 37 investigations of different aircraft types[16] and discussed the effects of aforementioned design parameters.

Furthermore, Smith et al. [139] provided a broad review of experimental efforts mainly in the United Kingdom, but also in the United States and in Germany until 1948. The authors reported about testing techniques (free and guided impact experiments at sub- and full-scale), main results in terms of effects of manifold parameters affecting the ditching behavior, as well as design requirements. Especially the included series of photographs, which compare the ditching behavior of models with and without structural damage and with different configurations, are highly interesting as they illustrate the strong effects on the aircraft motion[17].

As mentioned previously, structural damages are likely to occur during a ditching and they generally affect both the aircraft motion during impact and landing, but also the subsequent floatation. Therefore, damages have been taken into account in numerous experiments. The simplest means to model effects due to structural damages was by removal of parts of the bottom fuselage [82]. Some tests also used pre-damaged, "crumpled" [43] sections. More sophisticated investigations included models with approximate scale-strength bottom sections (see Fig. 2.4) in order to qualitatively determine the typical location and the extent of damages as well as their effect on the global kinematics of the airplane depending on the impact conditions [44, 46, 152, 153]. These bottom sections were typically made of cardboard and balsa wood stringers and frames covered by waterproof paper or thin aluminum foil to model the skin [42, 43, 152]. The failure strength of these sections was determined by dimensions of the scaled stringers and frames; the aluminum skin was not strength-scaled as it only served to transfer the hydrodynamic loads to the structure. Deformable sections were constructed to be attached to the rigid fuselage models, which allowed replacement after testing.

Fisher and Thompson [46] conducted an interesting test program in 1949 where a previously tested Lockheed Constellation aircraft model [44] was equipped with a large external cargo container below the fuselage leading to a unique configuration. Based on

---

[16]A large variety of designs including bomber, fighter as well as transport aircraft with various configurations has been investigated; for instance, high, mid, and low wing configurations, aircraft of different size, and also with different bottom fuselage geometry (convex, flat, concave). It is particularly interesting to note that also unconventional designs such as a blended wing body type aircraft and some unusual fuselage shapes were considered.

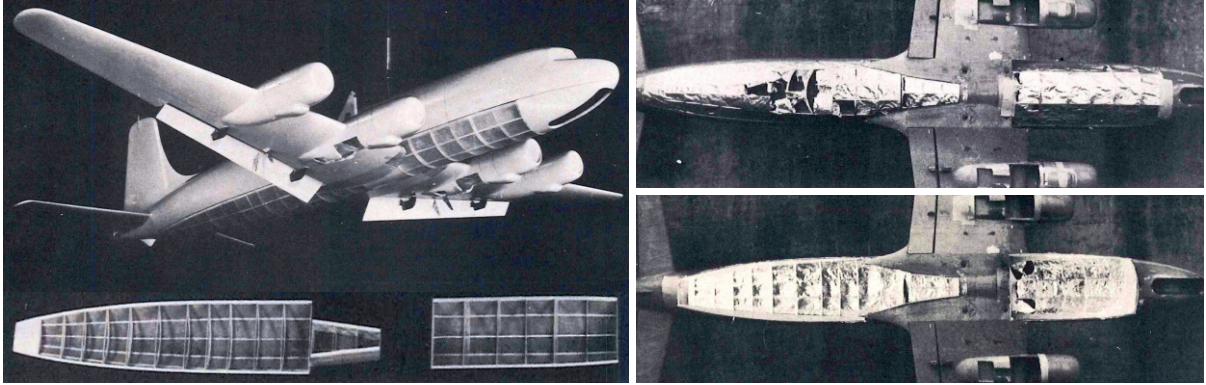[17]See for instance Fig. 9–13 in [139].

Figure 2.4: Exemplary sub-scale ditching experiments: DC-6 model with scale-strength bottom fuselage (left) and typical damage under different impact conditions (top right: DC-6, calm water; bottom right: DC-4, rough water). Images taken from [42].

comparisons of experiments with rigid and scale-strength containers, the authors found that the flexible cargo container absorbed sufficient amounts of energy to protect the behind fuselage structure, thus resulting in a significantly less severe ditching behavior.

In 1972, Thompson [155] investigated the ditching performance of a large jet transport aircraft with two different scale-strength bottom sections in order to determine whether there is a meaningful effect due to the change in bottom fuselage strength. The author concluded that there were "very little differences in the test results" between the different bottom sections; however, photographs presented in [155] show significantly more deformation of the weaker structures. Typically, considerable damage occurred in the rear part of the fuselage, which caused strong pitch down moments and larger decelerations compared to rigid models. Also, it is interesting to note that Thompson found very little damage for an impact condition at medium pitch and slower velocity (7° and 70.5 m/s) compared to very severe damage for the same airplane configuration impacting at small pitch angle and higher velocity (4° and 78.7 m/s).

Nowadays, typically rigid sub-scale models are utilized due to the large cost of testing deformable structures, which require replacing the deformable parts of the structure for every test repeat. One of the most recent test campaigns is that of the EADS CN-235 carried out in 2004, which comprised 112 test runs [22].

Overall, documented effects of structural damages on the ditching behavior of different aircraft are inconclusive, as they did not reveal a clear pattern. However, some common aspects could be identified: damages sustained by different models seemed to be more severe for designs with flat bottom sections and they mostly occurred near the part of the fuselage that impacted the water first. Moreover, damages at the rear bottom fuselage prevented the models from the typical nose up motion due to suction. The latter in most cases initiated diving with severe decelerations; for few configurations, however, it reduced the strong nose up motion and therefore lead to a better ditching performance.

Regarding the validity of such investigations, it has to be noted that they allowed a fundamental analysis of the consequences due to structural failure with respect to the global aircraft motion. However, they did not reveal details of the structural response nor the related determining fluid-structure interaction mechanisms, which could serve to improve the analysis of structural designs.

Albeit the lack of large horizontal velocity, the effects of structural deformations on hydrodynamic loads have been investigated for the impact of space capsules and the results add to the knowledge in the field investigated within this thesis. Stubbs and Hathaway [146] conducted vertical impact experiments of a 1:4 sub-scale model of the Apollo command module. Comparison of results obtained using rigid and flexible models showed that maximum forces acting on the model nearly doubled due to the occurrence of structural deformations. This finding emphasizes the importance to account for structural deformations in the structural analysis.

Full-Scale Aircraft   Full-scale experiments are extremely rare mostly due to their huge economical efforts and their lack of flexibility for parameter studies, which make them impractical and not favorable. Nevertheless, NACA conducted two full-scale experiments in the 1940s. The motivation for these tests was to show correlation between sub- and full-scale experiments in order to justify the use of sub-scale experiments.

The first test was conducted in 1944 with a B-24D aircraft that was flown by two pilots. The aircraft impacted on calm water at approximately 43 m/s horizontal and 0.5 m/s vertical velocity with 7.5° pitch angle. Pressure measurements along the bottom fuselage showed large pressures exceeding the range of the equipment. Even more interesting, also negative relative pressures, which indicate suction effects, were detected and subsequently correlated with video recordings showing a nose up aircraft motion. [144]

Correlation between the full-scale and the respective sub-scale experiments [45] has been documented in [82]. The authors concluded that a comparison was difficult to establish as only one full-scale test was available. However, a reasonable agreement was found for trajectories and attitudes despite the fact that the maximum horizontal deceleration in the full-scale test was about 50% greater. Interestingly, suction occurred in both cases, but the effect showed with a noticeable time delay in the sub-scale test.

Unfortunately, a second full-scale test with the same aircraft type aimed to investigate the effectiveness of a ditching aid (hydro-scoup) failed. This test was conducted with a remotely controlled aircraft, which was claimed as the main reason for the failure. Prior to the water impact, the control was not precise causing the aircraft to impact at a nose down attitude, which lead to rapid decelerations and a violent ditching.

Summary   Experimental testing has offered insight into hydrodynamics as well as the qualitative effects of structural damage. However, available experimental data do not

provide a suitable basis for development and validation of advanced numerical tools. This has two main reasons: most experimental studies were using rigid structures and the rare experiments on deformable sub-scale models did not provide detailed structural results. Hence, there exists neither knowledge about the structural response nor about its correlation with the hydrodynamic pressure.

Finally, major advantages and disadvantages of experimental investigations are summarized in Tab. 2.1.

Table 2.1: Advantages and disadvantages of experimental investigations [22, 121].

Advantages

- accepted by authorities as means of compliance for certification
- broad experience and knowledge available from series of sub-scale model tests
- handling of complex shapes as well as influence of sea state possible

Disadvantages

- extensive financial and temporal efforts for experimental campaigns; testing of full-scale aircraft is even economically unfeasible
- inherent scale effects related to occurrence and effects of hydrodynamic phenomena
- restriction to rigid sub-scale models, which usually do not account for structural deformations
- limitations in terms of design changes and amount of scenarios (parameter studies) to be tested, due to cost and time restrictions
- small amount of measurable results due to limited number of probes, which restricts the insight into physical phenomena and, therefore, the understanding
- repeatability of sub-scale model experiments can be difficult, especially for free flight experiments; its proof requires several repeats per test condition (additional cost, time)

2.3.3 Analytical, Semi-Analytical and Hybrid Approaches

As (semi-)analytical approaches are associated with state-of-the-art certification procedures (cf. Section 2.2.2), their basic functionality is outlined below. In addition, recent efforts directed toward inclusion of the local structural response into such approaches are briefly discussed.

2D+t Approach   The application of (semi-)analytical models for the study of ditching at large horizontal velocity commonly adopts the $2D+t$ approach. It is based on a discretization of major structural components such as fuselage, wings, and tail modeled as a series of two-dimensional, rigid cross-sections impacting the water. These 2D sections are generated by the intersection of earth- or body-fixed, transverse planes with the aircraft geometry. Using the earth-fixed definition, cross-sections may change depending on the aircraft longitudinal shape and motion as it is advanced in space over time. In order to represent the global structural stiffness, the 2D sections may optionally be interconnected by beam elements. Otherwise, the aircraft model is represented as a rigid body.

The $2D+t$ approach reduces the 3D problem into many 2D problems; therefore, the fluid motion is assumed to be two-dimensional within the plane of cross-section. Moreover, the flow in out-of-plane direction, i.e. in longitudinal direction of the fuselage, is neglected.

For each section, a water entry problem is solved, which includes the computation of the wetted surface (that part of the 2D section in contact with water), the pressure distribution, and the in-plane hydrodynamic force. Applied hydrodynamic models are generally based on the momentum theory and the concept of added mass developed by von Kármán [159] and Wagner [160] in the 1930s: von Kármán developed an analytical method for vertical water impact of simple, two-dimensional rigid bodies. Therein the fluid is assumed to be ideal, inviscid, incompressible, initially at rest, and its free surface is flat. Also effects due to gravity, surface tension, and the interaction with air are neglected. Only a few years later, in 1932, Wagner [160] extended von Kármán's approach by taking into account the local elevation of the free surface to determine the wetted surface.

As the Wagner model is known to overestimate loads especially for moderate and low angles between structure and water, Korobkin [87] analyzed several models for water impact and derived new models, one of them being the Modified Logvinovich Model (MLM). It mainly differs from Wagner's theory by taking into account the nonlinear terms of the Bernoulli equation when computing the hydrodynamic pressure, which Wagner discarded by linearizing the equation. For further details on the MLM the reader is referred to [87, 88, 149, 150].

Finally, hydrodynamic forces on each section contribute to the global forces and moments applied to the center of gravity of the rigid structure or, in case the global structural stiffness is represented by an elastic structural model, to each node of the respective beams.

Ditch   The $2D+t$ approach is utilized within the hybrid tool *Ditch*, which includes several specific features beyond the fundamentals described above. The tool was initially developed by Söding [140] starting in 1998 to calculate ditching loads and the resulting aircraft kinematics of transport aircraft during impact and landing phase. It allows the aircraft to move with only three degrees of freedom (DOFs): vertical displacement, horizontal displacement, and pitch rotation. Furthermore, *Ditch* accommodates an aerodynamic

model that estimates lift and drag depending on aircraft velocity and angle of attack. Other assumptions include symmetry toward the vertical plane, no wind, and no water waves. The computation of hydrodynamic loads follows the work of von Kármán [159] and Wagner [160]. Several extensions account for emerging sections with knuckles, blunt bodies, hydrostatic forces, and the effects of flow separation for the upward motion of the impacting body. Furthermore, effects of hydrodynamic phenomena such as cavitation and ventilation are approximated by simply limiting computed pressures. *Ditch* allows modeling the global airframe stiffness based on FE beams as described in the previous paragraph, yet local structural deformations are not accounted for. More detailed information on *Ditch* and its numerous correction methods can be found in [63, 91, 134, 141].

DRI-KRASH Another approach combining a simple structural and a hydrodynamics model is available in the software *DRI-KRASH* [163]. There the structure is modeled using elastic FE beams and nodes with assigned mass, which represent the global structural stiffness and mass distribution. The hydrodynamic forces acting on each of the structural nodes are computed based on so-called hydrodynamic elements, which require proper setup following a mixed analytical-empirical procedure. Another possibility to calibrate the hydrodynamic elements is given by additional numerical simulations. The latter is referred to as *global/local methodology* [123, 156]. The basic idea is to conduct advanced numerical simulations for the pure vertical impact of detailed structural models of representative aircraft sections, which provide the necessary nonlinear stiffness data for the subsequent and thus uncoupled *DRI-KRASH* simulation. In order to mimic structural failure, the hydrodynamic elements allow switching the load model upon reaching a defined normal load. Subsequently, another load model in normal direction is activated and a load model in perpendicular direction is added, which accounts for drag due to potential openings in the fuselage skin that lead to loading of internal structures.

Overall, *DRI-KRASH* allows for phenomenological modeling of hydrodynamic forces, which affect the global response of the aircraft. However, it requires knowing the sequence of structural failure a priori, which does not allow for a fully predictive analysis. Moreover, it does not allow to analyze the local structural response due to hydrodynamic loading.

Current Efforts toward Inclusion of Local Structural Response Available approaches presented currently do not account for the local structural response due to hydrodynamic loading. Consequently, the influence of structural deformations on hydrodynamic loads (coupled FSI) is not considered and a detailed structural analysis is not possible. However, including elastic structural models in analytical approaches is a current topic of research. Reinhard [128], for example, recently extended a two-dimensional water entry model based on Wagner theory by an elastic formulation for the structure modeled by beams. The author found that for large hydrodynamic loads, the flexibility

of the plate significantly influences the FSI and increases the hydrodynamic loads acting.

Although based on simplifications and several assumptions, a 2D analytical solution for an elastic beam entering water at constant vertical velocity mentioned in [3] shows that the resulting maximum pressure is proportional to the velocity and not to the square of the velocity as in the solution for a rigid body using Wagner theory. This is an interesting aspect as it points out a reduction of peak pressures when structures are deformable.

In conclusion, although there are efforts toward coupling structural mechanics and hydrodynamics, models found in literature remain restricted to simple geometrical shapes in two dimensions. Existing solutions are highly case dependent and, therefore, do not permit to be applied to realistic aeronautical structures. They serve, however, as a mathematical basis useful to investigate fundamental relationships, which contributes to the knowledge in this field.

Summary   Available (semi-)analytical and hybrid approaches are highly efficient and in particular suited for the assessment of global aircraft kinematics. Their efficiency enables broad parameter studies within early design stages, such as for instance the influence of weight distribution or approach conditions on the global aircraft motion. In addition, they may provide reference data to support validation of other numerical approaches.

Despite their advantages, analytical models are based on a list of simplifications and assumptions and thus only suited for particular cases. Owing to their analytical formulation with asymptotic solutions, they are prone to failure when dealing with locally flat or discontinuous structures, which gives strong limitations concerning possible structural shapes and overall robustness. Furthermore, although potentially allowing to account for the global airframe flexibility, they are limited to locally rigid structures and do neither permit to analyze the local structural response nor the effect of structural deformations and failure on the global aircraft kinematics.

2.3.4 Advanced Numerical Simulations

The term "advanced numerical simulations" herein refers to those computational approaches that use explicit time integration and include a detailed structural model, which are essential requirements to investigate the structural response under hydrodynamic loading. Generally, the FSI can be considered either uncoupled or coupled. In uncoupled computational approaches, the fluid solution is obtained independent of the structural solution, thus both computations run successively. This category also contains hybrid approaches (experimental-computational), where structural models are loaded with experimentally acquired pressure time histories (cf. Section 2.2.2).

Coupled computational approaches, on the other hand, simultaneously solve the fluid and the structural problem within one simulation. Due to the nature of the ditching problem including large nonlinear structural deformations that significantly alter the fluid

boundary conditions, coupled approaches become necessary in order to provide sufficient accuracy. This is further supported by several experimental as well as analytical findings that generally showed an increase of loads when structural deformation was considered. However, coupled approaches are significantly more complex and require additional computational effort. Several coupled approaches exist in literature; they can be further distinguished by their description of the fluid in Lagrangian, Eulerian, or Arbitrary Eulerian-Lagrangian (ALE) fashion. Common among all approaches is that the structure is modeled in Lagrangian description using the Finite Element method, which is established practice in crashworthiness analysis of aeronautical structures.

An insight into coupled approaches is given in this section in order to assess the approaches with respect to the objectives of this thesis.

Coupled Eulerian-Lagrangian (CEL) Approach In the CEL approach, structure and fluid are discretized independently using different reference frames for the description. The structure is modeled in Lagrangian fashion, where the mesh is attached to the material, and it is embedded into or superimposed to the fluid mesh[18]. The fluid domain can be discretized using either a classic Eulerian description, where the mesh remains fixed in space and the material is transported through the mesh cells, or a more sophisticated ALE description. The latter is an enhancement of the Eulerian description allowing for an arbitrary motion of the Eulerian mesh during the simulation with combined advantages of both Eulerian and Lagrangian description. The pure Eulerian description of the fluid domain offers one important benefit: as the mesh is fixed in space, it does not suffer from distortion through large fluid displacements, which usually occurs when using mesh-based Lagrangian methods. This has a positive effect on the stability as well as on the computational time step that is unaffected.

Using the ALE description, the fluid mesh may be moved in an arbitrary fashion as in theory it is independent of the fluid motion. Therefore, the mesh is typically updated throughout the computation (referred to as rezoning), which maintains sufficient element quality and hence prevents degradation of the time step. However, one disadvantage of ALE related to the arbitrary motion of the mesh is that when there is a lot of splash and spray, it gives rise to an increasing mesh size as the number of fluid cells is constant. Moreover, this additional freedom is paid by increased complexity of the formulation, which has to account for the material motion as well as the motion of the underlying mesh. Finally, these mesh computations also require additional computational effort compared to pure Eulerian or Lagrangian formulations. As the fluid mesh is no longer

---

[18]Note that the embedded variant results in conforming or non-conforming meshes, i.e. the structural nodes match fluid nodes in their position, whereas the superimposed variant uses two independent meshes. Here only the variant with superimposed meshes is considered as the embedded one faces strong limitations when structural failure is to be modeled. This flexibility is however counteracted by reduced accuracy. [19]

fixed in space, it may also be translated, which constitutes an advantage over the classic Eulerian formulation. For fixed-wing aircraft ditching, this allows to model the fluid mesh only around the aircraft structure and then to translate the mesh as the aircraft moves, resulting in a considerable reduction of the required fluid domain size as well as the associated computational cost. [29]

The structural and the fluid mesh require being coupled for FSI simulations. There are two fundamental ways: strong and weak coupling. Strong coupling is achieved when constraints on velocities are imposed on both fluid and structure by application of kinematic conditions, which potentially requires several iterations within one time step to enforce the coupling condition. In contrast, the coupling may be based on a weak formulation, where the interaction is established based on pressure forces of the fluid, which are transmitted to the structure, whereas the motion of the structure provides a weak feedback on the fluid, i.e. through the resulting change of boundary conditions for the fluid in the next time step. In general, strong coupling is more accurate, yet at the expense of a larger computational cost. Also, it may suffer from numerical instabilities if the coupling condition cannot be enforced under certain circumstances, thus making it less robust. Regardless of the chosen coupling formulation, the involved nodes or cells of the fluid mesh need to be detected within a domain of influence around the structure when using superimposed meshes. Therefore, an efficient search algorithm is required as this is repeated at each time step. For each structural node, the corresponding fluid nodes or cells are identified and the specific coupling conditions are applied. Fluxes between involved fluid cells on opposite sides of the structure must be blocked. Caused by the computation of fluxes between fluid cells, this approach may suffer from leakage and requires special attention. In addition, the weak formulation was reported to be sensitive to the coupling parameters (gap parameter, which represents a measure for the domain of influence, and stiffness) [6, 26]. Thus additional care is required when refining the fluid mesh. Moreover, there is usually some numerical diffusion, which reduces the accuracy.

Although the modeling variant with superimposed meshes seems superior as it offers the possibility to simulate structural failure and the fluid mesh generation is much easier as it may use a simple regular grid, it also comprises drawbacks: it results in a lower accuracy compared to the embedded modeling variants and consequently it requires a locally fine fluid mesh, which adversely affects the computational time and potentially also the simulation time step. More detailed explanations of modeling variants based on CEL and ALE approaches can be found in [19, 26, 29].

Typically, applications of the CEL approach for ditching contain water as well as air, which is regarded beneficial considering the modeling of hydrodynamic phenomena involving air. For instance, Zhang et al. [165] conducted CEL simulations with a pure Eulerian fluid model in order to investigate the effects of suction on the aircraft motion. They modeled a hybrid layer between the water and the air domain in order to cope

with the large density gradient at the surface. The authors reported that this hybrid layer affects the suction force predicted by the numerical simulation. Yet, they were able to reproduce sub-scale experimental results with very good agreement. Unfortunately, the authors did not mention any structural aspects and hence it is assumed that they simulated a rigid aircraft model.

Furthermore, Guo et al. [64] used a CEL approach with ALE fluid description in order to investigate the effect of the initial pitch angle on the aircraft motion during the impact phase. The considered aircraft was a 1:38 sub-scale rigid half model of a civil transport airplane that was allowed to move in three degrees of freedom. The authors found that there is an effect of the initial pitch angle on the aircraft kinematics, whereas the motion becomes gentler for larger initial pitch angles. They also report that a configuration with low horizontal tail limits the consequences of the suction effect. There is, unfortunately, no information on the computational time. However, the authors report using a mesh consisting of 11.15 million cells with a cell height of only 20 μm at the boundary, which suggests a large computational effort.

There are no reported applications of the CEL approach to ditching at high horizontal velocity where deformable structures were analyzed.

Purely Lagrangian Approaches There are two variants following a pure Lagrangian approach to discretize both fluid and structure. Common to both is that the structure is modeled using the FE method. The difference is in the fluid discretization, which can be mesh-based or mesh-free. In general, one advantage of Lagrangian over Eulerian approaches is that they require modeling only the current fluid domain and thus void does not require to be discretized owing to the fact that the mesh is directly linked to the material.

The mesh-based Lagrangian approach uses solid finite elements to model the fluid. This approach has been applied by Climent et al. [22] to evaluate the effect of structural flexibility based on pure vertical impact simulations of a rigid and a deformable aircraft FE model. Results were subsequently compared to establish a correction law that accounts for the effect of flexibility. It is interesting to note that their analysis resulted in a reduction factor of 0.58 for peak pressures above a certain threshold value. For their structural assessment, experimental pressure time histories were accordingly corrected and applied to a detailed FE model as described in Section 2.2.2. Furthermore, Pentecôte and Kohlgrüber [124] as well as Toso [156] applied a pure Lagrangian, mesh-based modeling for the fluid domain in their ditching analyses. The authors concluded that the mesh-based Lagrangian approach becomes impractical as soon as large fluid displacements occur. This is due to the severe mesh distortions associated (see examples in Fig. 2.5), which cause a large reduction of the stable time step and also deteriorate the accuracy.

Due to these inherent problems with mesh deformation and, in addition, the inability
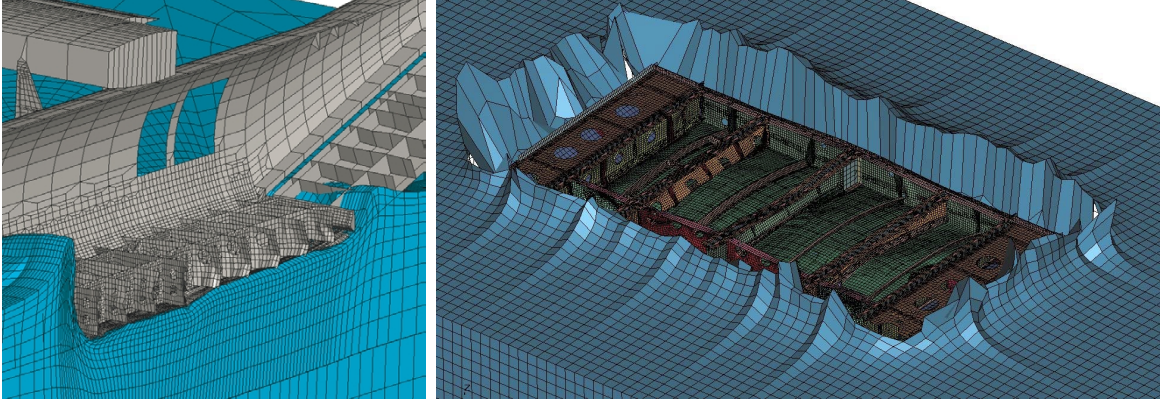
Figure 2.5: Typical mesh distortion using mesh-based Lagrangian formulation. Examples show pure vertical impact cases. Images taken from [22] (left) and [70] (right).

to account for complex, fragmented free surfaces (splash and spray), the mesh-based Lagrangian modeling for the fluid domain is neither suited for ditching simulations at large horizontal velocity nor for cases with significant structural deformations or failure.

The use of a mesh-free Lagrangian method to model the fluid domain allows to circumvent these problems and represents the second purely Lagrangian approach. One possibility for such an approach is the combination of the Smoothed Particle Hydrodynamics method for the fluid with the Finite Element method for the structure referred to as coupled SPH-FE approach. The approach has been reported to allow for significant advances compared to the mesh-based Lagrangian approach [15, 27, 156]. A more detailed review of this approach is provided in the subsequent section, as it is adopted for the numerical simulations in this work.

Assessment and Comparison   Although the SPH-FE approach is explained in the following section, at this point, a brief assessment of capabilities of the coupled CEL (pure Eulerian or ALE) and the SPH-FE approach in water impact applications is conducted in order to substantiate the choice for the SPH-FE approach in this work. This assessment is based on comparative studies found in the literature. Ortiz et al. [117] conducted full-aircraft ditching simulations using CEL/ALE and SPH formulations within the commercial solver *RADIOSS*. The authors mention the very large computational cost of both approaches (in the order of 300 hours for 500 ms of simulated time) and indicate that the ALE model quickly gave rise to numerical instabilities caused by mesh distortion. Furthermore, Francesconi et al. [49] simulated the vertical impact of rigid wedges and semi-cylinders as well as the ditching of a rigid model of a Puma helicopter using both CEL/ALE and SPH-FE approaches within the commercial FE program *LS-DYNA*. Whereas numerical acceleration results were of similar accuracy and in satisfactory agreement with experiments, the high computational effort of the CEL/ALE simulation was pointed out. Similar findings were published by Capone [17], who simulated the vertical

impact of a frame-reinforced semi-cylinder made of steel. Numerical results established with CEL/ALE and SPH-FE models using *LS-DYNA* were compared with experimental data. The author reported a closer correlation of results of the SPH-FE model with experiments in terms of accelerations as well as pressures for a range of three different impact velocities. Moreover, it was stated that the computational time was twice as long for the CEL/ALE simulation. Anghileri et al. [6] compared several numerical methods, among them mesh-based Lagrangian, ALE and SPH methods, with respect to their capabilities in reproducing the vertical water impact of a thin composite panel including panel rupture. Again *LS-DYNA* was employed. It was resumed that the ALE solution provided accurate results, but these depend on the choice of coupling parameters. The SPH solution was reported to offer the best ratio of computational time versus accuracy; however, the authors criticize the effort required to determine the required particle size.

Although the SPH-FE approach appears to be superior, a universal conclusion is inadmissible. In fact, the capabilities and the performance of different approaches depend on the stage of development of the software used as well as on the detailed parameter settings and the implemented formulation of the numerical method applied. Furthermore, results may vary depending on the specific application. Nevertheless, within this thesis, the SPH-FE approach is adopted as it has already been successfully applied by various researchers for water impact simulations involving structural analyses as will be shown in Section 2.4.3.

Interestingly, Seddon and Moatamedi [130] also pointed out SPH as a promising method to investigate water impact cases in their comprehensive review on water impact related research between 1929 and 2003.

Concluding this section, the advantages and disadvantages associated with advanced numerical simulations in the context of this work are summarized in Tab. 2.2.

Table 2.2: Advantages and disadvantages of advanced numerical simulations.

Advantages

- possible prediction of structural behavior of novel, unconventional designs and also complex structures such as stringer-reinforced panels, which would be extremely expensive to test (keep in mind that for testing with occurring damage, structures can only be used once)
- large flexibility for design changes using parametrized models
- numerical analyses allow identifying impact conditions, where structural failure is initiated; in return, this may support substantiation toward airworthiness authorities by proving safety factors and robustness (conservatism)
- improved preparation of experimental test programs through pre-test simulations, which may allow for reduction of extent, larger success rate, and superior test results; for instance, positions of probes may be chosen based on experience from simulations in order to yield precise, targeted measurements
- interpretation of experimental results is facilitated through accompanying simulations, thus allowing for enhanced understanding
- deeper insight into physics through investigation of detailed structural behavior and potential to extend experimental database (e.g. going beyond test conditions by variation of impact velocity or structural design)

Disadvantages

- large computational effort for advanced numerical simulations impedes broad parameter studies
- typically numerical difficulties, e.g. mesh dependency, numerical noise
- to date not accepted as means of compliance by airworthiness authorities due to lack of validation and thus low attributed reliability
- require detailed structural models, which may not exist during early design phases
- also not "for free" (cost of hard- and software, licenses, and operating costs of larger computing clusters)

2.4 Coupled SPH-FE Approach

The present section deals with the coupled approach of Smoothed Particle Hydrodynamics (SPH) and Finite Element (FE) method. Fundamentals, coupling methods, and selected applications of water impact with relevance for this work are presented.

2.4.1 Fundamentals

Using the mesh-free SPH method, the fluid domain is discretized with a set of Lagrangian particles that are not interconnected. These particles are to be understood as integration points with an associated volume, which carry the fluid properties, rather than discrete physical particles. As there is no mesh, SPH uses kernel interpolation to approximate field variables at any point in the domain. Particles move based on solving the conservation equations of continuum mechanics. The fundamentals of SPH are presented in more detail in Section 2.5.

Structures are modeled using the explicit FE method, which today is common practice for analyses in the field of structural dynamics. Therefore, for fundamentals of the FE method, the reader is referred to the comprehensive literature available (e.g. [67, 167]).

The coupled SPH-FE approach is particularly suited for the simulation of aircraft ditching. It combines the advantages of the FE method, which is well-established for the simulation of nonlinear structural dynamics, with those of the SPH method, which naturally handles large fluid displacements and complex free-surface shapes. The Lagrangian mesh-free character of SPH allows for flow around and through complex structures, which suits well to portray structural failure and progression of water into the aircraft including the subsequent loading of internal structure.

The advantages of the approach are, however, confronted by its large computational cost. On the one hand, this is due to the SPH solution, which is CPU intensive per time step as integration points are not interconnected like in mesh-based Lagrangian methods. Thus, interactions must be repeatedly redetermined. On the other hand, the combination of rather long physical times with small time steps required for the stable explicit time integration comprising deformable finite elements drives the computational effort. Finally, the large horizontal velocity typical for fixed-wing aircraft ditching requires long fluid domains, which in combination with a fine particle resolution needed to capture the main physics of the FSI represent an additional challenge. To deal with this, the amount of particles used for the simulation must be significantly reduced in order to allow for efficient computation.

One possibility facing this high computational effort is the hybrid modeling of the fluid domain shown in Figs. 2.6 and 2.7. There only the inner portion of the fluid domain, which is subject to large displacements, is discretized with SPH particles. The surrounding fluid necessary to provide a water domain of sufficient size to avoid boundary effects is modeled

using solid finite elements. These are computationally much cheaper compared to an SPH discretization of the same volume. For fluid regions with limited displacements, finite elements, therefore, provide an effective and more efficient solution. Within this hybrid fluid domain, the two methods are typically coupled using a tied contact formulation to connect the interface in such manner that displacements of the outer layers of particles and respective volume elements are linked by constraining their associated nodes. This hybrid modeling has been adopted within many investigations of various authors [22, 86, 124, 156].

2.4.2 Coupling

In order to allow for fluid-structure interaction, it is required to couple the SPH and the FE method. Resulting from the Lagrangian character of SPH, it may be easily coupled to finite elements using master-slave contact algorithms based on work by Attaway et al. [8] and Johnson [83]. Such contact algorithms aim to transmit loads between contact partners and to prevent penetration. This type of coupling may be understood as a weak coupling (cf. Section 2.3.4) where loads are exchanged through a penalty-type contact algorithm and the feedback of the structure, i.e. the change of boundary conditions for the fluid, acts in the subsequent time step when the structure has been displaced.

The specific formulation typically employed refers to a node-to-segment penalty contact [53, 58, 156]. Therein the finite elements of the structure represent the master segments and the fluid particles represent the slave nodes. Such a contact computation comprises two stages: contact search and force computation. Upon penetration of a slave node into a master segment's contact zone, which for shell elements is defined by an offset called contact thickness, contact partners are detected. For that purpose, a bucket search algorithm is typically employed, which increases the computational efficiency. Next, the contact force is computed as the product of penetration depth and contact stiffness. The latter is calculated based on an equivalent nodal mass and the stable finite element time step. As a result, the particle experiences a repelling contact force in the direction of the surface normal and the structural nodes belonging to the master segment in contact proportionately bear this force in opposite direction (Newton's third law). In order to prevent penetration for high energy impacts on thin structures, i.e. with very small contact thickness, a nonlinear, progressive stiffness may be defined.

An alternative coupling based on work by Campbell et al. [16] has been presented by DeVuyst et al. [24], who refer to it as node-to-node contact potential algorithm. In their approach, FE nodes detected within the kernel support domain of surrounding SPH particles are also treated as SPH particles in order to establish contact. Consequently, repulsive contact forces are computed based on SPH-like interactions. This contact model offers the advantage that it does not require computation of surface normals of contact segments [24].
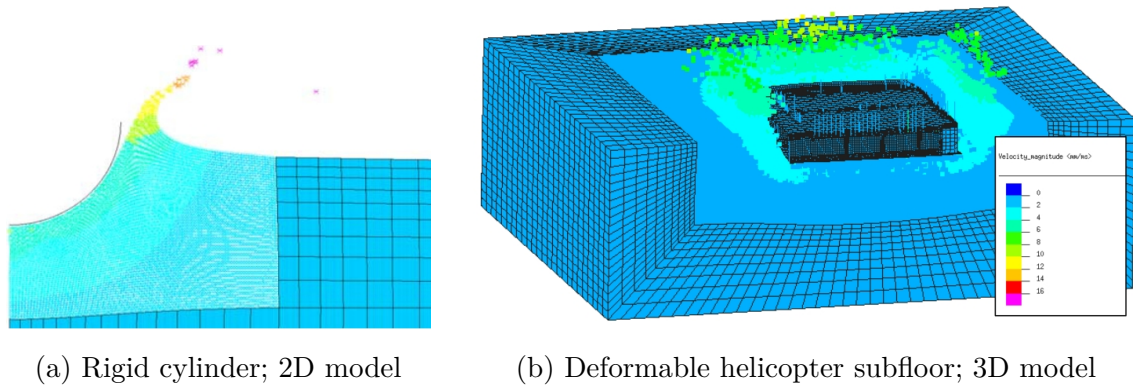
(a) Rigid cylinder; 2D model   (b) Deformable helicopter subfloor; 3D model

Figure 2.6: Examples of vertical water impact simulations using the hybrid SPH-FE modeling technique for the fluid domain. Images from [156].

For more detailed information on coupling methods between SPH and FE method, dedicated works by Sauer [129] and DeVuyst et al. [24] can be consulted.

2.4.3 Selected Applications

Vertical Impact Starting with fundamental investigations of vertical impact cases using simple, rigid geometries such as wedges, cylinders, and spheres by Pentecôte et al. [123], the application has been extended to vertical impacts of deformable aeronautical structures such as a fuselage section, a helicopter subfloor (see Fig. 2.6, b), and a full helicopter [70, 124, 156]. These studies were conducted using the explicit FE software package *PAM-CRASH* (now called *VPS*) in order to assess the performance of pure mesh-based Lagrangian and hybrid SPH-FE modeling approaches for the fluid domain as mentioned in Section 2.3.4.

After confidence in using the SPH-FE approach had been gained, Kohlgrüber et al. [86] applied the approach to simulate the vertical impact of a composite helicopter subfloor structure. Simulations using *PAM-CRASH* were conducted to support the development of a novel subfloor design. This design was supposed to be able to avoid skin rupture upon water impact in order to transfer water pressure loads to the primary structure, which is commonly designed to absorb impact energy. In regard to the objectives of their work, a detailed deformable structural model was developed. The authors found very good agreement between detailed numerical and experimental results in terms of observed damages to the structure. It is interesting to mention that based on the numerical analysis a large risk of skin failure was identified near stiff keel-beam intersections where large bending moments were observed. In addition to good structural results, the authors pointed out the large computational cost related to the SPH method.

More recently, Grimaldi et al. [53] simulated the vertical impact of stiffened semi-cylinders made of steel using the SPH-FE approach in *LS-DYNA*. Comparisons of accelerations as well as global structural behavior were found to be in good agreement with
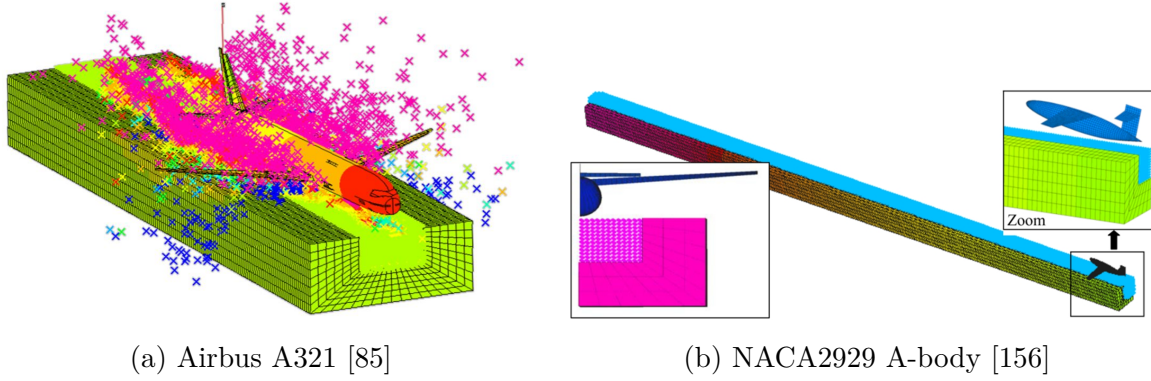
(a) Airbus A321 [85]   (b) NACA2929 A-body [156]

Figure 2.7: Examples of oblique water impact simulations using the hybrid SPH-FE modeling technique for the fluid domain and rigid aircraft models.

experimental data for three different impact velocities (3 m/s, 8 m/s, and 10 m/s). The authors stated: "the SPH approach appears to be a very effective formulation for the global reproduction of the water impact phenomena" [53].

Oblique Impact Ditching simulations of fixed-wing aircraft with predominant horizontal velocity component were first reported by Pentecôte and Kohlgrüber [124], who utilized *PAM-CRASH*. In general, the presence of a horizontal velocity requires a much larger fluid domain and longer physical times to be simulated, both making the simulation much more challenging. Due to the computational effort, a rigid body model of an Airbus A321 aircraft was used to assess different simulation methodologies for the fluid domain in terms of quality and computational time. The authors report that using a hybrid SPH-FE fluid model as discussed in Section 2.4.1, it was possible to simulate 1700 ms of physical time in about three weeks on a single processor workstation. An exemplary illustration of the simulation is shown in Fig. 2.7 (a). Despite the large computational effort, it was possible for the first time to assess the global aircraft motion based on an SPH-FE simulation. The model was subsequently used to evaluate the survivability in terms of accelerations acting on passengers at several locations along the aircraft fuselage.

The SPH-FE approach has also been applied to simulate the ditching of an EADS CN-235 aircraft [22]. As mentioned in Section 2.2.2, this work was done in addition to an extensive experimental test program conducted for the ditching certification of this aircraft. Consequently, the numerical rigid body aircraft model was scaled to match the experimental one and initial conditions for the simulation were adapted accordingly. Simulation results were assessed based on extensive comparison with experimental data. It was found that especially pitch kinematics are not reproduced by the numerical model as it did not account for the suction effect. Furthermore, pressures were largely overestimated and their time evolution was much sharper compared to experimental observations. However, the main disadvantage pointed out by the authors is the extreme computational effort.

Furthermore, Pentecôte and Kohlgrüber [124] and Toso [156] presented results of a ditching simulation of a rigid NACA2929 A-body aircraft model shown in Fig. 2.7 (b). This test case refers to an experimental campaign conducted by NACA investigating the effects of the rear-fuselage shape on the ditching behavior [103]. The simulations showed the necessity to account for the suction effect within numerical simulations in order to correctly reproduce the global aircraft kinematics.

More recently, Benítez Montañés et al. [11] demonstrated that it is possible to mimic the effect of suction on the global aircraft kinematics by application of a special penalty contact formulation that allows—besides the standard repelling contact forces—also for attracting contact forces. Comparison with experimental measurements showed a much better agreement of the pitch time history. Yet, the authors stated that there is a need to relate this purpose-based model to physical values.

In summary, the SPH-FE approach has been successfully employed within several ditching investigations; however, these either involved pure vertical impacts or rigid structures. Its application to analyze deformable structures impacting at high horizontal velocity has not been reported to date.

2.5 Smoothed Particle Hydrodynamics

Smoothed Particle Hydrodynamics was introduced independently by Gingold and Monaghan [51] and Lucy [95] in 1977 as a mesh-free Lagrangian particle method to solve astrophysical problems. In 1994, the method was applied by Monaghan [108] to simulate free-surface flows. Ever since, SPH went through substantial development and its application in the field of fluid mechanics as well as fluid-structure interaction rapidly evolved. In the field of aeronautical engineering, SPH is nowadays utilized to analyze, for example, bird strike [65, 104], ice impact [125], fuel sloshing [25], as well as ditching of helicopters [18, 156] and aircraft (see Section 2.4).

This section briefly introduces the fundamentals and the main aspects of the SPH method adopted in this work to enable a better understanding of its application and its enhancements throughout the course of work[19]. Among the variety of existing SPH formulations for fluid mechanics, the one presented here refers to the specific formulations available in the software *VPS*, which is used for the numerical simulations in this thesis.

2.5.1 Fundamentals

Kernel Approximation   SPH fundamentally builds upon the integral representation of a field function $f(\mathbf{r})$, where $\mathbf{r}$ is an n-dimensional position vector. It states in general,

---

[19]Detailed reviews on the development of the SPH method may be found in comprehensive reviews by e.g. Benz [12], Liu and Liu [94], Monaghan [107–110], and Randles and Libersky [127].

that the value of f at the position $\mathbf{r}$ is evaluated by interpolation of all known values of f at positions $\mathbf{r}'$ in the integration domain Ω. Considering $f(\mathbf{r})$ being continuous on the domain Ω, the exact integral interpolation of $f(\mathbf{r})$ can be written as

$$f(\mathbf{r}) = \int_\Omega f(\mathbf{r}')\delta(\mathbf{r}-\mathbf{r}')\mathrm{d}\mathbf{r}' \quad \text{with} \quad \delta(r-r') = \begin{cases} \infty & \text{for } r = r' \\ 0 & \text{otherwise .} \end{cases} \tag{2.1}$$

The Dirac δ-function in (2.1) has a value of zero everywhere except at zero where it has a theoretical value of infinity and it's integral value is unity. Approximating the δ-function in (2.1) with a well-conditioned weighting function referred to as kernel or smoothing function $W(\mathbf{r}-\mathbf{r}',h)$ provides the so-called kernel approximation of the SPH method as in (2.2)[20].

$$f(\mathbf{r}) \approx \langle f(\mathbf{r}) \rangle = \int_\Omega f(\mathbf{r}')W(\mathbf{r}-\mathbf{r}',h)\mathrm{d}\mathbf{r}' \tag{2.2}$$

The parameter h represents the smoothing length, which is the measure of the support domain of the kernel function W. The kernel function $W(\mathbf{r}-\mathbf{r}',h)$ should obey the following criteria:

- it has to represent the δ-function for $h \to 0$: $\lim\limits_{h \to 0} W(\mathbf{r}-\mathbf{r}',h) = \delta(\mathbf{r}-\mathbf{r}')$

- its integral value is equal to unity: $\int_\Omega W(\mathbf{r}-\mathbf{r}',h)\mathrm{d}\mathbf{r}' = 1$

- it should be at least as many times differentiable as the field function $f(\mathbf{r})$

- its value should be monotonically decreasing when increasing the distance $\mathbf{r}-\mathbf{r}'$

- it is an even function: $W(\mathbf{r}-\mathbf{r}',h) = W(|\mathbf{r}-\mathbf{r}'|,h)$

- its gradient is symmetric: $\nabla W(\mathbf{r}-\mathbf{r}',h) = -\nabla' W(\mathbf{r}-\mathbf{r}',h)$

- it has a compact support: $W(\mathbf{r}-\mathbf{r}',h) = 0$ for $|\mathbf{r}-\mathbf{r}'| > \kappa h$, with κh representing the boundary of the integration domain Ω

In literature, numerous kernel functions ranging from polynomial to Gaussian-type formulations are found. The different properties of the kernel functions may influence the results; therefore, the choice of the kernel function is essential. A typical shape is shown in Fig. 2.8.

Particle Approximation The second step in deriving the basic SPH formalism is the so-called particle approximation where the integral formulation is discretized onto a finite set of particles. The particles carry physical as well as numerical properties and are to be understood as interpolation points. In this step, the integral in (2.2) is replaced

---

[20]Brackets $\langle \cdot \rangle$ denote the approximation; however, for legibility, this notation will be discarded below.
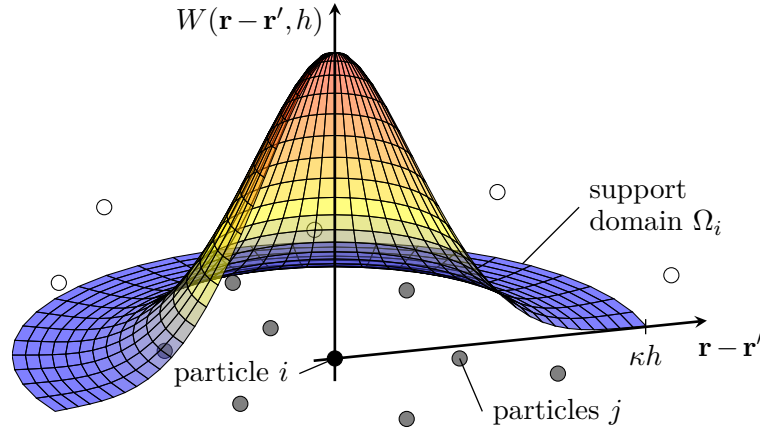
Figure 2.8: Fundamentals of SPH method: given a set of particles (all circles), properties of particle i (black) are calculated as a weighted sum of properties of neighboring particles j (grey) inside its compact support domain defined by the kernel function W, which weights the contribution of each particle depending on its distance $\mathbf{r} - \mathbf{r}'$.

by a summation over all neighbor particles $j \in N$, where N are the neighbors within the compact support domain Ω_i defined by the kernel function, which weights the interactions. Moreover, the infinitesimal volume $d\mathbf{r}'$ in (2.2) is replaced by the particle volume expressed as m/ρ, which introduces mass m and density ρ into the particle approximation. This is important for hydrodynamics because the density is an essential variable. The described procedure results in a weighted sum as in (2.3).

$$f(\mathbf{r}_i) = f_i \approx \sum_j^N \frac{m_j}{\rho_j} f(\mathbf{r}_j) W(\mathbf{r}_i - \mathbf{r}_j, h) \tag{2.3}$$

The indices i and j indicate particles where i is commonly used for the regarded particle and j for its neighbors. For reasons of simplicity, field variables $\phi(\mathbf{r}_i)$ are written as ϕ_i and $W(\mathbf{r}_i - \mathbf{r}_j, h)$ as W_{ij} below.

Spatial Derivatives   Another advantage of the SPH method in terms of simplicity but also computational efficiency is that spatial derivatives $\nabla f(\mathbf{r})$, which are required to solve the governing equations, can easily be calculated by using the analytically known derivatives of the kernel function $W(\mathbf{r} - \mathbf{r}', h)$. Evaluating the derivative through integration by parts leads to

$$\nabla f(\mathbf{r}) = \int_\Omega \nabla \left[f(\mathbf{r}') W(\mathbf{r} - \mathbf{r}', h) \right] d\mathbf{r}' - \int_\Omega f(\mathbf{r}') \nabla W(\mathbf{r} - \mathbf{r}', h) d\mathbf{r}' . \tag{2.4}$$

The application of the divergence theorem to the first integral in (2.4) yields a surface integral, which due to the compact support of the kernel function W becomes zero for particles with a support domain fully inside the computational domain[21]. Thus, the first

---

[21] At boundaries, where the support domain is truncated, a specific treatment is required (see e.g. [67]).

derivative reads

$$\nabla f(\mathbf{r}) = -\int_{\Omega} f(\mathbf{r}')\nabla W(\mathbf{r} - \mathbf{r}', h)\mathrm{d}\mathbf{r}' \,. \tag{2.5}$$

Finally, applying the particle approximation described above gives

$$\nabla f(\mathbf{r}_i) = \nabla f_i \approx -\sum_{j}^{N} \frac{m_j}{\rho_j} f(\mathbf{r}_j)\nabla W(\mathbf{r}_i - \mathbf{r}_j, h) \,. \tag{2.6}$$

2.5.2 Governing Equations

Conservation Equations The motion of fluids is generally described by the Navier-Stokes equations corresponding to Newton's second law, i.e. conservation of momentum. For the present high-speed water impact application, inertial and pressure forces dominate the fluid behavior, whereas viscosity, friction, and surface tension are of minor importance [4, 39, 156]. Therefore, the latter are commonly neglected and the Navier-Stokes equations may be simplified to form the so-called Euler equations. However, the full description of the fluid flow requires further information such as the conservation of mass and energy. Together these form the basic equations to be solved for the regarded fluid dynamics problem. In differential form they read:

$$\frac{\mathrm{d}\rho}{\mathrm{d}t} = -\rho\nabla \cdot \mathbf{v} \quad (2.7) \qquad \frac{\mathrm{d}\mathbf{v}}{\mathrm{d}t} = -\frac{1}{\rho}\nabla p + \mathbf{g} \quad (2.8) \qquad \frac{\mathrm{d}u}{\mathrm{d}t} = -\frac{p}{\rho}\nabla \cdot \mathbf{v} \,. \quad (2.9)$$

Above symbols refer to density ρ, time t, velocity vector $\mathbf{v}$, pressure p, vector of accelerations resulting from external body forces $\mathbf{g}$ (i.e. gravitation acceleration), and specific internal energy u.

Applying the particle approximation to the conservation equations (2.7–2.9) results in the standard SPH formulation (2.10–2.12) as proposed by Monaghan [108]. The mass conservation may be expressed simply by summing the weighted masses over the neighbor particles; yet dealing with free surfaces as well as boundaries of non-particle type, where particles have fewer neighbors, this would cause an erroneous density interpolation along the free surface. To overcome this, Monaghan [108] defined a mass conservation equation using a differential form, which allows for correct density calculation over the entire domain. Moreover, among diverse formulations for the momentum conservation, the anti-symmetric form (2.11) is chosen, because it conserves linear and angular momentum. It can be further noticed that the momentum and the energy conservation equations are uncoupled. Yet, the latter is necessary to control the energy conservation once work is

done on the fluid, i.e. when there are boundaries or when gravity is acting [13].

$$\frac{\mathrm{d}\rho_i}{\mathrm{d}t} = \rho_i \sum_j^N \frac{m_j}{\rho_j} (\mathbf{v}_i - \mathbf{v}_j) \nabla_i W_{ij} \tag{2.10}$$

$$\frac{\mathrm{d}\mathbf{v}_i}{\mathrm{d}t} = -\sum_j^N m_j \left(\frac{p_i}{\rho_i^2} + \frac{p_j}{\rho_j^2} + \Pi_{ij} \right) \nabla_i W_{ij} + \mathbf{g}_i \tag{2.11}$$

$$\frac{\mathrm{d}u_i}{\mathrm{d}t} = \frac{1}{2} \sum_j^N m_j \left(\frac{p_i}{\rho_i^2} + \frac{p_j}{\rho_j^2} + \Pi_{ij} \right) (\mathbf{v}_i - \mathbf{v}_j) \nabla_i W_{ij} \tag{2.12}$$

For numerical stability reasons the frequently used artificial viscosity term Π_{ij} is added to the momentum and energy equations following Monaghan [105, 107]. This viscous dissipation term serves to reduce numerical oscillations under the presence of shocks. The artificial viscosity tensor reads

$$\Pi_{ij} = \begin{cases} \frac{-\alpha_{AV} \cdot \bar{c}_{ij} \cdot \mu_{ij} + \beta_{AV} \cdot \mu_{ij}^2}{\bar{\rho}_{ij}} & \text{if } \mathbf{v}_{ij} \cdot \mathbf{r}_{ij} < 0 \text{ (compression)} \\ 0 & \text{otherwise (tension)} \end{cases} \tag{2.13}$$

where $\bar{\cdot}_{ij}$ are mean values of speed of sound c and density ρ, $\cdot_{ij}$ are differences of velocity vectors $\mathbf{v}$ and position vectors $\mathbf{r}$ of particles i and j, and

$$\mu_{ij} = \frac{h \cdot \mathbf{v}_{ij} \cdot \mathbf{r}_{ij}}{|\mathbf{r}_{ij}|^2 + \chi h^2} . \tag{2.14}$$

The two strength parameters, α_{AV} and β_{AV}, require a proper adjustment in order to sufficiently reduce numerical oscillations. However, since the typical artificial viscosity used is significantly greater than the physical viscosity of water, it has to be ensured that there are no spurious effects on the fluid behavior due to this numerical viscosity.

Particle Motion Equation In addition to the conservation equations, particle positions $\mathbf{r}_i$ are computed by time integration of the velocity at each time step based on

$$\frac{\mathrm{d}\mathbf{r}_i}{\mathrm{d}t} = \mathbf{v}_i + \varepsilon \sum_j^N \frac{2m_j}{\rho_i + \rho_j} \cdot (\mathbf{v}_j - \mathbf{v}_i) \cdot W_{ij} . \tag{2.15}$$

The second term therein refers to the eXtended SPH (XSPH) variant [106] and it is commonly used to regularize the particle motion. Applying this correction, the particle velocity is modified by a contribution of the averaged velocity of the neighboring particles, which is controlled by the dimensionless strength parameter $\varepsilon \in [0,1]$. The XSPH formulation helps to keep the movement of a particle consistent with its neighborhood and therefore prevents unphysical interpenetration. In spite of the velocity modification, linear as well as angular momentum are conserved [12].

Equation of State   The above system of differential equations (2.10–2.12) comprises five[22] equations, but it has six unknowns. Therefore, it requires an additional relationship to close the system. Two possible variants exist: incompressible SPH (ISPH) and weakly compressible SPH (WCSPH).

Despite the fact that water may be assumed quasi-incompressible under ditching conditions, the WCSPH variant is adopted in this work. The choice is motivated by the related advantage of a much lower computational cost per time step compared to the ISPH solution. This advantage originates from the way the pressure is computed: whereas WCSPH directly computes the pressure as a function of the fluid density using an equation of state (EOS), ISPH solves the pressure Poisson equation, which requires a more complicated, iterative procedure. However, this also entails few disadvantages such as significantly smaller time steps as well as strong numerical pressure fluctuations emanating from the equation of state. Nevertheless, regarding the application within a coupled SPH-FE approach involving deformable FE structures, the overall simulation time step is usually dictated by the structural model and the physics to be resolved, which causes this disadvantage to be ineffective and justifies the choice. As the ISPH variant is not employed in the present work, it will not be considered further. However, a detailed description as well as a comparison of WCSPH and ISPH are given by Lee et al. [89].

In the context of water impact, various equations of state can be found in the literature; the most frequent are polynomial, Tait[23], and Grüneisen EOS. They are all barotropic; thus, the pressure is solely a function of density. Within this thesis, the Tait EOS is adopted. It is defined as

$$p(\rho) = p_0 + \underbrace{\frac{c_0^2 \rho_0}{\gamma}}_{B} \left[\left(\frac{\rho}{\rho_0} \right)^{\gamma} - 1 \right] , \qquad (2.16)$$

wherein p_0 is the reference pressure, c_0 the speed of sound in the fluid at the state $\rho = \rho_0$, B the bulk modulus, ρ/ρ_0 the ratio of current over initial mass density, and γ the adiabatic exponent, which for water is equal to 7. The Tait EOS allows representing a fluid with artificially increased compressibility, i.e. with lower bulk modulus, through the definition of an artificial speed of sound. This approach is feasible for applications where compressibility effects are insignificant as the flow velocities $\mathbf{v}$ remain well below the corresponding speed of sound and satisfy the relation $c_0 \geq 10 \max(|\mathbf{v}|)$ [108, 109]. This ensures that superimposed acoustic effects to the main flow are insignificant for the latter. Assuming typical aircraft ditching conditions, anticipated flow velocities are much lower than the true speed of sound in water being approximately 1480 m/s, which offers the potential for the use of an artificially lower speed of sound. In simulations

---

[22] The momentum conservation in (2.11) comprises one equation for each spatial dimension of the problem.

[23] Although proposed by Tait [148], it is frequently referred to as Batchelor [10] or Murnaghan EOS in the literature. It was introduced in SPH by Monaghan [108].

where the stable time step is dominated by the SPH solution, the Tait EOS enables using a larger time step in conjunction with the lower speed of sound. As this directly yields shorter simulation runtimes, it is widely used within the SPH community. In the present application, however, this advantage does not apply as the simulation time step is commonly governed by the deformable FE structural model. Yet, a lower speed of sound reduces the numerical pressure oscillations, which are generally known to be strong for standard WCSPH.

Although the other two prominent EOS are not discussed in detail, there is one interesting aspect. As the Grüneisen EOS defines a very general relationship between pressure and volume, it appears quite different when written in its general form (see e.g. [53]). However, when it comes to modeling water, it simplifies considerably and yields an expression that is essentially equal to the linearized Tait EOS, i.e. with a γ equal to one. Regarding typical density changes in water impact simulations, this linearization of the Tait EOS does not cause relevant differences in the calculated pressure. In addition, when comparing the polynomial and the Tait EOS, it becomes evident that with appropriate parameter settings and within the typical density range they yield nearly identical pressures. Yet, the Tait EOS with a reduced speed of sound is less sensitive to density changes compared to the polynomial EOS and therefore shall provide weaker pressure fluctuations, which makes it superior for the present application.

2.5.3 Computational Aspects

Variable Smoothing Length   The above introduction of the fundamentals of SPH was based on a uniform smoothing length h in time and space. However, in order to allow for an improved spatial resolution, the concept of variable smoothing length was introduced into SPH [12]. The adopted SPH scheme uses this approach, where the smoothing length is updated according to

$$\frac{\mathrm{d}h_i}{\mathrm{d}t} = -\left(\frac{h_i}{\nu\rho_i}\right)\frac{\mathrm{d}\rho_i}{\mathrm{d}t} \tag{2.17}$$

with ν being the spatial dimension of the problem. Note that since a variable smoothing length scheme is employed, care has to be taken to satisfy symmetry of particle interactions in order to conserve momentum. Thus, the kernel W (and in similar fashion the kernel gradient ∇W) is expressed as the mean of W_i and W_j resulting in

$$W_{ij} = \frac{1}{2}\left(W(\mathbf{r}_i - \mathbf{r}_j, h_i) + W(\mathbf{r}_i - \mathbf{r}_j, h_j)\right). \tag{2.18}$$

However, another equal solution is to use the averaged smoothing length $h_{ij} = 0.5\,(h_i + h_j)$ to compute the kernel and respective kernel derivatives.

Neighbor Search   Being mesh-free, the SPH solution requires to repeatedly redetermine which particles interact. Particles, however, only interact if they are within each

other's kernel support length. Thus the efficiency of the SPH solution can be substantially increased by application of neighbor search algorithms. The simulation software used for the present work incorporates an algorithm referred to as cell-linked list [54], which uses a background Cartesian grid to subdivide the computational domain into cells of uniform size and assigns each particle to one cell. The SPH code then only considers particles of the present and its adjacent cells as potential neighbor particles within the summations. Such procedure is state of the art in today's SPH codes as it renders possible in the first place their application to larger problems.

2.6 Summary of Identified Challenges and Open Questions

Based on the fundamentals and the state of the art delineated in the previous sections, it is evident that the structural capacity is of great importance for the ditching capabilities of an aircraft. Despite the relevance of the structural capacity and the research activities in the field, there does not yet exist profound understanding of the structural behavior as well as the changes of the hydrodynamic loading due to structural deformations.

Past experimental work has provided a creditable basis for assessing the consequences of structural deformations and damages on the global aircraft motion. However, there has been neither a quantitative evaluation of acting loads nor a detailed analysis of the structural behavior under representative loading conditions. Thus, available data are insufficient to understand in depth the hydrodynamic processes relevant for the structural behavior, and it remains to be investigated how and to what extent structural deformations affect hydrodynamic loads.

Furthermore, current design and certification procedures rely on uncoupled finite element analysis for the assessment of the structural capacity. Using either computations or sub-scale experiments, rigid models are employed to establish hydrodynamic loads, which are processed and applied to deformable structural models in subsequent simulations. This procedure lacks the coupling of the structural with the hydrodynamic behavior as there is no influence of the deformed or damaged structure on the hydrodynamic response. The author claims that currently utilized means do not offer sufficient accuracy and are therefore inadequate for the analysis of the structural capacity, in particular when novel unusual designs are to be considered.

Consequently, there is a need for advanced numerical simulations that are capable of accounting for the coupled FSI. The SPH-FE approach has been proven to be suited for coupled FSI simulations as it has been successfully employed for vertical water impact simulations including structural analyses. However, for water impact at high horizontal velocity, only rigid body models have been simulated and thus the detailed structural

response has not been investigated. This is mainly attributed to the large computational effort required to simulate deformable structures with associated small time steps together with large fluid domains with a fine discretization to correctly capture relevant physics coupled in one simulation. Hence, runtimes of current simulation models are impractical and by far not compatible with aircraft design and certification processes. Furthermore, the SPH method is known to suffer from large numerical pressure fluctuations, which appear critical as the pressure is the essential quantity for the structural loading.

Finally, since advanced numerical simulations were not yet applied to the ditching problem including deformable structures impacting at high horizontal velocity, it remains to be demonstrated that the structural response can be captured with sufficient accuracy. Accordingly, there exists no validation, which however is essential to increase the acceptance of such numerical simulations by aircraft manufacturers as well as airworthiness authorities.

Based on the identified challenges presented in this section as well as the main objectives outlined in Section 1.2, the following major research questions can be formulated:

- To what extent do structural deformations affect hydrodynamic loads during water impact at high horizontal velocity?

- Which key mechanisms characterize and affect the structural response?

- Can the SPH-FE approach accurately predict the structural response of typical aeronautical structures impacting on water under ditching conditions?

- Which modeling techniques can be employed to increase the simulation efficiency and to reduce numerical pressure fluctuations?

2.7 Detailed Objectives

In order to cope with the challenges, to answer the research questions presented above, and to investigate the thesis claimed in Section 1.1, the detailed objectives of this work comprise:

- Evaluation of experimental data of a guided ditching test campaign in order (a) to investigate occurrence and extent of hydrodynamic phenomena, (b) to analyze effects of impact parameters on the hydrodynamic loading and the structural response, (c) to assess the effect of structural deformations on hydrodynamic loading, and (d) to identify key mechanisms affecting the structural response

- Development of a numerical model of above guided ditching experiments based on the coupled SPH-FE approach comprising enhanced modeling techniques to overcome current runtime limitations and to ensure robustness as well as accuracy

- Validation and verification of developed simulation model based on comparison of several numerical results with experimental data of aforementioned guided ditching experiments

- Assessment of capabilities and limitations of the numerical model

- Extension of understanding of the mechanisms involved in the structural response through profound analysis of numerical results

Overall, this thesis is devoted to the analysis of the structural behavior under hydrodynamic loading. It shall contribute to the understanding of the hydrodynamic phenomena and the mechanisms involved in ditching, and establish advanced numerical simulation techniques that enhance the capabilities toward the coupled numerical simulation of deformable full aircraft ditching, which thereby may become feasible in the near future.

3 Guided Ditching Experiment

Emerging from the absence of suitable experimental data to improve the general understanding and to support the development of appropriate numerical models with respect to their validation, an experimental campaign of guided ditching tests (GDT) was conducted[1] as part of the research project SMAES (SMart Aircraft in Emergency Situations, EU-FP7, 2011–2014 [14]). This pioneering experimental campaign provided an ample set of novel and unique data as alike experiments did not exist before.

The present chapter provides a brief description of this experimental campaign. In the first section, the background and the motivation as well as the main idea for this campaign are outlined. Subsequently, the experimental setup and the test specimens including their instrumentation are presented. Within the scope of this thesis, available experimental data are evaluated in order to increase the fundamental understanding and to support the subsequent development of the numerical model. The analysis presented comprises the investigation of main mechanisms as well as physical phenomena involved in ditching. In particular, the structural response as well as its effects on hydrodynamic loads are evaluated. The final section summarizes the major findings.

3.1 Introduction

As indicated in the previous chapter, the oblique water impact of deformable aeronautical structures under representative impact conditions has not been investigated yet. The only data available with impact conditions similar to those expected during aircraft ditching are those of Smiley [137] (cf. Section 2.3.2). Although Smiley's results provided a fundamental understanding of the hydrodynamics, available data are insufficient to support the development of advanced computational models, as only quasi-rigid, flat profiles were regarded. Moreover, there is neither information about the transient structural deformation nor about global loads, and the time resolution seems insufficient [158].

The lack of appropriate data has led to a new experimental campaign of guided ditching tests to provide test data under representative impact conditions. The objectives of this new experimental campaign were twofold: on the one hand, it was aimed to improve the understanding of physical phenomena associated with water impact under relevant

---

[1]The experimental campaign was carried out by CNR-INSEAN, Rome, Italy between April 2013 and June 2014.

ditching conditions and with occurrence of structural deformations; on the other hand, results should serve as a basis for the development and validation of advanced numerical models. Both objectives of the experimental campaign are in line with those of this thesis.

The fundamental idea for the experimental campaign consists of several aspects. It is assumed that structural loads are highest during the impact phase (cf. Section 2.1), which justifies to investigate only the very first part of the ditching scenario lasting less than approximately 250 ms. During the regarded impact phase, the large inertia of the aircraft prohibits noticeable pitch rotation, allowing for a guided experimental setup, i.e. constant flight path and pitch angle. The guided motion allows achieving controlled impact conditions in terms of velocity ratios and associated impact angles, which in addition is beneficial for the comparison with simulation results. Initial impact velocities and pitch angles of the specimens are chosen to resemble realistic flight mechanics. Moreover, the experiments are designed to be representative of full-scale ditching conditions in order to avoid the scaling problems inherent to sub-scale model tests (cf. Section 2.3.2).

The structural panel design for the guided ditching experiments represents a portion of a typical aft fuselage bottom part, where the first impact usually occurs (see Fig. 3.1). Civil and military transport aircraft bottom fuselages generally show three different cross-sectional shapes: convex sections in the aft as well as in front of the wings, flat sections due to wing-to-body fairings or loading ramps, and concave sections due to sponsons around landing gears. Typical materials used for the fuselage hull in aforementioned zones comprise classic aluminum alloys but also composite materials. For instance, the aft fuselage of an Airbus A320 is made of aluminum alloy, but large parts of the bottom fuselage are made of fiber reinforced plastics (e.g. the wing-to-body fairing).
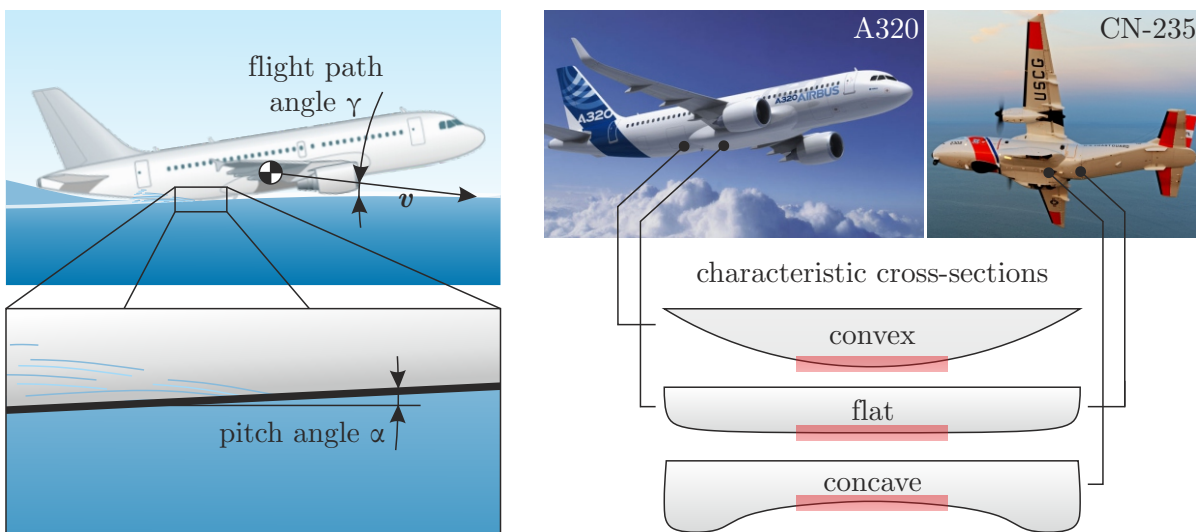

Figure 3.1: Background on selection of representative structural components (highlighted in red) for guided ditching test based on typical bottom fuselage sections of civil and military transport aircraft, e.g. Airbus A320 (left image [1]) and EADS CN-235 (right image [2]).

Based upon these typical design characteristics of today's aircraft, the experimental campaign of guided ditching tests focused on flat, convex, and concave panels of different thickness and materials comprising aluminum and composite that impact at representative flight path angles and impact velocity ratios. The tested panel size corresponds to a portion between approximately three frames and five stringers of a classic fuselage structure. However, in order to reduce the complexity and to limit costs of the experimental campaign, structural panels were kept as simple as possible, i.e. without stringers and frames.

3.2 Description of Experiment

3.2.1 Test Facility

As part of the EU-funded research project SMAES [14] (2011–2014), a large high-speed ditching facility has been designed, built, and installed at the end of towing tank #1 of the CNR-INSEAN site in Rome, Italy. Being one of today's largest towing tanks worldwide, it measures 470 m in length, 13.5 m in width, and 6.5 m in depth [23]. Moreover, it is located indoors thus guaranteeing for calm water with a smooth surface.

The experimental facility schematically displayed in Fig. 3.2 consists of a guide track connected to five height-adjustable bridges that allow varying its inclination and hence the ratio of horizontal to vertical impact velocity. Within the scope of this test campaign and the resulting design of the facility, the guide track inclination may be varied between 1.7° and 2.9° representing typical flight path angles with velocity ratios between 50 m/s and 30 m/s horizontally over 1.5 m/s vertically. The guide track spans over a length of about 64 m and it was especially reinforced in the impact zone to minimize structural deformations of the guide during impact. A catapult-like acceleration system made of elastic cords serves to accelerate the main trolley holding the test specimens to horizontal impact velocities ranging up to about 46 m/s. The acceleration system comprises an auxiliary trolley holding the elastic cords, which separates from the main trolley prior to impact. Both trolleys were designed with several wheels allowing for smooth motion along the guide track and they are made of steel in order to minimize deformations during the experiments. A winch at the beginning of the guide track is used to load the acceleration system. At the end of the guide track, a braking system was installed to stop the trolley after the relevant impact phase. Further information concerning the facility can be consulted in [78–80].

In addition to a lateral high-speed camera, an underwater camera system was installed to record high-speed movies of the impact seen from below. These recordings are beneficial to help understanding measurements in detail as they reveal the occurrence of hydrodynamic phenomena such as air entrapment but also the propagation of structural deformations.
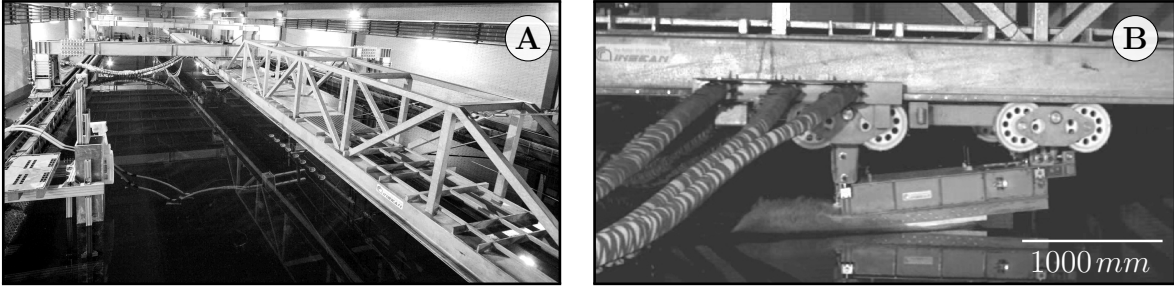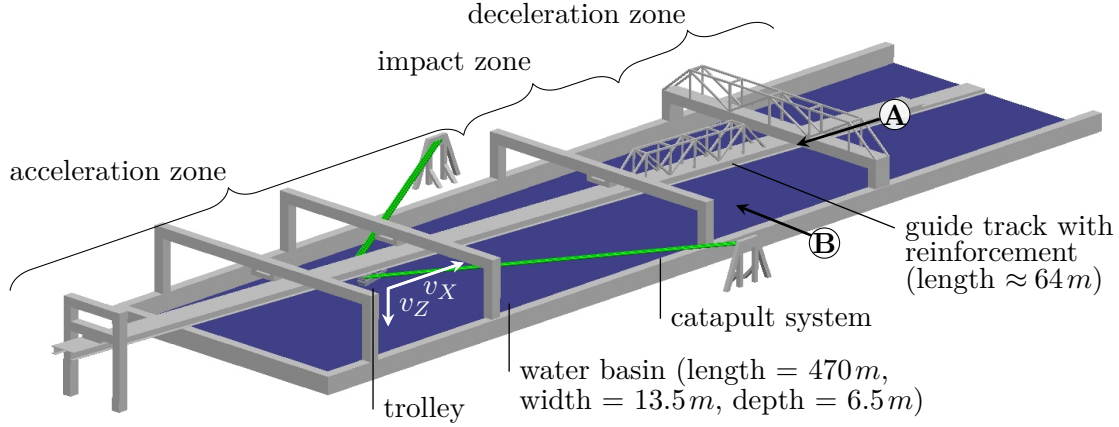
Figure 3.2: Schematic overview of guided ditching experimental facility (top), photograph of impact zone seen from A (left) and observation during impact stage using an external high-speed camera seen from B (right).

3.2.2 Trolley Assembly, Specimens, and Instrumentation

Trolley Assembly   The main trolley holds a box structure (see Fig. 3.2, bottom right), which accommodates the acquisition system as well as the test specimen. Both, the main trolley as well as the box structure are stiff yet lightweight constructions made of steel in order to minimize their structural deformations and to facilitate the acceleration by a relatively light mass.

The test specimens are attached to L-shaped aluminum frames (see Fig. 3.3), which are connected to the box structure, by means of a double-row bolt pattern in imitation of a typical skin-to-frame/stringer attachment[2]. Distances between joints in the experimental setup are selected to be similar to those in real aircraft structures. The specific design uses countersunk bolts for the thick panels and bolts with protruded heads for the thin panels to avoid the risk of structural failure due to the weakening effect arising from the countersink. There are three different L-frame designs for the quasi-rigid cases depending on the panel curvature, which all use a profile of 100 mm height, 75 mm width, and 10 mm thickness. In addition, there is one L-frame design for all deformable cases with a profile height of 100 mm, a width of 50 mm, and a thickness of 10 mm at the sides and 19 mm at the base. The resulting unsupported panel area measures 850 mm×350 mm

---

[2]In real aircraft structures, the typical configuration of joints is in double-row pattern with an overlapped region of skin panels and behind primary structure.
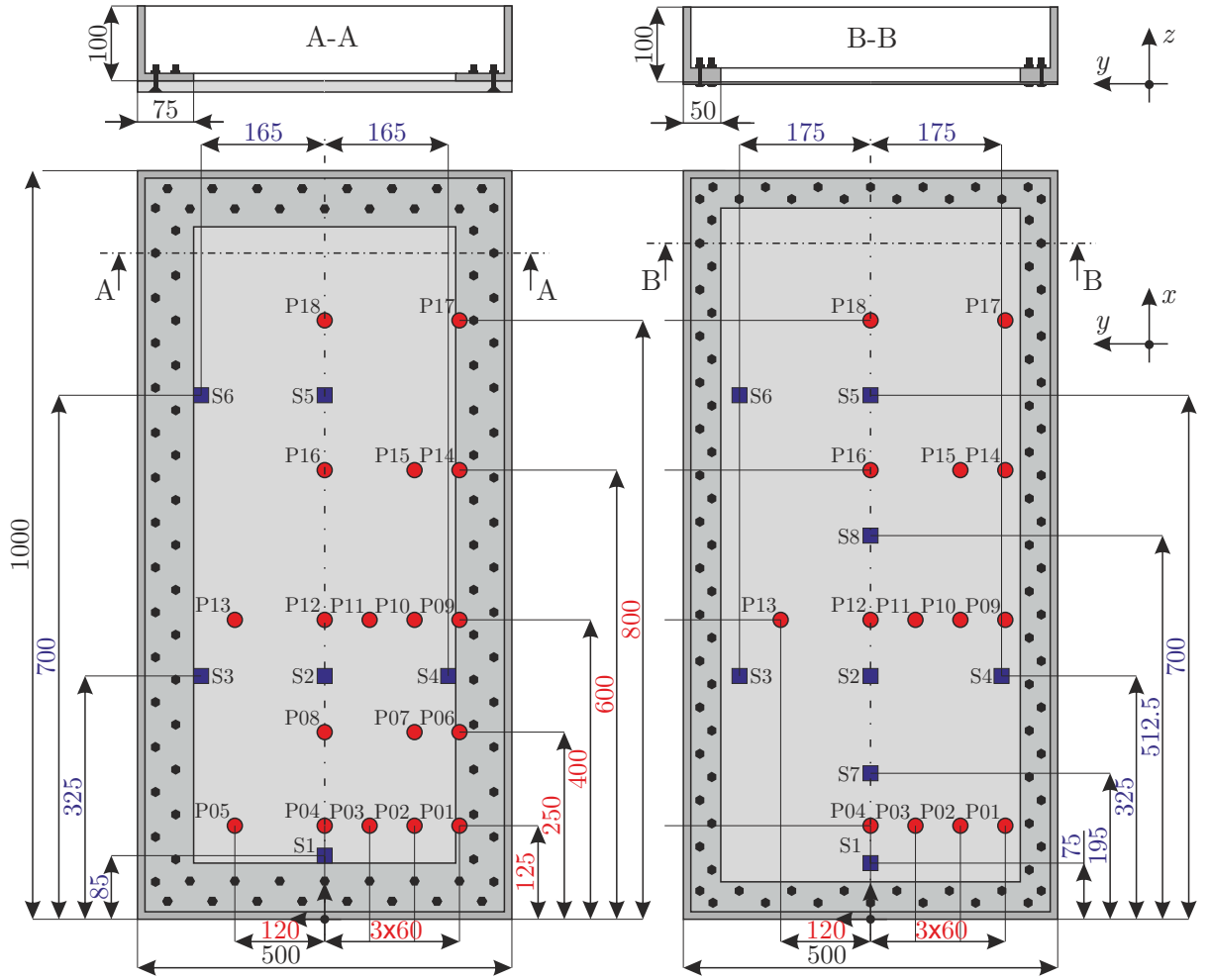
Figure 3.3: Assembly of quasi-rigid (left) and deformable (right) panels with L-frame, strain gauges (blue squares) and pressure probes (red circles).

and 900 mm×400 mm, respectively. The present frame junction is stiffer compared to a real airframe; however, it simplifies the experimental setup and facilitates the numerical modeling. Note that the test specimens are always attached to the trolley, which allows for controlled impact conditions in terms of constant pitch, heel, and flight path angle.

The impacting mass of the main trolley assembly including the test specimen as well as the acquisition system varies between 832 kg and 840 kg, which depends mainly on panel thickness and material (cf. Tab. A.5).

Specimens   All test specimens measure 1000 mm×500 mm, but they are made of different materials and have different thicknesses as well as transverse curvatures. Overall, a classification in two groups is established depending on the expected structural response: quasi-rigid and deformable test cases. With the quasi-rigid test cases, it is intended to analyze the hydrodynamic behavior independently of structural deformations. Therefore, 15 mm thick panels with flat, convex, and concave cross-sections made of classical aeronautical aluminum alloy Al2024-T351 were utilized. For the curved panels, radii of ±2000 mm representative of narrow-body aircraft fuselages were chosen.

In contrast, deformable test cases are intended to study the effects of structural deformations. Thus flat panels made of aluminum alloy Al2024-T3 in 3.0 mm and 0.8 mm thickness were tested, allowing for deformable and highly deformable structural responses. The low thickness of 0.8 mm refers to the minimum skin thickness that can be found in bottom fuselage areas with low load levels. In addition, composite panels were tested. These consist of 11 layers of unidirectional prepreg material of type AS4/8552 with a layer thickness of 0.15 mm in stacking (45/90/-45/0/-45/0/45/0/-45/90/45) resulting in a laminate with a thickness of 1.65 mm. The composite panels as well as the 0.8 mm aluminum panels were additionally equipped with boundary reinforcements respectively made of 1.65 mm thick composite and 3 mm thick aluminum stripes each of 54 mm width in order to prevent joint failure (bolt pull through, bearing, or shear failure).

Instrumentation   A variety of sensors is installed on both trolley and test specimens resulting in a total of up to 44 data channels. In order to measure the global forces acting on the panel, the box structure is connected to the main trolley through six load cells: four measure in normal (z) and two in parallel (x) direction to the panel. Load cells are set-up symmetrically concerning the direction of motion. Hence, in the rear part of the trolley, two measure the z-component; in the front part of the trolley, two measure the z- and two the x-component. In order to avoid possible interference with transverse loading, the load cells are integrated into the structure such that they are decoupled by means of cross-bars.

The trolley velocity is recorded using an on-board, non-contact, optical sensor, which is monitoring the inside flange of one guidance rail. Its functionality suffers however from spray crossing the optical route of the sensor, which may, therefore, result in malfunction. Alternatively, the velocity time history of the trolley can be calculated by simple numerical integration of the acceleration time histories (projection of x- and z-components). Another evaluation is possible using the high-speed recordings, which allow determining the velocity by dividing a characteristic length, e.g. that of the trolley, by the number of frames needed to pass this length, multiplied by the sampling rate of the recording. The accuracy of the latter method is limited by the sampling rate of the recording and the pixel size. Nevertheless, the latter method provides the highest accuracy and was therefore used to evaluate the initial impact velocity.

In addition, the test specimens are instrumented with accelerometers, strain gauges, and pressure probes. For all test cases, five miniature accelerometers are mounted to the inside of the L-frames and one is additionally glued to the backside of the 15 mm thick aluminum panels. The strain gauges were positioned in order to measure strains in zones where highest structural loads were anticipated. The quasi-rigid panels hold six and the deformable panels hold eight bi-directional strain gauges that simultaneously measure orthogonal strains on the inside surface in x- and y-direction of the panels.

Depending on the test case and the anticipated strains, gauges with different ranges were applied. Strain gauges were sealed with a thin silicone layer in order to protect them from any water contact. Pressure probes were placed with the objective to evaluate longitudinal and lateral pressure distributions at different cross-sections of the panels, but also to evaluate the symmetry of the hydrodynamic loading, which in turn may be used to assess the quality of results. Thus, 18 flush-mounted pressure probes are installed on the quasi-rigid panels. In the initial test matrix it was planned to install pressure probes only in quasi-rigid test cases; however, after identifying a high level of repeatability of the experiments, it was decided to alter the test matrix in order to allow also for pressure measurement in few deformable test cases. As these test cases contain two additional strain gauges that occupy four acquisition channels, it was possible to install 14 pressure probes in selected repeats indicated in Tab. A.5. Figure 3.3 illustrates the distribution of pressure probes and strain gauges, and Tabs. A.3 and A.4 give an overview of pressure probe and strain gauge locations for all test cases.

Data are recorded by the on-board acquisition system at sampling rates of 200 kHz for pressure and 20 kHz for all other quantities during the test. The high sampling rate of 200 kHz for the pressure was chosen based on findings by Van Nuffel et al. [158], who demonstrated that such a high frequency is essential to measure highly transient impact pressures. More detailed information about the acquisition system as well as sensor types and specifications are contained in Appendix A.2. For more information on the instrumentation see [80].

3.2.3 Test Program and Procedure

Test Program The test program comprised a total of 65 tests covering 22 impact conditions as summarized in Tab. A.5. In addition to the variation of test specimens presented in the previous section, tests were conducted under different impact conditions. Three target horizontal impact velocities of 30 m/s, 40 m/s, and 45 m/s in different combinations with three pitch angles of 4°, 6°, and 10° were investigated. The vertical impact velocity was kept constant at −1.5 m/s for all experiments. This was achieved by adjusting the guide track inclination, which portrays the flight path angle, depending on the target horizontal impact velocity. All test cases are identified by a four-digit code (ID, refer to Fig. A.1.) representing (1) material/thickness combination, (2) curvature, (3) pitch angle, and (4) target horizontal impact velocity as given in Tab. A.5.

Test Procedure In order to conduct a test, the acceleration system is preloaded using the recovery winch located at the end of the guide track. A load cell monitors the tension of the elastic ropes, which is used to control and to adopt the impact velocity. After release, the trolley is accelerated by the catapult-like acceleration system, prescribing the desired impact velocity. Prior to impact, the main trolley separates from the acceleration

system carriage (auxiliary trolley) allowing for an unaffected, free motion along the guide track. The main trolley then reaches the impact zone and the specimen's trailing edge contacts the water surface. Progressing along the guide track, the trolley decelerates due to the action of the hydrodynamic loads. The impact is accompanied by an increasing amount of spray and splash to the front and the sides. Once the leading edge immerses the nature of the flow along the test specimen changes rapidly and large amounts of water splash upwards and in the direction of motion. Finally, the motion is rapidly decelerated to rest after the trolley encounters the braking system at the end of the guide track.

3.3 Test Results

This section presents selected test results with the emphasis on the investigation of effects due to structural deformations on the hydrodynamic loads and related determining factors, which is one of the objectives of this thesis. In order to facilitate the understanding and also to establish a basis for the later development of the numerical model in Chapter 4, first a general description together with major observations is given. Next, the fundamental effects due to the impact conditions are presented to separate these effects from those arising from the structural deformation, which are analyzed subsequently. Statements made in the following are valid within the range of investigated impact parameters.

Note that only most relevant parts of the broad set of available experimental data are exploited. Considering the subject of this thesis, mainly force and strain time histories are used for the evaluation. Pressure results are only shown in order to illustrate their effect on the structural response as well as the influence of structural deformations on the pressure. More detailed analyses of the experiment beyond the scope of this thesis and in particular with regard to the hydrodynamic aspects can be found in [77, 80].

3.3.1 General Description

The main evaluation of test results is focused on the impact stage of the guided ditching experiment as it is most relevant for the application of aircraft ditching. This stage describes the time period between the initial water contact of the trailing edge and the immersion of the leading edge of the panel, both supplemented by margins to allow capturing relevant phenomena. The acceleration and the deceleration stage of the experiment are not considered.

Time Synchronization   The time of first water contact as well as that of the leading edge immersion are not ascertainable from measurements and thus require to be approximated. In this work, the time of first water contact, i.e. $t = 0$ ms, is estimated based on the rise of the normal force component and additionally synchronized for each repeat of the same test condition using the strain response S_1^{xx}, which shows a sharp rise soon after

the initial contact. Among several possible methods, the one pursued is most suitable, because required results are available for all test cases. A time synchronization based on pressure results as used in the analyses by Iafrati [77] and Iafrati et al. [80], which appears to be more accurate, is discarded as pressure results are not available for all test cases.

Furthermore, the time when the leading edge immerses into the water and thus the duration of the impact stage can be estimated as $t = l_{panel} \cdot \sin(\alpha)/v_Z$, which results in approximately 46 ms to 116 ms when considering only the geometry of a flat panel and neglecting free-surface deformations as well as any velocity reduction. Experimental data, however, reveal that the duration is typically shorter due to water pile-up ahead of the structure. Therefore, the time of the leading edge immersion is estimated from the drop of the normal force component or equally from the increase of the force in x-direction. It is indicated in the following charts by a vertical line for each test case.

Flow Formation   The flow field evolving below the structure can be divided into two regions: one flowing toward the trailing edge and the other forming a thin jet that flows toward the leading edge. Caused by the interaction with air, this thin jet soon breaks up into spray. Furthermore, the free surface experiences an upward displacement resulting from water pile-up in front of the jet root. Regarding flat panels, the flow pattern quickly evolves from a quasi 2D flow to a full 3D flow profile as the wetted surface grows over time. This results in a curvature of the jet root across the panel as the jet velocity is lower toward the sides of the panel where the fluid can escape. This 3D effect has already been reported by Smiley [137], where it was even more pronounced due to the larger aspect ratio of the structure[3] as well as the larger pitch angles. The curvature of jet root and thus the three-dimensionality is larger for cases with larger pitch angles and smaller horizontal impact velocities, and it increases over time, i.e. as the jet root propagates forward along the panel [77]. Convex and concave specimens show significantly different flow patterns due to their curvature. In the convex case, the central part of the panel touches the water surface earlier resulting in a larger curvature of the jet root compared to the reference case with a flat panel. In contrast, the concave panel generates an inversely curved flow pattern as the sides enter the water first (see Fig. 3.4, left). Also, the deformable panels show a similar flow pattern compared to the concave panels after they deform into a concave shape when being loaded.

Hydrodynamic Phenomena   The occurrence of free-surface perturbations prior to the impact as illustrated in Fig. 3.4 (center) was observed; these are stronger for cases with smaller pitch angle. This is confirmed by the analysis of two cases at 45 m/s impact velocity and pitch angles of 4° (ID 1113) and 10° (ID 1133) in [80].

---

[3]In experiments of Smiley [137] the aspect ratio (length:width) was 5:1, whereas in the present experiment it was 2:1.
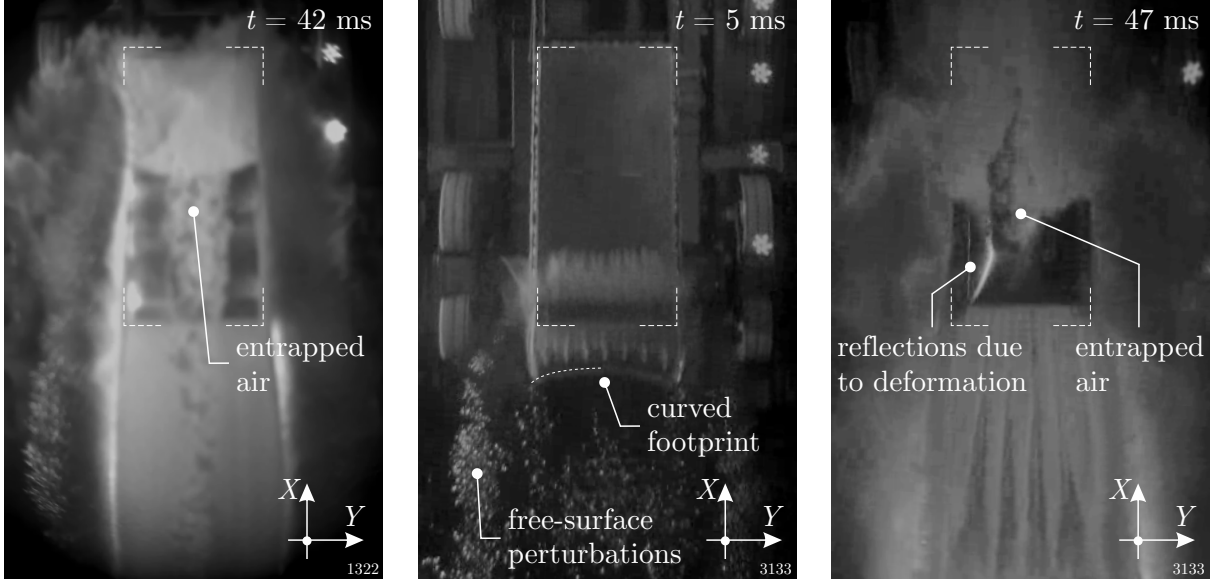
Figure 3.4: Hydrodynamic phenomena observed based on underwater high-speed recordings during experiments at horizontal impact velocity of 40 m/s and 6° (ID 1322, left) and 45 m/s and 10° (ID 3133, center and right).

Air cushioning occurs as can be recognized qualitatively from the rear shape of the footprint of a flat panel, i.e. with a straight trailing edge, as pointed out in the exemplary underwater recording in Fig. 3.4 (center). The curvature of the footprint reveals that in the center of the panel the water surface is pushed downward before the impact, which results from the compression of the air below the specimen. This effect is stronger for cases with higher horizontal velocity and smaller pitch angle. Furthermore, the delay of pressure peaks in the rear row of probes, which was analyzed and discussed in [80], confirms the occurrence of an air cushion. The authors found that for probes located in the last row, i.e. at $x = 125$ mm, the ones toward the outside respond earlier than the one at the center line, which results from the displacement of the free water surface due to the presence of an air cushion. Nonetheless, the analysis based on pressure signals potentially does not reveal smaller initial air cushioning effects, which due to the formation of the fluid jet may disappear by the time when the jet root arrives at these probes. In order to evaluate the magnitude of the free-surface displacement due to air cushioning, an estimation based on the guide track angle, the impact velocity, and the observed curvature of the footprint can be established (see Appendix A.4). For the present cases, this estimation results in a maximum vertical free-surface displacement in the order of 4 mm in negative Z-direction at the center of the panel.

Air entrapment was observed for cases with the quasi-rigid concave panel and for deformable cases (see Fig. 3.4, left and right). In concave cases, a large amount of entrapped air bubbles can be seen in underwater recordings. The air is fed underneath the structure from the front. This zone of air bubbles extends over the central portion of the panels and becomes wider during the immersion. Deformable cases result in a different type of

air entrapment: once the structure is deformed into a concave shape, a large zone of entrapped air suddenly appears in the region of the jet. It is evoked by the interaction of the fluid jet, the surrounding air, and the deformed panel, and it results in air being entrapped and fed underneath the central part of the panel. This large zone of entrapped air then breaks up into smaller bubbles that affect the pressure response (distinct oscillations).

Although vertical water impact has been considered, Chuang [20] and Huera-Huarte et al. [69] report similar findings with respect to the occurrence of air cushioning and air entrapment. Chuang [20] wrote that effects of entrapped air become important for angles of incidence between structure and water of less than 3°. The author also mentioned a great effect on the magnitude of the peak impact pressure. Huera-Huarte et al. [69] showed that effects due to air cushioning become important for angles of less than 5°.

Pressure Distribution The acting pressure is the driver for the hydrodynamic load and thus the structural response. It is primarily characterized by large gradients in time and space, very high peak values, and rapid propagation along the immersing panel (cf. Fig. 3.5). This pressure distribution mainly depends on pitch angle and impact velocity: larger pitch angles result in more voluminous pressure distributions yet with lower peaks, and pressure magnitudes generally scale with the impact velocity. Due to the longer time needed for immersion, pressure time histories are found to be longer in cases with larger pitch angles. The highest pressure occurs at a location on the structure near the jet root, where the stagnation point is located, and it travels along the panel. In transverse direction, there is a relatively small decay of the pressure magnitude toward the sides. Thus maximum pressures occur along the center line. The fluid propagates faster along the panel for cases with smaller pitch angles, as it has to traverse the same distance in much shorter time. In addition, the propagation velocity reduces with time, which leads to a successive reduction of the peak pressures measured for probes located more forward
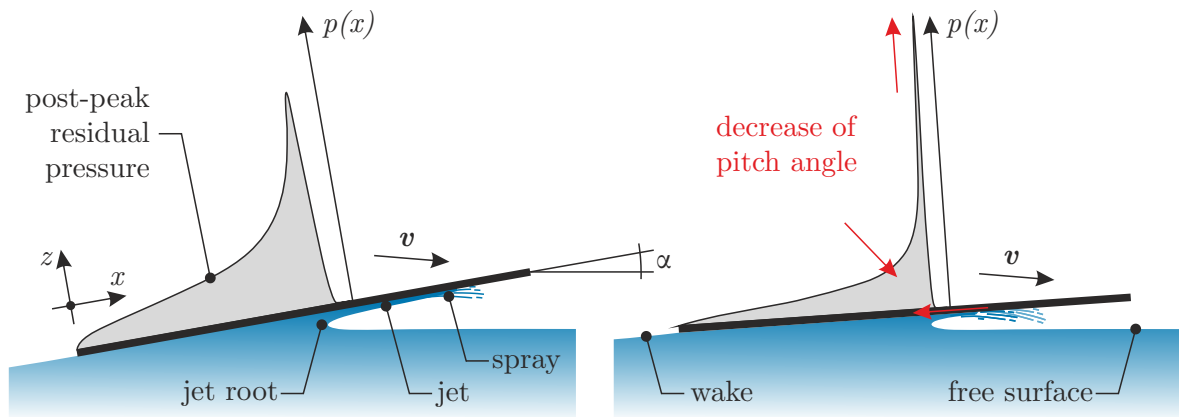

Figure 3.5: Schematic view on section of quasi-rigid panel to depict flow characteristics. The typical pressure distribution $p(x)$ in longitudinal direction becomes more voluminous with reduced peak values when increasing the pitch angle α.

(cf. Fig. 3.6, top), as the peak pressures are approximately proportional to the square of this velocity [77].

A significantly different pressure response is observed for cases with deformable panels (cf. Fig. 3.6, center and bottom). The highly dynamic deformation of the structure causes a temporary reduction of the local vertical impact velocity and the local pitch angle as well as the deadrise angle[4] change as the structure deforms. These mechanisms reduce peak pressures as mentioned above. Additionally, the fluid-structure interaction as well as the entrapped air cause pressure oscillations. Figure 3.6 (center) shows exemplary pressure time histories for a test case with a 3 mm panel; the pressure responses in the rear qualitatively compare to those of the reference test case with a quasi-rigid panel as deformations are small yet. As deformations get larger, aforementioned effects change the pressure response as can be seen, for instance, at probes P_{16} and P_{18}. Main differences are a reduction of peak pressure values and a time delay, which both result from the deformation. Of course, the more deformation occurs, the stronger these effects are.

Hydrodynamic Loads   Hydrodynamic loads acting on the structure correspond to the pressure integral over the wetted area. Consequently, highly dynamic, local pressure peaks are of relatively low importance for the hydrodynamic loading as they do not significantly contribute to the integral. Furthermore, high-frequency pressure oscillations and pressure peaks of short duration are insignificant for the structural response of investigated panels, because the inertia of the structure does not permit a response during such transient action. This agrees with findings discussed by Faltinsen [39] in conjunction with slamming. In general, more voluminous pressure distributions as exemplarily depicted in Fig. 3.5 (left) cause larger hydrodynamic loads.

For the current investigation and the underlying application mainly the resulting normal force component, F_z, is of interest, whereas the force parallel to the panel, F_x, is not relevant during the regarded impact stage. Nonetheless, it indicates the immersion of the leading edge, which is reflected as a sudden force increase. The acting normal force develops progressively as the panel immerses; it shows an initial sharp rise until the outflow develops and the slope reduces. The normal force increases further and reaches its maximum as the leading edge immerses, which defines the end of the regarded impact stage. Iafrati [77] concludes that the normal force component depends mainly on the velocity component normal to the panel, which is given by the pitch angle and the ratio as well as the magnitudes of impact velocities. Upon immersion of the leading edge into the water, there is an abrupt change of loading. On the one hand, the pressure acting on the panel reduces significantly, leading to a sharp drop of the hydrodynamic load normal to the panel. On the other hand, the force in x-direction of the panel increases rapidly due to the impact of the front face of the box structure at a large relative angle of incidence.

---

[4]The angle between structure and water in transverse direction.

During the impact stage, the deceleration due to the increasing action of hydrodynamic loads leads to a velocity reduction of the impacting structure. However, due to its high mass and the corresponding kinetic energy, the structure does not significantly slow down before the leading edge immerses. Afterward, the loading of the front face of the box structure causes a larger deceleration.

Error Sources and Repeatability Generally, the repeatability of fluid-structure interaction experiments is known to be difficult. Especially pressure results, which are most sensitive among the measured data, are known to be difficult to reproduce due to the nature of the impact and the occurrence of hydrodynamic phenomena such as air entrapment [25, 143]. Moreover, in the present experimental setup, particular difficulties arise due to differences in the orders of magnitude of hydrodynamic phenomena compared to the dimensions of the impact facility. The analysis of the experimental data hence started by an assessment of the repeatability based on pressure results. This study was performed for two test conditions at different pitch angles with ten repeats each. Results of this study presented in [80] indicate a very high level of repeatability as well as symmetry of the impact. In addition, forces and strains are found to be highly reproducible between repeats of the same test condition. Overall, results are mostly affected by the dispersion of the initial impact velocity, which is a consequence of using the catapult-like acceleration system. Nevertheless, due to the relation of impact velocity and pressure, which for rigid structures impacting water is approximately $p \propto v^2$, the resulting error remains small or is even negligible since $(v+\Delta v)^2 \approx v^2$ as long as Δv is much smaller than v. For the complete experimental campaign, the velocity dispersion is in the order of 1% or less [80], which allows to conclude that the resulting dispersion of the results between repeats is low and thus lies within tolerable limits.

3.3.2 Relation of Hydrodynamic and Structural Response

In order to relate the hydrodynamics to the structural dynamics, Figure 3.6 illustrates the relationship of the hydrodynamics-driven pressure response and the structural response in terms of strains. The analysis is based on probes and gauges along the center line of the panels.

For the quasi-rigid case, where deformations are negligible, the pressure time histories in Fig. 3.6 (top) show the typical response anticipated for water impact of rigid structures comprising a sharp rise followed by a decay of the peak pressure to a significantly lower mean pressure level. Pressure peaks recorded are highest at the beginning of the impact and show a reduction toward later stages, i.e. at more forward pressure probe locations. Nevertheless, pressure time histories recorded at more forward locations appear slightly more voluminous compared to those near the panel's trailing edge. Strains show a slower rise and decay than pressures. Comparing the locations of pressure probes and strain
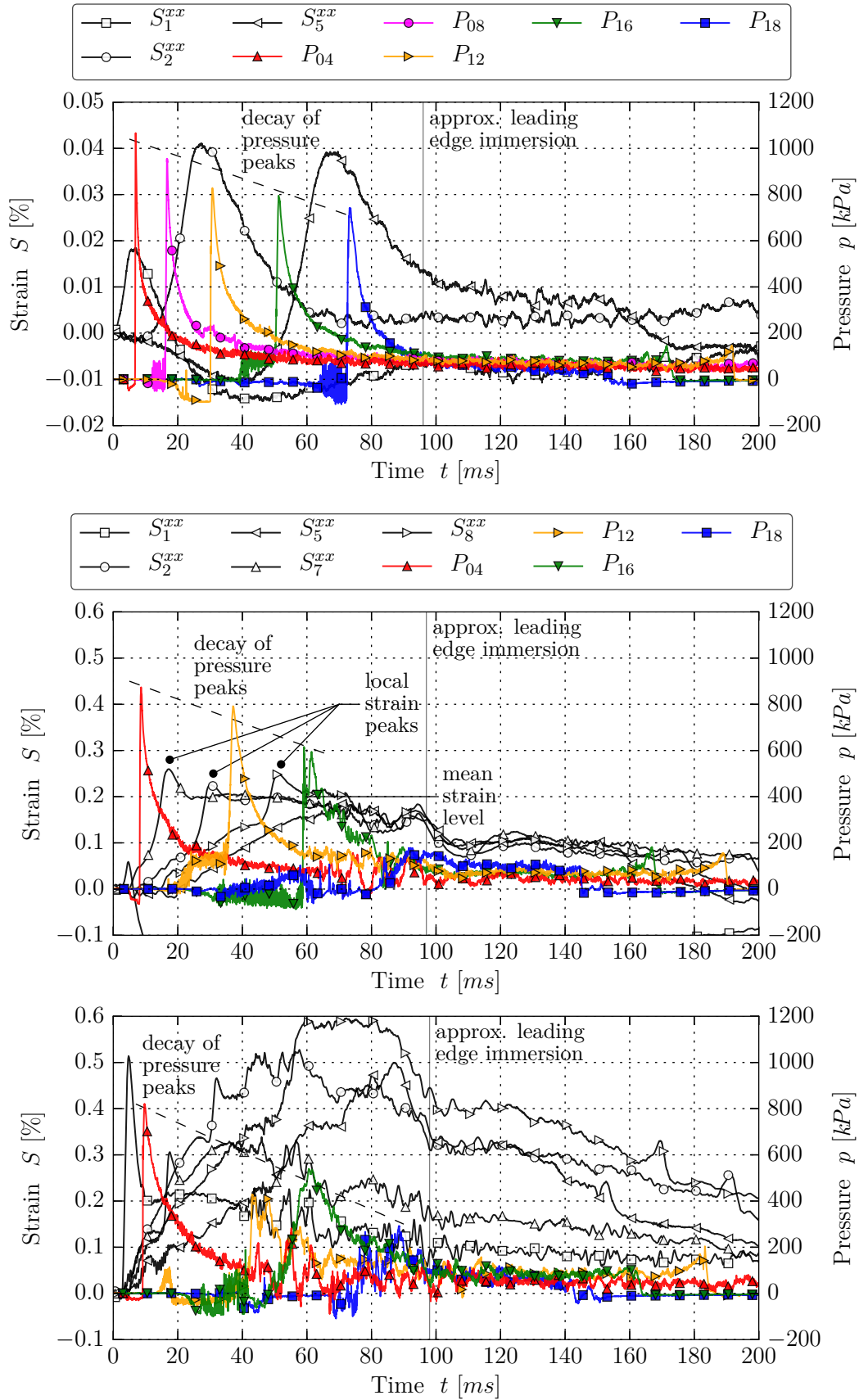
Figure 3.6: Relation between pressure and strain response for quasi-rigid test case (top) and deformable test cases with 3.0 mm and 0.8 mm aluminum panels (center and bottom) under identical impact conditions ($\alpha = 10°$ and $v_{X,0} = 30$ m/s, IDs x131).

gauges[5] with the occurrence of their respective maxima, it becomes evident that the local strain maxima occur just after the passage of the peak pressure zone. Moreover, the structural response is insensitive to high-frequency pressure oscillations.

For the test case with a 3 mm thick panel (ID 2131), which permits significant deformations in the elastic regime, the pressure response is different (see Fig. 3.6, center). Generally, the time response of pressures occurs later compared to the quasi-rigid case. This is due to the deformation of the panel, which causes a time delay of the water jet traveling along the panel and thus a slower wetting. The most rear pressure probe, P_{04}, shows a lower peak value, but the characteristic shape of the pressure time history is similar to the one of the reference case with the quasi-rigid panel. Moving forward, the pressure response of P_{12} shows a positive value before the peak that is attributed to the passage of a thicker fluid jet. Pressure probe P_{16}, which is located toward the leading edge, shows a reduction of the peak pressure about 25% compared to the reference case. The response recorded by probe P_{18} no longer shows the characteristic shape but a higher post-peak residual pressure. In addition, due to the entrapment of air discussed above, stronger pressure oscillations start to appear after approximately 60 ms. The analysis of pressure and strain results shows a similar correlation as described above; the occurrence of strain maxima correlates with the passage of the peak pressure zone. As the 3 mm panels deform much easier, a temporary yet pronounced strain peak is observed just when the pressure peak traverses. Nonetheless, the structural response is still considered insensitive to high-frequency pressure oscillations as well as peak pressure values of short duration. This results from the slower response time of the structure due to its inertia. In other words, the structure does not react on highly transient pressure peaks as well as pressure oscillations. The initial slope of the strain time curve, i.e. the strain rate, is lower for strain gauges located more forward. After the passage of the peak pressure zone the strain level remains nearly constant until aforementioned pressure oscillations due to entrapped air start to affect the structural response in terms small structural oscillations.

Results of test case 3131 with 0.8 mm panel thickness depicted in Fig. 3.6 (bottom) show a similar behavior as observed for test case 2131, yet the effects are much stronger as the structure is more deformable. The rear pressure probe, P_{04}, shows a smaller pressure peak (approx. -25%) and the curve is more voluminous compared to the case with the 3 mm panel, i.e. 2131. This is attributed to the larger local deformation already during early stages. Probe P_{12} no longer shows the characteristic pressure response; the peak pressure at P_{12} is about half of that recorded for test case 2131. Additionally, strong pressure oscillations are observed. More forward pressure probes show the same trend toward noisier pressure curves with significantly lower peak values. In the rear part of the panel, where characteristic pressure responses with large gradients are observed, very localized strain peaks are found, which are associated with the passage of the pressure

---

[5]Figure 3.3 and Tabs. A.3 and A.4 provide an overview of locations of pressure probes and strain gauges.

peak similar to observations made for the other test cases. Moving forward, strain results initially show oscillations. These are caused by free vibrations of the part of the structure that is not yet in contact with the water. A local strain increase can be observed approximately when the pressure peak traverses, yet strains increase further later on. Toward the center of the panel, where the pressure distribution is more voluminous, the structure undergoes largest strains. However, there are no pronounced local strain peaks as observed for the rear strain gauge as the acting pressure no longer shows the pronounced pressure peak. Oscillations associated with the entrapped air as described above appear earlier, i.e. after approximately 40 ms, and are stronger, because the extent of structural deformation is larger. These pressure oscillations affect the strain response, which shows more and stronger oscillations compared to test case 2131, especially in the rear part of the structure where the residual pressure is low (see e.g. S_1).

In summary, there is a distinct correlation between the occurrence of pressure and strain peaks for quasi-rigid as well as deformable test cases. Furthermore, the local pressure response changes significantly when the structure deforms: sharp pressure peaks diminish and the pressure response transforms toward more voluminous and noisier curves.

3.3.3 Effects of Impact Conditions and Panel Curvature

In order to identify exclusively the effects of impact conditions and panel curvature, this section regards only the test cases in which quasi-rigid, 15 mm thick aluminum panels with insignificant structural deformations in the low elastic range were used. In this section, charts show mean values of several repeats of the same test condition and their associated standard deviation is superposed as a shaded area.

3.3.3.1 Pitch Angle

Test cases using flat panels impacting at pitch angles of 4°, 6°, and 10°, and with horizontal impact velocities of 40 m/s and 45 m/s were studied. Results shown in Fig. 3.7 refer to the cases at 40 m/s.

Both investigated test series indicate significant differences in the results arising from the change in pitch angle. As the initial vertical velocity is constant among all tests of the experimental campaign, panels impacting at larger pitch angle take longer until leading edge immersion (indicated in charts by vertical lines). For smaller pitch angles, the pressure distribution is increasingly concentrated on the jet root, which leads to very sharp gradients in time and space. This results in very high peak values of short duration for the case at 4°, whereas the case at 10° shows smaller pressure peaks with longer duration and thus more voluminous distributions. Comparing pressure results at probe P_{04} located in the rear, there is no clear difference regarding different pitch angle cases as the flow has not developed yet. Later, however, pressure peaks are diminishing for the

case at 10° (see Fig. 3.6, top), whereas they remain high for the case at 4°. It is also interesting to note that by means of the underwater high-speed camera, the occurrence of free-surface disturbances and the entrainment of air bubbles are observed. This is reflected in stronger pressure oscillations and larger dispersion of pressure results for cases at small pitch angles as presented in [80].

The initial slope of the normal force time histories is found to be independent of the pitch angle. The change of this initial slope, which occurs around approximately 14 ms to 18 ms, is a result of the formation of the characteristic flow field consisting of a fluid jet and outflow toward the sides. Once these are established, the fluid can escape easier from underneath the structure and thus the rate of loading is reduced. The acting normal force increases with larger pitch angles as it is related to the acting pressure distribution and as the velocity in normal direction of the panel increases. This was verified by Iafrati [77] through normalization of the normal force component with the
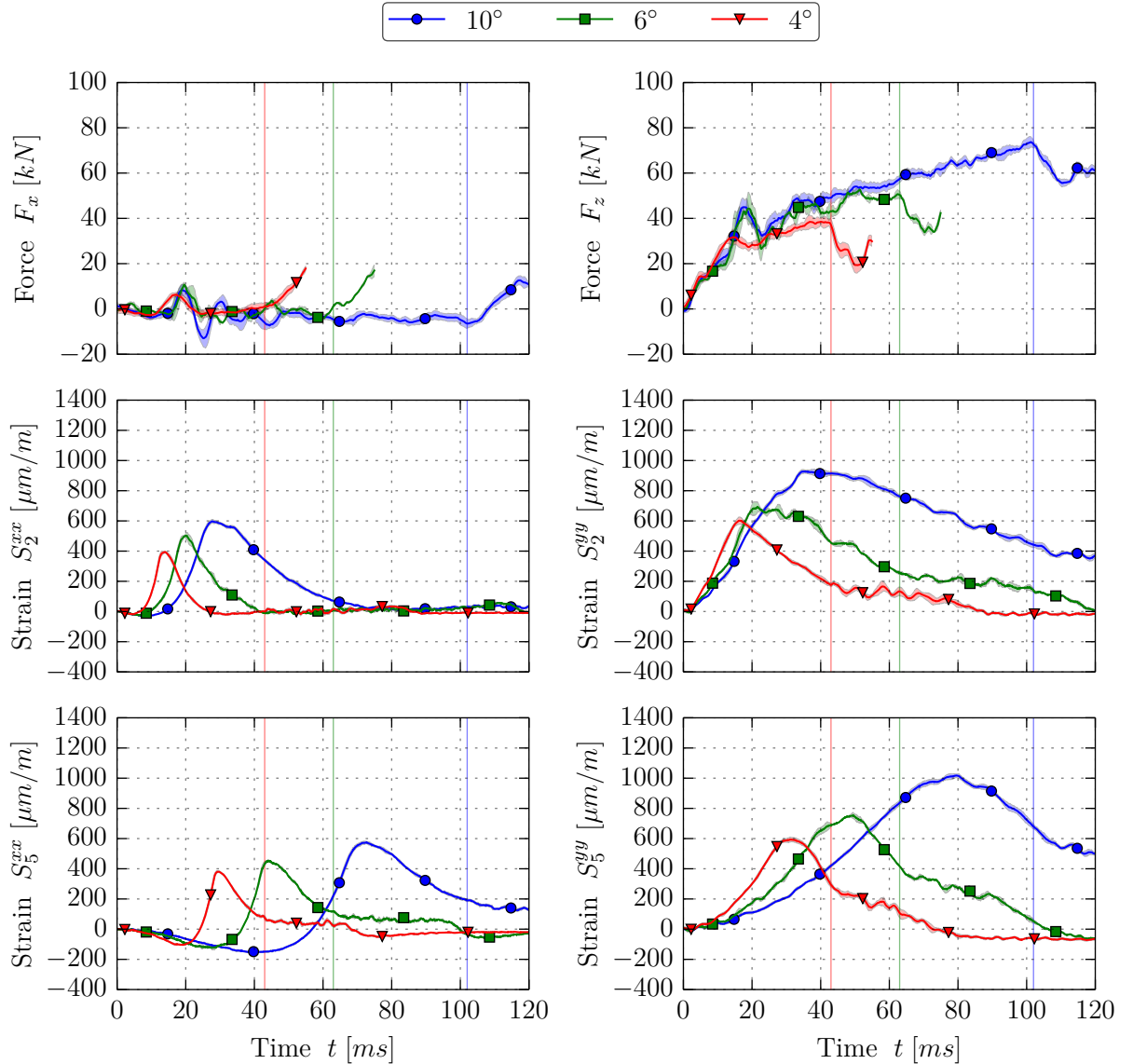

Figure 3.7: Force and strain time histories of experiments with different pitch angles and 40 m/s horizontal impact velocity (IDs 1112, 1122, 1132).

normal velocity, which results in very similar curves for the regarded test cases. Moreover, the projected area perpendicular to the direction of motion of the panel is larger and the time needed for immersion is longer as it can be seen from the drop of the normal force at approximately 43 ms, 63 ms, and 102 ms, respectively. Comparing the times of the leading edge immersion with the values anticipated neglecting free-surface deformations (46 ms to 116 ms; refer to page 55), it is noticed that for the case at 4° the difference is small. Due to the rapid immersion, there is almost no pile-up of the free water surface ahead of the structure. For the large pitch angle case, there is, however, a significant difference that can be attributed to the water pile-up ahead of the panel, which causes an earlier leading edge immersion. Furthermore, the standard deviation appears to be larger for the cases at 4° and 10°, which results from using ten repeats with superposed oscillations due to the guide motion rather than three repeats of the 6° case for the analysis.

Strain results show a time delay that is caused by the slower immersion of the panels impacting at larger pitch angles and approximately identical vertical velocity during the impact. Moreover, due to the slower wetting rate at larger pitch angle, the strain responses occur and decay slightly slower (smaller growth/decay rate of signals). Obtained strain levels grow with the acting pressure; more voluminous pressure curves as observed for larger pitch angle cases cause larger strains. Strains are highest along the center line and decay toward the sides. Even for the highest loading, strains are within the low elastic range of the material, i.e. below 25% of the strain corresponding to the yield point, which justifies assuming the panels to be quasi-rigid.

In order to quantify the increase of normal forces and strains depending on the pitch angle and to provide an estimate for comparison with other impact conditions, Fig. 3.10 (a) shows normal force and strain peak values normalized on the test case at 6°. A clear trend depending on the pitch angle is observed. Normal forces vary about −24% and +41% for cases with lower and higher pitch angles, respectively. Strains in average decrease about 20% and increase about 31% for the regarded pitch angles.

3.3.3.2 Impact Velocity

Test cases using flat panels impacting at pitch angles of 4°, 6°, and 10° and with horizontal impact velocities of 30 m/s, 40 m/s, and 45 m/s were studied. Results shown in Fig. 3.8 refer to the cases at 10° as tests at 30 m/s were only conducted for this pitch angle.

Theories of water impact indicate a strong dependency of the results on the impact velocity as the pressure is approximately proportional to the square of the impact velocity as long as deformations are insignificant (cf. Section 3.3.1). Accordingly, results show a general increase of both the pressure peak values as well as post-peak residual pressures when increasing the impact velocity.

Normal forces exhibit a strong influence of the impact velocity as anticipated based on the pressure response described. For higher impact velocities, normal forces as well

as accompanying oscillations are larger throughout the entire impact. Normal forces are found to scale approximately in proportion to the square of the impact velocity. Moreover, the growth rate of the force is steeper and its reduction occurs later, which may be explained by the fact that at lower impact velocity the flow develops a stronger three-dimensional character with more outflow to the sides and consequently weaker constraints for the fluid. Regarding the duration of the impact (time of leading edge immersion), cases with higher impact velocity show a later change of loading (decrease of F_z and increase of F_x). On the one hand, this is related to the fact that the water does not pile up as easily underneath the structure when it moves faster; thus it takes longer for the leading edge to immerse. On the other hand, any vertical displacement of the guide track during the immersion causes a reduction of the vertical velocity (cf. Section 4.2.1 and [80]). As this guide displacement increases with the force acting in vertical direction, the corresponding time delay is larger for cases with higher impact velocities.
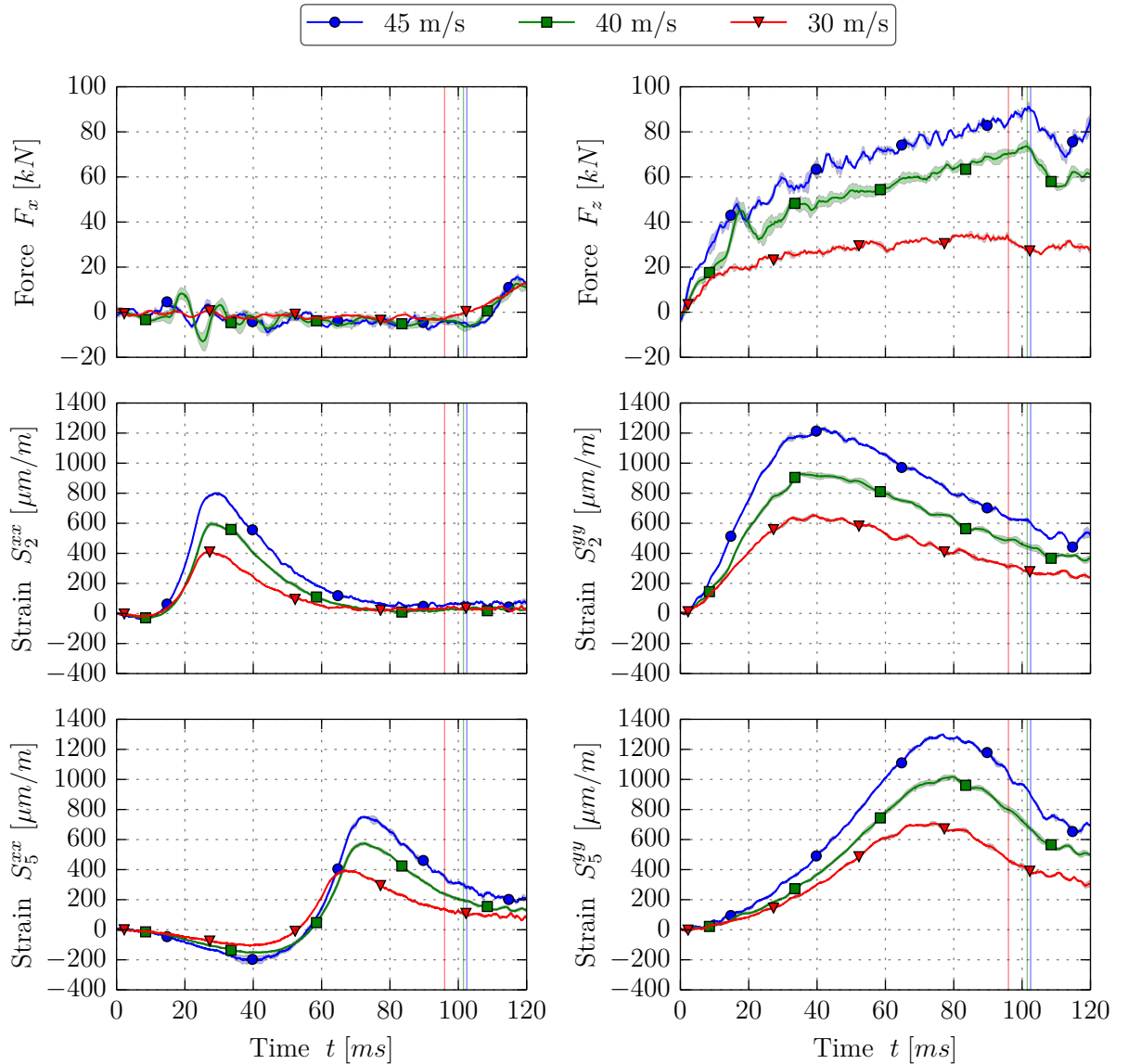

Figure 3.8: Force and strain time histories of experiments with different horizontal impact velocities and 10° pitch angle (IDs 1131, 1132, 1133).

Strain results show a similar yet less strong increase as for normal forces when increasing the impact velocity. Due to the same pitch angle and the almost identical time needed until leading edge immersion, strain peak values occur quasi-independent of the horizontal impact velocity at approximately the same time. Small differences are related to the aforementioned effects affecting the immersion time.

Similar to the evaluation in the preceding section, Fig. 3.10 (b) provides a quantitative comparison of normal force and strain peak values normalized on respective values of the test case at 40 m/s. There is a uniform trend in conjunction with the impact velocity. Normal forces approximately decrease 53% and increase 22% when decreasing or increasing the impact velocity, respectively. Strains exhibit an average increase of 35% and a decrease of 30% accordingly.

3.3.3.3 Panel Curvature

The effects of the panel curvature in lateral direction are studied based on experiments using differently curved panels impacting at a pitch angle of 6° and with a horizontal impact velocity of 40 m/s. Results are shown in Fig. 3.9.

In general, the lateral curvature of the structure causes relief (convex case) or additional constraints (concave case) for the fluid to escape from the impact zone. The flow field is highly three-dimensional with a strong curvature of the jet root depending on the curvature of the structure: for concave panels, the sides contact the water first, whereas for the convex panels, the central part establishes first contact. Also pressure results show strong effects related to the curvature. In the central part of the concave panel where air is entrapped (cf. Fig. 3.4, left), pressure responses are less sharp with lower peak values but significantly stronger oscillations. This effect is stronger toward the center line, where the largest amount of entrapped air is observed, and it vanishes toward the sides.

The lateral curvature of the panels results in a different initial slope of the normal force, which shows a progressive increase for concave cases due to the larger lateral inclination of the structure at the sides (local deadrise angle). The initial response for the convex panels, however, is similar to that for flat panels as their local deadrise angle is comparably small at the beginning of the impact or even zero in the moment of first contact. Measured normal force levels show only a low sensitivity to the panel curvatures investigated. This is attributed to the relatively large radii of curvature of ±2000 mm in combination with the panel width of 500 mm and to some extent also to the hydrodynamic phenomena arising from the increased amount of entrapped air in the concave cases.

Although qualitatively strains show a similar response, the values reached differ significantly between the investigated test cases with curved panels. The concave panels generally exhibit larger strains, because they inherently deform easier in the given loading direction and additionally the acting hydrodynamic loads are higher. Correspondingly, convex panels show a trend toward lower strains.

Again, a quantification of the effect of panel curvature is established in Fig. 3.10 (c), where peak values are normalized with those of the reference test case with a flat panel. Normal force peak values are approximately 16% lower in convex cases and 1% lower in concave cases compared to the reference case. For strains, no general statement can be made, as the change of strain peak values due to the different panel curvature depends on the gauge location. Yet, especially at locations near the L-frame, strains in perpendicular direction to the L-frame show a strong dependency (see S_1^{xx}, S_3^{yy}, S_4^{yy}, and S_6^{yy}) and are much higher in the concave case. Gauges located along the center line of the panel (S_1, S_2, and S_5) show lower strains for convex and larger strains for concave panels in both directions with a stronger dependency in x-direction[6].

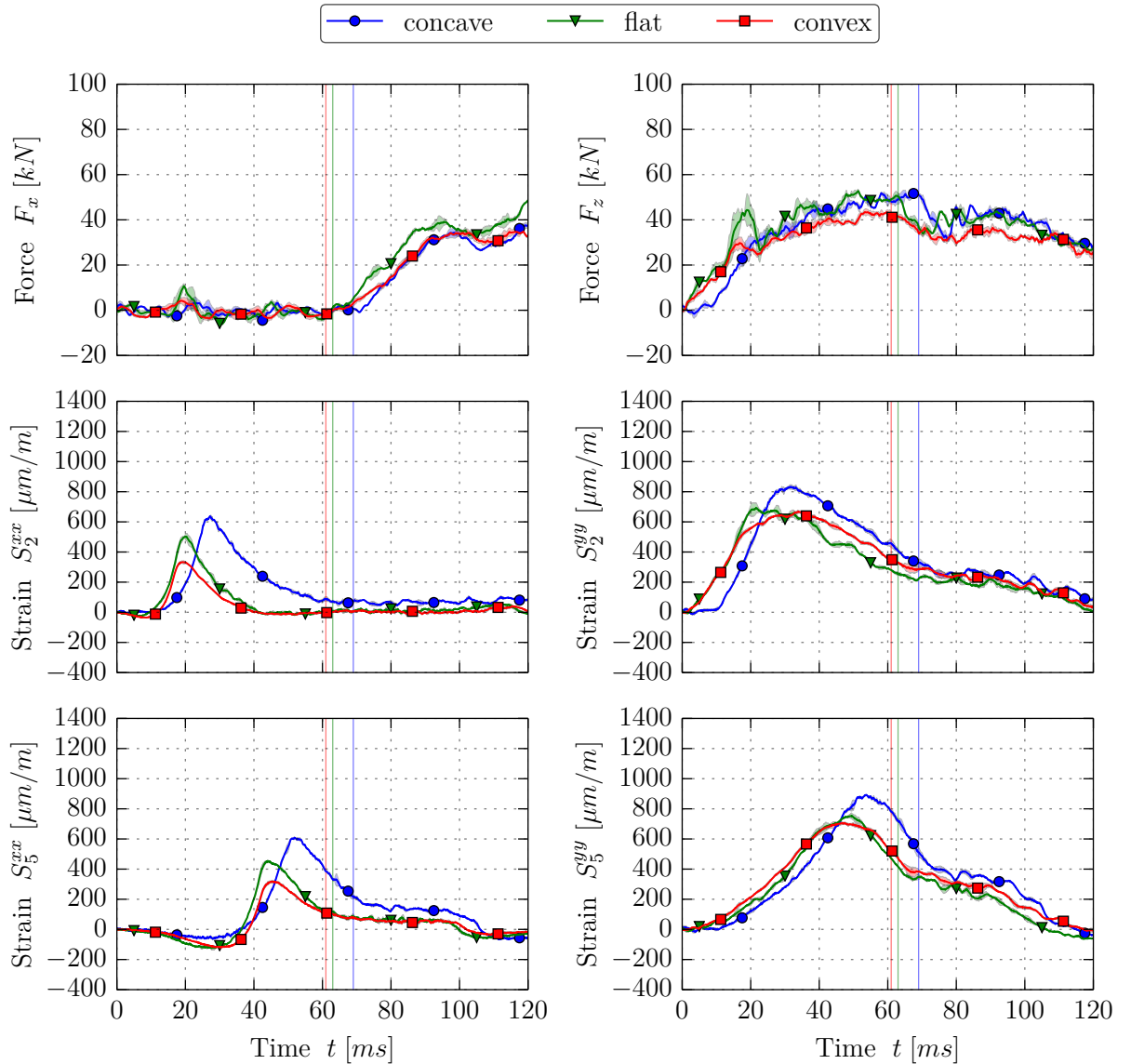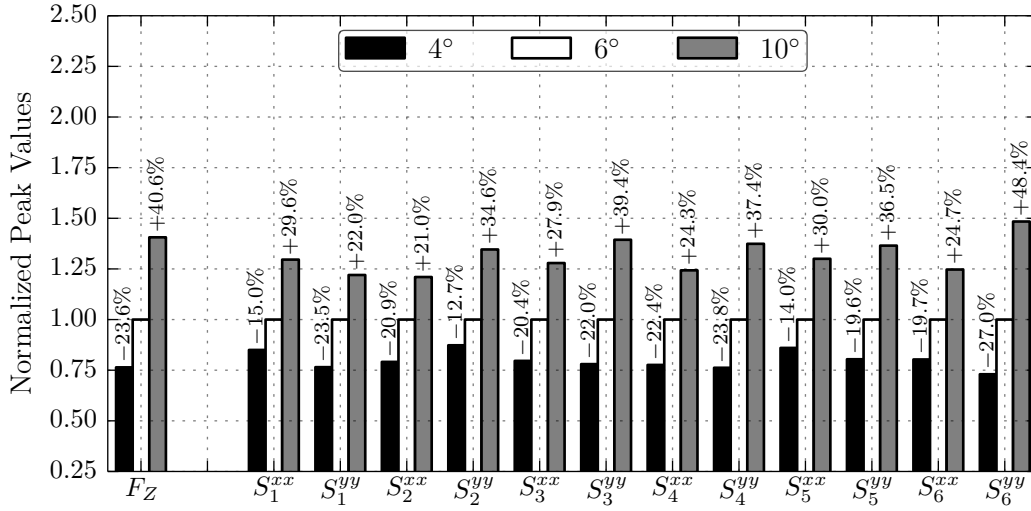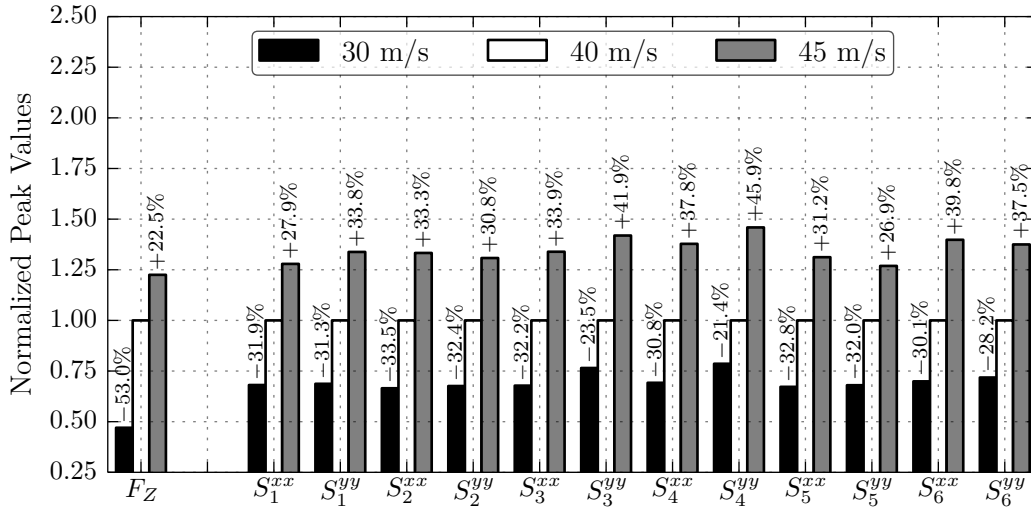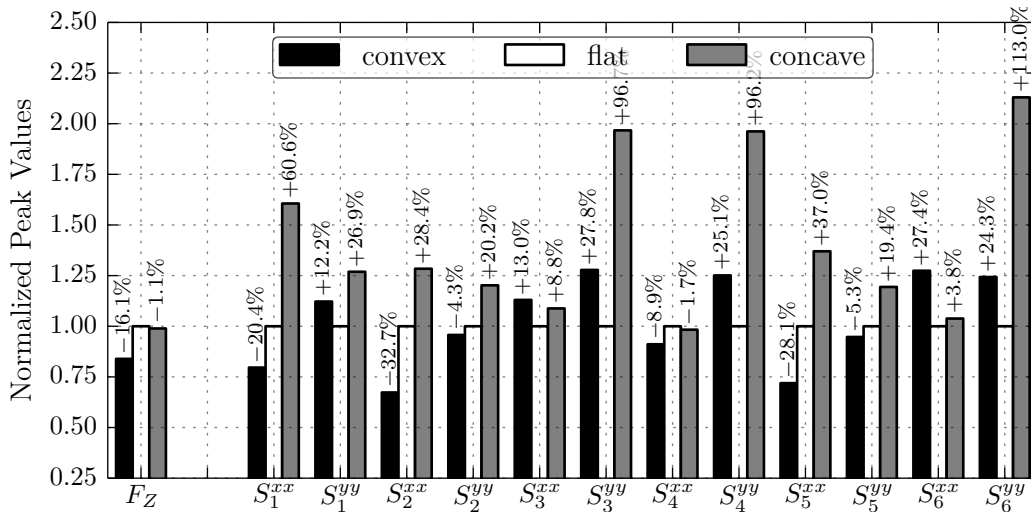[6]Note that S_1^{yy} does not strictly follow the general trend.

Figure 3.9: Force and strain time histories of experiments with different panel curvature at 6° pitch angle and 40 m/s horizontal impact velocity (IDs 1122, 1222, 1322).

(a) Variation of pitch angle at 40 m/s impact velocity (see Section 3.3.3.1).

(b) Variation of impact velocity at 10° pitch angle (see Section 3.3.3.2).

(c) Variation of panel curvature at 6° pitch angle and 40 m/s impact velocity (see Section 3.3.3.3).

Figure 3.10: Comparison of normalized normal force and strain peak values of experiments under different impact conditions and panel curvatures.

3.3.4 Effects of Structural Deformation

After presenting the effects due to impact conditions and panel curvature, data of test cases with deformable panels are evaluated in this section. The evaluation comprises test cases with aluminum panels of 3 mm and 0.8 mm thickness as well as composite panels of 1.65 mm thickness, which were tested with different combinations of impact conditions, i.e. 4° & 45 m/s, 6° & 40 m/s, and 10° & 30 m/s. These experiments permitted structural responses in the high elastic as well as the elastic-plastic range together with significant amounts of deformation during the impact as it can be observed in underwater high-speed recordings (see Fig. 3.4, right). Nevertheless, panel failure did not occur.

First, a general description of differences with respect to quasi-rigid panels is given. Figure 3.11 portrays the characteristic structural response and the corresponding hydrodynamics observed in experiments using deformable panels. The mechanisms involved are the changes of local pitch and deadrise angle, and the change of local vertical impact velocity. For most of the impact stage, the structural deformation increases the local pitch angle of the wetted portion of the panel. In addition, a deadrise angle develops due to the growing lateral curvature of the panel that deforms in a concave shape. Furthermore, while the structure deforms, the local vertical impact velocity is reduced. Later, the structural boundary condition given by the stiff L-frame causes the formation of a pocket. This pocket provokes a smaller, potentially negative local pitch angle toward the front part of the panel. Just prior to the leading edge immersion, the water piled up in the pocket is pushed out and thus accelerated (indicated by a red arrow in Fig. 3.11, right). Both the small or even negative local pitch angle and the additional acceleration the fluid undergoes are assumed to be responsible for a significant load peak prior to the leading edge immersion. Experimental measurements, however, do not permit sufficient evidence to prove this speculation. Yet, this will be further evaluated based on numerical simulation results in Section 5.2.

The growing structural deformation also changes the flow field toward a stronger three-dimensional behavior. Whereas in the quasi-rigid test case at 4° pitch angle the observed jet root curvature is very small, it is highly three-dimensional in the deformable test case under identical impact conditions. As a result of the panel deformation in a concave shape, the panel immerses into the water first with its lateral sides while points
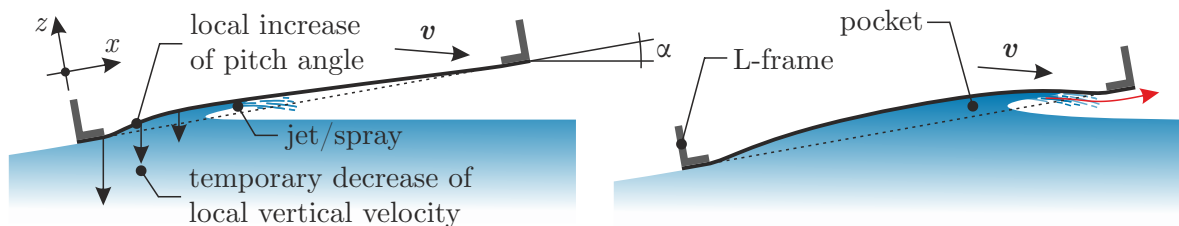

Figure 3.11: Schematic view on section of deformable panel to depict fluid-structure interaction characteristics at two instants of time.

located at the same x-coordinate but at the center line ($y = 0$ mm) get wetted later. Complementary to observations based on underwater high-speed recordings, this effect is verified by comparison of pressure responses recorded in the test case with a 3 mm aluminum panel impacting at 4° pitch angle and 45 m/s horizontal impact velocity (see Fig. A.3)[7]. For example, comparing the responses between probes P_{09} and P_{10}, which are located toward the lateral side of the panel (cf. Fig. 3.3), there is a distinct time delay between the peak values of approx. 2.5 ms with the response at the inner pressure probe (P_{10}) occurring later. The same comparison for the quasi-rigid reference case under identical impact conditions shows a small time lead of 0.02 ms at P_{10}.

In addition to the discussed time delay of pressure responses, the occurrence of structural deformations during the impact significantly affects the local pressure distribution as briefly discussed in Section 3.3.2. When panels deform, pressure peak values are significantly lower, whereas post-peak mean pressure levels are generally larger thus leading to more voluminous pressure distributions (see Fig. A.3). This effect is attributed to the larger local pitch angle, which was observed to result in more voluminous pressure distributions in the investigation in Section 3.3.3.1. Furthermore, pressure time histories change toward the inner probes, where highest deformations occur: the initial rise is less sharp, peak values are again lower, and significant oscillations arise. The latter are related to a large amount of air entrapped in the central part of the deformed panel. Toward the sides, there is less or even no air involved and hence the pressure time histories at the outer locations show a similarly sharp rise as observed for quasi-rigid panels.

Figure 3.12 compares time histories of normal forces for panels of different thickness grouped for each impact condition. Generally, normal forces increase when structural deformations occur during the impact. This increase is larger for cases with more deformable panels; thus it is strongest for 0.8 mm aluminum panels compared to the 3 mm aluminum as well as the composite panels. In addition, it was observed that the impact condition significantly affects the extent of the load increase originating from the structural deformation. The effect is stronger for smaller pitch angle cases because the relative change of the local pitch angle due to the structural deformation is larger compared to that in the case at large nominal pitch angle. Moreover, the higher velocity in the impact condition at 4° pitch angle contributes to the more pronounced appearance of the effect of structural deformation, which is confirmed when comparing the pure effect of impact velocity analyzed for quasi-rigid panels in Section 3.3.3.2. Also, the aforementioned normal force peak just prior to the leading edge immersion is more intense when the initial pitch angle is smaller and when the structure is more deformable. Figure 3.13 portrays the described effect on the normal force: based on normalized normal force peak values, a clear trend can be recognized. Depending on the combination of pitch angle, impact velocity, and panel type (material/thickness), the occurrence of structural deformations

---

[7]Note that only few deformable test cases were conducted with pressure probes (see Tab. A.5).
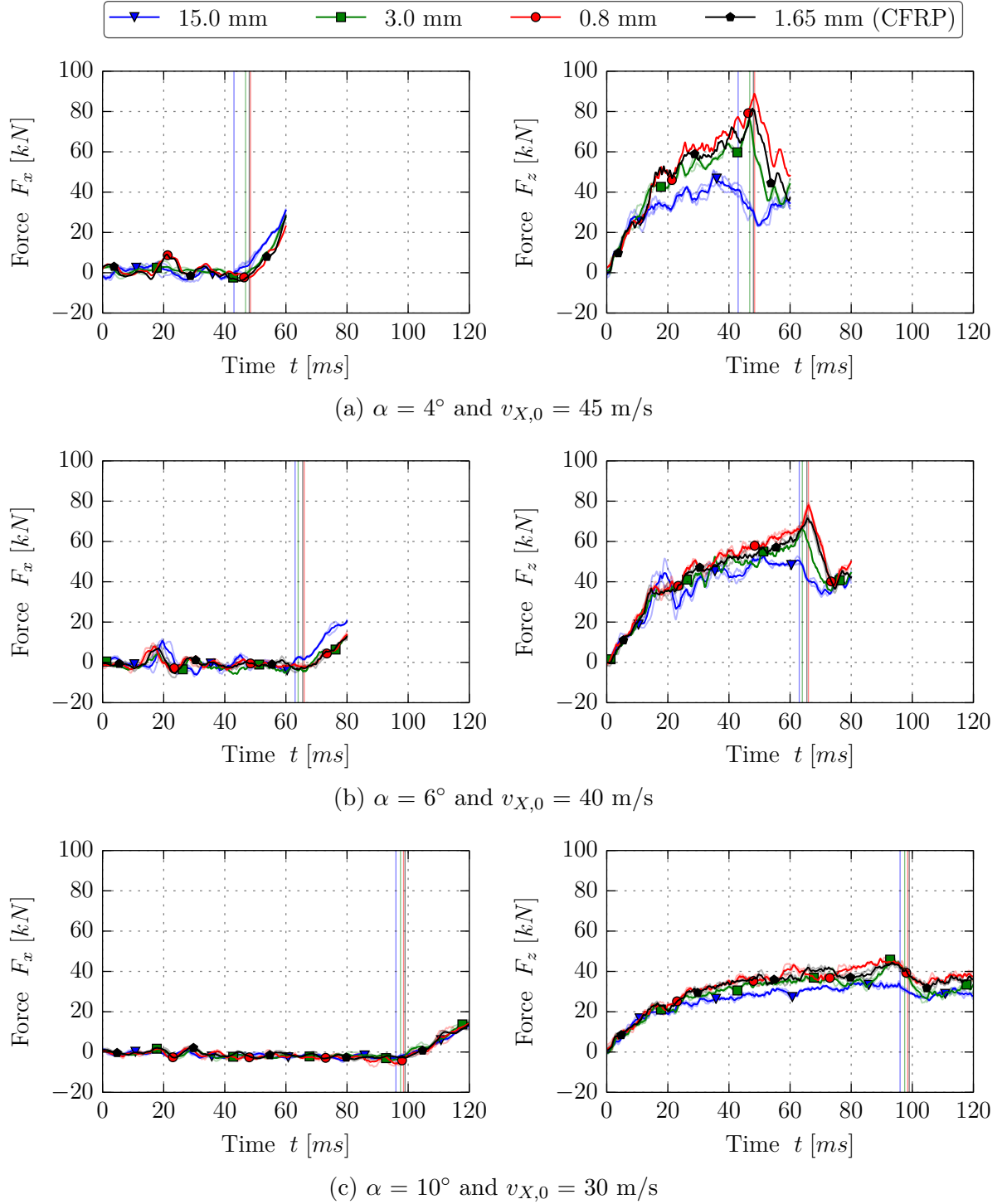
Figure 3.12: Force time histories of experiments with different panel types (material/thickness) and under different impact conditions.

accounts for a force increase of up to 82%, which emphasizes the necessity to account for structural deformations in the assessment of the structural capacity under ditching loads. Furthermore, the comparison of normalized normal force peak values for repeats at 10° pitch angle and 30 m/s or 45 m/s indicates that the effect of the structural deformation is quasi-independent of the impact velocity, i.e. the relative increase is similar in cases at 10° pitch angle and with 30 m/s or 45 m/s.
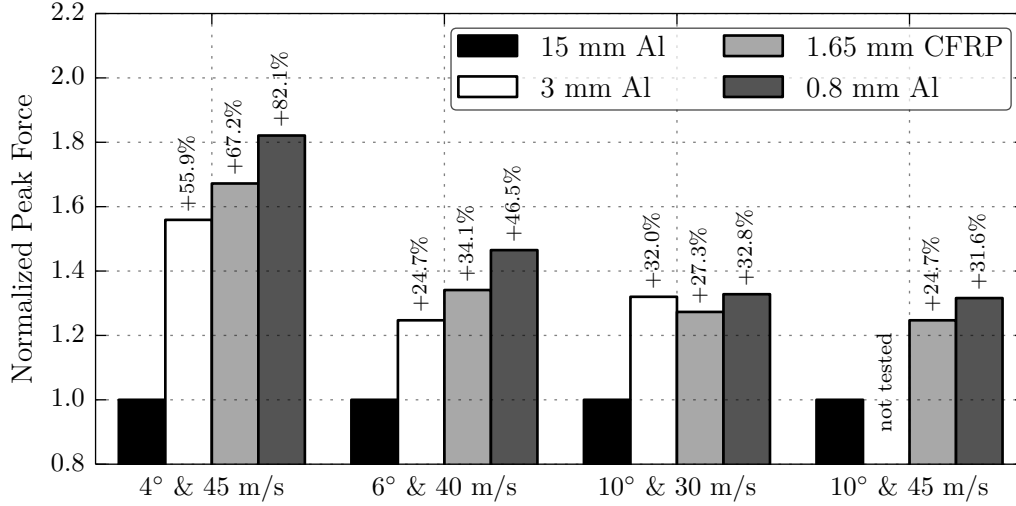
Figure 3.13: Comparison of normalized normal force peak values of experiments with different panel types (material/thickness) and variation of impact conditions.

Another interesting observation is that despite the occurrence of structural deformation, the normal forces measured in tests under identical impact conditions initially grow at the same rate. This suggests that the hydrodynamic response is largely independent of the structural response during this initial phase. Later, however, clear differences arise as discussed above. Moreover, the duration of the impact until leading edge immersion is found to extend with increasing deformation. This can be explained by the increased volume of the pocket formed by the structure, which causes the fluid to propagate slower along the panel. Again, the effect is stronger for cases with more deformable panels and with higher loads, which both contribute to the magnitude of deformation experienced.

Reached strain levels vary significantly due to the large difference of the structural flexibility between tested panels and, additionally, due to the considerably larger hydrodynamic loads resulting from the accompanying structural deformation. Yet, strain responses at identical locations are qualitatively similar. Figure 3.14 shows exemplary strain results at gauge S_2 for which a brief description is given hereafter. The strains measured on deformable panels generally exhibit large gradients in time as they are directly linked to the pressure response as discussed in Section 3.3.2. Overall, strains in x-direction show a stronger sensitivity to both the combination of impact conditions and the panel flexibility given by the combination of material and thickness. This can be attributed to the propagation of the pressure distribution along the panel in x-direction, which leads to stronger local pressure gradients in x-direction. Strain results indicate that largest measured strains typically occur at locations along the center line (S_2, S_7, S_5, S_8) with maximum values at S_8, which is located most central. Based on post-test analysis of the permanent deformation it is estimated, however, that large strains also occur in the corners of the panels and along the interface to the L-frame. As this exceeds the experimental evidence it will be part of the analysis of numerical results in Section 5.2.

(a) $\alpha = 4°$ and $v_{X,0} = 45$ m/s

(b) $\alpha = 6°$ and $v_{X,0} = 40$ m/s

(c) $\alpha = 10°$ and $v_{X,0} = 30$ m/s
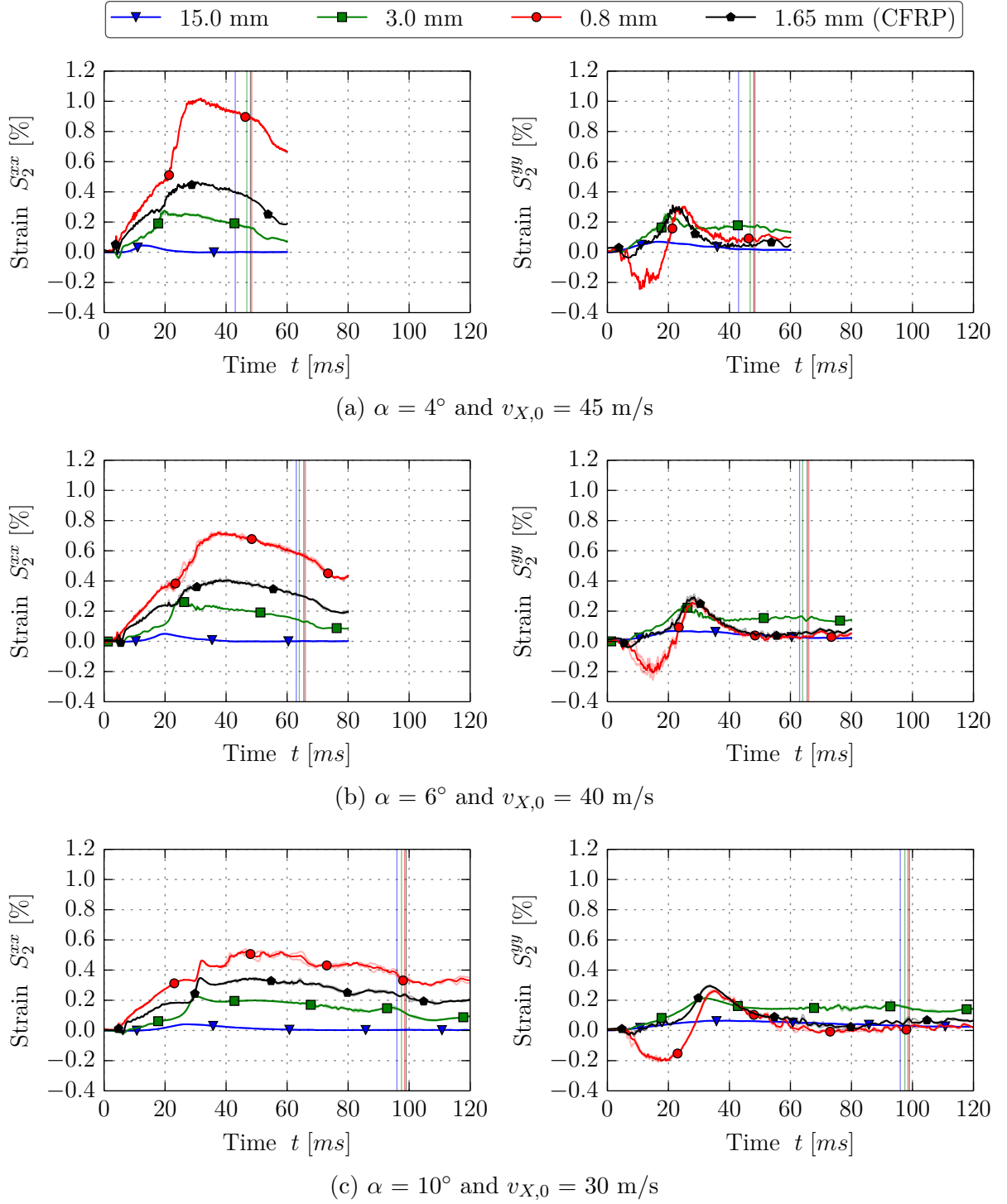
Figure 3.14: Strain time histories of experiments with different panel types (material/thickness) and under different impact conditions.

For the 3 mm aluminum panels, all measured strains remain within the elastic range although values of up to 0.32% are reached. Strains measured on 0.8 mm aluminum panels indicate plastic deformations as maximum values exceed the range of 0.4–0.5%, where plasticity starts to occur. Maximum measured peak strain values are in the order of 1.5% (measured at S_8). The composite panels reach strains of up to 0.47% at the gauge locations. Considering the increase of normal forces being only slightly smaller than the

one observed for the thin aluminum panels, their deformation is assumed to be of similar magnitude; however, strains remain within the elastic range and the composite panels completely recover to their initial, flat shape. Additional post-test non-destructive testing using computer tomography proved that none of the composite panels was damaged during the water impact.

Furthermore, experimental data enable an evaluation of spatial strain gradients. The applied strain gauges consist of two side-by-side grids for measurements in x- and y-direction. This results in a shift of the exact location of the strain measurement of approximately ± 2 mm with respect to the nominal location. The gauges S_3 and S_4 are applied at symmetric locations, yet with the same orientation. Consequently, as the side-by-side grids are slightly shifted from the nominal locations, the measured strain data permit an estimation of the strain gradients in y-direction near the borders of the unsupported panel surface. The evaluation assumes a perfectly symmetric impact without spurious effects due to an unsymmetrical lateral pressure distribution. This assumption is
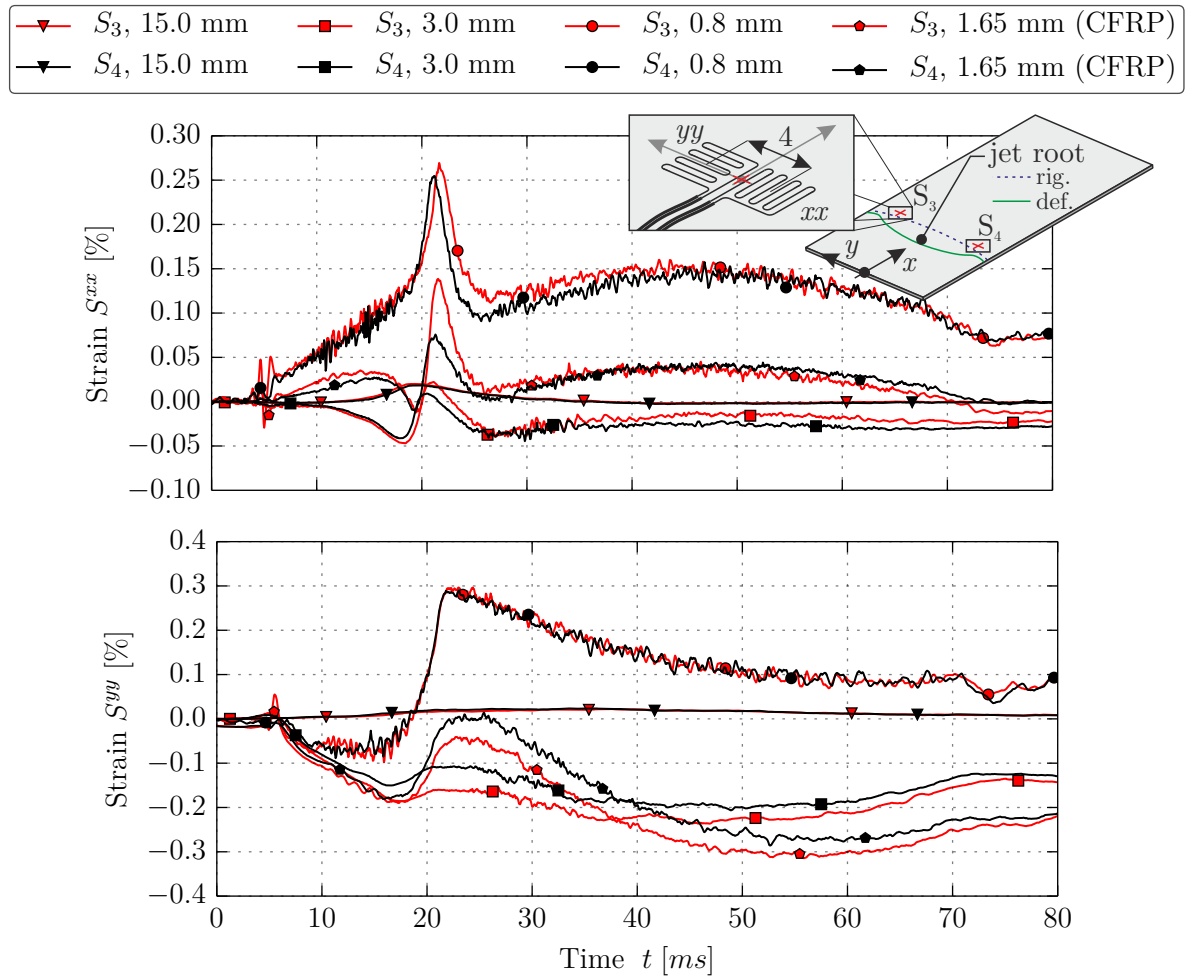

Figure 3.15: Strain gradients in experiments with different panels (material/thickness) and under identical impact conditions (pitch angle 6°, horizontal velocity 40 m/s, IDs x122). For clarity of the illustration only mean values are plotted.

valid as it was demonstrated by Iafrati et al. [80] based on pressure responses at symmetric locations, which correlate very well in time. Figure 3.15 illustrates exemplary results of the strain gradient evaluation for all panel types under one impact condition. For quasi-rigid as well as thin aluminum panels, the strain gradients at the gauge locations are small and time histories recorded at S_3 and S_4 are in agreement; however, for the 3 mm aluminum and also for the composite panels there are clear local gradients, which show as different magnitudes comparing the time histories of S_3 and S_4 for one panel type. These differences are largest at the time when the high-pressure zone passes the gauge locations, i.e. between 20–25 ms. The difference is more pronounced for strains in x-direction, which additionally show a small time lead of the response at S_4 for all cases with deformable panels. This shows that the time variation is related to the structural deformation and the resulting curvature of the jet root. In conclusion, spatial strain gradients, as illustrated comparing strains at locations S_3 and S_4, are expected along all boundaries where the panels bend as they are deformed. For the cases with thin aluminum panels, this bending is more concentrated at the interface to the L-frame, whereas it is less concentrated for those cases with the other two deformable panel types, which results in distinct spatial strain gradients at the regarded gauge locations that are located about 25 mm inside of the interface.

3.4 Summary and Discussion

The presented evaluation of guided ditching test results allowed to identify determining factors, main mechanisms, and hydrodynamic phenomena involved in the fluid-structure interaction. General findings comprise:

- The structural response is driven by the local pressure distribution with a high pressure zone located at the jet root that propagates along the structure as it immerses. Strain peak values correlate in time and space with the passage of the high-pressure zone. Yet, the structural response was found to be insensitive to highly transient pressure peak values as well as high-frequency pressure oscillations as these occur typically on a smaller time scale compared to the one of the structural response.

- The pitch angle is mainly responsible for more voluminous pressure distributions with lower peak values yet higher post-peak pressure levels and a stronger three-dimensional character of the flow field beneath the structure. It leads to higher loads and larger strains.

- The horizontal impact velocity scales the acting pressure in terms of both, peak values and residual pressures, and thus significantly increases hydrodynamic loads and resulting strains.

- A minor influence of the lateral panel curvature on hydrodynamics loads was observed. This is attributed to the large radii of curvature of ± 2000 mm. Nevertheless, convex panels give relief, whereas concave panels increase the loading.

Furthermore, the following knowledge regarding effects associated with structural deformations was gained:

- Structural deformations significantly affect the acting hydrodynamic loads. The main mechanisms involved are the increase of the local pitch angle and the development of a local deadrise angle. The temporary reduction of the local vertical impact velocity due to the deformation is assumed to be of minor importance as the resulting impact velocity is governed by the horizontal velocity.

- The pressure response changes toward significantly lower peak values, stronger oscillations, and higher post-peak residual pressures when deformations occur. These effects are stronger in zones where the deformation is larger.

- Normal forces increase substantially when structural deformations occur; this effect is more pronounced for smaller pitch angle cases due to the larger relative change of the local pitch angle provoked by the deformation as well as the higher velocity in these cases, which amplifies the effect. Distinct force peaks arise toward that instant when the fluid has to escape from the pocket formed by the deformed panel at the interface to the L-frame near the leading edge.

- The highly dynamic loading causes large temporal strain gradients. Furthermore, distinct spatial strain gradients were observed at the interface to the L-frame, where the structural bending is largest. This zone of large strain gradients is expected to become more concentrated toward the interface to the L-frame when panels are more deformable.

The following findings regarding hydrodynamic phenomena could be established:

- Air cushioning could be observed for test cases at small pitch angle. The extent of the air cushion is stronger when increasing the horizontal impact velocity.

- The concave lateral curvature of the structure leads to air entrapment, which affects the pressure response in terms of lower peak values and increased oscillations. Air entrapment could also be observed for deformable cases, where it is evoked by the dynamic deformation.

- Overall, the effects of occurring hydrodynamic phenomena on the structural response are rated to be minor.

To conclude, the high quality of the experimental results together with the range of effects and structural responses observed qualify this test campaign to support the subsequent development and assessment of the numerical model in Chapters 4 and 5.

4 Guided Ditching Simulation

Throughout this chapter, a numerical simulation model of the guided ditching experiments presented in Chapter 3 is developed following the SPH-FE approach outlined in Section 2.4. First, the developed numerical model with respect to the structural as well as the fluid modeling is described. Attention is put on modeling strategies for the fluid domain and especially on initial particle distributions, both highly useful means to increase the computational efficiency. The resulting simulation model is summarized in the final section.

4.1 Introduction

The numerical simulation of the guided ditching experiments is a very challenging multi-scale problem with a global scale referring to the motion of the structure and a local scale related to the complex fluid-structure interaction with various physical phenomena involved. It includes large fluid displacements resulting in rapidly changing interfaces, highly nonlinear structural behavior and their interaction.

The objective is to develop an accurate, efficient, and robust numerical model to replicate the main mechanisms and phenomena observed in the guided ditching experiments. It shall enable to predict the structural behavior in a finite element analysis and furthermore serve to understand determining physical phenomena. The aim is to keep the model simple and to increase the complexity only where required in order to maintain generality and to permit the application to larger aircraft structures in the future.

Building on the review presented in Section 2.4 and the evaluation of experimental data in Section 3.3, a detailed modeling approach using the FE method for the structural model and the SPH method for the fluid model is pursued. The intended application essentially requires a three-dimensional model to properly account for three-dimensional flow effects as observed in the experiment (cf. Section 3.4). Two-dimensional models used within preliminary studies were observed to largely overestimate global loads due to the additional, artificial constraints the fluid is facing. Nevertheless, it has to be noted that 2D models were instrumental for verification studies of modeling features as well as numerical parameters owing to their computational efficiency. Thus for the development of the model, a building block approach has been pursued to the extent possible.

Moreover, the possibility to use a symmetric model, which would reduce the CPU

effort, was discarded as potential local structural failure would lead to asymmetrical responses that otherwise could not be portrayed. Also for the later application to real aircraft structures, full 3D models are necessary due to the generally asymmetric design of the aircraft bottom fuselage (e.g. stiff cargo door area).

The solver used in the course of this thesis is a development version of the commercial, explicit finite element code *Virtual Performance Solution* (*VPS*, formerly *PAM-CRASH*) developed by ESI Group. The choice for a commercial solver has several advantages. For example, its ability to handle transient, nonlinear structural dynamics has been demonstrated for many applications in the field of crashworthiness simulation. Furthermore, it offers a fully integrated SPH solver, which facilitates the coupling of SPH and FE within one model. The numerical model developed in this chapter uses existing capabilities in *VPS*. However, recently implemented modeling features, which were partially developed with reference to this work, are currently available only in the referred development version of the solver based on version 2010, which has been utilized exclusively for this research.

The model generation (pre-processing) is fully parameterized based on an *ANSYS* script[1] to enable the simulation of all test cases of the experimental campaign. For the development of the model, however, the test case using a flat 15 mm thick aluminum panel impacting at 6° pitch angle and 40 m/s horizontal impact velocity (ID 1122) is chosen for illustration of modeling features unless indicated otherwise.

Figure 4.1 provides an overview of the developed simulation model, which is described in detail in this chapter. Note that X, Y, and Z are global, earth-fixed coordinates, whereas x, y, and z refer to the panel frame of reference with its origin located at the center point of the panel trailing edge.

4.2 Structural Model

4.2.1 Guide Track

Owing to the large size of the experimental facility and due to the large vertical loads of up to 120 kN acting, the guide track undergoes an evasive motion during the impact, which was measured based on optical tracking with a lateral high-speed camera [80]. Results show oscillations in X- and Z-direction due to the launch of the catapult mechanism as well as the motion of the trolley and a maximum vertical displacement in the order of 10 mm during the immersion of the structure (see Fig. 4.2). Consequently, this evasive motion lowers the effective vertical impact velocity and is believed to affect the results to a certain extent. In order to characterize and to account for experimental uncertainties originating from the guide motion, the numerical model contains the guide track and four

---

[1]The script is written in *ANSYS* Parametric Design Language (APDL) and creates the mesh that is subsequently converted by a DLR in-house tool into the *VPS* input format.
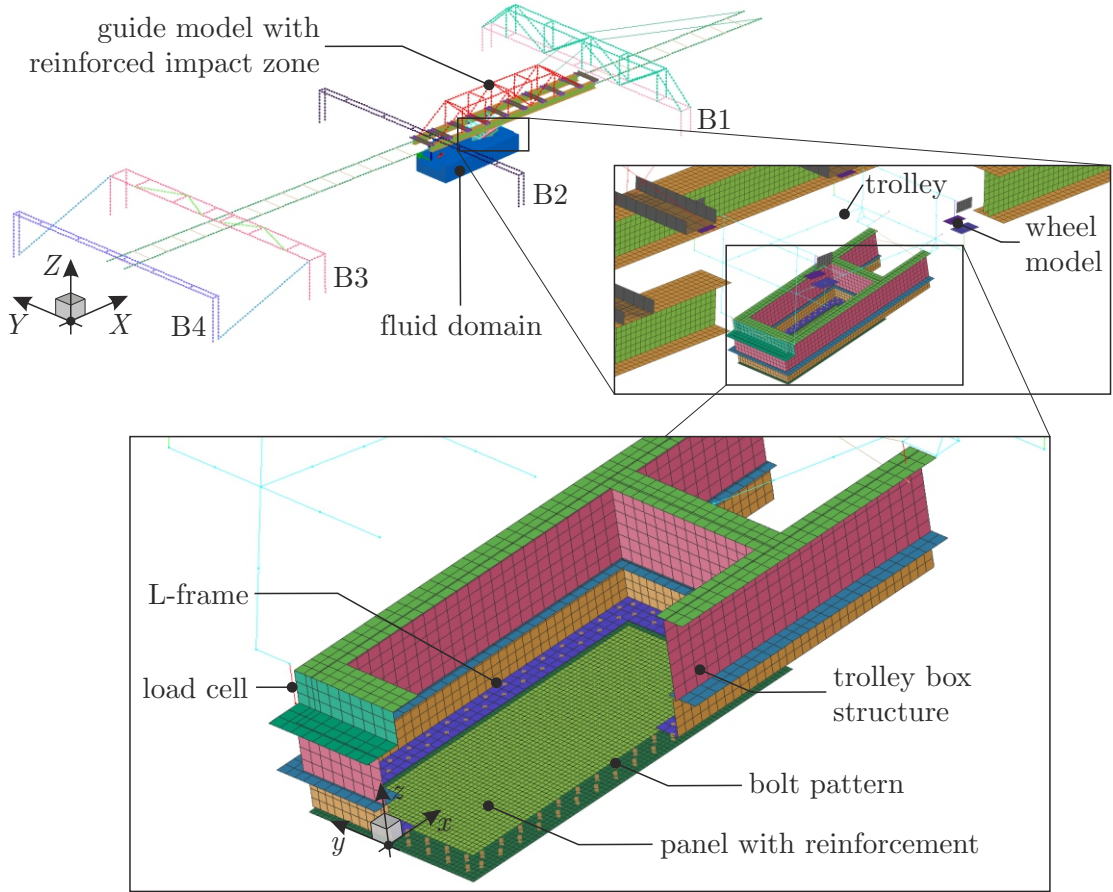
Figure 4.1: Overview of developed numerical model with zoom on trolley and specimen.

of the five bridges that are assumed to be relevant for the observed motion of the guide. The modeling uses elastic beam and bar elements in a rather coarse discretization to avoid a noticeable impact on the computational effort. This is feasible because deformations remain low compared to the overall size of the guide structure. In the impact zone, however, the guide rails are discretized using shell elements, which facilitate the coupling of the moving trolley to the guide track by means of numerical wheel models (see Section 4.2.2). Applied boundary conditions are representative of the experimental setup.

The guide model was validated against experimental observations published in [80], which refer to the test case of a 15 mm thick flat panel impacting at 10° pitch angle and 40 m/s horizontal impact velocity (ID 1132). Numerical results illustrated in Fig. 4.2 indicate similar displacement time histories compared to experimental measurements but without the oscillations associated with the catapult launch in the experiment. The vertical impact velocity as recorded on the trolley shows a reduction of up to 0.15 m/s (10%) for the regarded test case compared to a reference simulation without a guide model, where the trolley motion was constrained to the initial guide orientation, i.e. referring to the ratio of initial impact velocities of $v_{X,0} = 40$ m/s and $v_{Z,0} = -1.5$ m/s. Despite the effect on the vertical velocity, the guide motion was found to have a minor effect on the hydrodynamic loads, suggesting that the horizontal velocity plays a much more
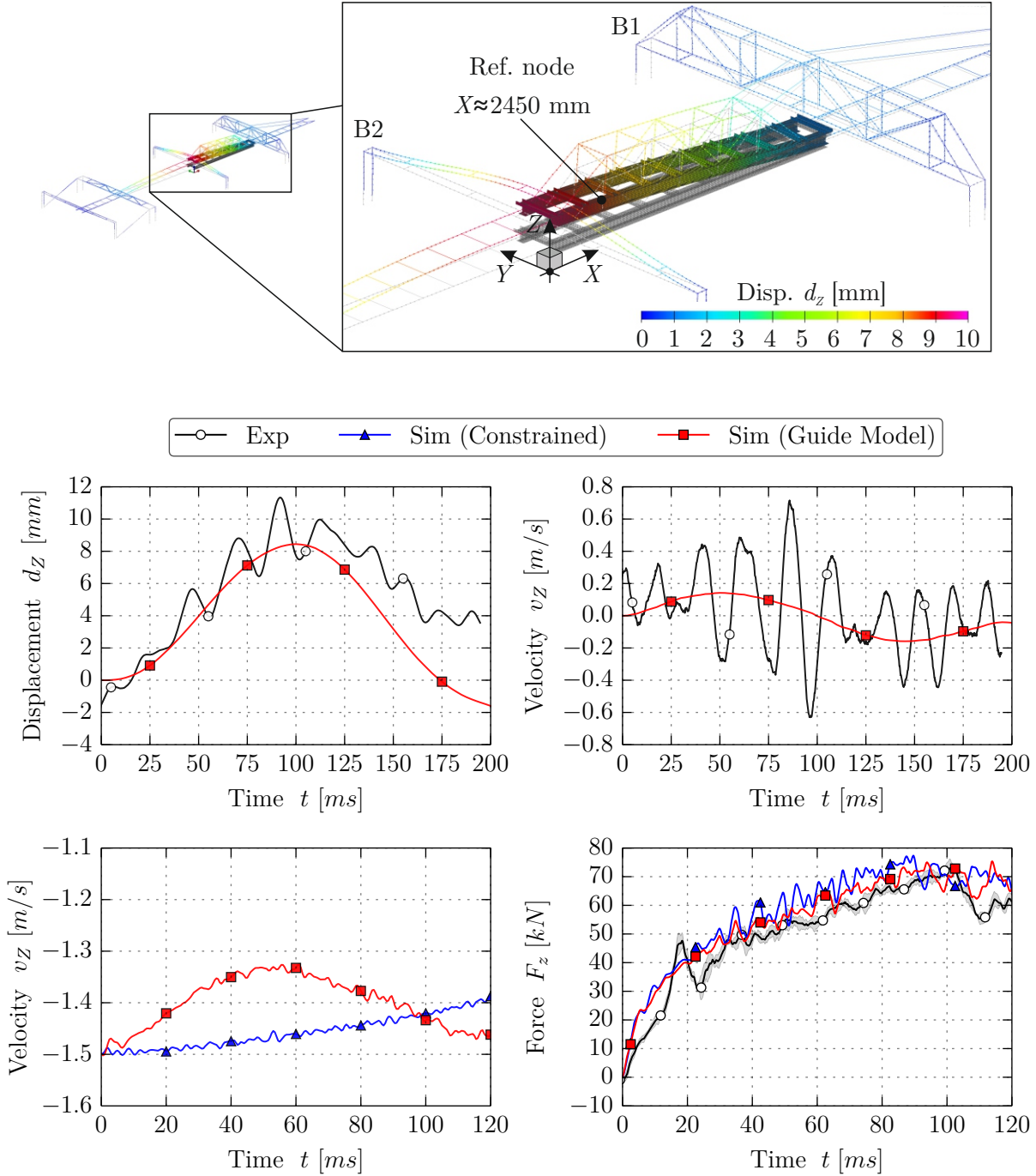
Figure 4.2: Results of guide motion analysis. The contour plot at $t = 100$ ms shows vertical displacement (amplified $\times 100$) together with initial mesh. Parts aside from the guide model are hidden for clarity. Measurements refer to a point on the guide track flange approximately 2450 mm ahead of bridge B2 in accordance with [80].

important role. Nevertheless, the evasive motion of the guide causes a slower immersion of the structure, which has a delaying effect regarding the timing; in particular, this is noticed for strain results in the forward portion of the panel and for the time associated with the leading edge immersion (approx. 5 ms or 5% of the total duration earlier for the constrained case), which correlate better when the guide motion is taken into account.

Numerical results show that the guide motion is mainly due to the flexibility of bridge B2 as the guide reinforcement in the impact zone successfully suppresses bending. The effect is approximately proportional to the acting vertical load, which is the main driver for the guide motion.

Based on presented observations, the guide model is used for all simulations, thus providing appropriate boundary conditions during the impact for all test cases. This ensures that uncertainties due to the experimental setup do not affect the comparison and validation of the numerical model.

4.2.2 Trolley and Panel

The intended finite element analysis of the structural response requires representing in detail the structural panels as well as their boundary conditions given by the L-frame and the box structure. Typical modeling strategies used in crashworthiness FE analysis of aeronautical structures are followed as delineated below.

Trolley and Box Structure   A detailed finite element model of the trolley and the box structure was developed (see Fig. 4.1) in order to accurately reproduce the boundary conditions of the panels. On the one hand, this was motivated by the fact that the structural response was found to be sensitive to the boundary conditions within preliminary simulations where the panel edges have been rigidly clamped. In particular for the thin panels, which result in a lower stiffness of the box structure compared to the thick ones, the box structures stiffness appeared to be responsible for large discrepancies in the structural behavior. On the other hand, it was preferred to evaluate the forces at the same locations as in the tests, which required a global representation of the trolley structure. As a result, the box structure is modeled using shell elements, whereas the main trolley is discretized using beam elements. The trolley and the box structure are made of steel and they do not undergo plastic deformations. Hence a simple linear-elastic material model for steel with a standard density of $\rho = 7.8{\cdot}10^{-6}$ kg/mm^3 and an elastic modulus of $E = 210$ GPa is applied.

Furthermore, the mass of the numerical model undergoing the impact is adjusted so that it corresponds to the experiments. It ranges from 832 kg to 840 kg depending on the panel type and L-frame (see Tab. A.5). The required additional mass of about 212 kg to 220 kg is equally distributed to the nodes of the trolley model.

Although the box structure and the trolley model appear very detailed, they are an idealization of the real structure and some details such as stiffening ribs as well as the acquisition system, which is mounted inside the box structure, are neglected. Despite the level of detail, the share of computational effort due to the complete structural model is almost negligible compared to that of the fluid model.

In the experimental setup, the main trolley is guided along the guide track by several

wheels. The numerical model represents these wheels by a combination of shell and beam elements. Therein the beam stiffness portrays the wheel flexibility and the shell elements are used to connect the numerical wheels to the guide track by means of frictionless sliding surface penalty contacts. Friction is neglected as it is estimated to be insignificant.

The sensitivity of results to the position of the trolley along the guide track at the moment of first water contact was investigated within the range observed during the experiments. No significant influence on the magnitude and the timing of results was found. Hence, the trolley position at initial water contact is kept constant for all simulations, i.e. with its origin at $X = 2350$ mm ahead of bridge B2.

Panels and L-frame   Panels as well as the L-frame are modeled using four-node, thin shell elements with fully integrated Hughes-Tezduyar shell formulation [75] and five integration points over the thickness to allow for a nonlinear stress distribution over the thickness. Full integration is chosen as the additional CPU cost per time step of the structural model is negligible compared to that of the fluid model. Modeling the thin-walled structure with shell elements is preferred over solid elements as this permits a considerable reduction of the computational effort[2] and also as it is the state of the art for structural modeling of aircraft structures. Element sizes are to be selected with care as they typically govern the critical time step of the simulation. Consequently, element sizes were defined such that the panel always determines the critical time step and the remaining structure allows for slightly larger time steps in order to not affect the resulting simulation time step. The typical characteristic edge length of the panel shell elements is in the order of 10 mm, which ensures sufficient accuracy as will be demonstrated in Chapter 5. The thin aluminum as well as the composite panels are additionally reinforced along the sides (cf. Section 3.2.2); the numerical model accounts for this reinforcement using a separate part definition (see Fig. 4.1) with increased shell thickness for the metallic panels and a different layup for the composite panels.

Experiments revealed material behavior up to the plastic regime for the thin metallic panels, but rupture did not occur. Therefore, the constitutive law applied to model the metallic panels is an elastic-plastic, isotropic thin shell material model. The same material model is used for the L-frame, which is also made of aluminum. Material properties for aluminum Al2024 alloy are provided in terms of density and elastic modulus for the elastic behavior, and the elastic-plastic behavior follows a polygonal stress-strain curve described by pairs of plastic tangent modulus and effective plastic stress [37]. Figure B.1 in the appendix provides the material input data.

For the composite panels, a multi-layered modeling approach, which represents the layup within one layer of shell elements over the thickness, is adopted. This choice is

---

[2]See, for example, Hiermaier [67, p. 263ff] for a more detailed discussion on advantages and disadvantages of shell elements.

based on the results of post-test non-destructive testing of the composite panels, which revealed that for all tested impact conditions no damages occurred. The multi-directional stacking of uni-directional layers (cf. Section 3.2.2) is defined as material input comprising orientation, thickness, and ply definition for each layer. Therein, plies are described by a bi-phase model that superimposes the properties of fiber and matrix to establish the element stiffness and strength. The employed composite material model only covers the elastic behavior as no damages were sustained within the experimental campaign. Material input data obtained from coupon tests carried out by CIRA are listed in Tab. B.1 in the appendix.

Bolts The modeling of the connection of the panels to the L-frame, which in the experiments was established using bolts in a double-row pattern, was found to have a significant influence on the structural behavior of the panels. A simple tied interface connection does not permit an accurate prediction of the structural response. Therefore, the bolts are discretized using point link (PLINK) elements following recommendations given in [122]. This mesh-independent joint model establishes the connection between two structural parts where required, thus exactly representing the bolt pattern, by defining a reference node between the structural parts that is used to generate the PLINK element based on a perpendicular projection onto the segments upon initialization of the simulation.

The chosen constitutive model for the PLINK elements is purely elastic and does not account for plasticity, energy absorption, damage nor failure, as required input data are not available. Hence, the present model uses a linear stiffness in axial direction with distinction between tension and compression, and a linear stiffness in shear direction, which are computed using the Huth-formula [76] and prescribed as force-displacement curves. Since these bolts should not carry significant loads under compression, the slope of the force-displacement curve (stiffness) under compression is selected at 0.1% of the one under tension. As a result, the compressive load is carried by the contact between panel and L-frame. This master-slave penalty contact formulation additionally contains friction with a coefficient of 0.4.

Due to its considerable efficiency, this modeling approach is well suited for the application to the guided ditching model as well as larger aeronautical structural models, where typically thousands of joints are used.

Initial Conditions In order to limit the computational effort and also because air is not modeled, the acceleration phase is not computed. Hence, the simulations begin just prior to the first water contact of the panel and an initial velocity vector in the direction of the guide track is assigned to all moving parts. The guide track angle γ thus defines the ratio of vertical over horizontal impact velocity as $\gamma = \arctan(v_Z/v_X)$ and depends on the specific test case. Note that for the ease of comparison between different test conditions, the target horizontal impact velocity is used rather than experimentally measured data.

Nevertheless, due to the low velocity dispersion (cf. Section 3.3.1), the resulting effect on the results is expected to be low. Moreover, gravity is applied to the model except to the guide track. The latter is excluded to avoid an unrealistic settling during the simulation due to gravity, which does not occur during the experiment, where the guide has settled into equilibrium before the test.

4.2.3 Instrumentation of Numerical Model

The quantitative assessment of the numerical model is based on comparisons of forces, strains, and pressures with experimental measurements. Applied evaluation techniques of respective results from the numerical model are outlined below. Numerical time history data are sampled at 200 kHz in accordance with the experiments.

Load Cells   Numerical load cells are modeled individually using beam elements between the trolley and the box structure in order to realistically mimic the attachment as used in the experimental setup. The beam elements are attached to sets of nodes of the trolley structure by means of nodal constraints; each of these sets is defined as a rigid body in order to transmit the loads to multiple nodes. Load cells are allowed to rotate around the global Y-axis, whereas other DOFs are constrained at each end. It has been verified that the numerical load cells do not experience noticeable lateral forces or bending moments. Finally, force results in normal (z) and in-plane (x) direction of the panel are evaluated as the axial force of respective beams, which allows direct comparison with experimental measurements.

Strain Gauges   Strains are extracted from the numerical model by evaluation of the strain tensor of those shell elements closest to the locations of strain gauges used in the experiments (see Fig. 3.3). This is possible because the outer integration points over the thickness are positioned at the surface location when using appropriate thickness integration schemes such as trapezoidal or Simpson rule. Accordingly, upper surface strain components in the element main directions denoted as xx and yy are used. The decision for this method is based on its simplicity; it does not require further modeling work and comes at no additional computational cost. However, especially in the presence of large strain gradients it may be prone to errors and must be regarded carefully. On the one hand, this is related to the mesh sensitivity and the accompanying averaging effect of the element strain. On the other hand, the mesh determines the location where the strain is evaluated, which not necessarily coincides with the exact gauge location as in the experiment. Consequently, a sensitivity study will be conducted in Section 5.2.2.

Pressure Probes   The local pressure on the moving, deformable structure is evaluated by means of SPH gauge particles as described in [58, 135]. Gauge particles are excluded

from the regular SPH algorithm as they shall only probe the local pressure and not affect the solution, i.e. they are invisible to the regular fluid particles. They extract the pressure as a weighted sum over particles within a domain of influence defined by a specific gauge smoothing length h_g as illustrated in Fig. 4.3 (left). The used equation for the gauge pressure reads:

$$p_i = \sum_j^N \frac{m_j}{\rho_j} p_j W_{ij}(h_g) \,. \tag{4.1}$$

The gauge smoothing length h_g is typically selected as a multiple of the smoothing length of regular fluid particles to ensure a sufficient number of particles within the evaluation and thus to provide smoother pressure results. Yet, it should be small enough to prevent the loss of local pressure information through smoothing. The correct use has been demonstrated by Siemann and Groenenboom [135], who presented sensitivity studies about the gauge smoothing length on pressure results and compared the method with a technique that evaluates the contact force over a corresponding area. Here a gauge size ratio $\Pi = h_g/h$ of 1.5 is adapted as recommended in [135]. Nevertheless, the resulting domain of influence in which the local pressure is sampled is typically larger than the size of the sensible element of experimental pressure probes, which most likely does not permit to capture experimental peak pressures. Similar approaches can be found in the SPH literature, e.g. [47, 115], yet the technique used here is much simpler as, for instance, it does not require to compute surface normals.

In order to attach arbitrarily distributed gauge particles to deformable FE structures without artificially constraining the structure, a special pre-processing algorithm was developed. This algorithm attaches the gauge particles to the nearest structural node (nodal constraints) so that they move with the structure when it deforms. The schematic attachment is shown in Fig. 4.3 (right).
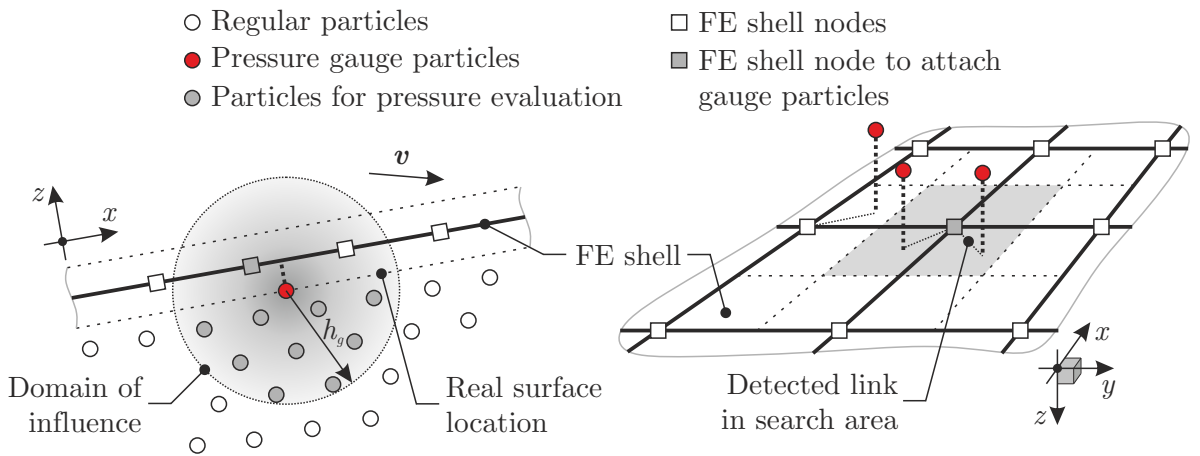

Figure 4.3: Schematic view on pressure evaluation method based on gauge particles (left) and bottom view on attachment of gauge particles to FE mesh of arbitrary, deformable structure (right).

4.3 Fluid Model

This section describes the hydrodynamic model as well as utilized modeling techniques for the fluid domain to reduce the computational effort.

In reality, the impacting structure is surrounded by water, air, and a mixture of both. The developed numerical model, however, solely contains water that is initially at rest with a flat free surface. Air is not modeled but treated as void, which is typically done when modeling free-surface flows with SPH as it would exceedingly increase the already large overall computational effort. This is on the one hand due to the additional number of particles required to model the air. On the other hand, the simulation would also need to last longer to achieve proper flow around the impacting structure. Resulting limitations with respect to reproducing associated hydrodynamic phenomena are further discussed in Section 4.3.1.4.

4.3.1 Hydrodynamic Model

The SPH formulation employed is based on the fundamentals described in Section 2.5. Specific modifications and enhancements required for the present application are described below.

4.3.1.1 Basic SPH Formulation

Kernel Function A quintic Wendland kernel is used in this work, as it was recently proven by Macià et al. [96] to be superior over the frequently used Gaussian kernel in free-surface flow simulations. Within studies of this work, it was furthermore found to alleviate the problem of standard SPH where particles tend to coincide[3]. The selected Wendland kernel function reads

$$W(q) = \begin{cases} \beta \cdot (2-q)^4 \cdot (1+2q) & \text{for } 0 \leq q \leq 2 \\ 0 & \text{for } q > 2 \end{cases} \quad \text{with} \quad \beta = \begin{cases} \frac{7}{64\pi} & \text{for 2D cases} \\ \frac{21}{256\pi} & \text{for 3D cases .} \end{cases} \quad (4.2)$$

Therein the dimension-dependent constant β controls the normalization criterion (i.e. $\int W(q)\mathrm{d}q = 1$), $q = r/h$, and r is the variable of the kernel function also referred to as kernel radius. The support domain is defined to be compact within $2h$ and the shape of the used Wendland kernel is shown in Fig. 2.8.

Smoothing Length The initial smoothing length $h(t = 0)$ is defined in relation to the particle radius r. Throughout this work a value of $h/r = 1.9$ is used. Furthermore, the variable smoothing length scheme described in Section 2.5.3 is employed; it adapts

---

[3]This is known as tensile instability of SPH, see e.g. Swegle et al. [147]. It may further be restrained as discussed in 4.3.1.3.

the smoothing length in relation to the density such that $h_i \propto (m_i/\rho_i)^{1/d}$ with d being the spatial dimension. This, however, was found to result in an excessive growth of the particle volume in the spray region, which causes the computation to become inefficient due to very few enlarged particles in the spray. These particles determine on the one hand the maximum smoothing length h_{max} that dictates the cell size for the nearest neighbor search algorithm[4], and, on the other hand, they have several thousands of neighbors. Both severely increase the computational effort per time step, which practically leads to a stop of the simulation. In order to retain the computational efficiency, the minimum and maximum smoothing length are limited to $\pm 25\%$ of the initial value $h(t=0)$. This does not affect the governing flow, yet it successfully overcomes the described problem.

Conservation Equations and Equation of State   The fundamental equations describe a fluid that is isothermal, barotropic, inviscid, and weakly compressible. Effects of fluid viscosity and surface tension are neglected, as they are of minor importance for water impact simulations (cf. Section 2.5.2). Nevertheless, a minimal amount of artificial viscosity is used in order to stabilize the SPH solution at shocks. Note that only the linear term in (2.13) is used since the quadratic term was found to not affect the simulation results. As the typical artificial viscosity used is much higher than the physical viscosity of water, hydrodynamic loads are potentially corrupted. Therefore, it was verified that for $\alpha_{AV} \leq 0.05$ there are no spurious effects. Even though gravity is often neglected within highly dynamic water impact studies, it is included in the SPH formulation, because it comes at no additional cost.

As the weakly compressible SPH variant is adopted, an equation of state is required to relate pressure to density. In this work, the Tait EOS is employed (cf. Section 2.5.2). Since air is neglected and the model includes a free surface, the background pressure p_0 in the EOS must be zero in order to avoid divergence at the free surface. Yet, the hydrostatic pressure distribution is applied upon initialization of the simulation to provide realistic initial conditions. As this initial pressure distribution is balanced by the acting gravity, it complies with the mentioned pressure condition at the free surface. The reference density ρ_0 is defined as $1 \cdot 10^{-6}$ kg/mm^3 and γ equals 7 for all simulations. Furthermore, the bulk modulus B is defined based on the incompressibility assumption discussed in Section 2.5.2, which requires $c_0 \geq 10 \max(|\mathbf{v}|)$. It results in

$$B \geq \frac{(10 \max(|\mathbf{v}|))^2 \rho_0}{\gamma} \ . \tag{4.3}$$

A sensitivity study demonstrated that the present simulation model is insensitive to the bulk modulus within a reasonable range of reference velocities between 30 m/s and 70 m/s. Moreover, results were compared with a solution employing the polynomial equation of state (cf. Section 2.5.2) with material constants from Toso [156]. Very similar results are

---

[4]For the employed kernel function in this work, the cell size is $\propto 2 h_{max}$ (cf. Section 2.5.3).

obtained, yet the numerical pressure oscillations are slightly lower for the model with the Tait EOS. Finally, for all simulations, a reference velocity of 50 m/s is adopted, which leads to $B = 3.57 \cdot 10^{-2}$ GPa. Note that for the application of the SPH method within the SPH-FE approach pursued in this work, the advantage of a larger critical time step commonly discussed in reference to the Tait EOS is generally circumvented as the FE solution of typical models requires an even lower time step.

For clarity, the fundamental system of differential equations is summarized below.

$$\frac{\mathrm{d}\rho_i}{\mathrm{d}t} = \rho_i \sum_j^N \frac{m_j}{\rho_j} (\mathbf{v}_i - \mathbf{v}_j) \nabla_i W_{ij} \tag{4.4}$$

$$\frac{\mathrm{d}\mathbf{v}_i}{\mathrm{d}t} = -\sum_j^N m_j \left(\frac{p_i}{\rho_i^2} + \frac{p_j}{\rho_j^2} + \Pi_{ij} \right) \nabla_i W_{ij} + \mathbf{g}_i \tag{4.5}$$

$$\frac{\mathrm{d}u_i}{\mathrm{d}t} = \frac{1}{2} \sum_j^N m_j \left(\frac{p_i}{\rho_i^2} + \frac{p_j}{\rho_j^2} + \Pi_{ij} \right) (\mathbf{v}_i - \mathbf{v}_j) \nabla_i W_{ij} \tag{4.6}$$

$$p(\rho) = p_0 + B \left[\left(\frac{\rho}{\rho_0} \right)^\gamma - 1 \right] \tag{4.7}$$

4.3.1.2 Enhanced SPH Formulation: Pressure Correction Methods

The standard weakly compressible SPH method is well-known to give poor pressure distributions in terms of high-frequency numerical noise in time and space, which is a result of using an equation of state wherein small density variations typically lead to large pressure fluctuations. This deficiency can be counteracted by pressure correction methods, which aim to yield more regular pressure distributions by filtering the acoustics out of the flow.

One simple means treating this acoustics problem is the use of an artificial viscosity (cf. Section 2.5.2), which in some cases may give relief. Moreover, there are enhanced SPH variants that help to counteract this discrepancy. Commonly diffusive terms are added to the fundamental equations as, for instance, in the δ-SPH scheme [98, 99] or in a technique referred to as Rusanov flux (see below). A more sophisticated means is to use Riemann solvers. The latter, however, come at a very large and perhaps prohibitive increase of computational cost and are therefore typically avoided.

In this work, established pressure correction methods like Shepard filtering and Rusanov flux are employed. Fundamentals of the respective correction methods together with a demonstration of their superiority on pressure results are presented below.

Shepard Filtering   One method that may reduce numerical noise in SPH pressure field computation is referred to as Shepard filtering. This density re-initialization method was derived from an interpolation technique initially published by Shepard [133]. As the SPH pressure calculation is based on an equation of state including the fluid density, re-initializing the density by Shepard filtering directly influences the pressure distribution.

The implemented SPH notation for the modified density $\widetilde{\rho}_i$ reads

$$\widetilde{\rho}_i = \sum_j^N m_j \frac{W_{ij}}{\sum_k^N \frac{m_k}{\rho_k} W_{jk}} \ . \tag{4.8}$$

The density field is periodically re-initialized at a user-defined cycle frequency f for which values between 10 and 40 provide the desired improvements in the pressure distribution.

Rusanov Flux The Rusanov flux is an efficient and robust but also more diffusive and non-conservative numerical scheme to solve Riemann problems proposed by Parshikov et al. [118, 119]. The main difference arises by replacing the pressure and velocity terms in the governing equations by approximate solutions that diffuse shock discontinuities and thus reduce pressure fluctuations. The conservation equations (4.4–4.6) are modified using intermediate velocity v_{ij}^* and pressure p_{ij}^* values, which approximate the acoustic solution between pairs of particles i and j[5], according to

$$\frac{\mathrm{d}\rho_i}{\mathrm{d}t} = 2\rho_i \sum_j^N \frac{m_j}{\rho_j} \left(\mathbf{v}_i - \mathbf{v}_{ij}^* \right) \nabla_i W_{ij} \tag{4.9}$$

$$\frac{\mathrm{d}\mathbf{v}_i}{\mathrm{d}t} = -\sum_j^N m_j p_{ij}^* \left(\frac{1}{\rho_i^2} + \frac{1}{\rho_j^2} + \frac{\Pi_{ij}}{p_{ij}^*} \right) \nabla_i W_{ij} + \mathbf{g}_i \tag{4.10}$$

$$\frac{\mathrm{d}u_i}{\mathrm{d}t} = \sum_j^N m_j p_{ij}^* \left(\frac{1}{\rho_i^2} + \frac{1}{\rho_j^2} + \frac{\Pi_{ij}}{p_{ij}^*} \right) \left(\mathbf{v}_i - \mathbf{v}_{ij}^* \right) \nabla_i W_{ij} \ , \tag{4.11}$$

where

$$p_{ij}^* = \frac{\rho_i c_i p_j + \rho_j c_j p_i - \rho_i c_i \rho_j c_j \left(v_j^R - v_i^R \right)}{\rho_i c_i + \rho_j c_j} \tag{4.12}$$

$$v_{ij}^{*R} = \frac{\rho_i c_i v_i^R + \rho_j c_j v_j^R + p_i - p_j}{\rho_i c_i + \rho_j c_j} \quad \text{with} \quad v^R = \mathbf{v} \frac{\mathbf{r}_{ji}}{r_{ji}} \ . \tag{4.13}$$

Assuming that variations of density and sound speed remain small (i.e. $\rho_i \approx \rho_j$ and $c_i \approx c_j$) and that the time step obeys the Courant-Friedrichs-Lewy criterion, the continuity equation (4.9), for instance, can be rewritten as

$$\frac{\mathrm{d}\widetilde{\rho}_i}{\mathrm{d}t} = \rho_i \sum_j^N \frac{m_j}{\rho_j} (\mathbf{v}_i - \mathbf{v}_j) \nabla_i W_{ij} - 2\varepsilon_{RF} \sum_j^N \frac{m_j}{\rho_j} \frac{(p_i - p_j)\mathbf{r}_{ij}\Delta t}{(r_{ij}^2 + \chi h^2)} \nabla_i W_{ij} \tag{4.14}$$

with an additional, *VPS*-specific strength parameter ε_{RF} that is in the order of 0.5 as discussed in [60]. For stability reasons the term χh^2 is added with χ in the order of 10^{-2}.

---

[5]Fluid properties at the locations of particles i and j compare to the left and right state of a discontinuity in a general Riemann problem.
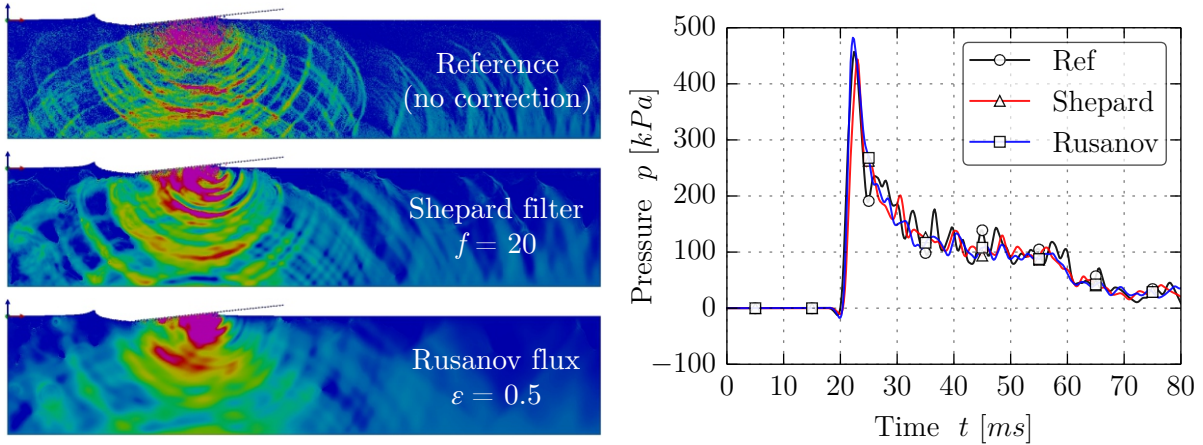
Figure 4.4: Effect of pressure correction methods on pressure field at $t = 30$ ms (left) and on pressure time history (right) for a 2D rigid flat plate impact test case.

Summary   Both pressure correction methods investigated effectively reduce the numerical noise originating from the WCSPH solution and thus yield more regular pressure distributions while still capturing the sharp pressure gradients that are characteristic of this violent water impact (see Fig. 4.4). Comparing pressure results achieved with the two methods, the Rusanov flux appears more diffusive. Yet, there are no significant effects on the kinematics of interfaces and hydrodynamic loads acting on the structure remain unaffected. The additional computational cost is negligible while in practice the stable SPH time step increases slightly due to the reduced numerical noise in the density field. This would be additionally beneficial for cases where the SPH solution defines the overall time step of the simulation (e.g. when using rigid structures).

4.3.1.3 Enhanced SPH Formulation: Particle Regularization Algorithms

Another deficiency of the standard SPH method is that particles may coincide in their position using the basic particle motion equation, i.e. the time integral of the particle velocity. The particle disorder resulting from this undesired clumping[6] increases the spatial discretization error, which decreases the overall accuracy of the SPH solution [7, 21]. Therefore, clumping accounts for numerical noise, poor and potentially unphysical results, or even breakdown of the simulation [7, 55, 60]. This is in particular problematic for the present water impact case with high relative velocities involved, as it comprises large particle displacements that cause a certain particle disorder.

Several algorithms have been developed in order to reduce or even avoid the tendency to clumping. Typically, particle positions or velocities are modified according to method-specific criteria and in reference to properties of their neighboring particles. The effect of correction should, however, be local and not smooth global flow characteristics. Conservation of mass, momentum, and energy should be maintained or changes in the conservation

---

[6]Clumping is also referred to as clustering or particle pairing in the SPH literature.

should remain very small. Furthermore, correction methods must be numerically stable and may not require considerably higher amounts of computational power. [60]

There are two fundamental approaches to regularization. The first one modifies the particle velocity and hence implicitly affects the particle position. An example of this approach is the XSPH variant in (2.15), which smoothes the velocity field. Although Monaghan [107] reported that the XSPH variant keeps particles orderly during simulations of nearly incompressible fluids in the absence of viscosity, it may not guarantee to avoid particles from clustering as it could be observed, for instance, along wetted contact surfaces in fluid-structure interaction simulations. Nevertheless, the XSPH variant may additionally be combined with the second approach, which explicitly alters the position of a particle as illustrated in Fig. 4.5: the red particle is shifted according to its neighbors in order to improve the local isotropy of the distribution. The objective of these methods is to yield a more regular particle distribution by redistributing the particles at regular intervals throughout the simulation. Whereas the velocity-based correction (first approach) is included in the computation of the particle motion during each cycle, the position correction (second approach) is conducted at the beginning of those cycles that are a multiple of the specified frequency f. Regularization algorithms of the second type of approach investigated in this thesis are briefly described in the following.

Lennard-Jones Repulsion Correction   The Lennard-Jones[7] repulsive correction proposed by Shadloo et al. [132] and later generalized by Groenenboom [55] takes into account the distance to the neighbor particles, which effectively prevents particles to coincide. The applied displacement correction is given as

$$\widetilde{\mathbf{r}}_i^{LJ} = \mathbf{r}_i + \begin{cases} \frac{\lambda}{\eta} \cdot \sum_j^N \frac{2m_j}{m_i+m_j} \cdot v_{max} \cdot \Delta t \cdot \left(\left(\frac{\alpha_r r_0}{r_{ij}} \right)^\eta - 1 \right) \cdot \frac{\mathbf{r}_{ij}}{r_{ij}} & \text{for } r_{ij} < \alpha_r r_0 \\ 0 & \text{else} \end{cases} \quad (4.15)$$

with the dimensionless strength λ, the exponent η, the maximum particle velocity v_{max}, the computational time step Δt, the initial particle spacing r_0, and the unit vector $\frac{\mathbf{r}_{ij}}{r_{ij}}$

---

[7]The name results from its similarity to the Lennard-Jones potential.
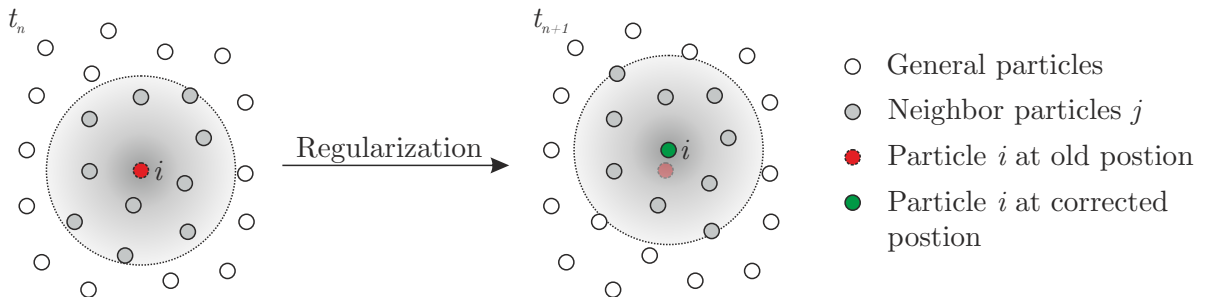

Figure 4.5: Effect of regularization algorithms on an irregular particle distribution: initial state (left) and subsequent state (right).

between particles i and j. Note that this correction is only operative for particles that are closer to each other than $\alpha_r \cdot r_0$ with α_r typically chosen to be 0.9–1.0. In contrast, when particles are at a distance larger than $\alpha_r \cdot r_0$, the correction does not act. The initial particle spacing r_0 is a constant within the present formulation, which marks a limitation compared to other regularization features when dealing with particles of non-uniform spacing and size. A strength of $\lambda = 0.2$ in combination with an exponent of $\eta = 6$ was proven to achieve good performance for the present simulation model.

Diffusion Smoothing   Another possible treatment to prevent the problem of irregular particle distributions is the diffusion smoothing algorithm proposed by Yu and Turk [164]. Therein a particle is displaced in the direction in which the distance to its neighbors is largest. This modification of the particle position uses a contribution of the mass-weighted average of the neighboring particle positions according to

$$\tilde{\mathbf{r}}_i^{DS} = \mathbf{r}_i + \lambda \sum_j^N \frac{m_j \cdot W_{ij} \cdot (\mathbf{r}_j - \mathbf{r}_i)}{\sum_j^N m_j W_{ij}} \tag{4.16}$$

with $\lambda \in (0,1)$ being the dimensionless relaxation parameter that needs to be in the order of 0.01 for proper functionality of this regularization within the present simulation model.

Color Gradient Smoothing   Initially developed by Lind et al. [90] for incompressible SPH, color gradient smoothing may also be applied using the WCSPH variant [60]. It is a diffusion-based shifting algorithm based on the gradient of the color field[8], which displaces a particle toward a position such that the color distribution becomes smoother, i.e. the color gradient is reduced. The correction reads

$$\tilde{\mathbf{r}}_i^{CS} = \mathbf{r}_i - \lambda h_i^2 \sum_j^N \frac{m_j}{\rho_j} \nabla_i W_{ij} \; . \tag{4.17}$$

The dimensionless strength parameter λ is selected in the order of 0.05.

Common Aspects   In order to avoid dispersion along free surfaces, particles near such boundaries must be excluded from regularization algorithms affecting particle positions. Moreover, such regularization algorithms were found to lead to instabilities of regarded water impact simulations when they are not applied carefully. This is due to the possible interference between the regularization methods and the used penalty-type contact for the FSI, and it occurs when the regularization shifts a particle deeper into the contact zone. In the subsequent calculation of the contact force, on the one hand, a very large, overestimated repulsive force acts on the particle, and, on the other hand, a large reaction force

---

[8]The color variable is a quantity that is zero everywhere except at the particle where it has a value of one. It describes the weighted particle volume.

acts on the structure. Particularly for thin-walled structures, this leads to unphysical, local deformations and to instabilities in the SPH model (showing up as unphysical changes in the energy balance), which can lead to a breakdown of the simulation. Consequently, particles along contact surfaces must be excluded from regularization.

Two options to exclude particles from regularization are available in *VPS*: one is based on a minimum number of neighbor particles N_{min} and the other uses a minimum value of the color function C_{min} to trigger the regularization algorithm. In this work, the minimum number of neighbors is used, yet there is no specific reason for this selection. As the specific value used depends on several SPH settings, such as the ratio of smoothing length to particle radius h/r and the kernel function W, no general recommendation can be given. For the present SPH settings, N_{min} is selected according to the observed number of neighbors along the boundaries and within the impact zone, which results in a value of $N_{min} = 48$.

Finally, after the total displacement corrections are applied and the resulting particle positions are evaluated, particle properties generally represented by ϕ are interpolated toward the new positions $\widetilde{\mathbf{r}}_i$ according to

$$\phi(\widetilde{\mathbf{r}}_i) = \phi_i - \sum_j^N \frac{m_j}{\rho_j} \left(\phi_j - \phi_i \right) \nabla_i W_{ij} \cdot \left(\widetilde{\mathbf{r}}_i - \mathbf{r}_i \right) . \qquad (4.18)$$

Moreover, the shifted particles no longer represent the same volume of the continuum. Hence, the particle masses need to be updated following

$$\widetilde{m}_i = \rho_i V_i \left(1 + \frac{\Delta \rho_i}{\rho_i} \right) \left(1 + \frac{\Delta h_i}{h_i} \right)^d . \qquad (4.19)$$

Referred updates are necessary to maintain accuracy and limit changes in mass, momentum, and energy conservation as the regularization causes a deviation from the fully Lagrangian character of the SPH method.

Summary The effectiveness of several regularization algorithms was investigated based on the evolution of the minimum particle spacing over time, which shows higher and more stable values when applying presented numerical corrections. Regularization algorithms directly affecting the particle positions were found to allow maintaining regular particle distributions more effectively compared to the XSPH variant. Nevertheless, they must be used carefully in order to not adversely affect the solution. Especially for the diffusion and the color gradient smoothing algorithms, a too large strength quickly leads to dramatic instabilities and breakdown of the simulation.

Most robust and stable results are obtained when combining XSPH with presented regularization algorithms, which are typically applied every 10 cycles. As a result, oscillations of force and strain results are reduced, and overall the stability and thus the robustness of the developed simulation model are improved. This improvement is greater for more violent cases where the effects due to the particle disorder are stronger.

4.3.1.4 Hydrodynamic Phenomena

Section 2.1 outlined possible hydrodynamic phenomena occurring during aircraft ditching. In general, hydrodynamic phenomena arise from the interaction of the water, the air, and the impacting structure, and they affect the pressure distribution acting on the structure. Regarding their spatial and temporal scale versus the estimated resolution required to capture such phenomena, their modeling appears challenging. Moreover, the complexity of the simulation model as well as the number of associated input parameters would increase. Possible modeling techniques are discussed in the following in order to substantiate their consideration in the developed model.

Modeling Air   As mentioned above, the fluid model solely contains water and the presence of air is neglected. Consequently, hydrodynamic phenomena related to the presence of air such as air cushioning, air entrapment, and ventilation cannot be captured by the present numerical model. Yet, it would be possible to additionally account for air if special care is taken to avoid instabilities that typically arise at the air-water interface due to the large difference in density, i.e. $\rho_{air}/\rho_{water} \approx 1.2/1000$. This requires, for instance, using a different formulation of the pressure term in the momentum and energy equations (2.11–2.12) leading to the following substitution:

$$\left(\frac{p_i}{\rho_i^2} + \frac{p_j}{\rho_j^2} \right) \longrightarrow \left(\frac{p_i + p_j}{\rho_i \rho_j} \right) . \tag{4.20}$$

Despite the technical possibility to include air in the model, it is not modeled for several reasons. The practical resolution of the fluid domain with respect to the computational time would not allow accounting for the small disturbances of the free surface just prior to the impact nor for air cushioning effects as observed in the experimental campaign (cf. Section 3.3.1 and Appendix A.4). Thus, a potential time delay of the impact as well as a possible reduction of the initial loads due to the acceleration of the fluid prior to the impact, i.e. the air cushioning effect, cannot be captured. Potentially resulting discrepancies will be assessed in Chapter 5. Furthermore, the present resolution seems insufficient to directly capture the mixture of water and air when comparing it to the estimated dimension of air bubbles, air layers, and cavities observed in the experimental campaign (cf. Fig. 3.4). Since entrapped air mainly results in a reduction of peak pressures, it is estimated to be insignificant for the structural response as the latter is rather insensitive to peak pressures of short duration as demonstrated in Section 3.3.2.

The referred general reasons to neglect air in water impact simulations together with the estimated minor effect of the air on the regarded water impact case justify that the presence of air is neglected in the developed simulation model.

Two-Phase and Cavitation Model   In order to model cavitation in numerical simulations, it is necessary to allow for multiple phases in the fluid model. In this work, the

two-phase fluid model described in [56] is considered. Adapted to the discretization scale of the simulation, it fundamentally treats the fluid as a mixture of water and gas that is transported by the particles assuming pressure equilibrium and a uniform velocity of the two phases within one particle. Hence a particle carries a volume fraction of water and gas, which is taken into account when computing the fluid density. This two-phase model can additionally be combined with the so-called *Full Cavitation Model* proposed by Singhal et al. [136] in order to model phase changes based on evaporation and condensation rates. For details on the formulation refer to [56].

The two-phase cavitation model has the potential to improve the accuracy of the simulation results compared to experimental data (see exemplary results in Appendix B.3). However, it also introduces ten new parameters to the model comprising, for instance, an initial gas volume fraction and empirical evaporation as well as condensation coefficients. These parameters are generally unknown and thus subject to estimation, which degrades the predictive power of the simulation. Therefore, it is decided to refrain from the use of the two-phase cavitation model for this work and to adopt a single-phase fluid model. Nevertheless, the effect of cavitation can be approximated through a simple model that limits the minimum pressure by cutting off the pressure calculated based on the EOS at a user-defined minimum value. In the present simulation model, a cutoff pressure of $p_{cut} = -1 \cdot 10^{-4}$ GPa, approximately equivalent to the vapor pressure, is used[9].

Summary The extent and magnitude of hydrodynamic phenomena observed in the experiments and their limited effects on the structural response do not justify the additional efforts required to account for them in the numerical model. Thus, it is preferred to avoid complicated modeling features as well as associated assumptions and to favor a simple, robust, and reproducible simulation methodology. Related discrepancies will be analyzed within the validation and verification studies presented in Chapter 5.

4.3.2 Modeling Strategies for the Fluid Domain

As the SPH fluid domain is responsible for the majority of the computational cost, it is common practice to limit its size by modeling particles only where they are needed. This is in regions where the fluid undergoes large displacements that lead to complex fluid interfaces, as for instance in the vicinity of the impacting structure. Farther away, where limited fluid displacements occur, the FE method provides an efficient solution. Nevertheless, arising from the relatively large horizontal velocity of aircraft during a ditching and the duration of the event, very long fluid domains are typically required. Although the structure in the guided ditching experiments is much smaller compared to an aircraft, it moves at similar forward velocities, therefore requiring a large fluid domain as well.

---

[9]Note that the cutoff pressure is negative as the background pressure is zero in the present model.

In addition, for a sufficiently accurate fluid-structure interaction simulation a locally fine fluid model is required, which implies that the computational effort will become very high if not prohibitive. Therefore, modeling strategies aimed at reducing the computational effort related to the SPH solution are investigated. Common among these is the idea to compute the fluid solution only in a sub-domain around the impacting structure and thus to reduce the number of particles within the computation.

4.3.2.1 Translating Active Domain

Using the translating active domain (TAD) feature, particles outside of a user-defined rectangular domain are set inactive and thus not computed within the SPH algorithm.

The active domain is defined by three nodes: two nodes set the size of a rectangular box and a third node can be used to link the motion of the active domain to a moving body. In the guided ditching simulation, the active domain is linked to a node of the trolley model in order to move the active domain with the impacting structure and therefore to provide active particles in its vicinity. As the active domain is translated, particles are activated once their position lies inside this domain. In contrast, particles are deactivated when they are no longer located inside the active domain. Additionally, there is a transition zone that provides proper boundary conditions for the active particles. This transition zone measures twice the smoothing length of particles near the active domain boundaries. Moreover, particles are assigned the hydrostatic pressure when they are activated, as the hydrostatic pressure is accounted for in the simulation. Figure 4.6 illustrates the described functionality.

The achievable increase in computational efficiency is approximately proportional to the number of active particles compared to the total number of particles.
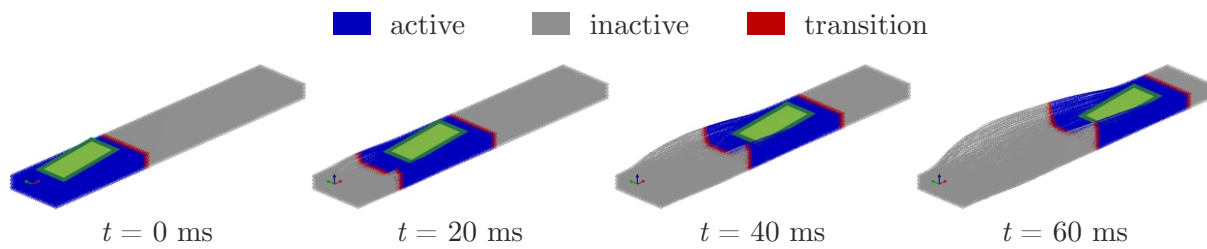

Figure 4.6: Sequence of guided ditching simulation using the translating active domain feature. Note that parts of the simulation model are hidden for clarity.

4.3.2.2 Translating Periodic Boundary Conditions

Another means to reduce the number of particles for the computation are translating periodic boundary conditions (TPBCs) as introduced in [59–62]. A schematic illustration is given in Fig. 4.7. This modeling feature extends the well-known concept of periodic boundaries with the possibility to allow these boundaries to translate according to the
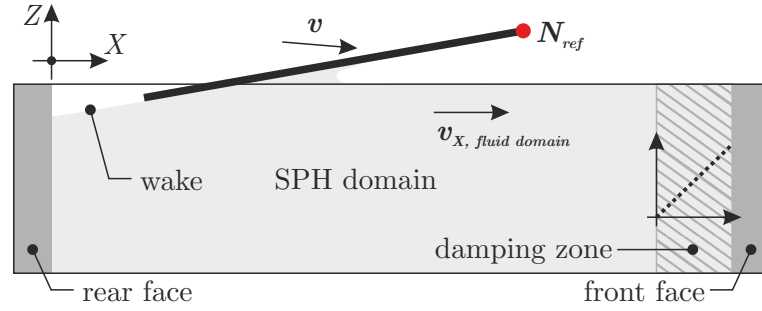
Figure 4.7: Schematic view on translating periodic boundary conditions with damping zone.

motion of a reference node. For the application to the guided ditching simulation, the horizontal motion of the TPBCs is linked to a node of the trolley similar as described for the TAD feature. As a result, the fluid domain moves in global X-direction at the same velocity as the impacting structure. Particles are only modeled around the impacting structure leading to a significantly reduced number of particles and thus to computational savings.

Generally, particles leaving the fluid domain over a periodic boundary are re-entered at the opposing boundary. In case the rear end of the fluid domain is relatively close to the impacting structure, there is, however, a strong wake and particles have not returned to their hydrostatic equilibrium position. Since it is undesirable to re-enter the particles with the distribution and velocities in the wake of the impact, all particle variables as well as the positions other than in translational direction are reset to the initial values upon re-entry.

Due to the interaction between particles on either side of the periodic boundaries, prescribed initial conditions assigned to re-entered particles are not exactly preserved. Consequently, the particle distribution in front of the structure may still be disturbed. In order to counteract this artifact, a damping zone is added to linearly decrease the non-equilibrium displacements and velocities to their initial values (in the present case equal to zero) while the particles traverse over the damping zone. This damping zone has a length of a few times the smoothing length and it moves with the fluid domain. It has been verified that this feature allows damping any remaining disturbances arising from the periodic boundaries and thus it provides quiescent water conditions during the entire impact.

4.3.2.3 Comparison and Assessment

Both aforementioned modeling strategies are easy-to-use and allow for a significant increase in efficiency by reducing the number of particles considered within the SPH algorithm. Achievable computational savings will be higher for simulations with larger horizontal velocity and with longer duration, as in these cases, the fluid domain must be longer and thus the ratio between active and inactive or not modeled particles grows.

In comparison to the TAD feature, using TPBCs results in a smaller number of particles in the model, which facilitates the handling during pre- and post-processing. In contrast, the TAD feature offers the advantage that it allows varying the size of the active domain throughout the simulation, which is not possible when using TPBCs.

4.3.2.4 Combination with Hybrid SPH-FE Fluid Modeling

Initially, the above modeling features were developed solely for a pure SPH fluid domain and it was not possible to employ them within a hybrid fluid model comprising SPH and FE continuum elements, as it has been previously used to reduce the computational effort (cf. Section 2.4.1). Using the hybrid fluid model, the water domain modeled with continuum elements was not properly supported in regions with inactive particles or void, i.e. regions where the SPH fluid domain is not present or inactive at a regarded instant of time. Being subject to gravity and inertia after the passage of the SPH fluid domain, the continuum fluid elements were severely displaced and caused numerical instabilities leading to a breakdown of the simulation.

In order to combine the novel modeling features with surrounding FE continuum elements, it was necessary to modify the computation of the fluid continuum elements. Therefore, velocities and accelerations of FE nodes outside the active domain (see Fig. 4.8) or outside the TPBC region are set to zero. This successfully prevents aforementioned numerical instabilities and permits using a hybrid fluid model in combination with a translating active domain or translating periodic boundary conditions for the SPH fluid domain. Consequently, the computational efficiency can be considerably increased compared to previous models. A benchmark is included in the following section.
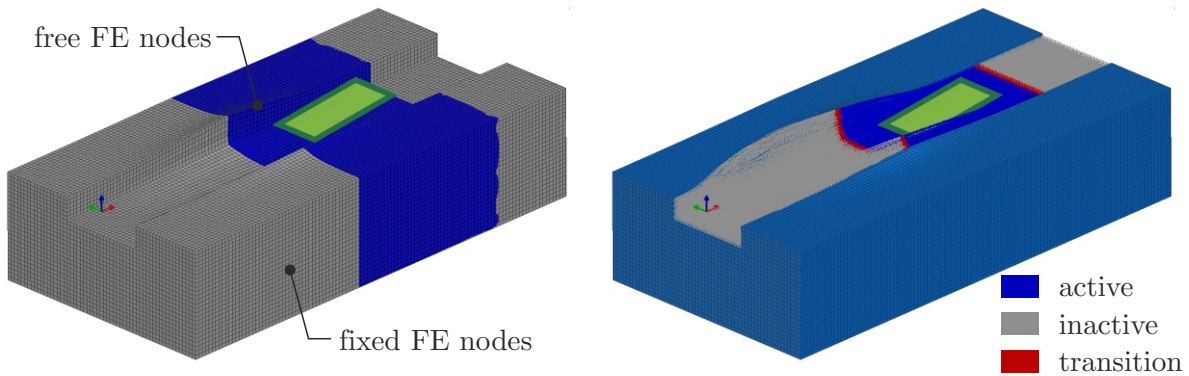

Figure 4.8: Guided ditching simulation with hybrid fluid model in combination with TAD. On the left, FE continuum elements are colored according to their velocity (blue represents non-zero velocity). On the right, the corresponding active domain of the same model is colored as indicated in the legend. Note that parts of the simulation model are hidden for clarity.

4.3.2.5 Minimum Fluid Domain Size

In general, modeling the full water basin as in the experiment is not necessary; however, the size of the computational fluid domain must be chosen to avoid spurious effects from the numerical boundaries. In addition, it is driven by the dimensions and the motion of the impacting structure. The objective is to discretize the fluid domain with SPH particles only where large displacements occur and to use surrounding continuum elements to provide a fluid domain of sufficient size, thus allowing for efficient simulations. In order to establish the minimum fluid domain size, the hybrid fluid model with a translating active domain is investigated. The vertical boundaries of the fluid domain are constrained in such a manner that the outer nodes of the associated continuum elements may only undergo displacement in vertical direction. Nodes of the bottom face as well as of the vertical edges are fully constrained, i.e. all DOFs fixed.

All simulations use particles with 20 mm spacing in a hexagonal lattice arrangement. The size of the continuum elements is chosen with an edge length equal to twice the particle spacing. Simulations cover 70 ms of the impact, which includes the leading edge immersion of the panel as observed in the corresponding experiment. Numerical force time histories filtered with a CFC1000 filter are compared to experimental data. First, the minimum size of the cross-section is established and then the required length of the (active) SPH domain is analyzed.

Cross-section Parameters varied include total width and height of the hybrid fluid domain (w_T, h_T) as well as width and height of the SPH domain (w_S, h_S) as given in Tab. 4.1 (see also Fig. 4.9, left). For simulations regarding the overall size of the fluid domain, the size of the SPH domain is kept constant with $h_S = 200$ mm and $w_S = 800$ mm. Similarly, for the studies about the size of the SPH domain, the overall size of the fluid domain is kept constant with $h_T = 1000$ mm and $w_T = 2200$ mm. The length of the active domain is kept constant with margins of 300 mm behind and in front of the structure.
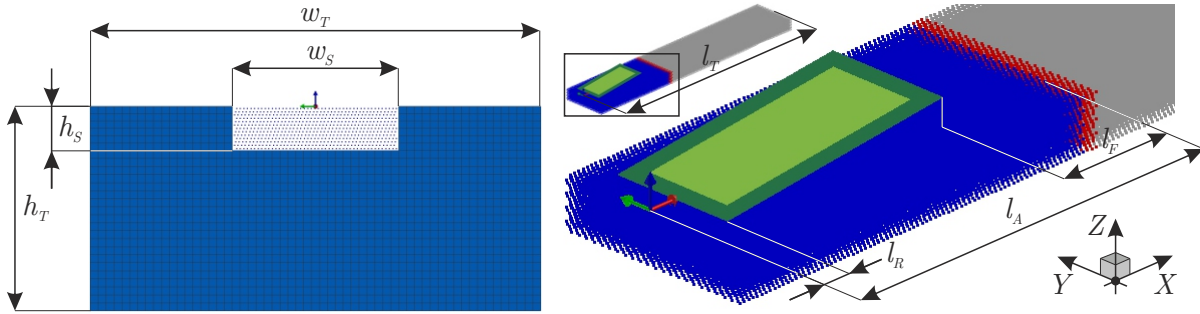
Results presented in Fig. 4.10 indicate that the total height of the fluid domain should be chosen no less than 1000 mm to eliminate boundary effects, yet the influence on the normal force remains small. The total width has a stronger influence; a narrow fluid domain restricts the fluid motion toward the sides. This adds a noticeable constraint to the fluid resulting in a considerably increased normal force. Based on presented results, the total width of the fluid domain is chosen to be 2200 mm. This is preferred since the computational effort associated with the continuum elements is comparatively small; for instance, the case with a total width of 1800 mm is only 2% faster.

Interestingly, height and width of the SPH domain do not show an appreciable influence on the normal force[10]. The width can be chosen just slightly larger than that of the structure, as the distortion experienced by the surrounding continuum elements

---

[10]Results are provided in Fig. B.3 for completeness.

Table 4.1: Overview of investigated sizes of cross-section of hybrid fluid domain.

<table>
<tr><td colspan="5" align="center">(a) Total fluid domain size.</td></tr>
<tr><td>h_T [mm]</td><td colspan="4" align="center">w_T [mm]</td></tr>
<tr><td></td><td>1000</td><td>1400</td><td>1800</td><td>2200</td></tr>
<tr><td>500</td><td></td><td></td><td></td><td>x</td></tr>
<tr><td>1000</td><td>x</td><td>x</td><td>x</td><td>x</td></tr>
<tr><td>2000</td><td></td><td></td><td></td><td>x</td></tr>
</table>

<table>
<tr><td colspan="4" align="center">(b) SPH domain size.</td></tr>
<tr><td>h_S [mm]</td><td colspan="3" align="center">w_S [mm]</td></tr>
<tr><td></td><td>600</td><td>800</td><td>1000</td></tr>
<tr><td>100</td><td></td><td>x</td><td></td></tr>
<tr><td>200</td><td>x</td><td>x</td><td>x</td></tr>
<tr><td>300</td><td></td><td>x</td><td></td></tr>
</table>

Figure 4.9: Definition of cross-section of hybrid fluid domain and length of active domain.

remains limited and does not affect the simulation time step; thus continuum elements can be successfully utilized to reduce the computational effort. Consequently, a width of the SPH domain of 600 mm is chosen. The height of the SPH domain cross-section is selected based on the immersion depth of the structure at the end of the simulation in order to provide a sufficient amount of particles around the structure during immersion. This depth depends primarily on the pitch angle: for larger pitch angles cases the structure immerses deeper into the fluid domain until the leading edge immerses. To allow for a general definition of the fluid domain covering all test cases to be investigated, the height of the SPH domain is defined to be 200 mm.

Length of active domain   Next, the necessary minimum length of the (active) fluid domain is investigated to quantify the increase in computational efficiency possible through application of modeling features discussed above. In particular, the length of the fluid domain in the rear and in the front of the impacting structure (l_R, l_F) is varied to allow for optimal efficiency (see Fig. 4.9, right). For simplicity, l_R and the length of the active domain l_A are prescribed causing l_F to minimally increase with the pitch angle of the structure. The total length of the fluid domain l_T is calculated as the sum of the active domain length l_A and the distance the structure travels during the simulation approximated as the product of initial horizontal velocity and duration of the simulation. When neglecting the deceleration experienced during the impact, the latter results in approximately 2800 mm for the regarded test case ($v_{X,0} = 40$ m/s and $t = 70$ ms). The reference
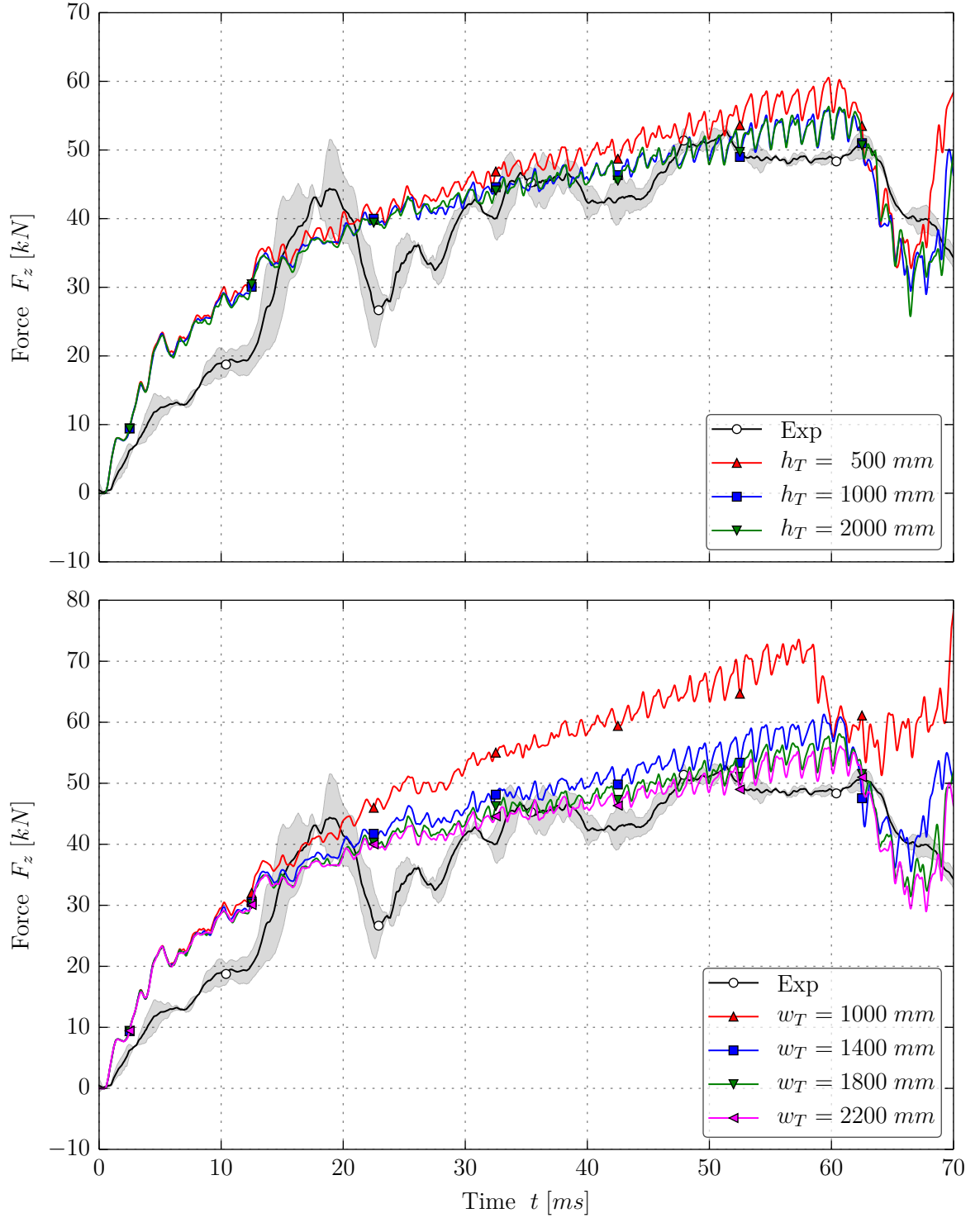
Figure 4.10: Comparison of normal forces for different total fluid domain heights h_T (top) and widths w_T (bottom) with experimental data.

model for comparison uses a conventional hybrid fluid model with an SPH domain extending over the entire length of the fluid domain. Table 4.3 presents investigated parameters and the associated elapsed time T_{Ela} of the simulations compared to the reference case.

Results presented in Fig. 4.11 show that during the initial stage of the impact, i.e. up to about 50 ms, there is no relevant effect on the normal force. Yet, differences appear toward the time when the leading edge immerses into the water. Compared to

Table 4.3: Overview of investigated lengths of the fluid domain as defined in Fig. 4.9 (right) and associated elapsed times T_{Ela}.

Modeling Strategy	l_T [mm]	l_A [mm]	l_R [mm]	l_F [mm]	# SPH active/total		T_{Ela} [h]	
	4000	1200	100	100	35581/119600	(29.8%)	2.90	(-)
TAD	4400	1600	300	300	47541/131560	(36.1%)	3.65	(-)
	5800	3000	1000	1000	89401/173420	(51.6%)	6.34	(-)
Classic	4400	4400	-	-	131560/131560	(100.0%)	8.28	(100.0%)
TAD	4400	1600	100	500	47541/131560	(36.1%)	3.64	(44.0%)
TPBC	1600	1600	100	500	47541/47541	(100.0%)	3.63	(43.9%)

the reference case using a full pool, cases with a shorter active domain lead to a later leading edge immersion. This results from the water ahead of the impacting structure being hindered from piling up as the related particles are inactive (TAD) or not modeled (TPBCs) and thus not displaced upward as seen in the reference case, where particles about 500 mm ahead of the structure show a vertical displacement in the order of 2 mm. Moreover, for the case with the shortest active domain with just 100 mm margins, an increase of the maximum normal force is observed, which is attributed to the reduced domain size. The other cases do not show an increase of the maximum normal force compared to the reference case.

Additional studies with different margins in front and rear indicate that the fluid domain behind the structure can be rather short, whereas a sufficient length of active particles must be provided ahead of the structure in order to not impair the timing. The best compromise of accuracy and simulation runtime is reached when using 100 mm margin behind and 500 mm margin in front of the structure. This setup allows the simulation to be 2.3 times faster compared to the reference case while the effect on the timing of results remains minor.

Conclusion Particles are only computed where they are needed at any given moment, which permits a significant reduction of the computational effort over the state of the art. Moreover, the amount of (active) particles necessary for a domain of sufficient size no longer increases with the simulation time and, hence, possible savings increase for simulations with larger horizontal velocity and with longer duration. Subsequently, the TAD feature is adopted for all simulations as it provides an ideal fluid domain when particles are activated in front of the impacting structure. The TPBC feature may suffer from small irregularities in the particle distribution arising toward later stages of the simulation (particles of one initial cross-section are not necessarily re-entered at the same time). As this potentially affects longer simulations, the TPBC feature is discarded.
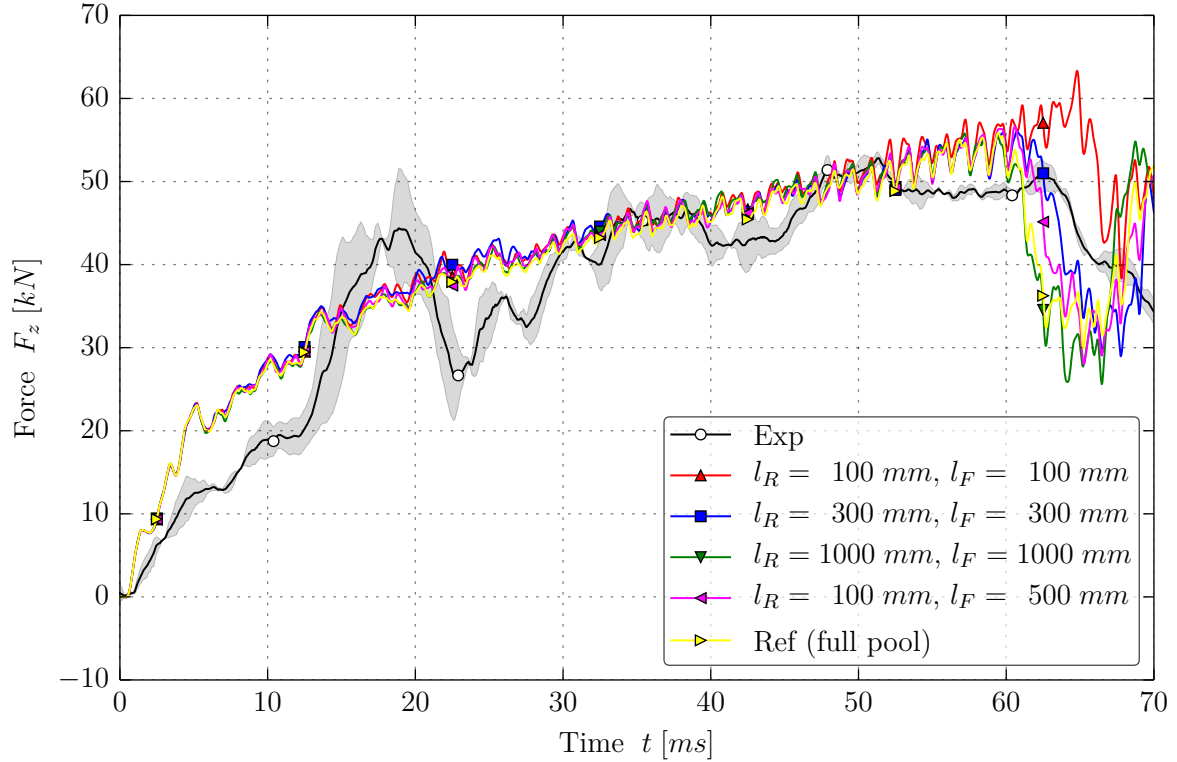
Figure 4.11: Comparison of normal forces for different active SPH domain lengths (TAD feature) and a reference simulation (full pool) with experimental data.

4.3.3 Particle Resolution

The particle resolution substantially affects the accuracy of the solution as well as its computational cost. As a compromise between the two must be established, a study of different SPH resolutions is conducted. Such a convergence study should always be conducted as several researchers have pointed out the associated sensitivity, e.g. [6, 81].

Investigated resolutions are defined through the particle spacing ds, for which values of 40, 20 (reference case), and 10 mm are regarded. Further refinement is not considered due to the prohibitive computational cost associated[11]. For this study, the fluid domain is discretized following the hybrid approach with a translating active domain as discussed above and particles are initially distributed in a uniform hexagonal lattice arrangement.

Force and strain results presented in Fig. 4.12 show a clear trend toward matching experimental measurements when refining the SPH resolution. Also, oscillations reduce noticeably. However, the timing of the leading edge immersion is adversely affected by the particle resolution. Investigations of the flow field underneath the structure indicate that the simulation fails to capture the detailed flow characteristics such as the jet root

---

[11]Since the computational cost is approximately proportional to the amount of SPH particles in the computation, a reduction of the particle spacing about a factor of two yields an increase of the total computational cost about a factor of eight (assuming no effects on the simulation time step, which is dictated by the FE solution of the structural model).

as well as the pile-up of particles when the resolution is coarse. In particular, for the case with 40 mm particle spacing no pile-up is observed and thus the leading edge immersion occurs later compared to the finer cases (63 ms vs. 60 ms vs. 58 ms). Nevertheless, the timing of the strains and thus the structural response is less dependent on the resolution, as it can be seen comparing the strain time histories at different locations. Yet, it can be noticed that strains decay later when the resolution is coarser. Despite the sensitivity to the resolution, findings further suggest that the time delay of the experimental results is related to occurring hydrodynamic phenomena (cf. Section 3.3), which are not accounted for in the simulation model.
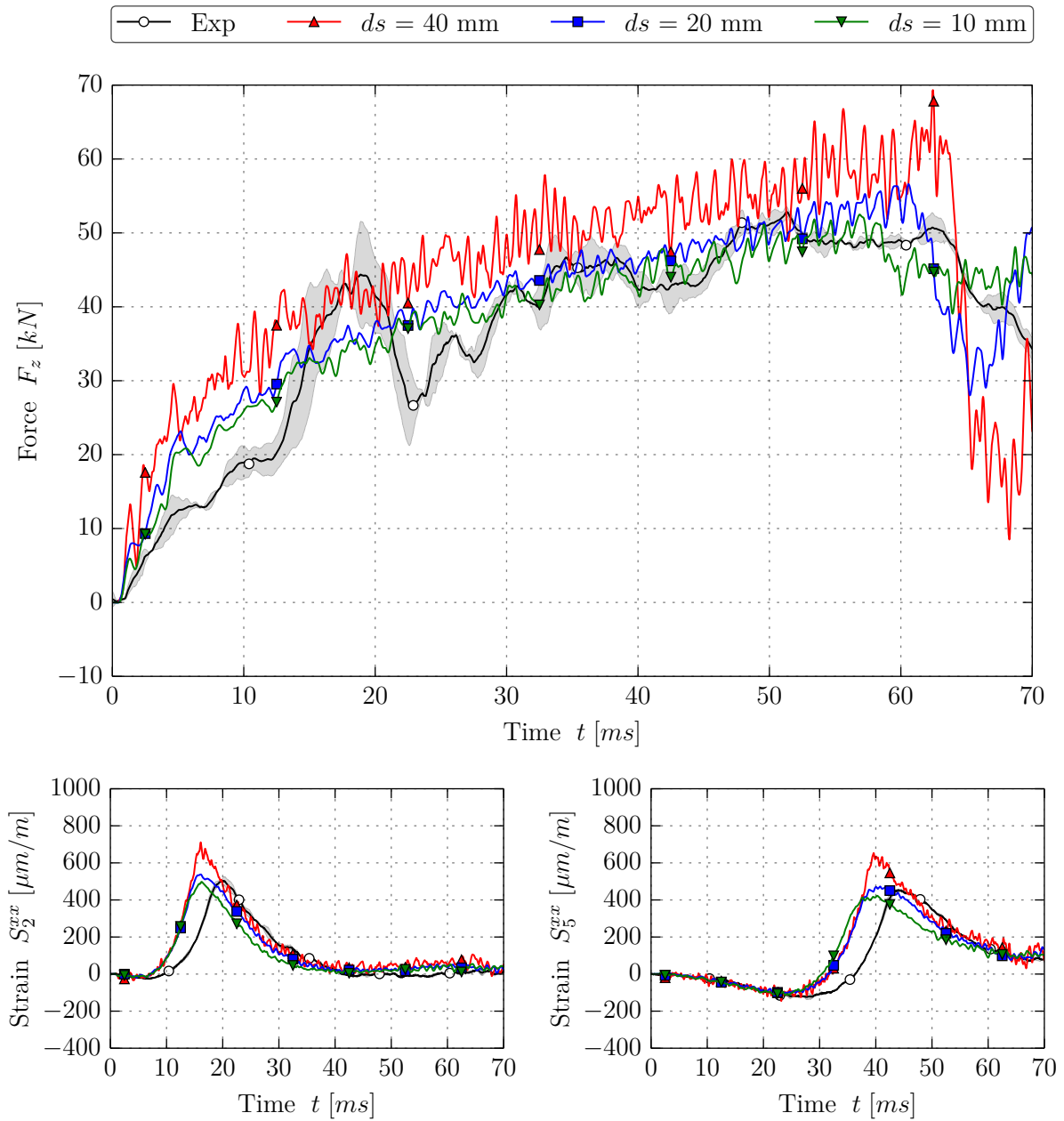

Figure 4.12: Comparison of normal forces (top) and exemplary strains (bottom) for different SPH resolutions with experimental data.

In consideration of the results achieved and the computational cost required, a resolution with 20 mm particle spacing appears sufficient for the regarded case with insignificant structural deformation. However, when there are larger structural deformations that require also a finer structural mesh, the particle resolution must be refined accordingly. Generally, the particle spacing as the measure for the particle size should not be larger than the characteristic element edge length of the structural mesh in order to achieve accurate local loading and strain results.

In order to further study the effect on the timing related to the particle resolution, additional investigations using a 2D model of a flat rigid plate impact are conducted. Due to the reduced amount of particles but also due to significantly fewer neighbor particles compared to a corresponding 3D case, the 2D simulations are computationally much less challenging and allow for further refinement. Particle spacings of 20 mm, 10 mm, 5 mm, and 2 mm are analyzed. Findings generally indicate that a certain minimum resolution is required to capture the characteristic flow field kinematics such as jet root and spray formation below the plate. Recalling that the high-pressure zone around the jet root location is responsible for the structural loading (cf. Section 3.3.1), an appropriate fluid behavior in this zone seems crucial. Results[12] illustrate that the characteristic flow field starts to appear for $ds \leq 10$ mm. The 2D case with a particle spacing of 20 mm, which does not show the characteristic flow field, even leads to an unphysical void zone below the jet root, i.e. particles at the free surface are displaced as a layer. Once the typical flow field kinematics are observed, the propagation of the jet root along the structure is found to be slower for models with smaller particles as documented in Tab. B.3. On the basis of this trend, it is anticipated that the discrepancy of timing as observed for the 3D guided ditching simulations further decreases and eventually converges when refining the particle distribution. Nevertheless, due to the large CPU effort associated and in regard to the quality of achieved results, further refinement of the 3D simulations is omitted in this work.

4.3.4 Initial Particle Distribution

In the literature, particles initially arranged on cubic lattice structures with uniform size as well as uniform spacing in all directions are typically used for SPH fluid flow and impact simulations. The focus usually lies on the resolution of the discretization in order to find a compromise between computational time and accuracy, whereas the arrangement of the particles is rarely investigated.

A general problem of distributions based on lattice structures is that their inherent alignment results in preferential directions, which may negatively affect the transmission

---

[12]Exemplary results of the 2D simulations are given in Fig. B.4 for completeness.

of loads [50, 111]. For the present guided ditching simulation, it was observed that particles initially arranged on a cubic lattice cause larger numerical oscillations in the simulation results. A hexagonal particle distribution, which is analytically prescribed by the developed pre-processing script, was found to alleviate this behavior and is therefore used as default.

Moreover, besides that a too coarse SPH resolution most likely fails to represent the hydrodynamics of the fluid-structure interaction, it also results in an insufficient amount of particles loading the structure. Especially for highly deformable structures, which require a fine structural mesh, this becomes apparent. It shows as a discontinuous, unphysical loading of the structure concentrated in a pattern of bands according to the particle size and distribution. This banding effect results from a disproportion of the ratio of particles per shell element. Therefore, sufficient refinement near the impacting structure is required to avoid banding and thus to properly load the structure.

It is obvious that the requirement of a fine spatial resolution to suitably model appropriate physics within the present multi-scale application quickly drives the computational effort to uneconomical orders of magnitude when using equispaced particles of uniform size (cf. Section 4.3.2). This scales mainly with the total amount of particles that is defined by the resolution; the effect of the resolution on the time step is insignificant as the overall simulation time step is typically governed by the structural mesh.

Above drawbacks and limitations related to the frequently used uniform lattice-type distributions motivated to study particle distributions in more detail. In mesh-based numerical methods, the use of non-uniform meshes is common practice, which led to the idea of using non-uniform initial particle distributions. These may enable a fine discretization where needed and yet allow for a reasonable amount of particles by gradually decreasing the particle resolution away from the impact zone. Nevertheless, resulting from the nature of the SPH method, where spherical symmetry is presumed, a uniform particle distribution is preferable in order to avoid numerical artifacts. Due to the robust character of SPH, however, a locally quasi-uniform configuration is sufficient to maintain stability. Regarding non-uniform distributions, this prescribes a limitation on the gradient of the particle resolution that needs to be small enough in order to keep the distribution quasi-uniform in a local reference frame.

The objective is to minimize the total amount of particles needed to model the ditching load case while retaining the high quality of results. Therefore, the focus lies on combining the advantages of a variable resolution with the reduction or even removal of preferential directions in order to find an optimal configuration. It is essential that resulting particle distributions remain numerically stable throughout the impact simulation to warrant robustness. Moreover, the work is directed to a simple process to generate non-uniform distributions. In order to select a well-suited approach for the present application, variable particle resolution strategies are briefly reviewed and assessed below.

4.3.4.1 Variable Particle Resolution Strategies

There are two main strategies for variable particle resolutions used within SPH simulations: static and dynamic refinement.

Static refinement refers to any method that is applied within the pre-processing phase of a simulation and thus provides an initially refined particle distribution to the solution. The simplest proposed setups divide the SPH domain in a series of nested sub-domains, each of which has a different but internally constant particle resolution (size, spacing, and smoothing length). For such distributions, it was observed that sudden jumps in particle size cause inaccuracies and eventually numerical instabilities. This is caused by the fact that relatively small particles do not find the surrounding large particles as neighbors, which typically leads to mixing of small and large particles [116] and referred problems. It highlights the necessity of a smooth transition of the particle resolution when using non-uniform distributions. Other setups found in the literature use analytically prescribed, quasi-continuous transitions of the particle resolution. Typically, particles near the impacting structure are of constant size and the increase in particle size is realized following simple analytical formulations [60, 100, 115]. One possibility is the generation of particles along semicircles with radially increasing smoothing length. Oger et al. [115], for example, calculate the smoothing length of particles located on subsequent semicircles denoted by i according to $h_i = \kappa^i h_0$ with h_0 being the basic smoothing length and κ a growth factor slightly larger than unity. Above authors successfully used such distributions for two-dimensional vertical wedge impact simulations and reported a large decrease of the necessary amount of particles and the associated runtime.

Dynamic refinement covers techniques applied during the solution phase that refine and coarsen the particle distribution based on various pre-defined criteria such as refinement zones, number of neighbors, or physics-based criteria (e.g. velocity gradients) [41]. For this purpose, particle splitting and merging algorithms are utilized to refine or to coarsen the particle distribution, for instance, around randomly moving objects, e.g. a ship or a sinking container [9, 41, 157]. Both splitting and merging require on the one hand a suitable identification procedure of so-called candidate (old) particles and on the other hand a careful treatment of candidate and daughter (new) particles in order to conserve basic properties of the system such as mass, momentum, and energy [41].

Assessment   Generally, dynamic refinement algorithms seem to be superior to static refinement techniques due to their inherent adaptivity to instantaneous, potentially changing conditions. This advantage, however, comes at a large cost in terms of complexity of the implementation as well as an increase in the computational effort during the simulation. Regarding the given case of aircraft ditching, the major direction of motion of the impacting structure is well-known and hence a static refinement appears to be best suited. Nevertheless, existing static refinement techniques are typically established for cases in

two dimensions and thus they are mostly applicable to academic test cases. The generation of such distributions for three-dimensional applications becomes much more complex and no literature about three-dimensional, non-uniform initial distributions for water impact simulations is available. In the field of astrophysics, however, the use of three-dimensional non-uniform initial particle distributions was recently published by Diehl et al. [28]. The paper is concerned with optimal initial conditions for SPH simulations in the referred field. The most relevant particle distribution suggested by the authors is obtained using a method based on Weighted Voronoi Tessellation (WVT). The fundamentals as well as the application of the WVT method within this thesis are described in the following section.

4.3.4.2 Non-Uniform Particle Distribution by Weighted Voronoi Tessellation

The Weighted Voronoi Tessellation algorithm is a geometry-based iteration technique suitable to generate uniform as well as non-uniform particle distributions. It can be used to redistribute particles or even to fill arbitrary shaped domains with particles, both in combination with applying any desired resolution.

Fundamentals   Provided with an arbitrary distribution of particles anywhere inside the domain to be filled, the WVT algorithm shifts particles according to

$$\Delta \mathbf{r}_i = \lambda h_i \sum_j f(h_{ij}, r_{ij}) \frac{\mathbf{r}_{ij}}{r_{ij}} \,. \tag{4.21}$$

In the above equation, λ is a strength parameter, h_i the smoothing length, $f(h_{ij}, r_{ij})$ a weighting function, r_{ij} the distance, and $\frac{\mathbf{r}_{ij}}{r_{ij}}$ the unit vector between neighbor particles i and j. Following recommendations in [28], the strength λ in (4.21) is decreased at each iteration cycle n by a user-defined constant κ, which here is defined as

$$\lambda^{n+1} = (1 - \kappa) \lambda^n \,. \tag{4.22}$$

Furthermore, Diehl et al. [28] recommend $f(h_{ij}, r_{ij})$ to decrease inversely proportional to the distance squared for best convergence behavior. Within this work, their proposed weighting function is used. It reads

$$f(h_{ij}, r_{ij}) = \begin{cases} \frac{1}{\left(\frac{r_{ij}}{h_{ij}} + \chi\right)^2} - \frac{1}{(2+\chi)^2} & \text{for } r_{ij} < 2h_{ij} \\ 0 & \text{else} \,. \end{cases} \tag{4.23}$$

Therein h_{ij} is the averaged smoothing length defined as $h_{ij} = 0.5\,(h_i + h_j)$ and χ is a very small number used to prevent diffusion in case particles coincide ($r_{ij} \to 0$), thus retaining numerical stability. The weighting function (4.23) has a compact support, achieved by adding a constant such that $f(r_{ij} = 2\,h_{ij}) = 0$, and hence yields zero for $r_{ij} \geq 2\,h_{ij}$.

The iteration runs until a user-defined maximum number of iteration cycles n_{max} is reached or until the distribution converges. The latter can be determined based on

various criteria; one possibility is to compare the ratio of the actual over the maximum summed square of the particle displacement per cycle and to stop the iteration once the user-defined threshold value C_R is reached, which expresses as

$$C_R \leq \frac{\Delta R^n}{\Delta R_{max}^n} \quad \text{with} \quad \Delta R = \sum_i (\Delta \mathbf{r}_i)^2 \,. \tag{4.24}$$

Regarding the convergence behavior, it was observed that the iteration converges faster when starting with a distribution that does not have a perfect alignment, e.g. by adding an initial displacement in a random direction and with a strength of up to 50% of the initial spacing to a cubic lattice arrangement. In case the iteration diverges, the initial strength λ must be reduced to achieve convergence within a reasonable amount of iteration cycles.

Extensions   Groenenboom [57] extended the original WVT algorithm (herein referred to as EWVT) to allow for superior treatment of boundaries and for particles varying in size depending on their position in the fluid domain.

Boundaries limiting the particle domain are defined by a rectangular box. Once a particle is shifted toward a boundary resulting in a distance less than $2h_i$, a mirrored ghost particle is created and included in the iteration process. This ghost particle is located at the mirrored position across the boundary and it has the same smoothing length as its parent. Ghost particles are updated at each iteration cycle, which provides suitable boundaries. As a result, the particle distribution in the vicinity of the boundaries is significantly improved. In case the non-uniform distribution is to be combined with the translating periodic boundary conditions for the subsequent water impact simulation (see Section 4.3.2.2), this modeling feature must be used already for the generation of the particle distribution to provide a consistent particle distribution also across the periodic boundaries.

In order to allow for a variable resolution, an analytically prescribed, position-dependent particle spacing $\delta(\mathbf{r})$ is assigned to the set of particles during the iteration by a multiplicative combination of spatial functions $\delta(r_k)$ of Cartesian $(x,\ y,\ z)$, cylindrical (r), and spherical (s) coordinates as in (4.25). Smoothing lengths h_i are related to the prescribed particle spacing by a proportionality factor such that the total volume remains constant. As mentioned above, there is the requirement of a sufficiently smooth transition of particle size, which limits the gradient in spacing resulting from the product of the defined functions.

$$\delta(\mathbf{r}) = \prod_k \delta(r_k) = \delta(x)\delta(y)\delta(z)\delta(r)\delta(s) \tag{4.25}$$

Figure 4.13 (left) illustrates the generation of a three-dimensional non-uniform distribution with resolution gradients in two directions, i.e. *Y*- and *Z*-direction. For clarity, only a slice of the fluid domain is considered and ghost particles are hidden.

Quality Assessment   In order to ensure the stability of non-uniform particle distributions, the assessment of their quality is essential. The easiest way is to use qualitative measures such as the distributions of smoothing length, minimum particle spacing, or their ratio. They can be assessed visually and should show smooth distributions. These measures, however, are not suitable to reveal anisotropy in case of non-uniform distributions. Furthermore, qualitative measures are generally prone to subjectivity. Therefore, quantitative measures are necessary to better assess and to compare the quality of particle distributions. One important measure is the ratio of the summed particle volumes in arbitrary sub-domains over the sub-domain volume. It should approach unity, yet small discrepancies typically arise due to the discrete nature of the particle distribution. Nevertheless, a uniform distribution of this volume ratio is crucial for proper stability. Moreover, as referred above the SPH method presumes spherical symmetry, which should be reflected in the distribution of neighbor particles. Hence, a particle distribution should be isotropic in order to be stable. A quantitative measure for the isotropy of a particle distribution based on the SPH inertia tensor[13] was proposed by Groenenboom [57]. For ideal isotropic distributions, the SPH inertia tensor is a multiple of the unit tensor and thus its eigenvalues are all equal. Consequently, the ratio Λ of the lowest to the highest eigenvalue is equal to unity. In contrast, for increasingly anisotropic distributions the eigenvalues are increasingly different and Λ approaches zero. Therefore, the eigenvalue ratio Λ is a powerful measure of the local anisotropy, which equally works for two- and three-dimensional setups.

If a non-uniform distribution sufficiently fulfills above criteria, it behaves stable, i.e. such that any artificial particle motion after initialization of gravity loading is negligible and that the pressure field quickly approaches its hydrostatic distribution. This was verified based on hydrostatic tank tests covering as much as 10 s of simulated time. Also, non-uniform distributions were used for 2D rigid wedge impact simulations proving that hydrodynamic loads acting on the structure remain similar compared to SPH solutions using uniform particle distributions and another reference solution from literature. Exemplary results of these studies are provided in Appendix B.6.

4.3.4.3 Application to Guided Ditching Simulation

After it was proven that the EWVT algorithm can be used to generate stable non-uniform distributions, these are applied in the guided ditching simulation in order to demonstrate their functionality as well as their capabilities in the three-dimensional application.

The guided ditching simulation model uses a pure SPH fluid domain with translating periodic boundary conditions at the front and the rear face (in *X*-direction). Boundaries at the sides and at the bottom are modeled by columns of fixed particles spanning over a range of twice the maximum smoothing length in order to avoid leakage. For non-uniform

---

[13]The SPH inertia tensor is further explained in Appendix B.6.

particle distributions, the smoothing length in the impact zone is kept constant over a width of 600 mm and a depth of 400 mm. The resolution is decreased toward the boundaries in Y- and Z-direction, but there is no gradient in X-direction. The achieved savings in terms of the total amount of particles in the model are listed in Tab. 4.4.

On the right hand side of Fig. 4.13, a cut view of the model at $t = 50$ ms is presented. It shows that the particle distribution remains stable and that no artificial mixing occurs due to the impact. Figure 4.14 exemplarily depicts the normal force time histories of respective simulations compared with experimental data. Simulation results are essentially equal to those achieved with a conventional uniform particle distribution of the same minimum resolution, but the simulations with non-uniform particle distributions run faster (see Tab. 4.4). Nevertheless, despite reported time savings and the large amount of particles saved through the application of non-uniform particle distributions, the solution times of the simulations do not show proportional savings. This mismatch could be identified to be due to the neighbor search algorithm implemented in *VPS*, i.e. cell-linked list as described in Section 2.5.3, which is based on cells of $2\,h_{max}$ edge size. Consequently, the larger the resolution gradient in the model (h_{max}/h_{min}), the worse the efficiency of the available neighbor search algorithm and thus the lower the efficiency increase.
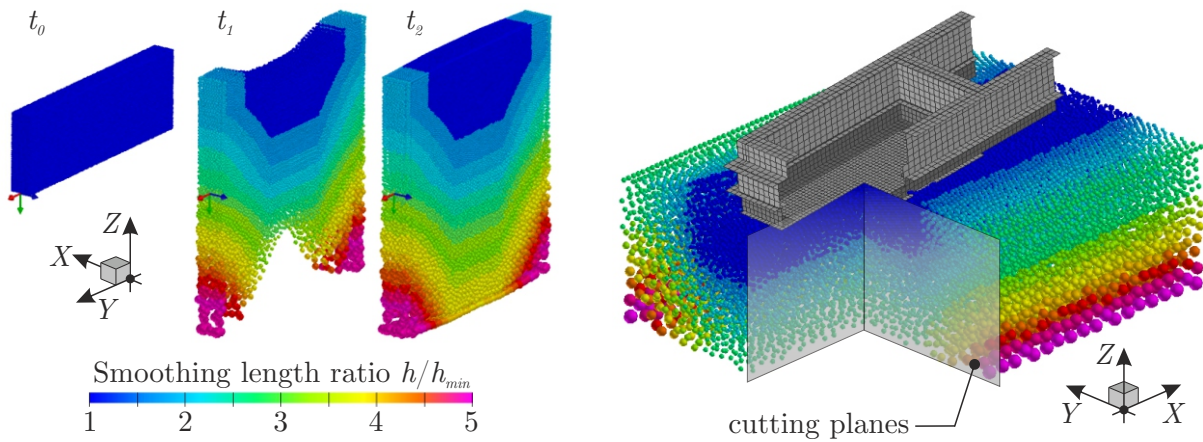

Figure 4.13: Exemplary generation of non-uniform distribution (left). Guided ditching simulation with non-uniform particle distribution combined with translating periodic boundary conditions at $t = 50$ ms (right).

Table 4.4: Overview of guided ditching simulation models with uniform and non-uniform particle distributions and associated ratio of elapsed times.

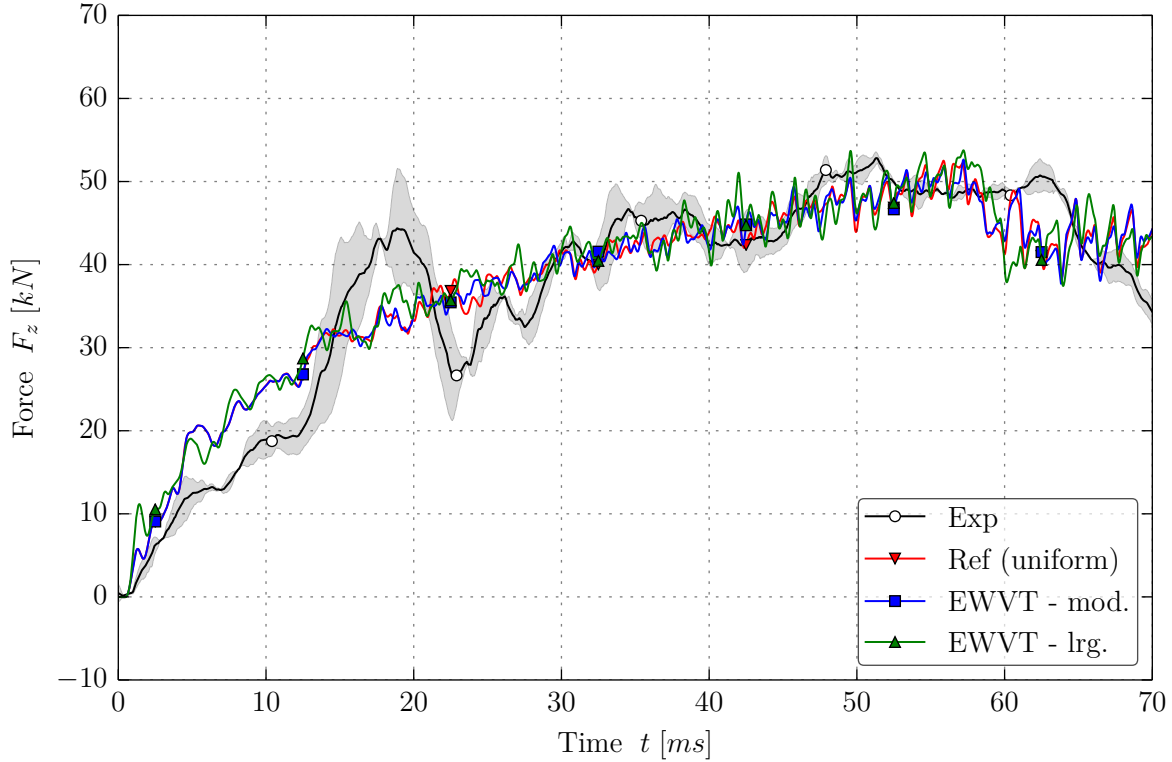| Simulation model	$\#SPH/\#SPH_{ref}$	h_{max}/h_{min}	$T_{Ela}/T_{Ela,ref}$
Reference (uniform)	1.0	1.0	1.00
EWVT - moderate gradient	0.5	2.7	0.62
EWVT - large gradient	0.1	5.2	0.45

Figure 4.14: Comparison of normal forces for cases with non-uniform and uniform (reference) initial particle distributions with experimental data.

Conclusion   The extended WVT algorithm permits to generate non-uniform particle distributions with prescribed gradients in particle size. It provides the user with full control of the particle resolution and hence allows for local refinement at any location within the particle domain. The numerical stability was demonstrated for different test cases comprising hydrostatic tank tests and wedge impacts in two dimensions as well as guided ditching simulations in three dimensions.

The application of non-uniform particle distributions dramatically reduces the amount of particles necessary to represent the fluid domain while obtained results are of same quality as those using uniform particle distributions. Nevertheless, in order to properly rate the achieved efficiency increase through the use of non-uniform particle distributions, it has to be noted that reported savings are highly case dependent as they vary depending, for instance, on the overall size of the computational fluid domain and the particle size. Thus it is very difficult to generalize the possible efficiency increase.

In consideration of the limited increase in efficiency resulting from the available neighbor search algorithm in *VPS* and the remaining overall effort required to generate a non-uniform distribution, it is decided to use uniform distributions for the remaining simulations in this thesis. Nevertheless, once an adequate neighbor search algorithm would be available, the developed approach to non-uniform particle distributions offers the potential for a dramatic reduction of the CPU effort and should, therefore, be employed.

4.4 Fluid-Structure Interaction

The interaction of fluid and structure is enabled using a non-symmetric node-to-segment penalty contact algorithm on the basis of what was described in Section 2.4.2. It treats the particles as slave nodes and the structure as master segments. The contact thickness is chosen to represent the particle radius plus half the thickness of the shell elements of the structure. When using non-uniform particle distributions, the particle radius used to compute the contact thickness is that of the particles in the vicinity of the structure, where the particle size is kept constant. Such contacts are modeled between SPH particles and the panel, the L-frame, as well as the trolley box structure.

In *VPS* the mass specific force is computed as

$$\mathbf{f}_{in} = \alpha \frac{h_c - r_{in}}{(\Delta t)^2} \frac{m_n}{m_i + m_n} \frac{\mathbf{r}_{in}}{r_{in}} \,, \tag{4.26}$$

where α is the penalty scale factor, h_c the contact thickness, Δt the time step, m_i and m_n the particle mass and the nodal mass associated with the master segment n, and $\mathbf{r}_{in}$ as well as r_{in} are distance vector and magnitude between particle i and the master segment [55].

Furthermore, a stiffness-proportional nodal damping [36, 37] with a strength of 0.2 is included in the contact formulation in order to avoid detrimental effects due to highly-dynamic peak contact forces evoked by the numerical noise in the SPH pressure field. A sensitivity study confirmed that forces and strains are less noisy, while the overall quality of the solution is unaffected.

4.5 Summary of Developed Simulation Model

The SPH-FE approach introduced in Section 2.4 was adopted to develop a numerical simulation model of the guided ditching experiments. Several modeling aspects and variants were investigated and assessed based on sensitivity studies. Based on the results, modeling guidelines were derived. This section describes the developed simulation model as it will be used for the subsequent validation and verification studies in Chapter 5. Table 4.5 summarizes the main aspects of the simulation model.

Potential experimental uncertainties associated with the guide and its dynamic motion were evaluated. The timing of simulation results was found to be sensitive to the vertical velocity of the trolley, which is temporarily reduced due to the evasive motion of the guide. Consequently, the structural model contains the guide model described in Section 4.2.1 in order to provide correct boundary conditions during the impact. A further sensitivity study revealed that results are insensitive to the position of the trolley along the guide track at the time of first water contact.

Panels are discretized with shell elements of approximately 10 mm edge length. This choice originates from the intention to use one simulation model for all parameter studies

in Chapter 5, which shall prove the versatility of the developed model. Moreover, the chosen element size is a compromise: on the one hand, a sufficiently small element size is required to capture the structural response of the highly deformable panels; on the other hand, the practicable simulation runtime limits the minimum element size as it determines the simulation time step as well as the necessary particle resolution, which both have a significant impact on the simulation runtime. The trolley box structure is discretized with slightly larger shell elements in order to not affect the simulation time step.

For the fluid model, the hybrid approach combining FE in the far field with an SPH discretization in the impact zone is adopted. The cross-section (width×height) measures 2200 mm×1000 mm in total and 600 mm×200 mm for the SPH domain, respectively. The fluid model contains solely water and neglects air. It is preferred to keep the fluid material description simple and to avoid additional assumptions as far as possible. For this reason, a single-phase material model based on the weakly compressible formulation using the Tait equation of state is used. The simulation results were demonstrated to be insensitive to the fluid bulk modulus within a reasonable range. Results were further verified by comparison with a solution using the polynomial equation of state.

The SPH model includes specific enhancements to improve its accuracy and robustness. In particular, the Rusanov flux is employed to reduce the numerical noise in the pressure field. Furthermore, the combination of XSPH and Lennard-Jones repulsion correction applied every 10 cycles helps to maintain more regular particle distributions. Furthermore, the translating active domain feature, which permits a significant increase in efficiency over the state of the art, is adopted. For the regarded test cases, the achieved efficiency increase is about a factor of 2.2 to 3.7 depending on horizontal impact velocity and pitch angle, which determine the total length of the fluid domain. The length of the active domain is kept constant at 1600 mm with margins of 100 mm and 500 mm in the rear and in the front of the structure, respectively. Although an additional efficiency increase could be achieved through the use of non-uniform particle distributions generated based on the procedure described in Section 4.3.4.2, their use is omitted; possible savings are currently limited by the available neighbor search algorithm in *VPS* and hence the remaining effort to generate such distributions does not justify their use. Therefore, a uniform initial particle distribution in a hexagonal arrangement is used. A constant particle spacing of 10 mm is chosen according to the structural discretization discussed above. It results in a particle volume of 720 mm^3.

Overall, the developed simulation model demonstrated good agreement of results against experimental measurements for the reference test case regarded in this chapter. In the subsequent chapter, its versatility is investigated for a broad range of test cases in order to validate the model, but also to identify its capabilities and limitations.

Table 4.5: Overview of final simulation model for parameter studies.

Structural Model	
Guide	Guide track model included (see Section 4.2.1)
Panel	Characteristic shell element edge length $l_c = 10$ mm, elastic-plastic material model (*VPS* material type 103) for aluminum panels with generic Al2024 input parameters given in Fig. B.1, multi-layered shell approach with bi-phase ply model (*VPS* material type 131) for composite panels with input parameters given in Tab. B.1 (see Section 4.2.2)
Bolts	PLINK elements with linear stiffness properties in normal and shear direction according to Huth formula (see Section 4.2.2)

Fluid Model	
Geometric dimensions	Total cross-section $w_T = 2200$ mm and $h_T = 1000$ mm, SPH cross-section $w_S = 600$ mm and $h_S = 200$ mm, total length $x_T = 3600$–7000 mm depending on test case (pitch angle, horizontal velocity), length of active domain $l_A = 1600$ mm, margins $l_R = 100$ mm and $l_F = 500$ mm (see Section 4.3.2.5)
Particle distribution	Uniform initial distribution in a hexagonal arrangement, spacing $ds = 10$ mm, particle volume $V_i = 720$ mm^3
SPH settings	WCSPH formulation with variable smoothing length, Wendland kernel function (4.2), ratio of smoothing length to particle radius $h/r = 1.9$, artificial viscosity $\alpha_{AV} = 0.02$ and $\beta_{AV} = 0$
Material model and properties	Single-phase model based on Tait EOS (4.7) (*VPS* material type 28), $\rho_0 = 1 \cdot 10^{-6}$ kg/mm^3, $B = 3.57 \cdot 10^{-2}$ GPa, $\gamma = 7$, $p_0 = 0$ GPa, $p_{cut} = -1 \cdot 10^{-4}$ GPa (see Sections 4.3.1.1 and 4.3.1.4)
Pressure correction	Rusanov flux $\varepsilon_{RF} = 0.5$ (see Section 4.3.1.2)
Regularization	XSPH $\varepsilon = 0.2$ (see Section 2.5.2) combined with Lennard-Jones repulsive correction $\alpha_r = 0.95$, $\lambda = 0.2$, $\eta = 6$ (see Section 4.3.1.3)

Fluid-Structure Interaction	
Contact properties	Non-symmetric node-to-segment penalty contact (*VPS* contact type 34), contact thickness $h_c = 0.5 (t_{panel} + r_{SPH})$, nodal damping strength parameter of 0.2 (see Section 4.4)

5 Validation and Verification Studies

This chapter provides results of parameter studies with the objective to validate the numerical model developed in Chapter 4. For this purpose, numerical results are compared to those of corresponding experiments covering a wide range of test cases. Furthermore, the structural behavior is evaluated in detail in order to verify the findings discussed in Section 3.3.4. Finally, a discussion of the results serves to assess the capabilities of the developed simulation model and to point out its limitations.

5.1 Parameter Studies

In order to assess the validity of the developed numerical model, but also to evaluate its capabilities and limitations, numerical results are compared with experimental data of test cases presented in Sections 3.3.3 and 3.3.4. The parameters investigated within this study are pitch angle, horizontal impact velocity, lateral panel curvature, and panel type (combination of material and thickness). The validation work comprised all 22 test cases of the experimental campaign (cf. Tab. A.5); however, only selected results are presented due to the constraints for this thesis.

The numerical model is that described in Section 4.5 and changes only concern the parameters studied in order to demonstrate the versatility of the model. Simulations cover the time until the leading edge immerses plus a margin, resulting in simulated times of 50 ms, 70 ms, and 120 ms depending on the pitch angle of the structure, which defines the time until immersion. Models typically have a size in the order of $1.5 \cdot 10^6$–$2.5 \cdot 10^6$ nodes and elements. All computations are conducted with the hard- and software specified in Appendix B.1 resulting in simulation runtimes of 21 hours (ID 1112) to 80 hours (ID 3133).

Results considered for comparison in the parameter study comprise forces and representative strains predicted by the numerical model, which are filtered using CFC1000 and CFC600 filters, respectively. Experimental data are cut for clarity thus covering slightly more time than the corresponding simulations. Numerical pressure results are not used for the evaluation; despite noticeable improvements through the application of pressure correction schemes and particle regularization algorithms, pressure time histories[1] remain very noisy and thus do not permit a meaningful comparison with experimental measurements. Nevertheless, the influence of such high-frequency pressure oscillations on the

---

[1]Figure C.1 shows exemplary pressure time histories to illustrate their typical appearance.

structural response was assessed as negligible (cf. Section 3.3). Furthermore, velocity time histories are not shown in the thesis as they do not give deeper insight into the capabilities of the numerical model. However, the velocity time histories and hence the deceleration of the specimens are predicted with high accuracy for all test cases.

5.1.1 Impact Conditions and Panel Curvature

In similar procedure to the evaluation of experimental results in Section 3.3.3, the first part of the parameter study comprises test cases with quasi-rigid panels and parameters varied are pitch angle, horizontal impact velocity, and lateral panel curvature.

5.1.1.1 Pitch Angle

This study compares results of test cases with 40 m/s horizontal impact velocity and different pitch angles of 4°, 6°, and 10° (IDs 1112, 1122, 1132).

Overall, the numerical model reproduces the evolution of the flow field underneath the structure for all investigated cases. The curvature of the jet root across the panel observed in the numerical results is stronger for cases with larger pitch angles, which agrees well with experimental underwater high-speed recordings. Nevertheless, the formation of a thin fluid jet only occurs for the 10° case as the practical particle resolution prohibits a jet formation for test cases with smaller pitch angle (see Fig. 5.1).

Forces are in excellent agreement both in terms of their magnitude as well as the prediction of the decay of normal force upon immersion of the panel leading edge (see Fig. 5.2). Yet, simulations show a too early immersion of the panel leading edge, identified as the increase of F_x and equally as the drop of F_z. This deviation is larger for cases with larger pitch angle and it appears to scale with the duration of the impact. It is assumed that the deviation in timing is due to the occurrence of hydrodynamic phenomena such as air cushioning and air entrapment. These both extend the impact duration in the experiment, but they are not considered in the numerical model. Interestingly, the initial slope of numerical normal forces is identical up to $t \approx 13$ ms, which is in accordance with experimental observations apart from the time lead of the simulations mentioned. The trend toward higher normal forces yet with a nearly identical growth rate in the subsequent stage is well captured. The slope of F_x after the leading edge immersion is
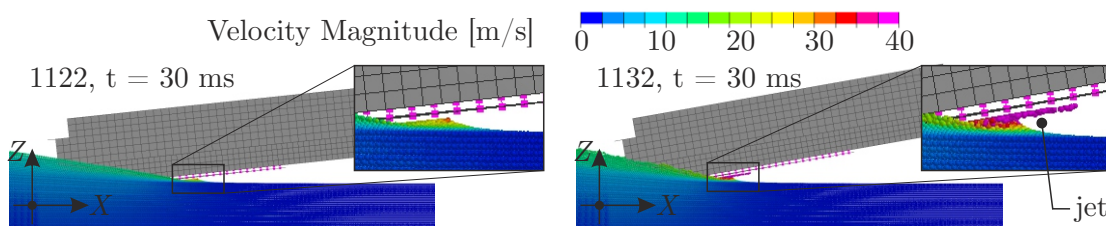

Figure 5.1: Side view on fluid flow underneath panels for test cases with 6° and 10° pitch angle at 40 m/s horizontal impact velocity (IDs 1122, 1132).
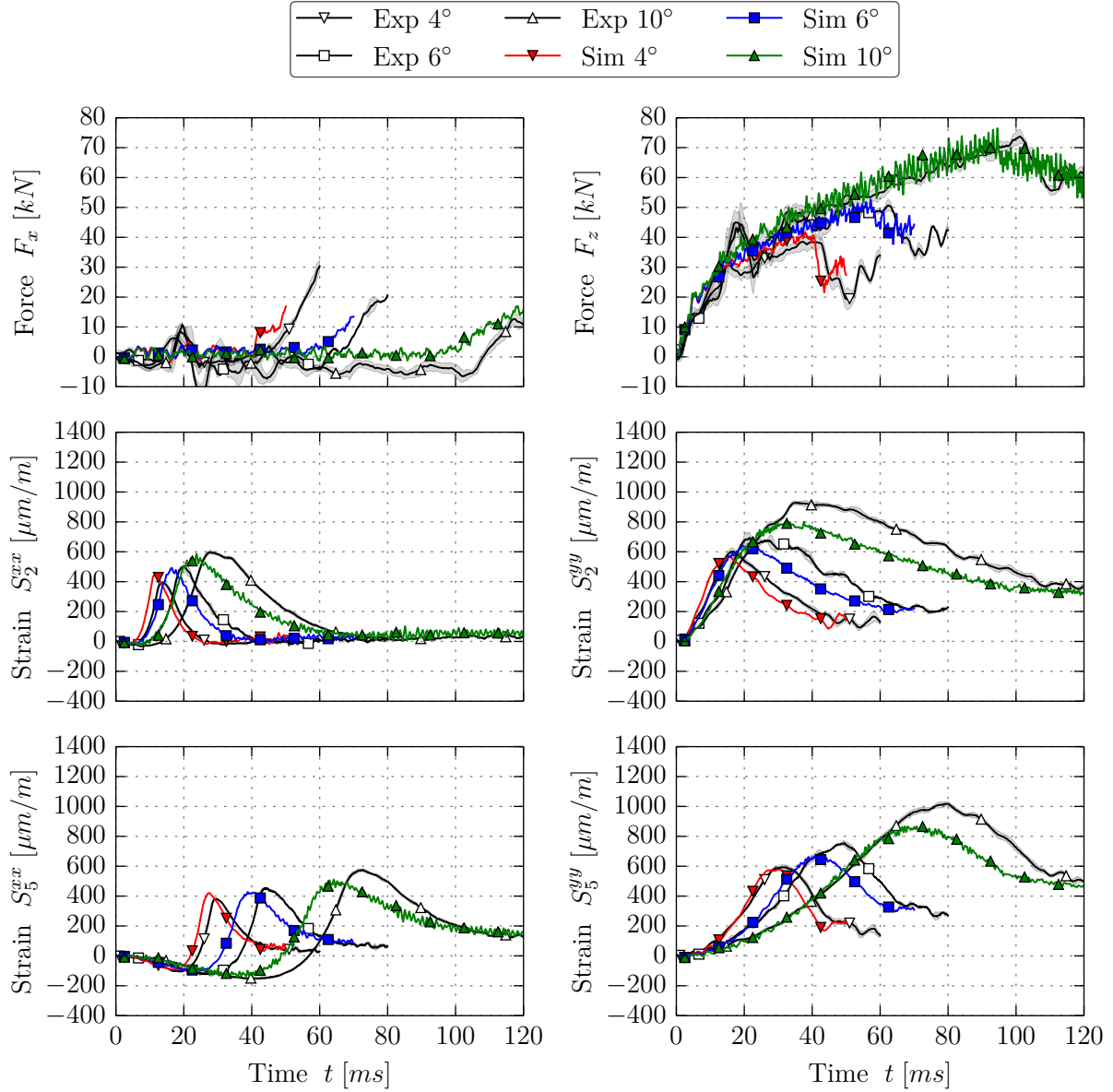
Figure 5.2: Force and strain time histories of simulations and experiments with different pitch angles at 40 m/s horizontal impact velocity (IDs 1112, 1122, 1132).

steeper for cases with smaller pitch angle as the angle between the front face of the box structure and the fluid increases. Oscillations in force signals are noticeably stronger for cases with larger pitch angle, which is attributed to the increased particle disorder developing due to the larger fluid displacement.

The qualitative strain response and its trend associated with the pitch angle compare very well. Yet, there is a tendency to underestimating strain peak values for larger pitch angle cases. Largest discrepancies of strain peak values are in the order of $\pm 12\%$. Strains in x-direction rise slightly too early, which is again attributed to the general time advance of simulation results. In contrast, strains in y-direction show an excellent timing compared to experimental data as they are less sensitive to the propagation of the hydrodynamic loading. Oscillations observed in force results also appear in strain results, but their magnitude remains insignificant.

5.1.1.2 Impact Velocity

The present study on the impact velocity contains test cases at 10° pitch angle impacting with 30 m/s, 40 m/s, and 45 m/s horizontal impact velocity (IDs 1131, 1132, 1133). The default setting, i.e. with a pitch angle of 6°, is not shown as respective tests were conducted only for 40 m/s and 45 m/s impact velocity (IDs 1122, 1123).

The evolution of the flow underneath the structure is in excellent qualitative agreement with underwater observations. The shape of the jet root across the panel is observed to be rather independent of the horizontal impact velocity. For cases with higher impact velocity, the forward traveling jet is more voluminous; however, the jet root arrives later at the leading edge.
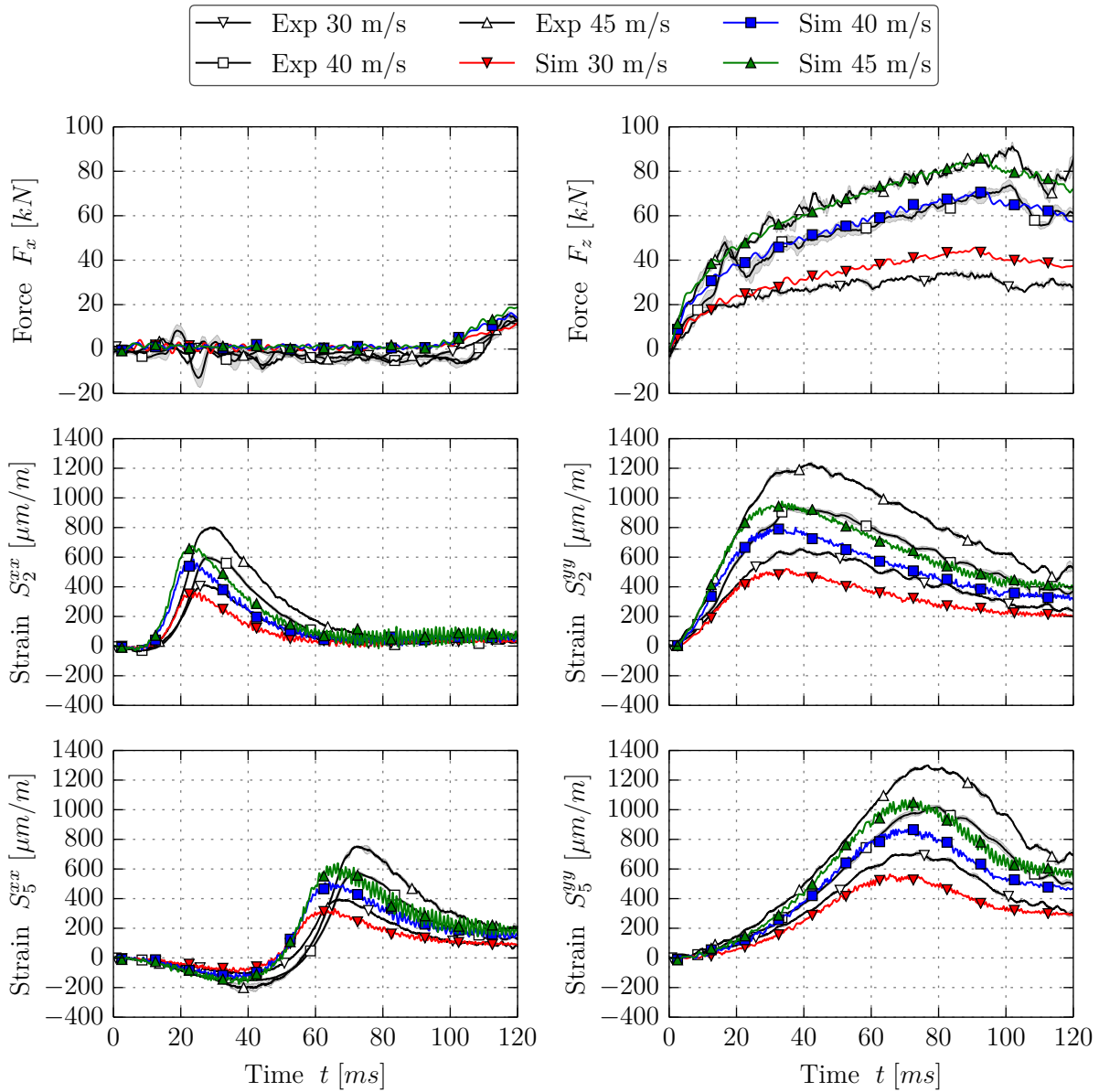
Figure 5.3: Force and strain time histories of simulations and experiments with different horizontal impact velocities at 10° pitch angle (IDs 1131, 1132, 1133).

Results indicate significantly larger force oscillations for cases with higher impact velocity, which is attributed to the larger developing particle disorder. Therefore, the force results shown in Fig. 5.3 are CFC180-filtered in order to allow for proper comparison with experimental data[2]. Normal forces increase considerably with the impact velocity. This is attributed to the increased mean hydrodynamic pressure, which is approximately proportional to the square of the impact velocity. The numerical model correctly predicts the different growth rates of the normal force depending on the impact velocities as well as the decay of the normal force, which occurs slightly earlier for the slower cases due to the larger water pile-up in front of the jet root. Yet, in the simulations, the leading edge immerses approximately 5 ms (5% of the total duration of the impact) earlier than in the experiments. Whereas normal force time histories are in excellent agreement for the cases at 40 m/s and 45 m/s, they are overestimated by the numerical model for the case at 30 m/s. This discrepancy grows over time and reaches a maximum difference of +25%.

Strain results show a similar increase with the impact velocity. Qualitatively, results agree well and the trend toward earlier strain responses for cases with lower impact velocity is observed. However, strain magnitudes remain clearly below experimental measurements with maximum differences in the order of −20%. Oscillations attributed to the particle disorder also show in strain results. They are generally stronger for the case at 45 m/s and additionally intensify over time.

5.1.1.3 Panel Curvature

The effect of the lateral panel curvature is investigated comparing flat, convex, and concave panels for the test condition with 40 m/s horizontal impact velocity and 6° pitch angle (IDs 1122, 1222, 1322).

Figure 5.4 depicts that the strong three-dimensionality of the flow field predicted by the simulations is in excellent agreement with experimental underwater observations.

---

[2]The CFC1000-filtered force time histories are additionally provided in Fig. C.2 in the appendix.
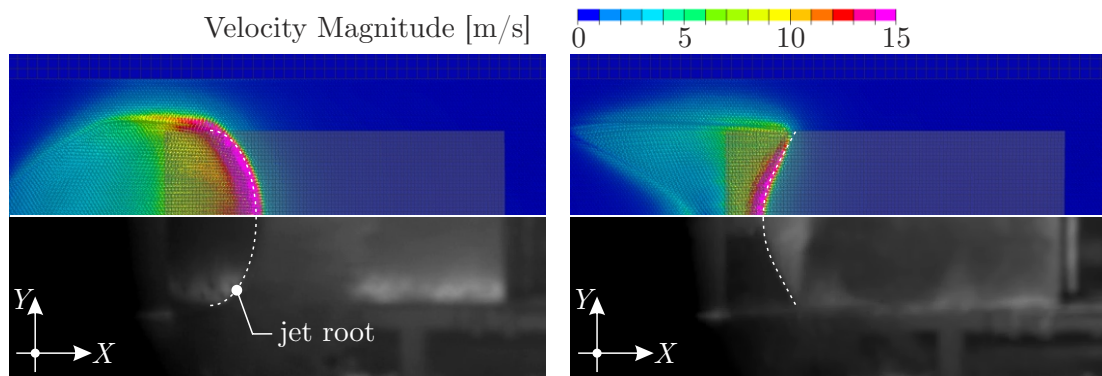

Figure 5.4: Comparison of numerical with experimental jet root shape for convex (ID 1222, left) and concave (ID 1322, right) cases at $t \approx 12$ ms.

The jet root is curved positive or negative depending on the panel curvature as expected. In the experiment, a stripe of air bubbles was observed along the central part of the concave panel, which points at air being entrained due to the shape of the panel (cf. Section 3.3.1). This hydrodynamic phenomenon, however, cannot be reproduced by the numerical model as it does not account for air.

For clarity of illustration, force and strain results are displayed separately for each test case in Fig. 5.5. Force and strain results are both in very well agreement with experimental data. The effect of the lateral curvature observed in the experiments is reproduced by the numerical model: forces are lower for the convex case and higher for the concave case due to the respectively reduced or increased constraints for the fluid. Moreover, the delay
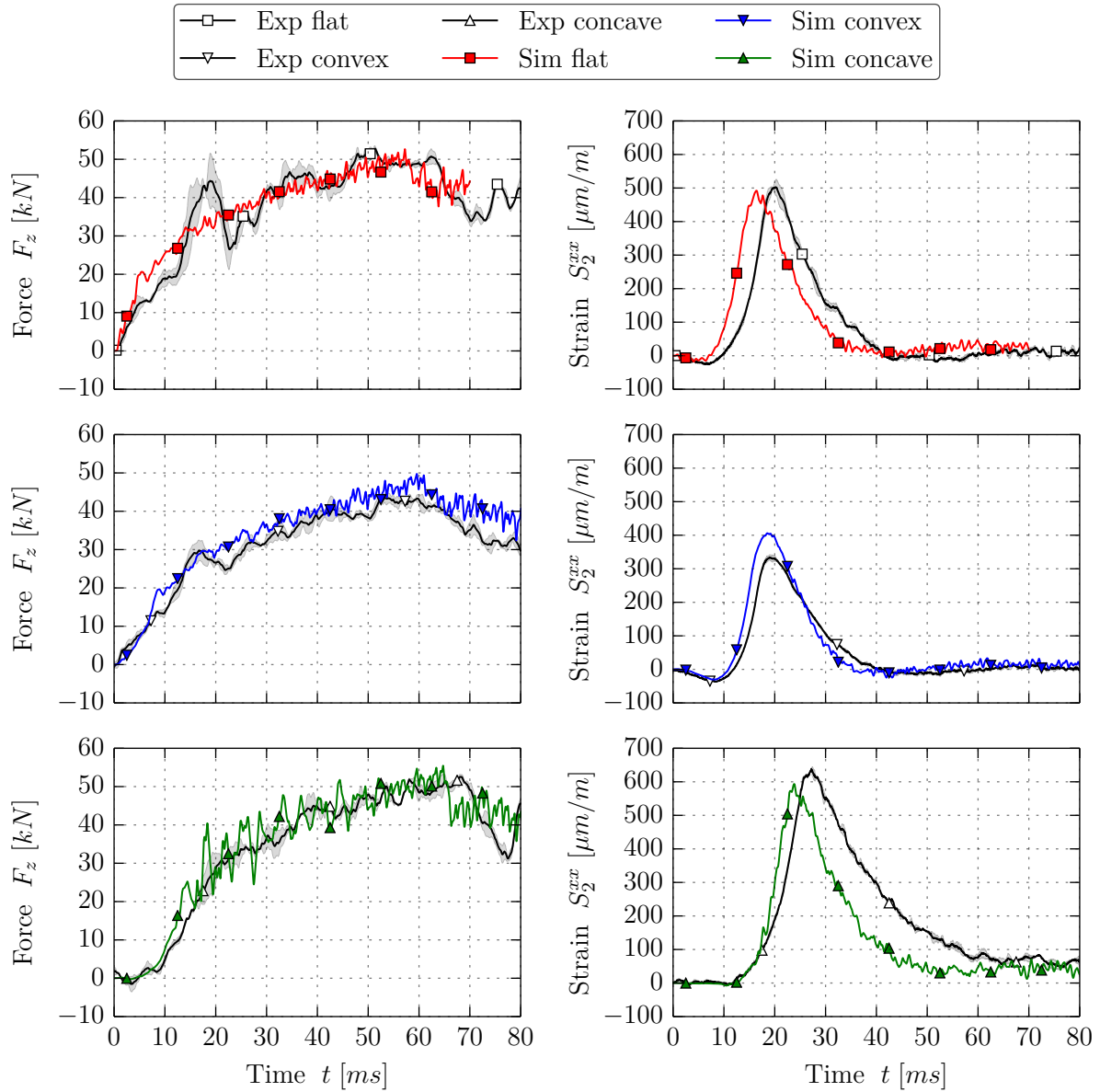

Figure 5.5: Force and strain time histories of simulations and experiments with different panel curvature at 6° pitch angle and 40 m/s horizontal impact velocity (IDs 1122, 1222, 1322).

of the loading in the curved cases compared to the flat case is correctly reproduced by the simulation model. This delay is small in the convex case and significantly larger in the concave case. Analyzing the flow field evolution predicted by the simulations, this can be attributed to the differences in the water entry, and in particular the wetted area, during the beginning of the impact (see Fig. C.3). In the convex case, the wetted area grows slower and is, therefore, smaller compared to the flat case at the same time, which leads to a reduced loading rate. In the concave case, the wetted area is much smaller compared to the other cases at the same time; Fig. C.3 (bottom row) shows contour plots at $t = 12$ ms after initial water contact to illustrate the difference. Additionally, the sides of the panel, where the local deadrise angle is larger, contact the water first, which results in lower hydrodynamic pressures. Furthermore, numerical results show significantly more force oscillations in the concave case. Contour plots reveal that at the beginning of the impact two fluid jets develop and flow from the rear corners to the inside. Consequently, these jets impact each other after approx. 12 ms and cause a larger particle disorder, which is identified to be the source of the enlarged oscillations for this test case.

Strain results are in very well agreement with experimental measurements despite the general time lead of the simulations discussed beforehand. Differences in strain peak values are within $\pm 20\%$. Due to the delayed loading in the concave case, the strain response occurs later accordingly. Interestingly, the strong force oscillations in the concave case only minimally affect the strain response.

5.1.2 Structural Deformation

The second part of the parameter study comprises test cases with deformable panels impacting under different impact conditions, i.e. 45 m/s & 4°, 40 m/s & 6°, and 30 m/s & 10°. Force and strain results are presented in the order of intensity of the observed structural responses: first, test cases with 3 mm aluminum and with composite panels and, finally, test cases with 0.8 mm aluminum panels are evaluated; see Figs. 5.7–5.9.

Simulations with deformable panels generally show a considerable indentation of the panel during the impact, which affects the flow field and the hydrodynamic loading compared to quasi-rigid cases. Figure 5.6 portrays a qualitative comparison of the flow field evolution between two cases with quasi-rigid and deformable (3 mm aluminum) panels. During the initial impact stage the flow fields are very similar; however, this changes once deformations increase. Whereas the jet root shape across the panel develops a positive curvature in cases with quasi-rigid panels, it develops a strong negative curvature in cases with deformable panels. Furthermore, in the deformable case the velocity field along the wetted panel shows higher values over a larger area compared to the quasi-rigid case, indicating that a larger volume of fluid undergoes noticeable acceleration. A detailed evaluation of the structural response is presented in Section 5.2. In the remainder of this section, force and strain time histories predicted by the numerical model are analyzed.
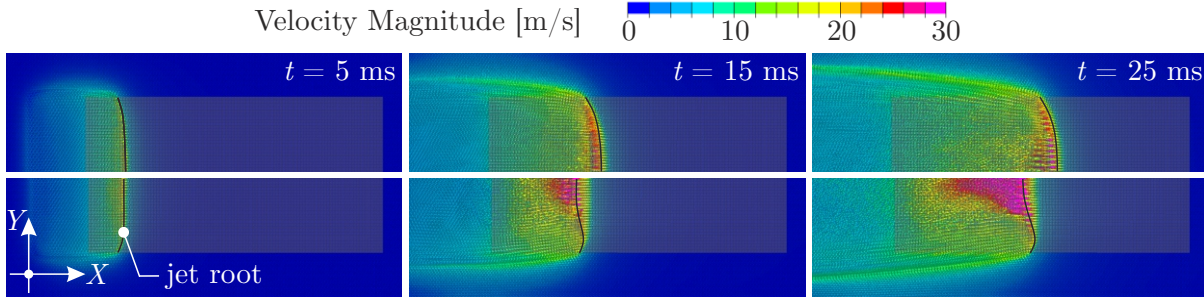
Figure 5.6: Comparison of flow field evolution for quasi-rigid (top) and deformable (bottom, 3 mm aluminum) test cases at 6° pitch angle and 40 m/s horizontal impact velocity (IDs 1122, 2122).

For all deformable test cases, the normal force time histories are in very good agreement between simulations and experiments. This holds for the different initial growth rate, the subsequent reduction of the growth rate and the corresponding general force level, the peak force, as well as the decay of the normal force prior to the leading edge immersion. In the cases at 30 m/s and 10°, the normal forces measured in the experiments are lower toward the end of the impact, whereas the numerical predictions do not show this reduction. Nevertheless, the maximum normal force and the drop at leading edge immersion are well predicted. Furthermore, the distinct normal force peak prior to the leading edge immersion, which is associated with the structural deformation of the panels, is captured by the numerical simulation for all impact conditions. In the simulations under impact conditions of 45 m/s and 4°, however, the force peak is overestimated by 5–10%. The time lead of the simulations expressed by the early drop of F_z is similar to the one discussed for simulations with quasi-rigid panels and thus not affected by the deformation. Overall, findings highlight that the simulation model is able to capture the total hydrodynamic loading also for very thin and highly deformable structures.

Strain results are discussed separately for each panel type in the following. For clarity of illustration, strain time histories are presented individually for each test case. Common among all the strain responses is that they also show the general time lead of the simulations referred.

- **3 mm Aluminum Panels:** The simulations predict strains with excellent agreement in terms of rise and decay behavior as well as peak values as exemplarily shown in Fig. 5.7. The numerical model successfully captures the sharp rise at around 10 ms when the peak pressure zone passes the gauge location. Also, the transient strain peak associated with the passage of the peak pressure zone described in Section 3.3.2 is captured. Strain peak values are within ±10% of the experimental measurements for all gauge locations. The strains measured at the gauge locations reach the intermediate elastic range of the material (plasticity would start at around 0.4–0.5% of strain).

- **1.65 mm Composite Panels:** Strain results are generally in very good qualitative agreement with a reasonable prediction of the sharp rise as well as the peak value. However, strains in x-direction are commonly lower compared to experimental measurements, in particular during the later stage of the impact, i.e. after the passage of the peak pressure zone (cf. exemplary results in Fig. 5.8). The sharp rise of strains in x-direction at the time when the peak pressure zone passes the gauge location is reproduced. Yet, there are additional oscillations in the numerical results and the peak strain value reached shows a trend toward underestimating the experimentally measured value for cases at larger pitch angle and slower impact velocity. Nevertheless, strains in y-direction are captured with good accuracy. Strain peak values are at most within $\pm 20\%$ of the experimental measurements for all gauge locations, while the typical deviation of peak values is much smaller (approx. $\pm 10\%$).

- **0.8 mm Aluminum Panels:** In general, the qualitative strain time histories are successfully predicted for all test cases with thin aluminum panels. Also, the quantitative agreement for strains in x-direction is good. However, strains in y-direction are larger and reach the plastic region of the material behavior. As the stress-strain curve of the aluminum alloy significantly changes its slope after reaching the yield stress (cf. Fig. B.1), the material behavior is affected; already small differences in the nonlinear behavior lead to larger discrepancies in strain results. The numerical model appears to begin its plastic behavior too early and thus results in larger plastic deformations at the gauge locations compared to experimental data. This becomes evident as the absolute difference in peak strain values is similar to the one during the later simulation, which indicates the amount of plastic strain experienced in the simulations. Moreover, the larger differences of strains in y-direction suggest that the material behaves anisotropic, which is common for thin sheet metal panels made of Al2024-T3 (cf. literature review in [131, p. 7–8]). Strain results, therefore, point out the limitations of the present model. Based on the presented investigations, discrepancies in strain results for cases with thin aluminum panels are attributed to the isotropic material model and the material input data describing the plastic behavior. These are generic and identical among all cases with aluminum panels despite their different panel thickness, heat treatment, and potentially anisotropic material properties due to the specific manufacturing processes, as no specific material data are available.

Overall, the simulation model demonstrates good predictive capabilities within the range of investigated parameters. Achieved results generally prove that the fluid-structure interaction is well predicted. Thus, the model can be validated within the range of reported discrepancies.
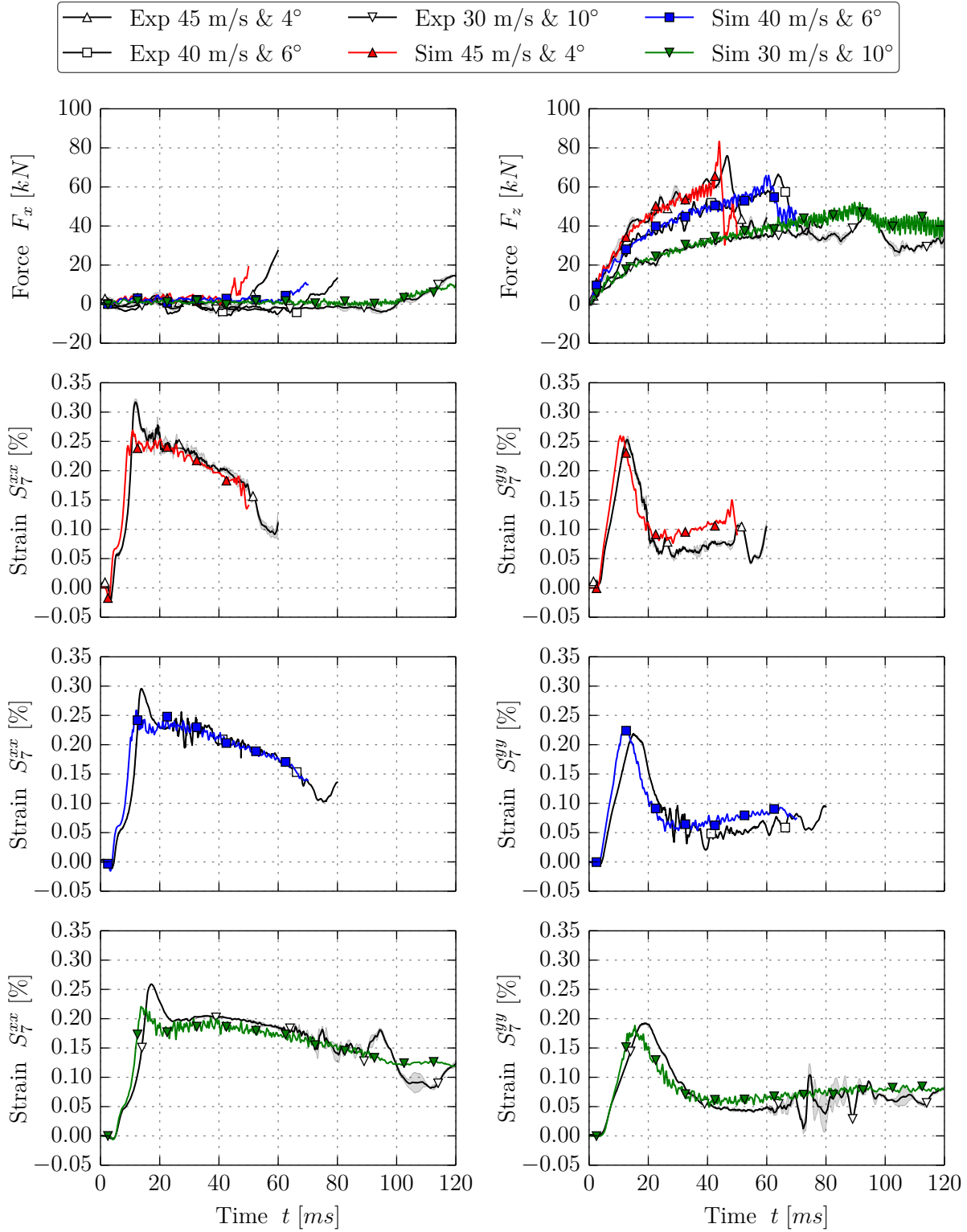
Figure 5.7: Force and strain time histories of simulations and experiments with 3 mm aluminum panels and under different impact conditions, i.e. horizontal impact velocity and pitch angle (IDs 2113, 2122, 2131).
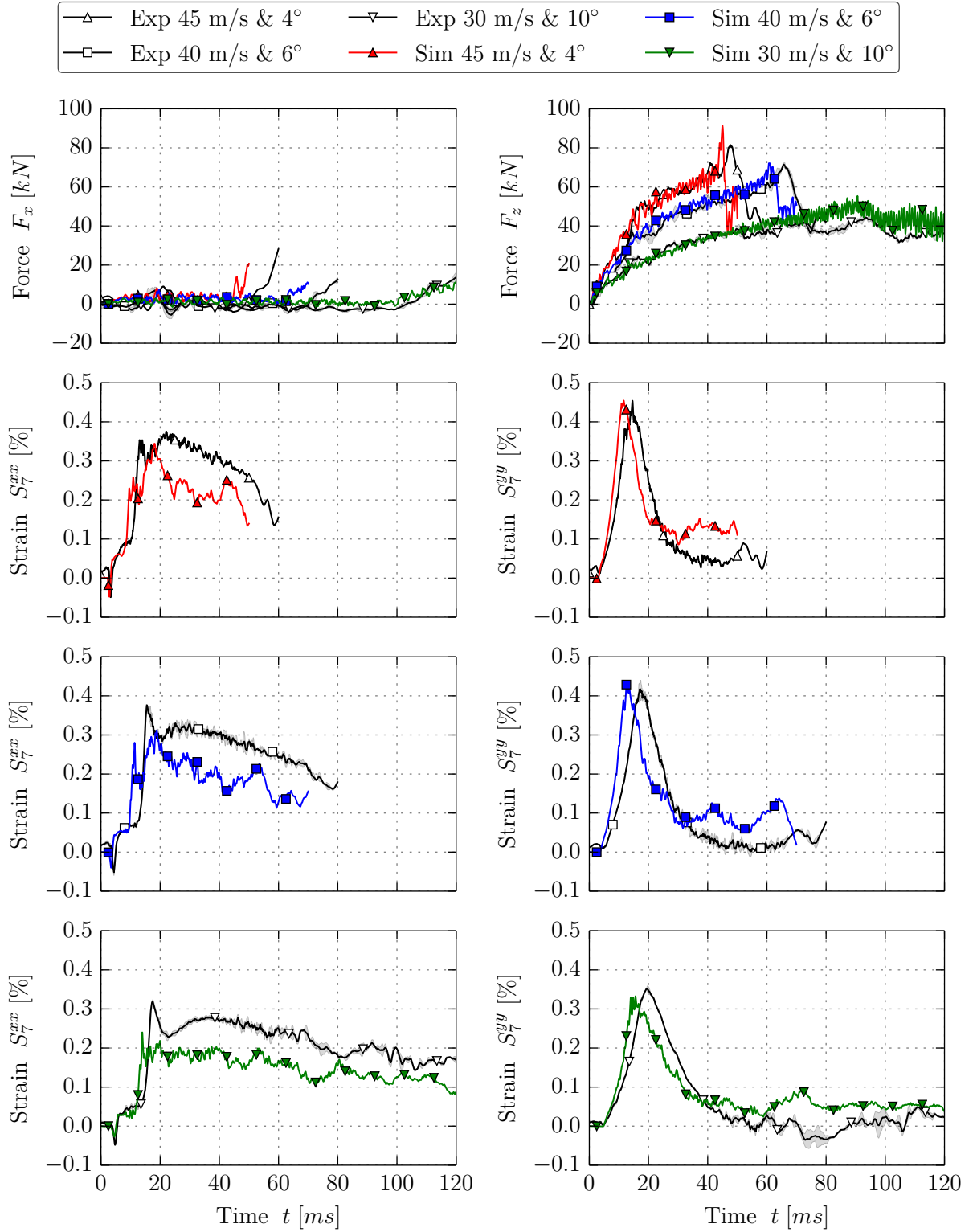
Figure 5.8: Force and strain time histories of simulations and experiments with 1.65 mm composite panels and under different impact conditions, i.e. horizontal impact velocity and pitch angle (IDs 5113, 5122, 5131).
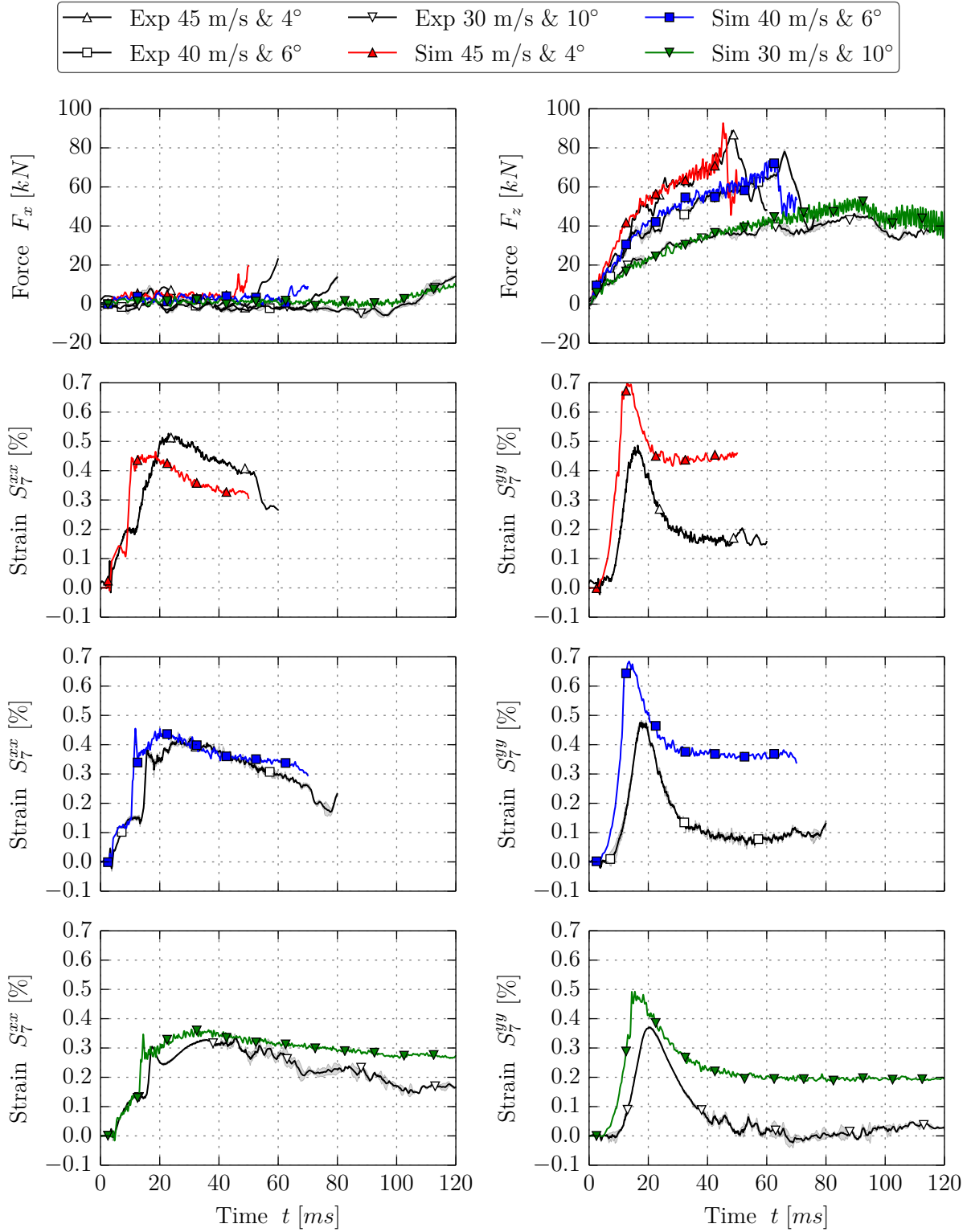
Figure 5.9: Force and strain time histories of simulations and experiments with 0.8 mm aluminum panels and under different impact conditions, i.e. horizontal impact velocity and pitch angle (IDs 3113, 3122, 3131).

5.2 Investigation of Structural Behavior

After the developed numerical model has been validated against a range of test cases with overall good agreement, it is used to investigate the structural behavior in detail.

5.2.1 Key Mechanisms of Structural Response

The key mechanisms identified and discussed in Section 3.3.4, which cause the increase in hydrodynamic loading when deformations occur, are evaluated. Understanding these key mechanisms and the resulting structural response provides the basis to transfer the gained knowledge to simulations of more complex water impact cases. Figure 5.10 exemplarily illustrates the dynamic structural response. From the sequence of contour plots, the formation of a pocket, which is successively filled with fluid, can be recognized. Toward the end of the impact, the fluid jet impacts on the front part of the panel. Subsequently, it is forced out of the pocket and passes the stiff L-frame. During this moment, hydrodynamic loads and thus the normal force show a distinct increase, which is reproduced by the numerical model (cf. Figs. 5.7–5.9).
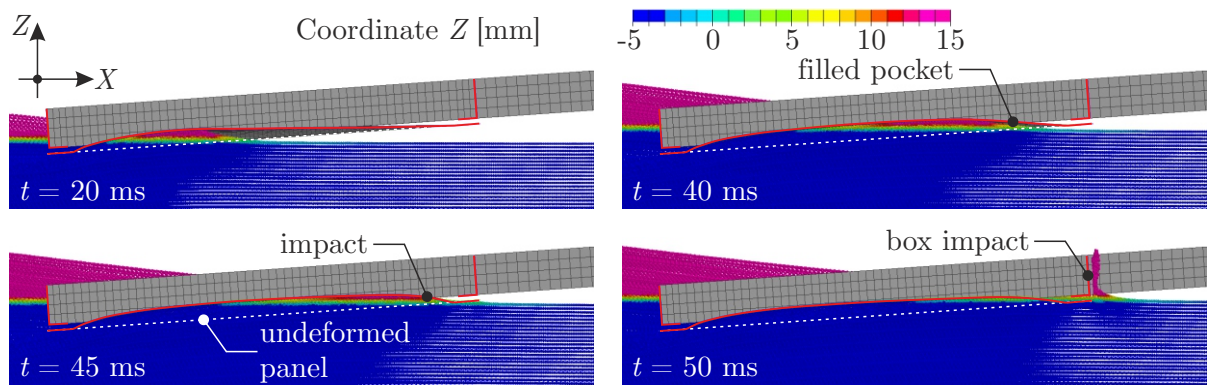

Figure 5.10: Illustration of pocket formed by the structure for test case with 0.8 mm aluminum panel at 4° and 45 m/s (ID 3113).

In order to quantify the amount of deformation experienced by the panels, the local displacement in normal direction of the panel, d_z, is evaluated along the center line of the panel ($y = 0$ mm), where the deepest indentation occurs (results are provided in Fig. C.4). Fundamentally, an upward displacement of the unsupported area of the panels is observed, as expected based on the acting hydrodynamic pressure. Common among all test cases, the displacement is largest at a location between 40% to 50% of the panel length. Within the investigated range of impact conditions quasi-rigid panels deform about 2.2 mm at most, which justifies the assumption that their structural deformation is negligible. The deformable panels show maximum displacements in the order of 25 mm, 30 mm, and 35 mm for 3 mm aluminum, composite, and 0.8 mm aluminum panels, respectively. In addition, the thin aluminum and the composite panels exhibit oscillations of the forward

part of the panels as long as it is still dry (see e.g. response of elements 70–90 in Fig. C.4, bottom). These oscillations are stronger in the cases with 0.8 mm aluminum panels.

The evaluation of experimental and numerical data showed a general increase of hydrodynamic loading attributed to structural deformations during the entire impact. The effect is more pronounced for cases with higher horizontal impact velocities and smaller pitch angles (cf. Sections 3.3.4 and 5.1.2). The analysis of numerical results permits a deeper insight into the structural response, indicating that the increased loading results from the changing structural dynamics during impact. Three mechanisms are identified: the local pitch angle, the lateral panel curvature, and the local vertical impact velocity. These are subsequently analyzed and assessed based on simulations of test cases with 3 mm aluminum panels, for which the simulation model could be validated.

- Due to the deformation of the panels, the local pitch angle α^* varies over time. For quasi-rigid panels, the pitch angle was found to increase the hydrodynamic loads significantly (see Section 5.1.1.1). Thus, the local pitch angle of the deformable panels is evaluated along the center line ($y = 0$ mm) and the results are presented
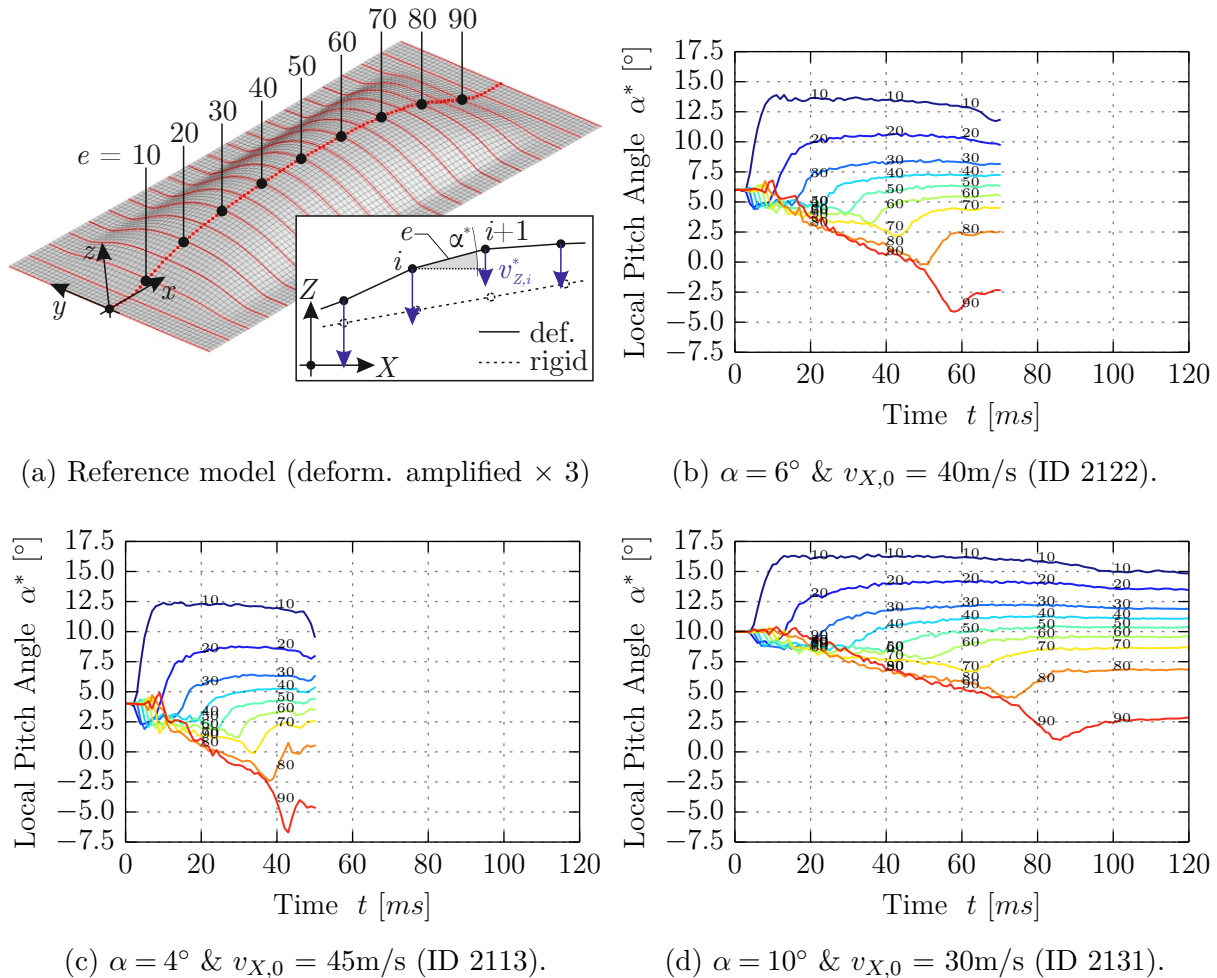

(a) Reference model (deform. amplified × 3)

(b) $\alpha = 6°$ & $v_{X,0} = 40$m/s (ID 2122).

(c) $\alpha = 4°$ & $v_{X,0} = 45$m/s (ID 2113).

(d) $\alpha = 10°$ & $v_{X,0} = 30$m/s (ID 2131).

Figure 5.11: Evaluation of local pitch angle time histories along center line ($y = 0$ mm) of 3 mm aluminum panel.

for every tenth element e as illustrated in Fig. 5.11. The analysis shows that the local pitch angle in the rear part of the panel rapidly increases. Once the increase is established, the local pitch angle remains nearly constant until the leading edge immersion where the pressure acting on the panel suddenly diminishes. Afterward, the elastic deformation reduces due to the unloading, which causes the local pitch angle to decline slightly toward its initial value. In contrast, the local pitch angle decreases in the front part of the panel and even reaches negative absolute values (see e.g. Fig. 5.11, b & c). This effect is stronger for cases at low nominal pitch angle and high velocity, which also show the strongest normal force peak (cf. Fig. 5.9). The present analysis indicates that the force peak is stronger for cases where the local pitch angle at the front of the panel is more negative. Moreover, the relative change of pitch angle and thus the change of loading is larger for cases at low nominal pitch angle, which confirms the findings discussed in Section 3.3.4.

- The panels deform increasingly into a shape with a strong concave curvature, which is more pronounced in lateral direction. Measurements of the smallest radii of the deformed panels in transverse direction show values of up to approximately 700 mm at the panel's center ($x = 500$ mm), where largest deformations are found. This curvature is stronger compared to the one of the concave quasi-rigid panels. Yet, as the lateral panel curvature was found to affect the loads only to a small extent in test cases with quasi-rigid panels (see Section 5.1.1.3), its contribution to the increased load is still assumed to be small.

- Numerical results reveal that the local vertical velocity v_Z^* is substantially reduced during the time when the structure deforms. Due to oscillations, however, it is difficult to quantify the local vertical velocity. Yet, to provide an estimate, the nodal vertical velocity along the center line of the panel is evaluated. Results show changes from the initial value of -1.5 m/s up to temporary values of 1–2 m/s in upward direction while the structure is being deformed. Once the deformation is established, the local vertical velocity is that of the total structure superimposed by oscillations. Although the hydrodynamic pressure distribution depends on the resulting normal velocity of the flow with respect to the panel, which is sensitive to the vertical velocity component [77], the local reduction of the vertical velocity occurs over a very short period of time and therefore does not significantly affect the hydrodynamic loading. Moreover, the velocity reduction is highest in the rear of the panel where the deformation occurs rapidly, while it is smaller toward the front where the deformation grows over longer time, which further reduces the effect.

In summary, it is verified that the increase in hydrodynamic loading is mainly caused by the increase of the local pitch angle and to a minor extent by the increasing concave lateral curvature, whereas the reduced vertical velocity plays a minor role.

5.2.2 Analysis of Strain Distribution and Local Strain Gradients

Numerical results are further used to investigate the characteristic strain distributions. Moreover, as the evaluation of experimental data indicated large strain gradients along the boundaries (see Section 3.3.4), these are analyzed in detail using the numerical model.

Strain Distribution   Figure 5.12 presents exemplary strain distributions for test cases with 3 mm and 0.8 mm aluminum panels under impact conditions of 6° and 40 m/s at $t = 30$ ms, which is about half of the impact duration. The strain contour plots show pronounced gradients in perpendicular direction to the L-frame. These lead to strain concentrations along the interface to the L-frame, where consequently highest magnitudes are found. The strain distributions are overall smooth in the case with the 3 mm panel. In the case with the 0.8 mm panel, the strain distributions are closely linked to the propagation of the high-pressure zone and thus the structure additionally exhibits large spatial gradients at the location of the jet root.
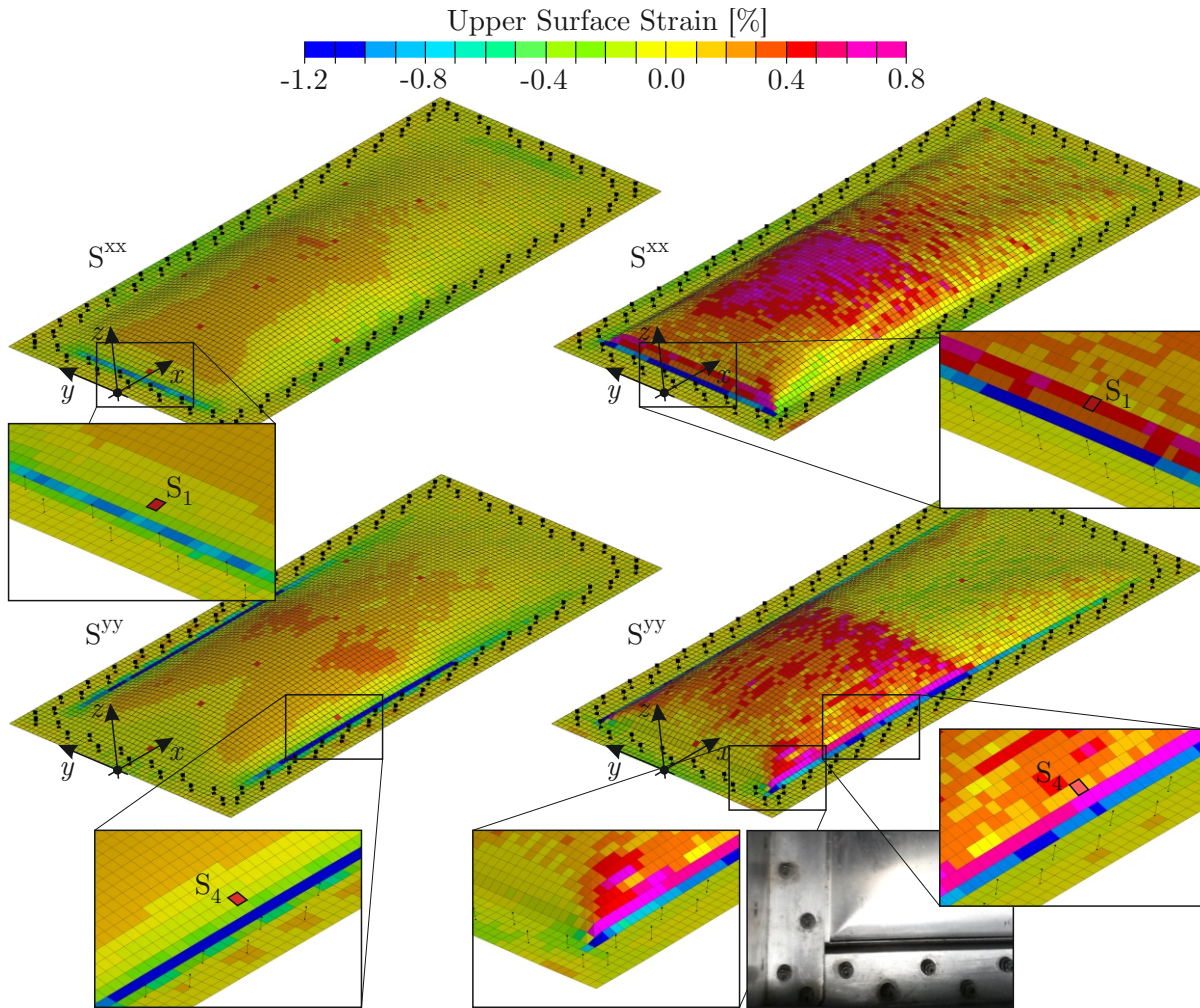

Figure 5.12: Exemplary upper surface strain distributions for cases with 3 mm (ID 2122, left) and 0.8 mm (ID 3122, right) aluminum panels at $t = 30$ ms. Impact conditions: 6° & 40 m/s. Deformation amplified ×2.

The comparison of numerical strain results on lower and upper element surfaces allows investigating the dominant mechanisms of the structural behavior beyond experimental findings. Results indicate that the central area of panels experiences membrane loading[3] conditions in x-direction with small, local amounts of bending in the moment of passage of the high-pressure zone as well as at the front and rear interfaces to the L-frame. In y-direction, the structural response of the 3 mm panels is dominated by bending loads[4]; only very small local areas in the front and rear part of the panel exhibit similar strains at the lower and upper surface pointing at membrane loading. The 0.8 mm panels, however, also experience membrane loading conditions in y-direction and bending loads are found only very concentrated along the interface to the L-frame.

Commonly, highest strains are found at the interface to the L-frame, where bending is predominant, and also at the corners, where strain concentrations are superimposed. In cases with the 0.8 mm aluminum panels, the very local bending at the interface to the L-frame causes strain concentrations with lowest and highest strain values in adjacent shell elements (see Fig. 5.12, bottom right). Results with 3 mm panels show less strain concentration, but there is still a noticeable gradient near the interface to the L-frame.

Strain Gradients Above findings indicate the difficulties associated with resolving the local strain distributions. It is obvious that there is a strong mesh dependency. In particular, the shell element size determines the exact location of the elements used to evaluate the strain, which can result in a spatial difference of up to half the shell edge length compared to the nominal gauge locations[5] in the experiment. In addition, the type of gauge applied in the experiments uses side-by-side grids, which are about ± 2 mm aside from the nominal location (cf. Section 3.3.4). Finally, the experimental strain gauge grid is about 3.8 mm long, which permits capturing more local strain distributions compared to the present numerical model with a common shell edge length of 10 mm.

In order to evaluate the spatial strain gradients around the gauge locations and also to extend the experimental measurements by employing the developed numerical model, the simulation output is extended by a field of strain gauge elements around the nominal gauge location as portrayed in Fig. 5.13 (a).

Figure 5.13 exemplarily shows strain results at gauge locations S_1 and S_4 for five adjacent shell elements in perpendicular direction to the L-frame. Results reveal the extent of the spatial strain gradients in the vicinity of the L-frame, which are more pronounced for the strain component in perpendicular direction to the frame. Strain results around gauge location S_1 show an additional difference in timing of the strain curves depending on the selected shell element, where peak values occur later for elements farther ahead in x-direction. This effect is stronger for strains in x-direction than for those in y-direction,
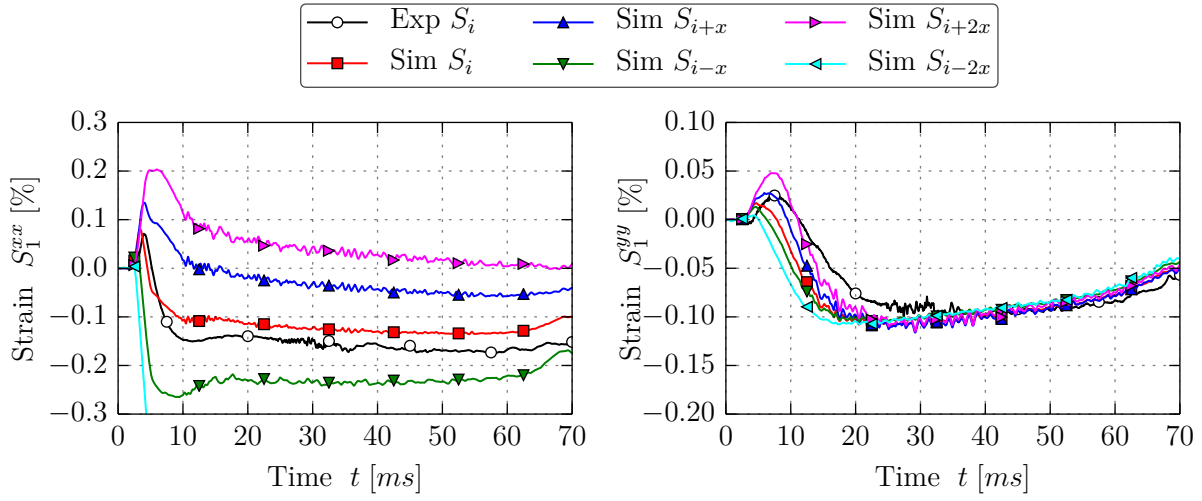
---

[3]Membrane loading is identified by similar strain results on both element surfaces.

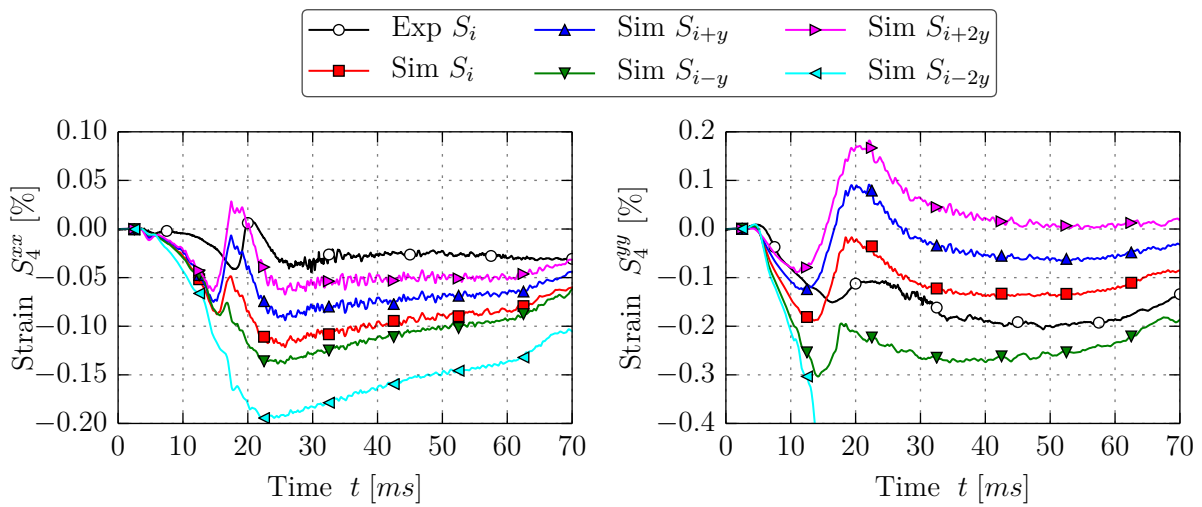[4]Bending loads are characterized by contrary or significantly different surface strain values.

[5]The nominal gauge locations refer to the locations used in the experiment, which are given in Tab. A.4.
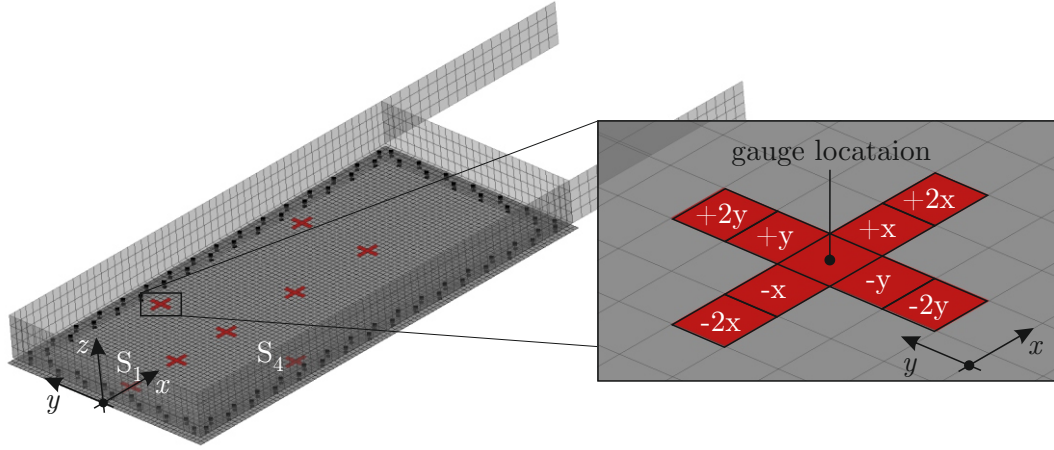
(a) Detailed view on numerical model for strain gradient analysis.

(b) Strain gradient in x-direction.

(c) Strain gradient in y-direction.

Figure 5.13: Analysis of strain gradients near boundaries around gauges S_1 and S_4 for test case with 3 mm aluminum panel at 6° pitch angle and 40 m/s horizontal impact velocity (ID 2122).

which is a consequence of the dynamic loading where the peak pressure zone propagates in x-direction during the impact. At location S_4 there is a large spatial strain gradient in y-direction for both S^{xx} and S^{yy}, and thus strains of adjacent elements differ significantly. The comparison of the exact location of the shell elements with the location of the grid in the experiments demonstrates that the model would predict the strains more accurate if the strain gauge elements would be placed closer to the grid location in the experiments. However, results of S_4^{xx} still show a noticeable discrepancy to experimental data. Further evaluation of the strain gradient at gauge S_4 in x-direction proves that the two elements ahead in x-direction predict the experimental strain response with a better agreement, which suggests that the present discrepancies are to some extent related to the general time lead of the simulation results previously discussed.

The strain gradient analysis further proves that there are no significant gradients for gauges along the center line of the panel (S_2, S_5, S_7, S_8); however, the timing of strain curves is affected in similar fashion as explained above, i.e. with increments in time of approximately 0.5 ms for the regarded impact condition (6° & 40 m/s) and a characteristic shell element edge length of 10 mm. Based on strain contour plots this absence of strain gradients is found to be related to the locally uniform strain distribution in the center of the panels (cf. Fig. 5.12).

In summary, the extent of spatial strain gradients was evaluated and in particular, the large strain gradients along the interfaces between panel and L-frame could be quantified. By comparison with experimental data, it could further be demonstrated that local strain results are mesh-dependent. Nevertheless, the numerical model is valid as the fluid-structure interaction and the structural response are reproduced with high accuracy. Presented discrepancies were proven to be related to the nonconformity of the location of the strain evaluation in the numerical model and in the experimental setup. Therefore, the presence of large spatial strain gradients requires an appropriately fine structural mesh if these are to be captured. As this directly affects the simulation time step and indirectly also to the particle resolution, which has to be adapted to the mesh size of the structure, it highly affects the computational effort and hence a trade-off must be established.

Plastic Strain In order to point out most critical zones of the structure, the distributions of the maximum plastic strain at the end of the simulation are given in Fig. 5.14 for test cases with deformable aluminum panels (3 mm and 0.8 mm aluminum panels). In analogy to the distributions of total strain discussed above, there are concentrations of plastic strains at the interface to the L-frame. Due to the aspect ratio of the panels, these strains are larger at the lateral edges compared to the front and rear edges.

Cases with 3 mm aluminum panels show very small amounts of plastic strain over the rest of the panel. Only under the impact conditions with higher loads (IDs 2122, 2113), low plastic strains arise starting from the corners. These are more evident at the front, which
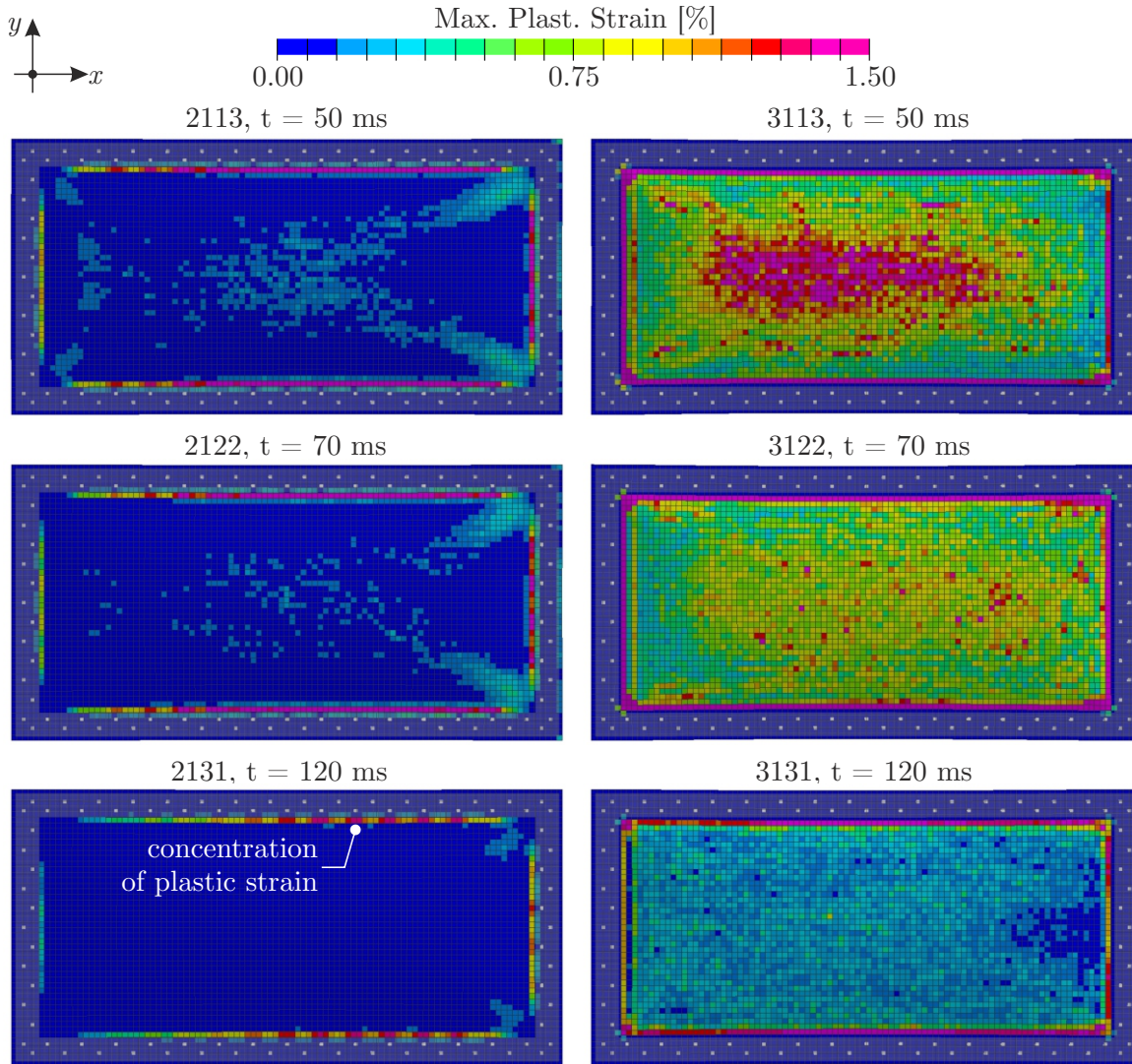
Figure 5.14: Analysis of maximum plastic strain over thickness at the end of the simulations with 3 mm (left) and 0.8 mm (right) aluminum panels under different impact conditions (top to bottom: 4° & 45 m/s, 6° & 40 m/s, and 10° & 30 m/s).

is attributed to the locally increased hydrodynamic loading due to the deformation with negative local pitch angles that also causes the referred force peak (cf. Section 5.2.1). Aside from the localized plastic strains in the vicinity of the L-frame, the numerical simulations predict very low plastic strains. This compares well with experimental post-test observations, where almost no plastic deformation is visible[6]. In contrast, the thin aluminum panels of 0.8 mm thickness exhibit plastic strains over the entire panel. The level of plastic strain increases with the loading; for the case with highest loads (ID 3113), high plastic strains concentrate at the center of the panel with a tendency to the rear.

Numerical results additionally reveal strain concentrations around the inner bolts (PLINKs) for the aluminum panels with 3 mm thickness as indicated in Fig. 5.14. By means of a visual inspection of the panels after the experiments, such concentrations of plastic strain cannot be detected as the plastic deformations are extremely small.

---

[6]Only a minimal amount of deformation becomes visible by light reflections.

If loads would be increased further, potential skin failure, which did not occur in the present test campaign, is expected to be initiated along the lateral interfaces to the L-frame where highest strains are found. Nevertheless, frames and stringers surrounding the skin fields of real aircraft structures are less stiff compared to the L-frame used in the experimental setup. Thus a direct transformation of the findings from the generic test specimens to real aircraft structures is not meaningful and requires further investigations taking into account more realistic aircraft structures.

5.3 Discussion of Results

Concluding the chapter, this section gives a critical review of the demonstrated capabilities and the experienced limitations of the developed simulation model. Finally, achieved results of the investigation of the structural behavior are discussed.

5.3.1 Capabilities and Limitations

The capabilities of the developed model to reproduce the hydrodynamic as well as the structural response, and thus the validity of the numerical approach, were demonstrated based on a comprehensive parameter study. Overall, the model proved to be robust, since all simulations were performed with the same input varying solely the parameters investigated, e.g. pitch angle, horizontal impact velocity, lateral panel curvature, and panel type (combination of material and thickness[7]).

The flow field is accurately predicted by the simulation and numerical fluid dynamics show a realistic behavior in comparison to experimental high-speed underwater observations for quasi-rigid as well as deformable panels. The latter generate a significantly different, more complex jet root shape across the panel that varies as the deformation grows over time. Despite large structural deformations, the simulation model reproduces the elementary characteristics of the fluid-structure interaction.

Numerical force time histories are predicted with very good agreement. This concerns the initial growth rate, the subsequent reduction of the growth rate and the corresponding general force level, the peak force, as well as the decay of the normal force prior to the leading edge immersion, which all highly depend on the impact conditions. The overall increase of the normal force due to the occurrence of structural deformations is correctly predicted for all test cases comprising deformable panels. Furthermore, the distinct normal force peak prior to the leading edge immersion is captured by the simulation model. However, the initial slope of the normal force appears to be slightly overestimated in cases at small pitch angle and with high horizontal impact velocity, which is attributed to the lack of an air cushion in the simulations (see below for further discussion).

---

[7]Note when varying the panel thickness, the contact thickness is adapted accordingly (cf. Section 4.4).

Strain results generally agree with experimental data. For quasi-rigid panels, the qualitative shape as well as the trend of the strain time histories depending on the impact conditions are well reproduced; however, the peak strain is underestimated compared to experimental data. In test cases with 3 mm aluminum panels, which exhibit only minor plastic deformations, strain time histories are captured with excellent agreement. Also for test cases with composite panels, a reasonable agreement could be demonstrated. However, despite good qualitative results for all investigated cases involving thin aluminum panels, the quantitative agreement of strain results displays the limitations of the simulation model. The numerical model predicts too large peak strains, which reach the plastic region and consequently cause a similar difference during the later stage of the impact where strains do not decline to the experimental post-peak values. This discrepancy is attributed to the material description. Due to the lack of precise material input data for each panel type regarding its thickness, heat treatment, and potentially anisotropic material properties resulting from the specific manufacturing processes, identical and generic Al2024 input data were used to model all aluminum panels. However, in particular the yield point and the plastic behavior are affected by the different manufacturing processes and thus made responsible for observed differences, which mainly occur when strains reach the plastic region. Results further suggest an additional anisotropy of the material behavior, which is common for thin metallic panels; especially for very thin sheet metals made of Al2024-T3 (0.3–1.27 mm), a strong direction-dependency of the material response was reported in [131].

Moreover, there are few uncertainties with respect to the structural modeling, which may limit the accuracy of the numerical predictions. Post-test investigations of the 0.8 mm panels showed low plastic deformation around the bolt holes and partial debonding of the glued boundary reinforcement. The numerical model, however, regards the joint connection as purely elastic and the boundary reinforcement was not explicitly discretized but modeled with elements of higher thickness. Therefore, the model cannot reproduce these effects. Since both mechanisms absorb energy and most likely affect the structural response, there may be additional errors especially along the interface to the L-frame, where highest strains are concentrated and large strain gradients are found.

The extreme pressure gradients observed in the experiments are not accurately captured by the numerical model as the used particle resolution is too coarse. In fact, the resolution required to resolve such highly transient phenomena would drive the computational effort to an impractical level. Moreover, despite the application of pressure correction methods and the consequential reduction of the numerical pressure oscillations inherent to the weakly compressible SPH method, pressure time histories remain noisy and do not permit a meaningful evaluation of pressure time histories. Nevertheless, the high quality of achieved results demonstrates that an effective assessment of the structural response under hydrodynamic loading does not necessarily require low noise pressure results

as high-frequency oscillations do not notably contribute to the hydrodynamic loads.

All simulation results are characterized by a small time lead with respect to experimental measurements, which grows with the simulation time. On the one hand, the timing of numerical results was found to depend on the particle resolution, which affects the formation of the flow field underneath the panel (cf. Section 4.3.3). Hence, the particle resolution is made responsible to some extent for the time discrepancy between simulation and experimental results. On the other hand, the fluid model is based on a single-phase material description and also air is not modeled. Thus, the model does not account for hydrodynamic phenomena involving air. In reality, however, air gets entrapped in the water underneath the panel, which is expected to reduce the fluid density. As hydrodynamic loads scale with the fluid density, they will be lower accordingly and therefore the deceleration of the impacting structure will be smaller. This effect was demonstrated by simulations employing a two-phase fluid model, which showed a noticeable effect on the timing, whereas hydrodynamic loads remained nearly unaffected (cf. Appendix B.3). Despite the improved correlation with experimental data, the two-phase fluid model was discarded as it comprises ten additional input parameters, some of which are subject to assumptions, and therefore increases the complexity of the model while not adding significant benefits. Moreover, in the experiments air cushioning was observed (cf. Section 3.3.1), which leads to a further yet approximately small delay of the loading that is not reproduced by the numerical model. Nevertheless, despite that the deviation in timing is partially justified by the occurrence of hydrodynamic phenomena, the comparison of numerical and experimental results showed that the model is sufficiently accurate for the evaluation of the structural response within the range of investigated impact conditions.

Furthermore, the employed initial conditions limit the accuracy of the present study. The parameter study was performed using the target horizontal impact velocity of each test case. In the experiments, however, the actual impact velocity was subject to dispersion as discussed in Section 3.3.1. Although the resulting effect on the results is expected to be low, it certainly causes additional discrepancies between numerical and experimental results.

Overall, the simulation model predicts the fluid-structure interaction with good accuracy; time histories of global forces as well as the structural response in terms of strains are captured and trends depending on the impact conditions are well reproduced. Comparing the achieved results with the objectives of this thesis allows declaring the developed model as valid for the investigated range of impact conditions and within the range of reported discrepancies.

5.3.2 Investigation of Structural Behavior

The performed numerical simulations enabled for the first time an insight into the mechanisms involved in the structural response that are responsible for the increase of the

hydrodynamic loading under given impact conditions. Based on the presented analysis, the increase of the local pitch angle was identified as the main source of the increased hydrodynamic loading under the presence of structural deformation. Furthermore, the growing lateral curvature due to the deformation in a concave shape contributes to the increase of hydrodynamic loading. The temporary reduction of the local vertical impact velocity, however, is considered negligible although it temporarily reaches significant values.

In addition, the occurrence of large spatial strain gradients with locally high strain concentrations at the interface to the stiff L-frame was demonstrated. Subsequently, these gradients were quantified based on an evaluation of strains at adjacent shell elements in the proximity of the gauge location. The analysis revealed that differences in strains along the boundaries of the panels are highly dependent on the structural discretization, which reaches its limits under the presence of such large strain gradients. Also, the nonconformity of the exact location of the shell elements with respect to the ones of the strain gauge grids in the experiments introduces noticeable variance in zones of high strain gradients. As a result, measured strains in the numerical model depend on the conformity of the locations of the experimental strain gauges with those of the elements used for strain evaluation in the simulation as well as on the mesh fineness. A further refinement of the structural model[8], however, is hardly feasible considering the associated increase of the simulation runtime based on the available hardware. In particular, recalling the intended application to larger, more realistic aircraft structures in the future, the structural resolution should not be increased. However, reported discrepancies of local strain results are acceptable as it was demonstrated that the overall structural response is accurately captured.

The analysis of the structural behavior and the strain field was based on simulations with 3 mm aluminum panels, for which the numerical model was validated. However, results of simulations with 0.8 mm aluminum panels are solely to be regarded as qualitative as the accuracy of the predicted strain fields was limited by the material data describing the plastic behavior as discussed above. Nevertheless, the structural behavior in the simulations was found to be in qualitative agreement with experimental observations for all test cases considered in the test program. Results therefore permitted an insight into the expected structural response of such highly deformable panels.

---

[8]A refinement of the structural mesh directly affects the critical time step of the simulation and it additionally requires to adapt the fluid resolution accordingly. Both of these refinements would significantly increase the simulation runtime (cf. Section 4.3.3).

6 Conclusion and Outlook

The present research work was set out to investigate the structural behavior as well as the effects of structural deformations on hydrodynamic loads acting during a ditching based on both an evaluation of novel experimental results and numerical simulations using the coupled SPH-FE approach. The subject is of particular interest since currently employed numerical simulations for the substantiation of the structural capacity under ditching loads are uncoupled and thus do not account for effects of structural deformations. Furthermore, there was no fundamental understanding of the involved physics in ditching regarding the occurring hydrodynamic phenomena, the detailed fluid-structure interaction, and the structural response. The author claimed that structural deformations significantly affect the hydrodynamic loads acting during a ditching, as they modify the boundary conditions the fluid is facing.

In the following, the main contributions of this thesis to the investigated field are summarized and conclusions based thereon are presented. Encountered limitations are discussed and, finally, an outlook on future research that could address these limitations and build upon the attained knowledge is pointed out.

6.1 Contributions and Conclusions

The interpretation of results emanating from both experimental evaluation and numerical simulations presented in this thesis contributes to the body of knowledge. Below major findings are synthesized proceeding from experimental to numerical aspects. Finally, possible implications for the ditching analysis are discussed.

Experimental Evaluation

1. The fundamental characteristics of the fluid-structure interaction were studied based on comprehensive analyses of experimental data provided by CNR-INSEAN within the research project SMAES. A distinct relation between the hydrodynamic and the structural response could be demonstrated; strain peak values correlate with the passage of the high-pressure zone located at the jet root. In addition, it was found that the structural response is insensitive to high-frequency pressure oscillations as well as highly dynamic pressure peaks.

2. The occurrence and the extent of hydrodynamic phenomena such as air entrapment and air cushioning were discussed based on selected underwater high-speed recordings provided by CNR-INSEAN. A simple model was used to approximate the extent of the air cushion, which resulted in an approximate thickness of 4 mm at most. Although occurring hydrodynamic phenomena were found to affect the pressure distributions in terms of reduced peak values and stronger oscillations, they were estimated to be of minor importance for the structural response. However, if larger aircraft structures are to be analyzed, other hydrodynamic phenomena could occur and potentially affect the structural response as they can alter the global aircraft motion.

3. The effects of impact velocity, pitch angle, and lateral panel curvature on the global forces as well as the structural behavior were evaluated and quantified. Both the impact velocity and the pitch angle significantly determine the hydrodynamic loading. The lateral panel curvature, however, only showed limited effects, which was assumed to be related to the large radii of curvature (± 2000 mm) in combination with the panel width of 500 mm. Nevertheless, hydrodynamic loads are generally expected to be lower for convex aircraft bottom fuselages.

4. It was proven that hydrodynamic loads and resulting normal forces acting on the panel significantly increase when structural deformations occur. Results demonstrate that the effects are stronger for cases with larger horizontal impact velocity and smaller pitch angle because the relative increase of the local pitch angle is larger therein.

5. Moreover, this evaluation permitted to identify the key mechanisms that characterize the structural response and thus cause the load increase. These are the increase of local pitch angle, the development of a concave lateral curvature resulting in a local deadrise angle, and the transient reduction of the local vertical impact velocity.

Numerical Simulation

6. Building on the attained knowledge from the experimental evaluation, a coupled numerical simulation model of the guided ditching experiments based on the SPH-FE approach was developed in Chapter 4. The focus was put on simplicity (in particular regarding the required input parameters), reproducibility, efficiency, and accuracy.

7. Previously usual and prohibitive simulation runtimes associated with such coupled simulations could be reduced considerably by application of specific modeling strategies for the fluid domain. Due to the adopted modeling techniques such as the

translating active domain feature, the simulations are between 2.2 and 3.7 times[1] faster compared to the previous state of the art. The adopted modeling techniques are especially effective for applications involving large horizontal velocities as computational savings further increase for simulations with longer fluid domains and longer simulation times.

8. It was shown how the efficiency of the SPH model can additionally be improved over the state of the art by applying a static refinement technique to generate non-uniform initial particle distributions. Simulation results of 2D test cases as well as guided ditching simulations successfully demonstrated the applicability of such non-uniform particle distributions. However, the efficiency increase due to the derived refinement technique was found to be restricted by the neighbor search algorithm implemented in the employed software. It was therefore decided to refrain from its use for the validation and verification studies in this work. Nevertheless, with an appropriate neighbor search algorithm becoming available, the presented static refinement technique is expected to permit significant speed-ups of the simulations.

9. The use of pressure correction methods demonstrated possible improvements with respect to the numerical oscillations in the pressure field; however, in guided ditching simulations, the pressure responses evaluated using numerical pressure probes remained noisy and did not permit a meaningful comparison with experimental data. This was attributed to the particle resolution, which requires further refinement if pressure responses are to be captured. Moreover, particle regularization algorithms were shown to increase stability and robustness of the simulations as they reduce the developing particle disorder. This is of great importance for cases with larger fluid displacement, i.e. for cases with larger pitch angle or larger structural deformation, where the developing particle disorder is larger.

10. All adopted modeling techniques were evaluated and assessed based on sensitivity studies that demonstrated their effectiveness as well as the robustness of the developed model. The sensitivity studies in particular emphasized the dependency of results on the particle resolution. Finally, all adopted modeling techniques are of direct relevance for the application to more complex aeronautical structures.

11. In order to assess the validity of the developed simulation model, parameter studies covering the extent of the experimental campaign were performed. The wide range of regarded impact conditions and panel types as well as the use of one model for all simulations both emphasize the strength of these studies. The validation consisted of analyzing the qualitative responses of fluid and structure as well as quantitative measures such as velocity, force, and strain time histories. Simulation results in terms of the hydrodynamics, the structural response, and the acting forces showed

---

[1]The speed-up depends on pitch angle and horizontal impact velocity as discussed in Section 4.3.2.

very good agreement with experimental data for all investigated impact conditions and panel types. In particular, the increase of hydrodynamic loads due to structural deformations is correctly reproduced. However, the accuracy of numerical strain results was found to be confined by the lack of accurate material data as well as the nonconformity of the mesh and the exact gauge locations in the experiments. Nevertheless, for the range of parameters investigated within this work, the numerical model could be validated within the range of reported discrepancies. Therefore, the simulation approach is considered to predict the structural behavior under hydrodynamic loading within the scope of its intended application.

12. For the first time, the experimentally identified mechanisms involved in the structural response that cause the increase of hydrodynamic loads when structural deformations occur (see point 5) were quantified based on validated simulation results. This evaluation extended the experimental evidence and established a fundamental understanding of the structural behavior under representative impact conditions. The attained knowledge, therefore, provides the basis for investigations of the water impact of more complex structures.

13. In many test cases with deformable panels, a distinct normal force peak was observed just prior to the leading edge immersion. The numerical analysis revealed that this load peak is related to the formation of a locally negative pitch angle at the front of the panels. While this finding is of general validity, its source, the locally negative pitch angle, is attributed to the stiff boundary condition of the panels in the present experimental setup (L-frame). The lower stiffness of frames of real aircraft structures thus suggests that such distinct force peaks would be less pronounced or would not even occur, as frames most likely also undergo deformations.

Possible Implications

The thesis that structural deformations affect hydrodynamic loads under ditching impact conditions was corroborated based on an evaluation of experimental results as well as profound numerical analyses. The results of this research, therefore, may influence the debate on the subject as they suggest that currently used means for numerical ditching substantiation are inadequate as they neglect structural deformations and thus underestimate the acting hydrodynamic loads. Due to the significant increase in hydrodynamic loads as a result of structural deformations, it is recommended that these are taken into account within the assessment of the structural capacity in ditching analyses by employing coupled numerical simulations. Through the considerable efficiency increase by application of modeling strategies delineated in this thesis as well as its demonstrated validity, the SPH-FE approach became feasible for such purposes. It can decisively contribute to more accurate analyses of the structural behavior under ditching loads compared to the

state of the art in design and certification, and it could reduce the extent of experimental investigations. Moreover, it enables to develop and to analyze what-if scenarios and virtual prototypes of sub- and full-scale (non-testable) aircraft structures under ditching conditions, which could become part of novel design and certification routes in the next years. In the near future, it is expected that further hardware improvements as well as ongoing developments regarding high-performance computing will qualify the developed simulation methodology for comprehensive studies involving large aircraft structures.

6.2 Future Work

The achieved results and encountered limitations during this work suggest further research building thereon as discussed in the following.

Experimental Investigation

1. Prior to the guided ditching experimental campaign presented in this thesis, it was planned to break the thin panels during the experiment, which in turn would have enabled to study failure under representative hydrodynamic loading. During the experimental campaign, however, no structural failure occurred. Therefore, it is suggested to conduct additional experiments at higher impact velocities with the aim to break the panels in order to further increase the understanding of the structural behavior including failure.

2. The generic structure used within this work provided a fundamental understanding of the involved physics, the occurrence of hydrodynamic phenomena and the mechanisms of the structural response. Furthermore, its simplicity compared to a real aircraft structure considerably facilitated the validation of the numerical model; however, it also limited the validity of findings with respect to their transferability to real aircraft structures. Thus, the interpretation of results requires special attention as it has to be distinguished which effects are due to the present experimental setup and which can occur on a real aircraft structure. Therefore, the level of structural complexity should be advanced from the generic panels investigated in the present work to more realistic, stringer-frame-reinforced specimens in a future test campaign.

Development of Numerical Simulation Capabilities

3. A limitation encountered within the validation studies was the lack of accurate material data describing the plastic behavior of the aluminum panels. In order to fully validate the developed model also for the test cases involving the thin aluminum panels and thus for the complete experimental database of guided ditching

tests, further validation studies should be carried out with more accurate, specific[2] material data and sophisticated material models that account for the anisotropic material behavior.

4. One of the simplifications of the developed model is that air was neglected. Yet, the occurrence of an air cushion as well as air entrapment was observed in the experiments. Therefore, the numerical model could be extended by modeling air. This would permit investigating the capability of the numerical model to reproduce these hydrodynamic phenomena. However, the required particle resolution anticipated based on the approximation discussed in this work (cf. Appendix A.4) will challenge the practical computational time.

5. Despite the realized efficiency increase through the application of presented modeling techniques, coupled simulations remain computationally intensive. The present research was conducted on two quad-core processors belonging to one node of a computing cluster running in shared memory processing mode. Recently, a development version of the solver capable of distributed memory processing was released, which allows a more extensive use of hardware resources. In addition, this processing mode permits splitting the solution into sub-models that can run with individual time steps. This technique, which is referred to as Multi-Model Coupling [37], additionally permits optimizing the use of resources assigned to the fluid/SPH and the structural/FE solution and thus allows for a further reduction of the computational time. A theoretical assessment yields expected speed-ups by a factor of 5 to 10.

6. Another great leap in terms of computational efficiency could be realized by implementing an improved neighbor search algorithm that permits fully benefiting from the use of non-uniform particle distributions developed in the context of this work (cf. Section 4.3.4.2 and Appendix B.6). Possible speed-ups are expected to be in the order of 10 and more.

Application of Numerical Simulations

7. After the simulation model was validated for a range of impact conditions, it could be used to numerically extend the test matrix by parameter combinations that were not considered in the experimental campaign such as the combination of deformable panels with a lateral curvature.

8. In a next step, the presented numerical simulation methodology could be applied to analyze a more realistic, stringer-frame-reinforced aircraft structure. Such work would consequently establish routes for the application of the developed simulation methodology in design and certification of future aircraft.

---

[2]Accounting for panel thickness, heat treatment, and potentially anisotropic material properties due to specific manufacturing processes.

Appendix

A Guided Ditching Experiment

A.1 Facility Tolerances

Below the tolerances of the guided ditching facility with respect to parameters of the test campaign are given. For more details refer to [80].

Table A.1: Tolerances of guided ditching facility. [80]

Parameter	Symbol	Tolerances
Horizontal velocity	v_X	±0.2–0.3 m/s
Pitch angle	α	$\pm0.1°$
Heel angle	β	$\pm0.1°$
Guide track inclination	γ	$\pm0.017°$

A.2 Overview of Instrumentation

The main trolley and the test specimens are equipped with a variety of sensors, probes, and gauges according to the summary in table A.2. Furthermore, pressure probe and strain gauge locations are given in Tables A.3 and A.4. Measures refer to the panel coordinate system with its origin at the lateral center of the panel trailing edge and orientation as illustrated in Fig. 3.3.

Table A.2: Overview of instrumentation in guided ditching experiments.

Acquisition System

- Remotely operated on-board computer
- 4 × Dewesoft Sirius acquisition modules
- 1 × Dewesoft Dewe-43 acquisition module
- 200 kHz sampling rate with 44 kHz internal (hardware) pre-filter

Table A.2: Overview of instrumentation in guided ditching experiments. (continued)

Force @ 20 kHz

- Unidirectional load cells
- $2 \times$ Kistler 9363A, full scale range of 120 kN, used for loads in x-direction
- $4 \times$ Kistler 9343A, full scale range of 70 kN, used for loads in z-direction

Strain @ 20 kHz

- Bi-directional strain gauges (90° tee rosettes, side-by-side grids)
- $6 \times$ Vishay C2A-13-125LT-350, range of $\pm 3\%$, used for quasi-rigid cases
- $8 \times$ Vishay EP-08-125TQ-350, range of $\pm 20\%$, used for deformable cases with aluminum panels
- $8 \times$ Vishay C2A-06-125LT-350, range of $\pm 3\%$, used for deformable cases with composite panels

Pressure @ 200 kHz

- $18/14 \times$ Kulite XTL-123BEG-190M-300PSIA, range of 20.68 bar (300 psi) absolute pressure, used for quasi-rigid and selected deformable cases (see Tab. A.5)
- Pressure probes are flush-mounted to the surface with a tolerance of ± 0.1 mm; the sensible element is separated from the water by a silicon layer

Velocity @ 20 kHz

- Non-contact optical sensor
- $1 \times$ CORRSYS-DATRON Correvit LFII

Acceleration @ 20 kHz

- Resistive, uni- and triaxial, miniature accelerometers of type Kistler M101A/M301A, range of 1000 g
- $6 \times$ for quasi-rigid cases
- $5 \times$ for deformable cases

Table A.3: Pressure probe locations in guided ditching tests. * denotes probes solely used in quasi-rigid test cases.

	P_{01}	P_{02}	P_{03}	P_{04}	P_{05}^*	P_{06}^*	P_{07}^*	P_{08}^*	P_{09}	P_{10}	P_{11}	P_{12}	P_{13}	P_{14}	P_{15}	P_{16}	P_{17}	P_{18}
x [mm]			125				250				400				600		800	
y [mm]	-180	-120	-60	0	120	-180	-120	120	-180	-120	-60	0	120	-180	-120	0	-180	0

Table A.4: Strain gauge locations in guided ditching tests. * denotes locations solely used in quasi-rigid test cases and † denotes locations/gauges solely used in deformable test cases.

	S_1	S_2	S_3	S_4	S_5	S_6	$S_7^\dagger$	$S_8^\dagger$
x [mm]	85*/75†		325			700	195	512.5
y [mm]	0	0	165*/175†	-165*/175†	0	165*/175†	0	0

A.3 Test Matrix

Table A.5: Test matrix of guided ditching experimental campaign. The given velocity refers to the target horizontal impact velocity. [†] and [††] denote deformable cases where pressure probes were employed in one or two repeats, respectively.

Test case identifier[1]	Curvature	Pitch angle α [∘]	Horizontal impact velocity v_X [m/s]	Repeats successful/total
Al2024-T351, $t_{panel} = 15.0$ mm, $m_{tot} = 840$ kg				
1113	flat	4	45	3/3
1122	flat	6	40	3/3
1131	flat	10	30	3/3
1133	flat	10	45	3/3
1123	flat	6	45	3/3
1132	flat	10	40	10/10
1112	flat	4	40	10/10
1222	convex	6	40	3/3
1212	convex	4	40	3/3
1213	convex	4	45	3/3
1322	concave	6	40	3/3
Al2024-T3, $t_{panel} = 3.0$ mm, $m_{tot} = 834$ kg				
2113[†]	flat	4	45	2/2
2122	flat	6	40	1/2
2131[††]	flat	10	30	2/2
Al2024-T3, $t_{panel} = 0.8$ mm, $m_{tot} = 832$ kg				
3113	flat	4	45	1/1
3122	flat	6	40	2/2
3131[†]	flat	10	30	2/2
3133	flat	10	45	1/1
Composite AS4/8552, $t_{panel} = 1.65$ mm, $m_{tot} = 832$ kg				
5113	flat	4	45	1/1
5122	flat	6	40	2/2
5131[†]	flat	10	30	2/2
5133	flat	10	45	1/1

---

[1]The four digits contain (1) material/thickness combination, (2) curvature, (3) pitch angle, and (4) target horizontal impact velocity according to notation shown in Fig. A.1.
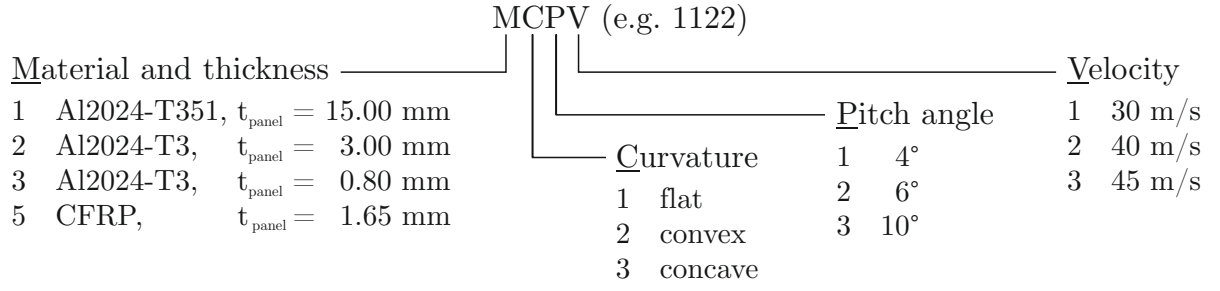
Figure A.1: Explanation of test case identifier (ID).

A.4 Model for Estimation of Air Cushion

Figure A.2 portrays a simple geometrical model to estimate the magnitude of the air cushion observed in guided ditching tests.
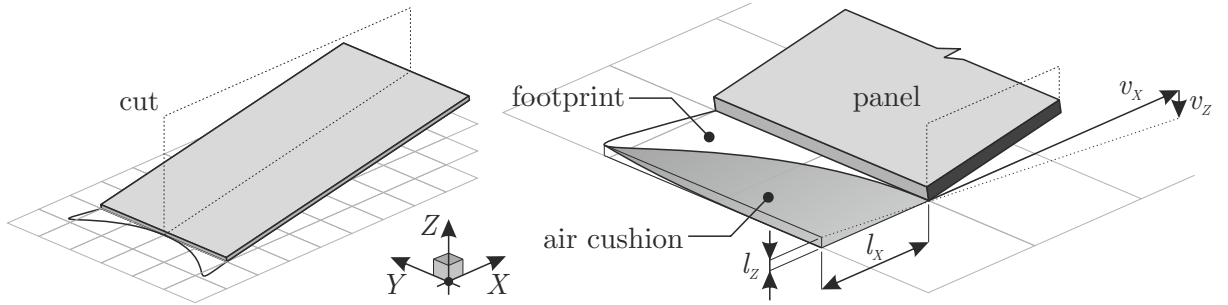

Figure A.2: Model for estimation of magnitude of air cushion.

The model assumes that the ratio of impact velocities is approximately equal to the ratio of length to height of the air cushion, resulting in

$$\frac{v_X}{v_Z} \approx \frac{l_X}{l_Z} \; . \tag{A.1}$$

With the length l_X of the air cushion taken from underwater high-speed recordings (see e.g. Fig. 3.4) and the defined ratio of impact velocities, the model estimates the maximum vertical displacement of the free surface l_Z at the center of the panel to be in the order of 4 mm in negative Z-direction. Such estimation is instrumental in order to estimate the required discretization fineness of numerical models aimed to capture the air cushion effect.

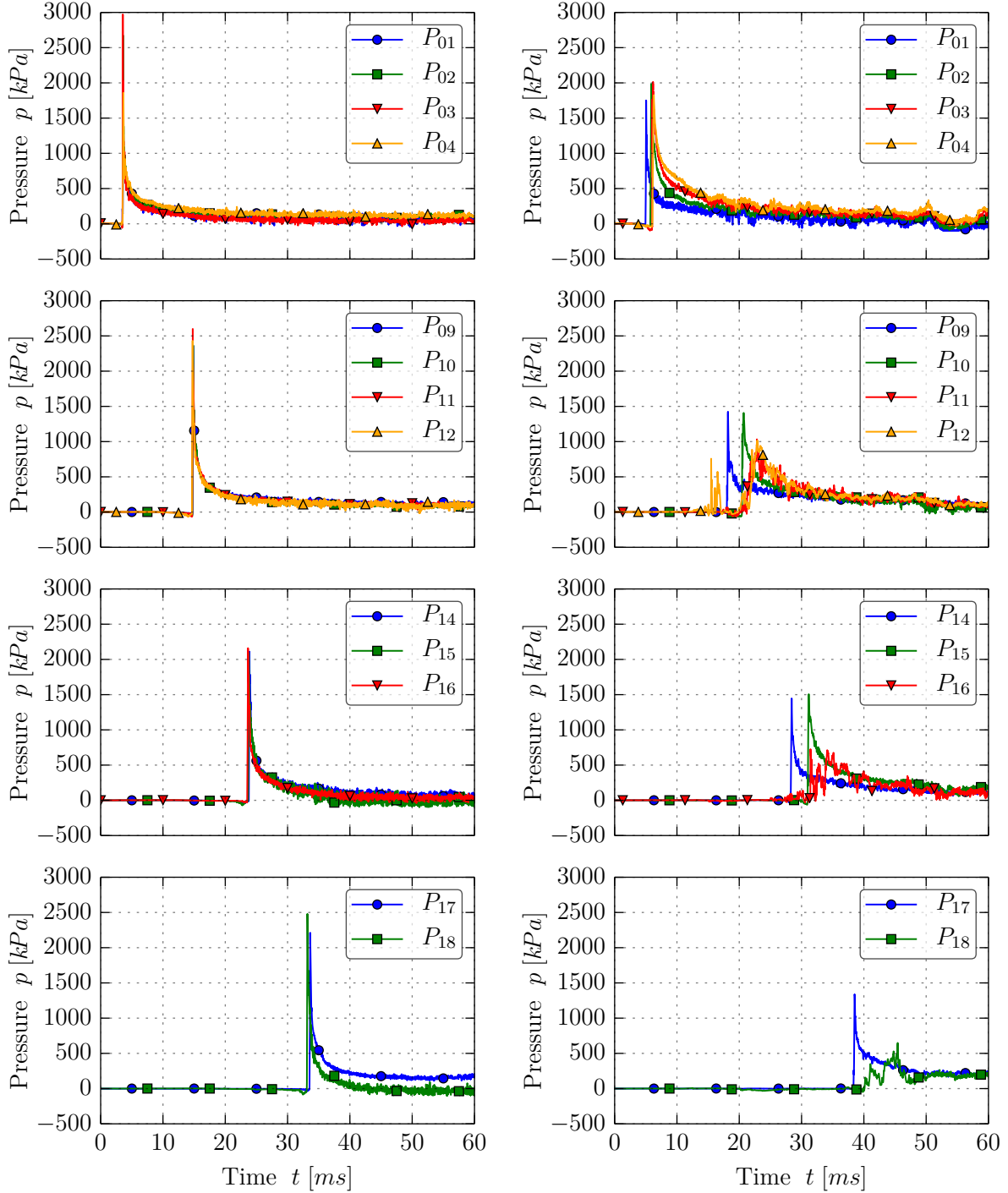# A.5 Supplementary Results: Effects of Structural Deformation

Figure A.3: Pressure time histories of experiments with quasi-rigid (left) and deformable, 3 mm thick aluminum (right) panels at 4° pitch angle and 45 m/s horizontal impact velocity (IDs 1113, 2113).

B Guided Ditching Simulation

B.1 Hard- and Software

In general, Python scripts were used to control all phases of the simulation, e.g. execution of pre-processing, submission of simulation job to computing cluster, execution of post-processing. Below the used hard- and software is briefly presented.

Hardware

Pre-processing and solution were carried out on a computing cluster (12 nodes, each equipped with 2 quad-core 64-bit Intel Xeon E5540 processors, @ 2.53 GHz). Employed settings for the solution are given below. Post-processing was conducted on a standard workstation running Windows. All interaction with the computing cluster was done using the remote clients *Plink* and *Putty*.

Software

Pre-Processing   The pre-processing comprised three parts, which ran fully automated:

1. First, *ANSYS* (version 15.0) was employed to create the model geometry and mesh. This step was based on a parametric *ANSYS* Parametric Design Language (APDL) script that enabled generating models for all test cases required.

2. Next, a DLR in-house converter was used to transform the mesh file from *ANSYS* to *VPS* input format.

3. Finally, specific Python scripts were executed to generate larger *VPS* inputs such as the ones required for the attachment of numerical pressure probes to the structure as well as for the definition of output variables (e.g. elements for strain field analysis). All other *VPS* input cards were set up in a generic, modular manner in separate files, which permitted to use identical inputs for all simulations. Varied parameters were accounted for by using variables that were automatically provided by the *ANSYS* script.

Solution All simulations presented in this work were performed with a development version of the commercial, explicit finite element solver *Virtual Performance Solution* (*VPS*, formerly called *PAM-CRASH*), which itself is based on solver version 2010. The used job settings on the computational cluster were:

- 8 CPUs in shared memory processing mode (one full node on the present cluster)

- single precision mode

Post-Processing Time history outputs (.THP files) were processed using a comprehensive set of individual Python scripts controlled by one main Python script for post-processing. These scripts extract the data using template files that are fed to *Visual Viewer* (ESI Group) running in batch mode. Data were finally plotted against other numerical results and experimental data for comparison.

The contour plots (.DSY files) were evaluated interactively using *Visual Viewer*.

B.2 Material Input Data

Metallic Panels

Generic Al2024 material data employed to model the aluminum panels made of alloys Al2024-T351 (15 mm panels) and Al2024-T3 (3 mm and 0.8 mm panels) are given below. These data were not established based on the specific panels used for the guided ditching test campaign.

- boundary reinforcement of 0.8 mm panels: 54 mm wide, 3 mm thick, glued

- density $\rho = 2.8 \cdot 10^{-6}$ kg/mm^3 and Poisson ratio $\nu = 0.33$
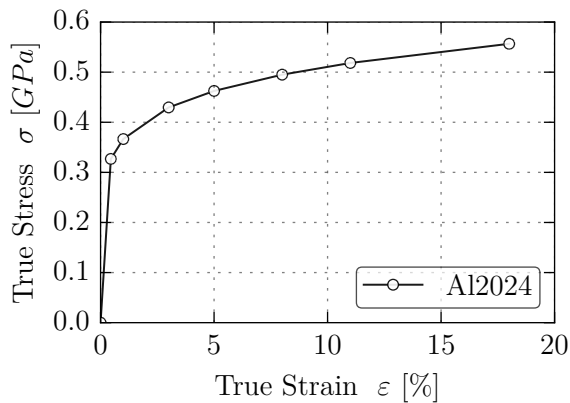
E [GPa]	σ [GPa]	ε [%]
72.1400	0.3268	0.453
7.2470	0.3665	1.000
3.1540	0.4296	3.000
1.6460	0.4625	5.000
1.0840	0.4950	8.000
0.7776	0.5183	11.000
0.5465	0.5566	18.000

Figure B.1: Stress-strain material data for Al2024.

Composite Panels

Material data for the composite panels were obtained from coupon tests of unidirectional specimens conducted by CIRA during the SMAES project. The specimens were made of the prepreg system of carbon fibers AS4 and epoxy resin 8552 manufactured and distributed by Hexcel. The employed composite panel and material data are summarized below.

- 11 layers in stacking (45/90/-45/0/-45/0/45/0/-45/90/45) with a total thickness of 1.65 mm (0.15 mm per layer)

- boundary reinforcement: 54 mm wide, 1.65 mm thick (inverse stacking), attached to panel via secondary bonding

- density $\rho = 1.4 \cdot 10^{-6}$ kg/mm^3

Table B.1: Material data for AS4/8552.

	E_{11} [GPa]	E_{22} [GPa]	E_{33} [GPa]
Tension	137.80	9.23	9.23
Compression	125.20	9.65	9.65
	G_{12} [GPa]	G_{23} [GPa]	G_{13} [GPa]
Tension	5.03	4.03	5.03
Compression	5.03	4.03	5.03
	ν_{12} [-]	ν_{23} [-]	ν_{13} [-]
Tension	0.330	0.147	0.330
Compression	0.330	0.147	0.330

B.3 Results with Two-Phase Cavitation Model

The two-phase model briefly introduced in Section 4.3.1.4 is employed to demonstrate its effects on the simulation results. It allows representing the fluid as a homogeneous mixture of water and air. The main parameter of the model affecting the results is the initial gas volume fraction α_0, which reduces the fluid density. As there is no reference input data for this parameter, it is chosen to be 2% or 4% for the illustration below. Physical input parameters are set to default values from literature assuming a standard atmosphere at a temperature of 10 ℃. The limiting pressure p_{lim} is a pure numerical parameter included to prevent numerical instability. Evaporation and condensation coefficients are empirical parameters recommended by Singhal et al. [136]. Specific simulation settings in addition to those described in Chapter 4 are summarized in Tab. B.2.

Presented results refer to a quasi-rigid test case with a flat panel impacting at 6° pitch angle and 40 m/s horizontal impact velocity (ID 1122). The solution with the two-phase cavitation model takes about 5% longer than the reference simulation with single-phase model. Simulation results reveal an influence on the force time history in terms of a smaller initial slope when increasing the initial gas volume fraction. After approximately 20 ms, the curves are nearly identical. Toward the end of the impact, which is defined by the sharp drop of the normal force upon leading edge immersion, simulations with a higher gas volume fraction show a later drop together with slightly larger maximum forces. This indicates that the fluid propagates slower along the panel compared to the single-phase reference case. In addition, strain results confirm the identified delay of the fluid propagation along the panel as a strong effect on the timing can be observed. Strain magnitudes do not significantly change, yet peak strain values are minimally higher for cases with larger initial gas volume fraction.

Table B.2: Specific simulation inputs for studies on two-phase fluid material data.

| Parameter	Symbol	Value	Unit
Density of liquid phase	ρ_l	$1000 \cdot 10^{-9}$	kg/mm^3
Density of gas phase	ρ_g	$1.247 \cdot 10^{-9}$	kg/mm^3
Initial gas volume fraction	$\alpha_{g,0}$	$0.02 - 0.04$	-
Minimal gas volume fraction	$\alpha_{g,min}$	$1 \cdot 10^{-4}$	-
Isentropic exponent (gas)	κ	1.4	-
Atmospheric pressure	p_{atm}	$101.3 \cdot 10^{-6}$	GPa
Limiting pressure	p_{lim}	$1 \cdot 10^{-1}$	GPa
Vapor pressure	p_v	$1227 \cdot 10^{-9}$	GPa
Surface tension	σ	$74.2 \cdot 10^{-9}$	kN/mm
Evaporation coefficient	C_e	0.02	-
Condensation coefficient	C_c	0.01	-
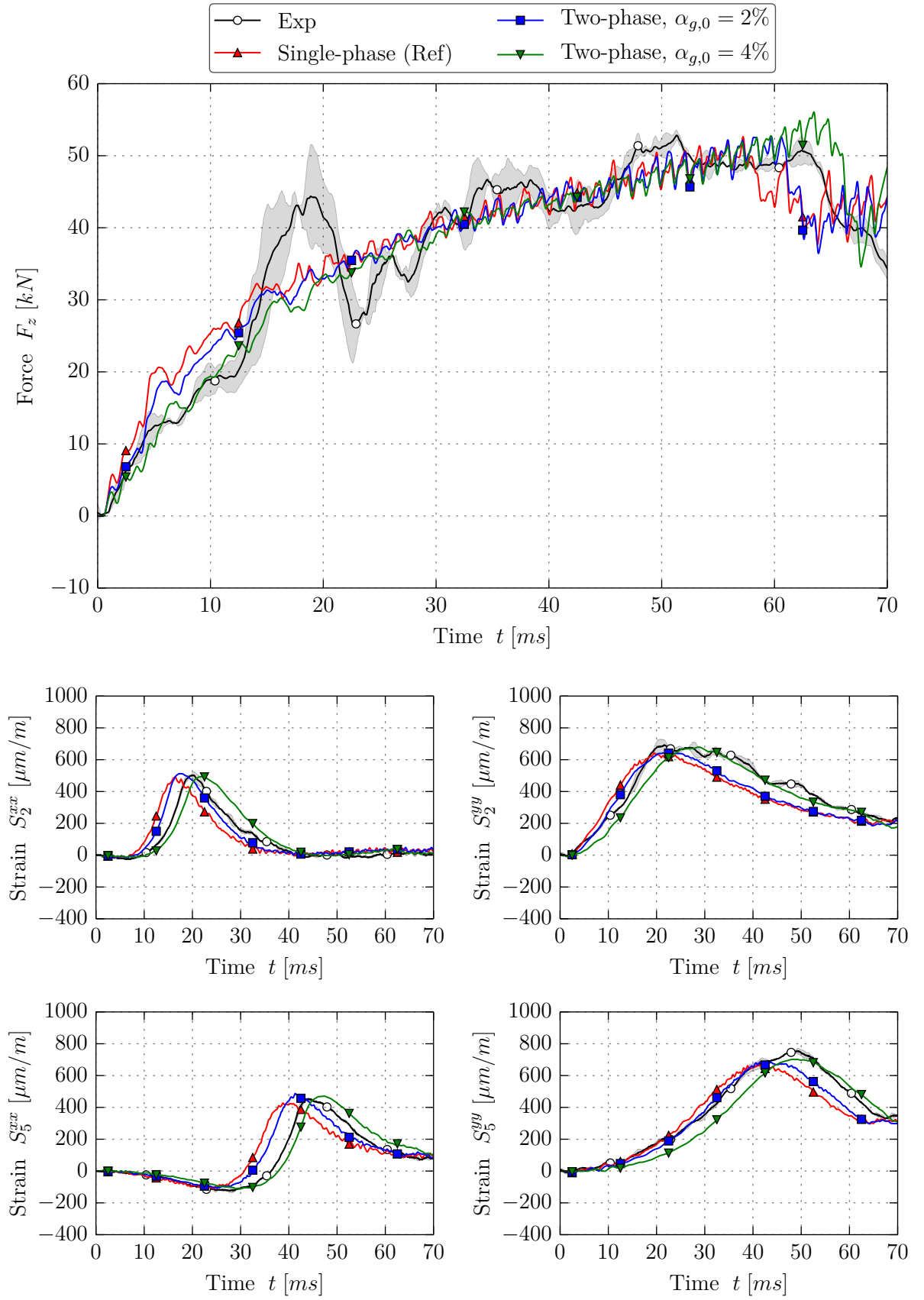
Figure B.2: Comparison of normal forces (top) and exemplary strains (bottom) for simulations with single phase and two-phase fluid material model with experimental data.

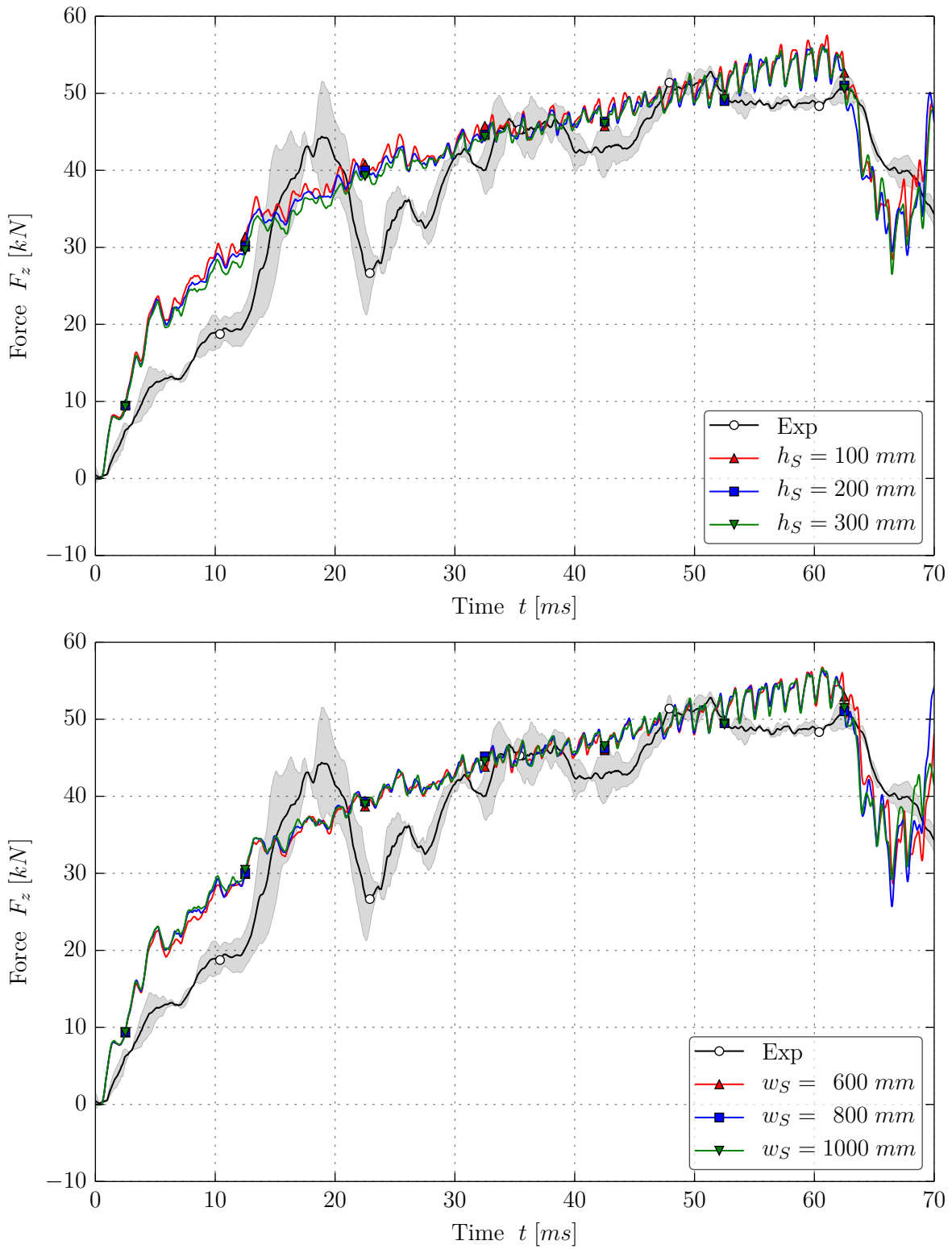## B.4 Results of SPH Domain Size Investigation

Figure B.3: Comparison of normal forces for different SPH domain heights h_S (top) and widths w_S (bottom) with experimental data.

B.5 Results of SPH Resolution Study in 2D

In order to further study the effects related to the particle resolution, a 2D model of a flat rigid plate impact is used for illustration. Test conditions refer to the guided ditching test case 1132, i.e. 10° pitch angle and 40 m/s horizontal impact velocity. Figure B.4 illustrates the jet root shape and its approximate location for simulations with different SPH resolutions defined by the initial particle spacing ds. In addition, Tab. B.3 documents the approximate jet root location x_{jr} measured from the plate's trailing edge for the studied cases.

Based on presented results, the particle size is found to affect the timing of the loading as the jet root advances slower for cases with smaller particles. Note that the case with 20 mm spacing is excluded from this conclusion as it fails to capture the characteristic flow field in the 2D simulation.
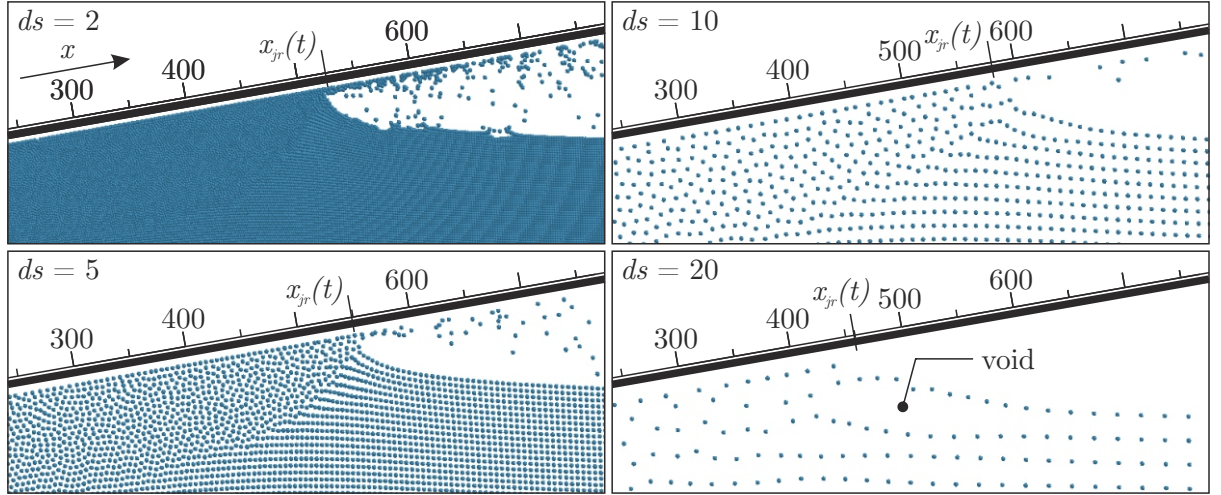

Figure B.4: Zoom on jet root zone for different particle resolutions in 2D model. All measures in mm.

Table B.3: Effect of particle resolution on flow field kinematics.

Particle spacing ds [mm]	Jet root location $x_{jr}(t = 25\,ms)$ [mm]	Comments
2	525	proper flow field kinematics
5	550	proper flow field kinematics
10	580	onset of spray
20	460	fails to capture flow field kinematics

B.6 Non-Uniform Particle Distributions

This section provides additional information regarding the developed capabilities to generate and evaluate non-uniform particle distributions based on the EWVT algorithm. Furthermore, exemplary results of verification and validation studies are presented. The shown test cases are two-dimensional for the ease of illustration.

Exemplary distributions   In order to illustrate the capabilities of the EWVT algorithm, Fig. B.5 shows exemplary particle distributions in two and three dimensions with different resolution gradients.
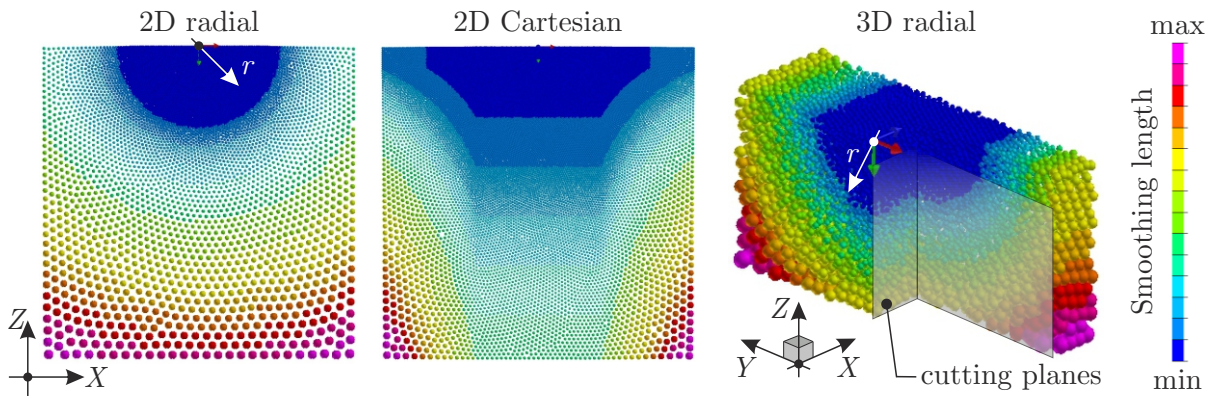
Figure B.5: Exemplary 2D distributions with different gradients in radial (left) and two Cartesian directions (center) and 3D distribution with gradient in radial direction (right).

Quality Assessment: SPH Inertia Tensor   Similar to the inertia tensor in classical mechanics, an SPH inertia tensor $\mathbf{I}$ may be defined. For particle i with neighboring particles j and directions $a,b \in x,y,z$ it is expressed as

$$\mathbf{I_i} = \begin{pmatrix} I_i^{xx} & I_i^{xy} & I_i^{xz} \\ I_i^{yx} & I_i^{yy} & I_i^{yz} \\ I_i^{zx} & I_i^{zy} & I_i^{zz} \end{pmatrix} \qquad \text{with} \qquad I_i^{ab} = \sum_j \frac{m_j}{\rho_j} \left(\mathbf{r}_i^a - \mathbf{r}_j^a \right) \left(\mathbf{r}_i^b - \mathbf{r}_j^b \right) W_{ij} \,. \qquad (\text{B.1})$$

The eigenvalues λ of the tensor $\mathbf{I}$ may be used to assess the isotropy of a particle distribution. They are calculated by solving the system

$$0 = \det \left(\mathbf{I} - \lambda \mathbf{U} \right) \,, \qquad (\text{B.2})$$

where $\mathbf{U}$ is the unit matrix, i.e. $\mathbf{U} = diag(1)$. Assuming a constant material density and an ideal isotropic distribution, all eigenvalues are equal and hence the ratio Λ of the lowest to the highest eigenvalue, $\lambda_{min}/\lambda_{max}$, is equal to unity. In contrast, Λ approaches zero for increasingly non-isotropic distributions because the eigenvalues are increasingly different.

The quality of a particle distribution can, therefore, be assessed by regarding the spatial distribution (contour plot) or the minimum of the ratio Λ of eigenvalues as exemplarily illustrated in Fig. B.6 for a 2D particle distribution. Apart from the boundaries of the computational domain, high-quality particle distributions yield a homogeneous distribution of Λ with values approaching unity. Remaining discrepancies, which are due to the finite number of iterations, are negligible.
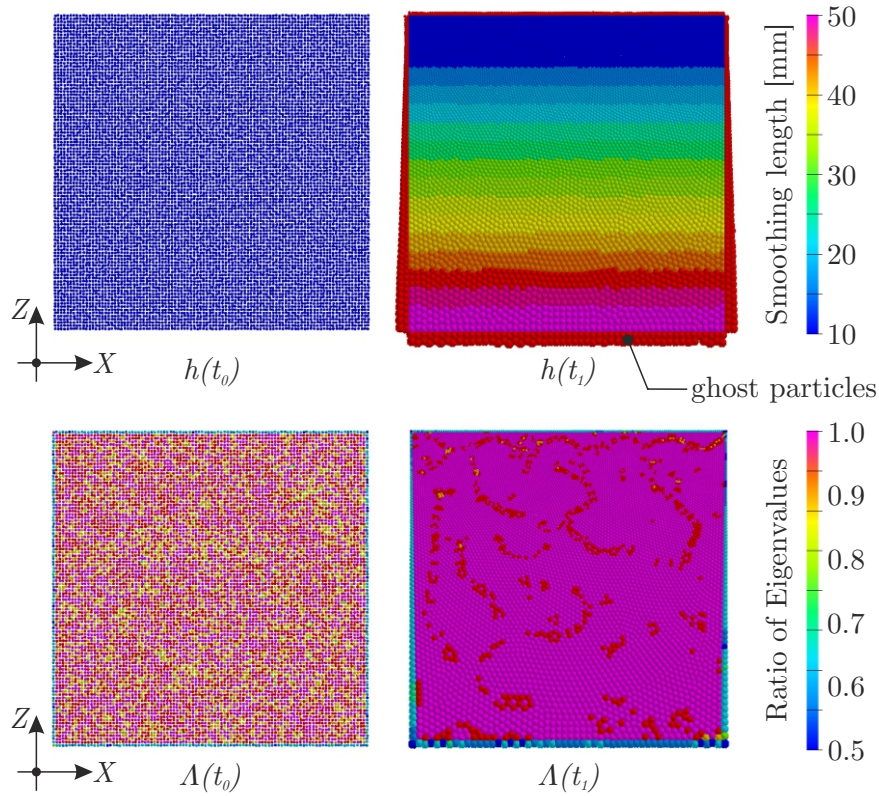

Figure B.6: Non-uniform particle distribution with gradient in *Z*-direction generated using the EWVT algorithm. The initial distribution (left) is based on a cubic lattice with small additional displacements in random direction. The final distribution is shown on the right. Ghost particles exemplarily depicted in the top right image are hidden elsewhere.

Validation and Verification   A common benchmark test case for water impact simulations is that of Zhao and Faltinsen [166]. It consists of a rigid wedge with a horizontal width of $b_w = 5.5$ m that symmetrically impacts on a smooth water surface at a constant vertical velocity of $v_Z = -5$ m/s. Here the case with a deadrise angle of $20°$ is selected for the simulation using a non-uniform initial particle distribution. The impact generates a large displacement of the fluid and is therefore well suited to investigate the performance of the non-uniform distributions in a simple impact case.

The two-dimensional fluid domain measures 15 m×15 m and features gradients of the particle resolution in two directions as shown in Fig. B.7 (left). In the impact zone, the

particle spacing is kept constant and it is gradually increased towards the boundaries as defined by a combination of two Cartesian functions. The examples shown use a particle spacing of approximately 42 mm in the vicinity of the wedge that increases tenfold toward the bottom corners of the domain. Hence, the non-uniform distribution comprises only 18% of the particles necessary for the reference model with uniformly spaced particles. In order to minimize effects emerging from the boundaries, the SPH domain is bounded by columns of fixed particles located in a range of $2h_{max}$ from the boundaries, where h_{max} refers to the largest smoothing length in the fluid domain. The boundary particles were previously arranged within the same EWVT iteration as the regular fluid particles.

Before simulating the wedge impact, a hydrostatic simulation is performed to assess the stability of the particle distribution under simple gravity loading. On the right hand side of Fig. B.7, the corresponding pressure contour plot after 10 s of simulated time is depicted. The model displays the correct hydrostatic pressure distribution. Furthermore, results show no spurious mixing or artificial flow due to the high quality of the particle distribution. Although this seems trivial, it requires particular care; non-uniform distributions with too large anisotropy and thus a poor eigenvalue ratio Λ were found to quickly lead to unphysical particle motion. Therefore, results demonstrate that the stability of non-uniform distributions is linked to the isotropy of the SPH inertia tensor.
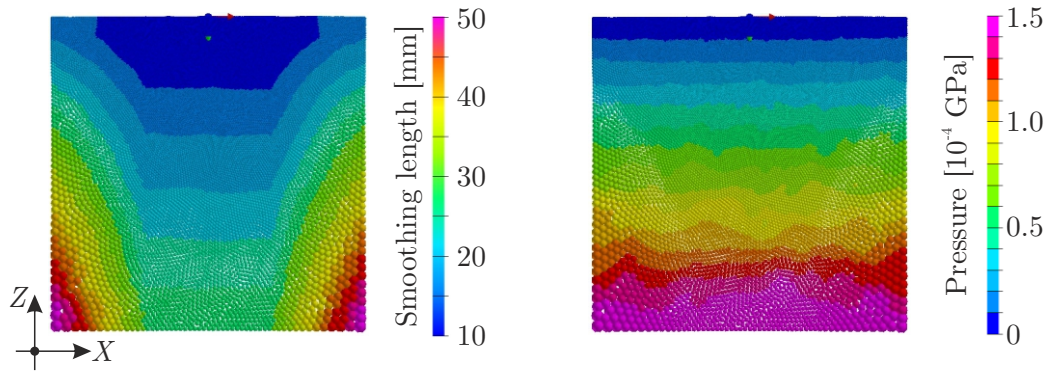

Figure B.7: Contour plots of smoothing length and pressure at $t = 10$ s for hydrostatic tank test case.

Finally, for the wedge impact simulation, the same fluid model is initialized with a hydrostatic pressure distribution. Simulation results verify that despite the large fluid displacement due to the impact no mixing occurs. Figure B.8 shows two exemplary pressure distributions: one at the initial state and one at about half of the immersion. The pressure field during the impact appears reasonable. Quantitative results in terms of normalized vertical forces presented in Fig. B.9 indicate very good agreement between the reference solution of Zhao and Faltinsen [166] and SPH solutions using uniform and non-uniform particle distributions.
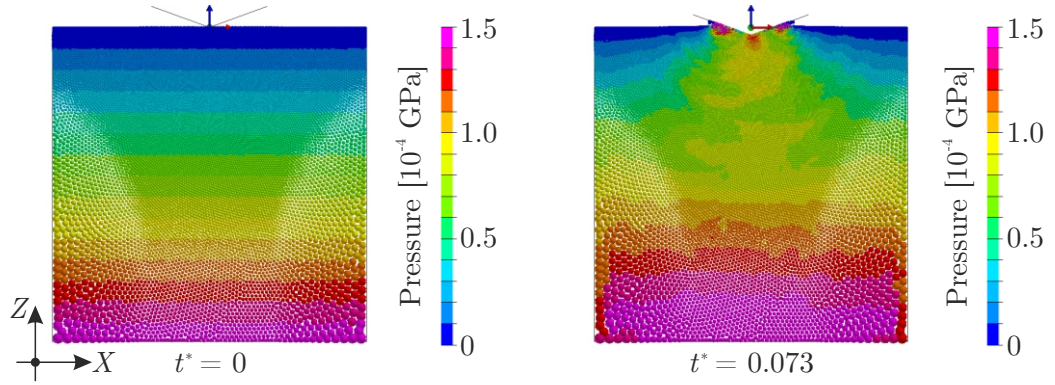
Figure B.8: Contour plots of pressure at $t^* = 0$ (left) and $t^* = 0.073$ (right) for wedge impact test case.
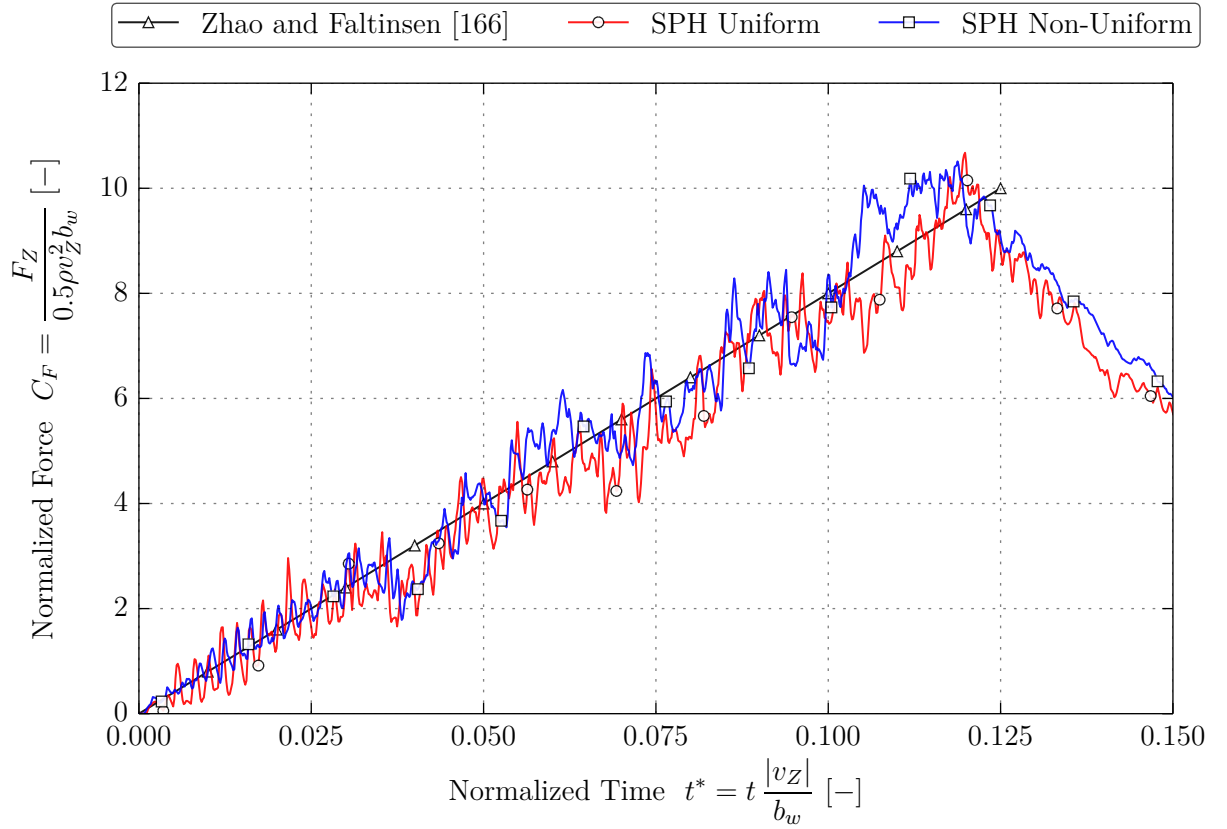

Figure B.9: Comparison of normalized force over normalized time for two SPH solutions and a reference solution from Zhao and Faltinsen [166] for wedge impact test case.

C Validation and Verification Studies
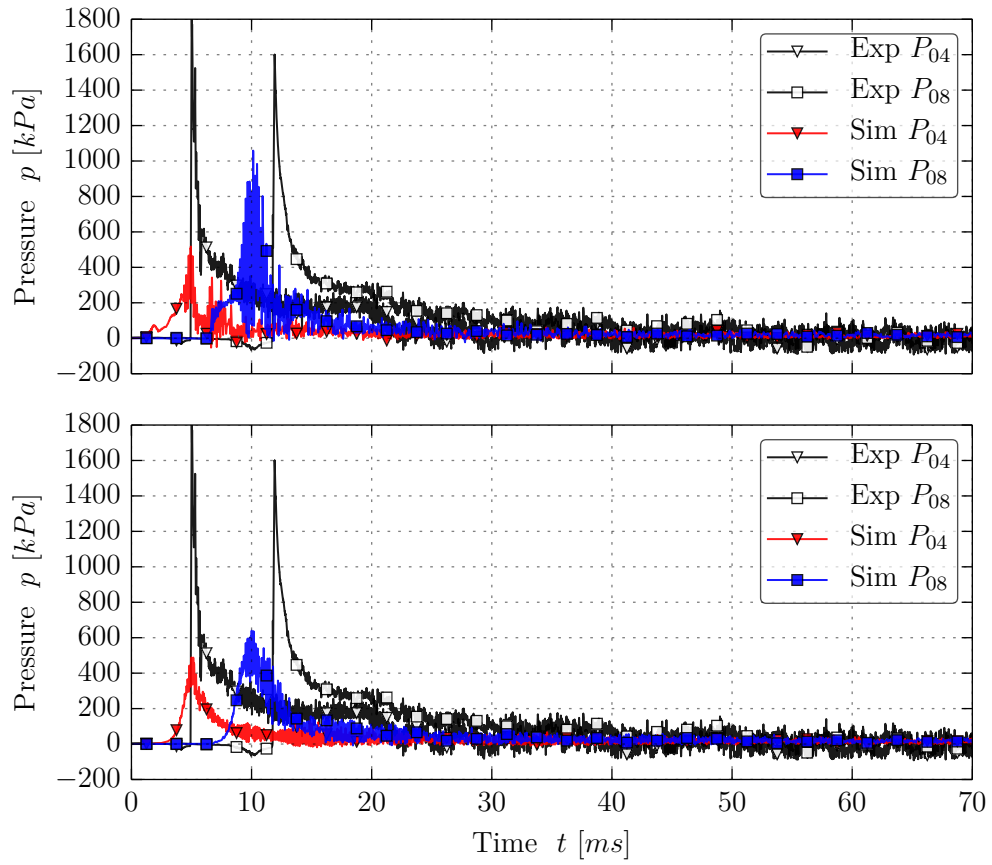
C.1 Exemplary Pressure Time Histories

Figure C.1: Pressure time histories at two gauge locations for test case at 4° pitch angle and 40 m/s horizontal impact velocity (ID 1122). Charts show results using a standard (top) and an enhanced (bottom) SPH formulation.

C.2 Supplemental Results: Parameter Studies

Impact Velocity

Here the curves filtered with the default CFC1000 filter are provided for completeness and to show the extent of oscillations in cases with higher impact velocity.
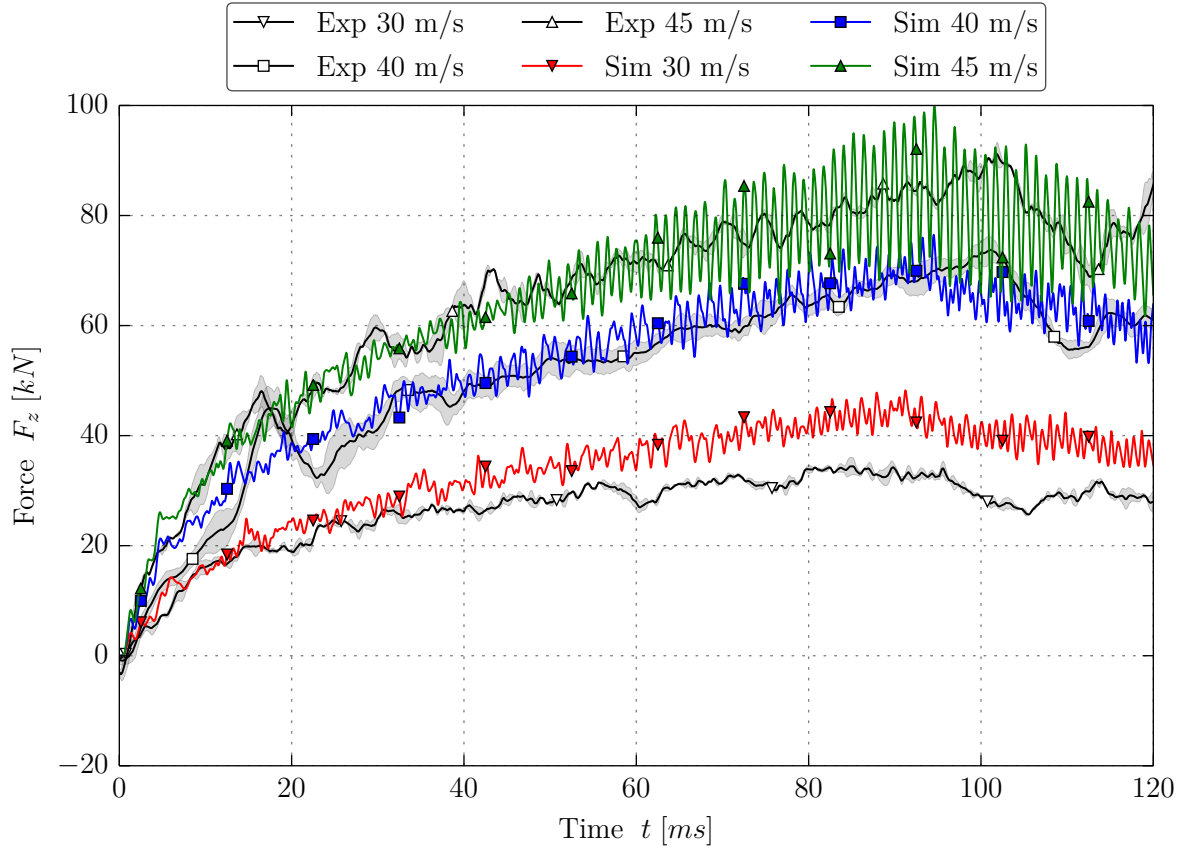

Figure C.2: Force time histories of simulations (CFC1000-filtered) and experiments with different horizontal impact velocities at 10° pitch angle (IDs 1131, 1132, 1133).

Panel Curvature

Figure C.3 shows the evolution of the fluid flow underneath the structure for cases with different lateral panel curvature. Note that for the concave case (right), two fluid jets develop and approach each other toward the inside. Upon penetration of these two fluid jets, the particle disorder increases, which is held responsible for the significantly enlarged force oscillations observed in Fig. 5.5.
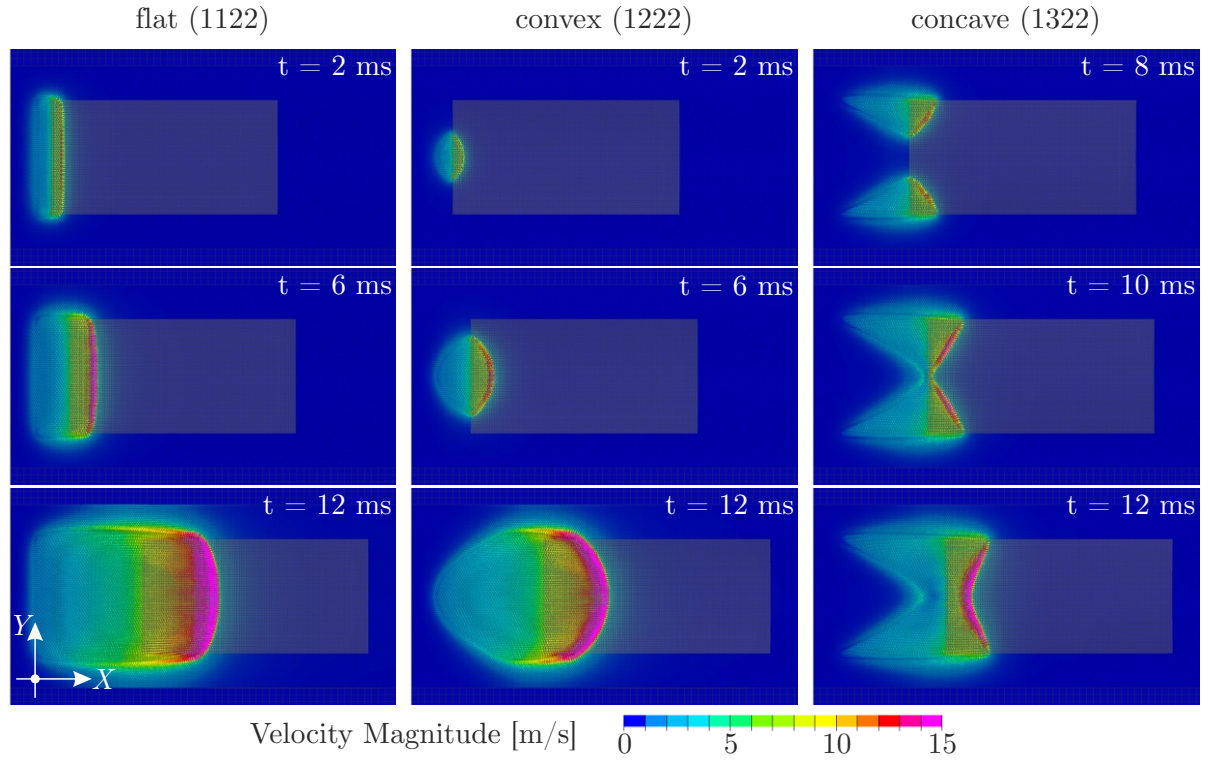

Figure C.3: Contour plots of the velocity field showing the evolution of the fluid flow underneath the structure at different time instants. Note the different times of the contour plots for the concave case.

C.3 Analysis of Panel Deformation

The local displacement of the deformable panels in normal direction (z) was evaluated along the center line ($y = 0$ mm) for all test cases. Figure C.4 shows exemplary results for all panel types at one impact condition ($\alpha = 6°$ and $v_{X,0} = 40$ m/s).
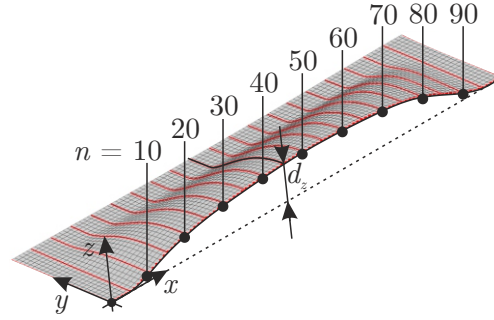
(a) Reference model (deformation amplified $\times 3$).
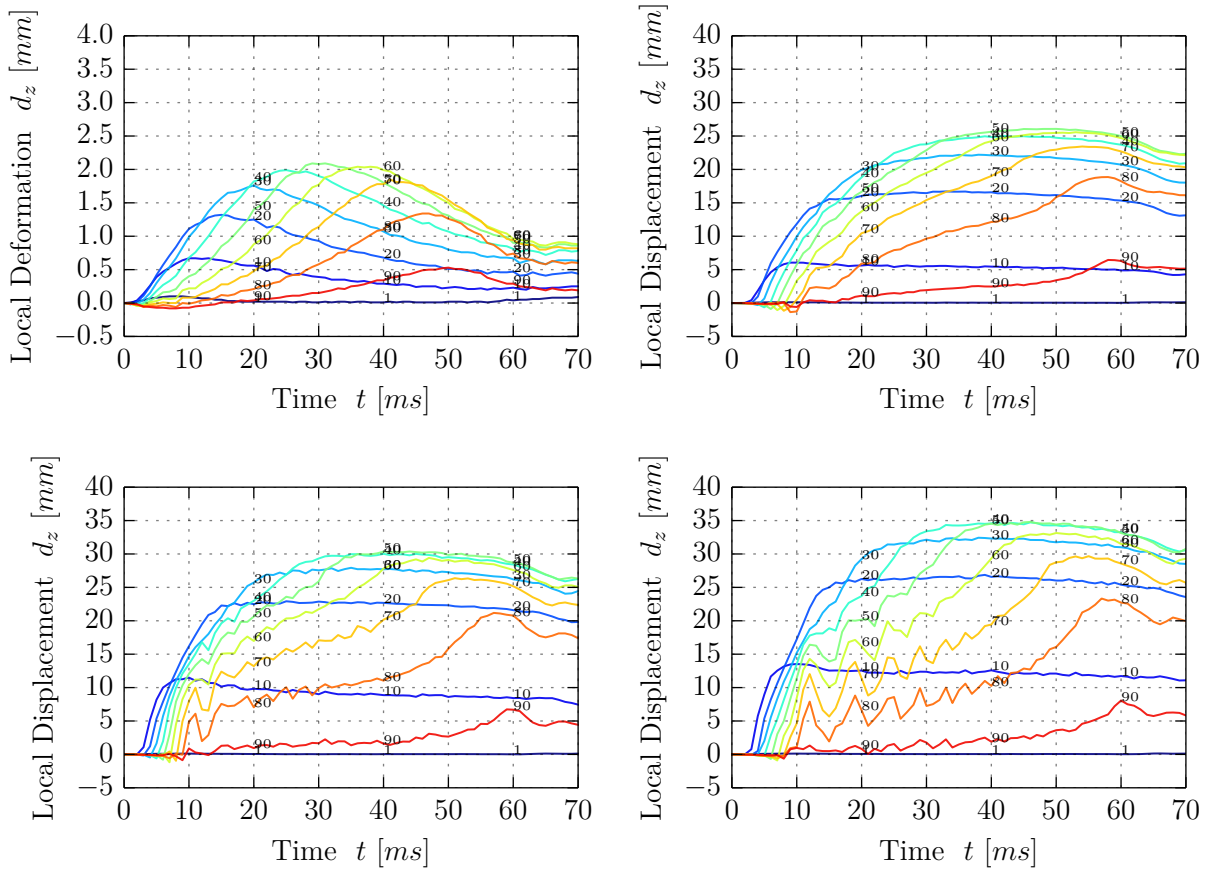
(b) Time histories of local displacement d_z for test cases with quasi-rigid (top left), 3 mm aluminum (top right), composite (bottom left) and 0.8 mm aluminum (bottom right) panels.

Figure C.4: Evaluation of local displacement in normal direction of the panel along center line ($y = 0$ mm).

Bibliography

[1] *Airbus A320 Family - A320*, accessed 14.02.2015, available at http://www.airbus.com/aircraftfamilies/passengeraircraft/a320family/a320/.

[2] *CN235 Photo Gallery*, accessed 14.02.2015, available at http://militaryaircraft-airbusds.com/Multimedia/CN235PhotoGallery.aspx.

[3] O. Aagaard, *Hydroelastic Analysis of Flexible Wedges*, Master thesis, Norwegian University of Science and Technology, 2013.

[4] S. Abrate, *Hull Slamming*, Applied Mechanics Reviews 64 (2013).

[5] Airbus, *US Airways Flight 1549 Accident Investigation*, Tech. Rep., 2009.

[6] M. Anghileri, L.M.L. Castelletti, E. Francesconi, A. Milanese, and M. Pittofrati, *Survey of numerical approaches to analyse the behavior of a composite skin panel during a water impact*, International Journal of Impact Engineering 63 (2014), pp. 43–51.

[7] M. Antuono, A. Colagrossi, S. Marrone, and B. Bouscasse, *Measures of Particle Disorder*, in *8th international SPHERIC workshop*, Trondheim, Norway, 2013.

[8] S.W. Attaway, M.W. Heinstein, and J.W. Swegle, *Coupling of smooth particle hydrodynamics with the finite element method*, Nuclear Engineering and Design 150 (1994), pp. 199–205.

[9] D.A. Barcarolo, *Improvement of the Precision and the Efficiency of the SPH Method: Theoretical and Numerical Study*, Ph.D. thesis, Ecole Centrale de Nantes, 2013.

[10] G.K. Batchelor, *An Introduction to Fluid Dynamics*, Cambridge University Press, 1967.

[11] L. Benítez Montañés, H. Climent Máñez, M. Siemann, and D. Kohlgrueber, *Ditching Numerical Simulations: Recent Steps in Industrial Applications*, in *Aerospace Structural Impact Dynamics International Conference*, Wichita, USA, 2012.

[12] W. Benz, *Smooth Particle Hydrodynamics: A Review*, The Numerical Modelling of Nonlinear Stellar Pulsatations (1990), pp. 269–288.

[13] B. Bouscasse, A. Colagrossi, S. Marrone, and M. Antuono, *Nonlinear water wave interaction with floating bodies in SPH*, Journal of Fluids and Structures 42 (2013), pp. 112–129.

[14] J. Campbell, *Prediction of aircraft structural response during ditching: An overview of the SMAES project*, in *Aerospace Structural Impact Dynamics International Conference*, Wichita, USA, 2012.

[15] J. Campbell and R. Vignjevic, *Simulating Structural Response to Water Impact*, International Journal of Impact Engineering 49 (2012), pp. 1–10.

[16] J. Campbell, R. Vignjevic, and L. Libersky, *A contact algorithm for smoothed particle hydrodynamics*, Computer Methods in Applied Mechanics and Engineering 184 (2000), pp. 49–65.

[17] C. Capone, *Numerical Simulation of Fluid-Structure Interaction comparing SPH and ALE Approaches*, in *Sixth Pegasus-AIAA Student Conference*, Seville, Spain, 2010, pp. 1–11.

[18] B.K. Cartwright, A. Chhor, and P.H.L. Groenenboom, *Numerical Simulation of a Helicopter Ditching with Emergency Flotation Devices*, in *5th international SPHERIC workshop*, Manchester, UK, 2010.

[19] F. Casadei, M. Larcher, and N. Leconte, *Strong and Weak Forms of a Fully Nonconforming FSI Algorithm in Fast Transient Dynamics for Blast Loading of Structures*, in *3rd International Conference on Computational Methods in Structural Dynamics and Earthquake Engineering*, 2012, pp. 1120–1139.

[20] S.L. Chuang, *Slamming of rigid wedge-shaped bodies with various deadrise angles*, Tech. Rep. October, Structural Mechanics Laboratory, Navy, Washington, D. C., USA, 1966.

[21] P.W. Cleary and J.J. Monaghan, *Conduction Modelling Using Smoothed Particle Hydrodynamics*, Journal of Computational Physics 148 (1999), pp. 227–264.

[22] H. Climent, L. Benítez, F. Rosich, F. Rueda, and N. Pentecôte, *Aircraft Ditching Numerical Simulation*, in *25th International Congress of the Aeronautical Sciences*, Hamburg, Germany, 2006.

[23] CNR-INSEAN, *Towing Tanks*, accessed 14.02.2015, available at http://www.insean.cnr.it/en/content/towing-tanks.

[24] T. De Vuyst, R. Vignjevic, and J. Campbell, *Coupling between meshless and finite element methods*, International Journal of Impact Engineering 31 (2005), pp. 1054–1064.

[25] L. Delorme, *Sloshing Flows: Experimental Investigation and Numerical Simulations with Smoothed Particle Hydrodynamics*, Ph.D. thesis, Universidad Politecnica de Madrid, 2008.

[26] D. Delsart, B. Langrand, and A. Vagnot, *Evaluation of an Euler/Lagrange coupling method for the ditching simulation of helicopter structures*, in *5th International Conference on Fluid Structure Interaction*, Royal Mare Village, Crete, Greece, 2009.

[27] D. Delsart, N. Toso-Pentecôte, A. Vagnot, L. Castelletti, U. Mercurio, and S. Alguadich, *Fluid/structure interaction analysis Smooth Particle Hydrodynamic method*, in *8th International Conference on Advances in Fluid Mechanics*, Algarve, Portugal, 2010.

[28] S. Diehl, G. Rockefeller, C.L. Fryer, D. Riethmiller, and T.S. Statler, *Generating Optimal Initial Conditions for Smooth Particle Hydrodynamics Simulations*, Preprint submitted to Mon. Not. R. Astron. Soc. (2012).

[29] J. Donea, A. Huerta, J.P. Ponthot, and A. Rodríguez-Ferran, *Chapter 14: Arbitrary Lagrangian-Eulerian Methods*, in *Encyclopedia of Computational Mechanics*, E. Stein, R. de Borst, and T.J. Hughes, eds., 1st ed., JohnWiley & Sons, Ltd., 2004.

[30] EASA, *Certification Review Item - Structural Ditching Conditions*, Tech. Rep., EASA, Cologne, Germany, 2012.

[31] EASA, *Certification Specifications and Acceptable Means of Compliance for Large Aeroplanes CS-25/Amdt 15*, Tech. Rep., EASA, Cologne, Germany, 2014.

[32] P.M. Edge Jr., *Impact-Loads Investigation of Chine-Immersed Model having a Circular-Arc Transverse Shape*, Tech. Rep., NACA, Langley Field, Virginia, USA, 1957.

[33] P.M. Edge Jr., *Impact-Loads Investigation of Chine-Immersed Models Having Concave-Convex Transverse Shape and Straight or Curved Keel Lines - TN 3940*, Tech. Rep., Langley Field, Virginia, USA, 1957.

[34] P.M. Edge Jr., *Hydrodynamic Impact Loads of a -20 Degrees Dead-Rise Inverted-V Model and Comparisons with Loads of a Flat-Bottom Model*, Tech. Rep., NACA, Langley Field, Virginia, USA, 1958.

[35] P.M. Edge Jr. and J.S. Mixson, *Impact-Loads Investigation of a Chine-Immersed Model Having a Longitudinal Curved Bow and a V-Bottom with a Dead-Rise Angle of 30 Degrees - TN 4106*, Tech. Rep., NACA, Langley Field, Virginia, USA, 1957.

[36] ESI Group, *Virtual Performance Solution 2010: Explicit Solver Refrence Manual* (2010).

[37] ESI Group, *Virtual Performance Solution 2010: Solver Notes Manual* (2010).

[38] European Commission, *Commission Regulation (EC) No 859/2008 of 20 August 2008 amending Council Regulation (EEC) No 3922/91 as regards common technical requirements and administrative procedures applicable to commercial transportation by aeroplane*, Official Journal of the European Union (2008).

[39] O.M. Faltinsen, *Hydrodynamics of High-Speed Marine Vehicles*, Cambridge University Press, 2005.

[40] J.T. Fedok, *NTSB Factual Report on Survival Factors of Hudson River Water Impact Accident*, Tech. Rep., NTSB, Washington, D. C., USA, 2009.

[41] J. Feldman, *Dynamic refinement and boundary contact forces in Smoothed Particle Hydrodynamics with applications in fluid flow problems*, Ph.D. thesis, University of Wales Swansea, 2006.

[42] L.J. Fisher and E.L. Hoffman, *Model ditching investigation of the Douglas DC-4 and DC-6 airplanes*, Tech. Rep., NACA, Langley Air Force Base, Virginia, USA, 1949.

[43] L.J. Fisher and E.L. Hoffman, *Ditching investigations of dynamic models and effect of design parameters on ditching characteristics, Report 1347*, Tech. Rep., NACA, 1957.

[44] L.J. Fisher and G.J. Morris, *Ditching Tests of a 1/18-scale Model of the Lockheed Constellation Airplane*, Tech. Rep., NACA, Langley Air Force Base, Virginia, USA, 1948.

[45] L.J. Fisher and M.F. Steiner, *Ditching Tests with a 1/16-size Dynamic Model of the Army B-24 Airplane in Langley Tank No. 2 and on an Outdoor Catapult*, Tech. Rep., NACA, Langley Field, Virginia, USA, 1945.

[46] L.J. Fisher and W.C. Thompson, *Ditching Tests of a 1/18-scale Model of the Lockheed Constellation Airplane with Speedpack Attached*, Tech. Rep., Langley Air Force Base, Virginia, USA, 1949.

[47] G. Fourey, G. Oger, D. Le Touzé, and B. Alessandrini, *Violent Fluid-Structure Interaction simulations using a coupled SPH/FEM method*, IOP Conference Series: Materials Science and Engineering 10 (2010), pp. 1–9.

[48] E. Francesconi and M. Anghileri, *A Numerical-Experimental Investigations on Crash Behaviour of Skin Panels during a Water Impact Comparing ALE and SPH Approaches*, in *7th European LS-DYNA Conference*, Salzburg, Austria, 2009.

[49] E. Francesconi, M. Pittofrati, M. Anghileri, L.M.L. Castelletti, and A. Milanese, *Helicopter Water Landing Adopting Coupled Rigid Body/SPH and Coupled Rigid Body/ALE Approaches*, in *IKUS6*, Stuttgart, Germany, 2006.

[50] D.A. Fulk, *A Numerical Analysis of Smoothed Particle Hydrodynamics*, Ph.D. thesis, Air Force Institute of Technology Air University, 1994.

[51] R.A. Gingold and J.J. Monaghan, *Smoothed particle hydrodynamics - Theory and application to non-spherical stars*, Monthly Notices of the Royal Astronomical Society 181 (1977), pp. 375–389.

[52] J. Gobeltz and P. Gythiel, *Rapport sur les essais d'amerrissage forcé sur bassin d'une maquette au 1/16éme de l'avion MERCURE. (Water-Tank Tests of the Water-Landing Forces on a 1/16 Scale Model of the Mercure Aircraft), Report No. 74-5*, Tech. Rep., IMF, Lille, France, 1974.

[53] A. Grimaldi, D.J. Benson, F. Marulo, and M. Guida, *Steel Structure Impacting onto Water: Coupled Finite Element-Smoothed-Particle-Hydrodynamics Numerical Modeling*, Journal of Aircraft 48 (2011), pp. 1299–1308.

[54] P.H.L. Groenenboom, *New features and applications of the hybrid SPH/FE approach in PAM-CRASH*, in *3rd international SPHERIC workshop*, Lausanne, Switzerland, 2008, pp. 249–255.

[55] P.H.L. Groenenboom, *A unified view of SPH wall boundary conditions and particle motion correction methods*, in *6th SPHERIC workshop*, Hamburg, Germany, 2011.

[56] P.H.L. Groenenboom, *SPH for two-phase fluid flow including cavitation*, in *7th international SPHERIC workshop*, Prato, Italy, 2012, pp. 333–339.

[57] P.H.L. Groenenboom, *Particle Filling and the Importance of the SPH Inertia Tensor*, in *9th international SPHERIC workshop*, Paris, France, 2014, pp. 185–191.

[58] P.H.L. Groenenboom and B.K. Cartwright, *Hydrodynamics and fluid-structure interaction by coupled SPH-FE method*, Journal of Hydraulic Research 48 (2010), pp. 61–73.

[59] P.H.L. Groenenboom and B.K. Cartwright, *SPH Simulations of Free Surface Waves and the Interaction with Objects*, in *5th European Conference on Computational Fluid Dynamics*, June, Lisbon, Portugal, 2010.

[60] P.H.L. Groenenboom and B.K. Cartwright, *Pressure-corrected SPH with innovative particle regularization algorithms and non-uniform, initial particle distributions*, in *8th international SPHERIC workshop*, Trondheim, Norway, 2013.

[61] P.H.L. Groenenboom and M.H. Siemann, *Fluid-structure interaction by the mixed SPH-FE method with application to aircraft ditching*, The International Journal of Multiphysics 9 (2015), pp. 249–265.

[62] P.H.L. Groenenboom, J. Campbell, L. Benítez Montañés, and M. Siemann, *Innovative SPH Methods for Aircraft Ditching*, in *WCCM XI - ECCM V - ECFD VI*, Barcelona, Spain, 2014, pp. 4555–4566.

[63] W. Gropengiesser and T. Rung, *Real-time Simulation of Aircraft Ditching Using Enhanced Potential Flow Methods*, in *2nd International Conference on Violent Flows*, Nantes, France, 2012.

[64] B. Guo, P. Liu, Q. Qu, and J. Wang, *Effect of pitch angle on initial stage of a transport airplane ditching*, Chinese Journal of Aeronautics 26 (2013), pp. 17–26.

[65] S. Heimbs, *Computational methods for bird strike simulations: A review*, Computers and Structures 89 (2011), pp. 2093–2112.

[66] D.A.P. Hersman, C.A. Hart, and R.L. Sumwalt, *Loss of Thrust in Both Engines After Encountering a Flock of Birds and Subsequent Ditching on the Hudson River US Airways Flight 1549*, Tech. Rep., NTSB, Washington, D. C., USA, 2010.

[67] S.J. Hiermaier, *Structures Under Crash and Impact: Continuum Mechanics, Discretization and Experimental Characterization*, Springer, 2008.

[68] S. Hradecky, *Accident: Lionair B738 at Denpasar on Apr 13th 2013, landed short of runway and came to stop in sea*, 2013, accessed 12.08.2014, available at http://avherald.com/h?article=460aeabb.

[69] F.J. Huera-Huarte, D. Jeon, and M. Gharib, *Experimental investigation of water slamming loads on panels*, Ocean Engineering 38 (2011), pp. 1347–1355.

[70] K. Hughes, *Application of improved Lagrangian techniques for helicopter crashworthiness on water*, Ph.D. thesis, Cranfield University, 2005.

[71] K. Hughes and J. Campbell, *Helicopter crashworthiness : a chronological review of water impact related research from 1982 to 2006*, Journal of American Helicopter Society 53 (2008), pp. 429–442.

[72] K. Hughes, R. Vignjevic, and J. Campbell, *Experimental observations of an 8 m/s drop test of a metallic helicopter underfloor structure onto a hard surface: part 1*, Journal of Aerospace Engineering 221 (2007), pp. 661–678.

[73] K. Hughes, R. Vignjevic, and J. Campbell, *Experimental observations of an 8 m/s drop test of a metallic helicopter underfloor structure onto water: part 2*, Journal of Aerospace Engineering 221 (2007), pp. 679–690.

[74] K. Hughes, R. Vignjevic, J. Campbell, T. DeVuyst, N. Djordjevic, and L. Papagiannis, *From Aerospace to Offshore: Bridging the Numerical Simulation Gaps*, International Journal of Impact Engineering 61 (2013), pp. 48–63.

[75] T.J.R. Hughes and T.E. Tezduyar, *Finite Elements Based Upon Mindlin Plate Theory With Particular Reference to the Four-Node Bilinear lsoparametric Element*, Journal of Applied Mechanics 48 (1981).

[76] H. Huth, *Influence of Fastener Flexibility on the Prediction of Load Transfer and Fatigue Life for Multiple-Row Joints*, in *Fatigue in Mechanically Fastened Composite and Metallic Joints*, 1985, pp. 221–250.

[77] A. Iafrati, *Experimental investigation of the water entry of a rectangular plate at high horizontal velocity*, Journal of Fluid Mechanics 799 (2016), pp. 637–672.

[78] A. Iafrati, M.H. Siemann, and L. Benítez Montañés, *Experimental study of high speed plate ditching*, in *29th IWWWFB*, Osaka, Japan, 2014.

[79] A. Iafrati, S. Grizzi, M. Siemann, and L. Benítez Montañés, *Experimental analysis of the water entry of a plate at high horizontal speed*, in *30th Symposium on Naval Hydrodynamics*, Hobart, Tasmania, 2014.

[80] A. Iafrati, S. Grizzi, M.H. Siemann, and L. Benítez Montañés, *High-speed ditching of a flat plate: Experimental data and uncertainty assessment*, Journal of Fluids and Structures 55 (2015), pp. 501–525.

[81] K.E. Jackson and Y.T. Fuchs, *Comparison of ALE and SPH Simulations of Vertical Drop Tests of a Composite Fuselage Section into Water*, in *10th International LS-DYNA Users Conference Users Conference*, Dearborn, Michigan, USA, 2008.

[82] G.A. Jarvis and L.J. Fisher, *Correlation tests of the ditching behavior of an army B-24D airplane and a 1/16-size model*, Tech. Rep., NACA, Langley Field, USA, 1946.

[83] G.R. Johnson, *Linking of Lagrangian particle methods to standard finite element methods for high velocity impact computations*, Nuclear Engineering and Design 150 (1994), pp. 265–274.

[84] R. Johnson, *Study on Transport Airplane Unplanned Water Contact*, Tech. Rep., Federal Aviation Administration, Atlantic City Airport, New Jersey, USA, 1984.

[85] D. Kohlgrüber, *Simulation results and data of A321 full-scale ditching including cabin load database (PAM-SHOCK including SPH), CRAHVI Deliveravle D4.3.7/D4.4.4b*, Tech. Rep., DLR, Stuttgart, Germany, 2003.

[86] D. Kohlgrüber, A. Vigliotti, V. Weissberg, and H. Bartosch, *Numerical simulation of a composite helicopter sub-floor structure subjected to water impact*, in *American Helicopter Society 60th Annual Forum*, Baltimore, USA, 2004.

[87] A. Korobkin, *Analytical models of water impact*, European Journal of Applied Mathematics (2004), pp. 821–838.

[88] A.A. Korobkin and S. Malenica, *Modified Logvinovich model for hydrodynamic loads on asymmetric contours entering water*, in *IWWWFB 20*, Spitzbergen, Norway, 2005.

[89] E.S. Lee, C. Moulinec, R. Xu, D. Violeau, D. Laurence, and P. Stansby, *Comparisons of weakly compressible and truly incompressible algorithms for the SPH mesh free particle method*, Journal of Computational Physics 227 (2008), pp. 8417–8436.

[90] S.J. Lind, R. Xu, P.K. Stansby, and B.D. Rogers, *A Stabilising Diffusion-Based Shifting Algorithm for Incompressible Smoothed Particle Hydrodynamics*, in *6th international SPHERIC workshop*, Hamburg, Germany, 2011, pp. 14–21.

[91] O. Lindenau, *Advances in Simulation of Ditching of Airplanes*, in *International Conference on High-Performance Marine Vehicles*, 1, 2004, pp. 152–161.

[92] O. Lindenau, *Validation of a Transport Aircraft Ditching Simulation Tool*, in *6th International KRASH Users' Seminar (IKUS6)*, Stuttgart, Germany, 2009.

[93] O. Lindenau and T. Rung, *Review of Transport Aircraft Ditching Accidents*, in *6th International KRASH Users' Seminar (IKUS6)*, Stuttgart, Germany, 2009.

[94] M.B. Liu and G.R. Liu, *Smoothed Particle Hydrodynamics (SPH): an Overview and Recent Developments*, Archives of Computational Methods in Engineering 17 (2010), pp. 25–76.

[95] L.B. Lucy, *A numerical approach to the testing of the fission hypothesis*, The Astronomical Journal 82 (1977), pp. 1013–1024.

[96] F. Macià, A. Souto-Iglesias, M. Antuono, and A. Colagrossi, *Benefits of using a Wendland kernel for free-surface flows*, in *6th international SPHERIC workshop*, Hamburg, Germany, 2011, pp. 30–37.

[97] T. Mai, D. Greaves, and A. Raby, *Aeration Effects on Impact: Drop Test of a Flat Plate*, in *Twenty-fourth International Ocean and Polar Engineering Conference*, Busan, Korea, 2014.

[98] S. Marrone, *Enhanced SPH modeling of free-surface flows with large deformations*, Ph.D. thesis, University of Rome La Sapienza, 2011.

[99] S. Marrone, M. Antuono, A. Colagrossi, G. Colicchio, D. Le Touzé, and G. Graziani, *δ-SPH model for simulating violent impact flows*, Computer Methods in Applied Mechanics and Engineering 200 (2011), pp. 1526–1542.

[100] A. Marsh, G. Oger, D. Le Touzé, and D. Guibert, *Validation of a conservative variable-resolution SPH scheme including grad(h) terms*, in *6th international SPHERIC workshop*, Hamburg, Germany, 2011, pp. 86–92.

[101] T. Mashio, S. Kawano, A. Urano, and H. Koinuma, *MRJ Scale Model Test for Ditching Certification*, Mitsubishi Heavy Industries Tehnical Review 48 (2011), pp. 61–64.

[102] E.E. McBride, *Preliminary Investigation of the Effects of External Wing Fuel Tanks on Ditching Behavior of a Sweptback-Wing Airplane*, Tech. Rep., NACA, Langley Field, Virginia, USA, 1956.

[103] E.E. McBride and L.J. Fisher, *Experimental investigation of the effect of rear-fuselage shape on ditching behavior, TN 2929*, Tech. Rep., NACA, Langley Field, Virginia, USA, 1953.

[104] S. McCallum, H. Shoji, and H. Akiyama, *Development of an advanced multi-material bird-strike model using the smoothed particle hydrodynamics method*, International Journal of Crashworthiness 18 (2013), pp. 579–597.

[105] J.J. Monaghan, *Shock Simulation by the Particle Method SPH*, Journal of Computational Physics 52 (1983), pp. 374–389.

[106] J.J. Monaghan, *On the problem of penetration in particle methods*, Journal of Computational Physics 82 (1989), pp. 1–15.

[107] J.J. Monaghan, *Smoothed particle hydrodynamics*, Annual Review of Astronomy and Astrophysics 30 (1992), pp. 543–574.

[108] J.J. Monaghan, *Simulating Free Surface Flows with SPH*, Journal of Computational Physics 110 (1994), pp. 399–406.

[109] J.J. Monaghan, *Smoothed particle hydrodynamics*, Reports on Progress in Physics 68 (2005), pp. 1703–1759.

[110] J.J. Monaghan, *Smoothed Particle Hydrodynamics and Its Diverse Applications*, Annual Review of Fluid Mechanics 44 (2012), pp. 323–346.

[111] J.P. Morris, *An Overview of the Method of Smoothed Particle Hydrodynamics*, Tech. Rep., Universität Kaiserslautern/Monash University, Kaiserslautern, Germany, 1995.

[112] NTSB, *Structures Group Chairman's Factual Report, Addendum 1, Attachment 2, Photos, SA-532 7-F*, Tech. Rep., NTSB, Washington, D. C., USA, 2009.

[113] NTSC, *Aircraft Accident Report PT. Garuda Indonesia GA421, B737-300*, Tech. Rep., 2006.

[114] J. O'Callaghan, *NTSB Report on Aircraft Performance of Hudson River Water Impact Accident*, Tech. Rep., NTSB, Washington, D. C., USA, 2009.

[115] G. Oger, M. Doring, B. Alessandrini, and P. Ferrant, *Two-dimensional SPH simulations of wedge water entries*, Journal of Computational Physics 213 (2006), pp. 803–822.

[116] P. Omidvar, P.K. Stansby, and B.D. Rogers, *Wave body interaction in 2D using smoothed particle hydrodynamics (SPH) with variable particle mass*, International Journal for Numerical Methods in Fluids 68 (2012), pp. 686–705.

[117] R. Ortiz, G. Portemont, J.L. Charles, and J.F. Sobry, *Assessment of explicit FE capabilities for full scale coupled fluid/structure aircraft ditching simulation*, in *23rd Congress of ICAS*, 2002.

[118] A.N. Parshikov and S.A. Medin, *Smoothed Particle Hydrodynamics Using Interparticle Contact Algorithms*, Journal of Computational Physics 180 (2002), pp. 358–382.

[119] A.N. Parshikov, S.A. Medin, I.I. Loukashenko, and V.A. Milekhin, *Improvements in SPH method by means of interparticle contact algorithm and analysis of perforation tests at moderate projectile velocities*, International Journal of Impact Engineering 24 (2000), pp. 779–796.

[120] A. Pasick, *Hudson River plane crash: Breaking news from the office window*, 2009, accessed 12.08.2014, available at http://blogs.reuters.com/global/2009/01/15/hudson-river-plane-crash-breaking-news-from-the-office-window/.

[121] A.A. Patel and R.P. Greenwood Jr., *Transport Water Impact and Ditching Performance*, Tech. Rep., FAA, Washington, D. C., USA, 1996.

[122] G.M.K. Pearce, *High Strain-rate Behaviour of Bolted Joints in Carbon Fibre Composite Structures*, Ph.D. thesis, University of New South Wales, 2009.

[123] N. Pentecôte, C.M. Kindervater, and F.J. Arendts, *Airframe Water Impact Analysis*, in *CEAS Forum on Crash Questions*, Capua, Italy, 2000.

[124] N. Pentecôte and D. Kohlgrüber, *Full-scale Simulation of Aircraft Impacting on Water*, in *International Crashworthiness Conference*, San Francisco, USA, 2004.

[125] J.L. Pérez, L.H. Benítez, M. Oliver, and H. Climent, *Survey of aircraft structural dynamics non-linear problems and some recent solutions*, The Aeronautical Journal 115 (2011), pp. 653–668.

[126] M. Pilorget, *Development of a dynamic calculation tool for simulation of ditching*, Master thesis, SUPAERO - École nationale supérieure de l'aéronautique et de l'espace, 2010.

[127] P.W. Randles and L.D. Libersky, *Smoothed Particle Hydrodynamics: Some recent improvements and applications*, Computational Methods in Applied Mechanics and Engineering 139 (1996), pp. 375–408.

[128] M.V. Reinhard, *Free Elastic Plate Impact into Water*, Ph.D. thesis, University of East Anglia, 2013.

[129] M. Sauer, *Adaptive Kopplung des netzfreien SPH-Verfahrens mit finiten Elementen zur Berechnung von Impaktvorgängen*, Doctoral thesis, Universität der Bundeswehr München, 2000.

[130] C. Seddon and M. Moatamedi, *Review of water entry with applications to aerospace structures*, International Journal of Impact Engineering 32 (2006), pp. 1045–1067.

[131] J.D. Seidt, *Plastic Deformation and Ductile Fracture of 2024-T351 Aluminum under Various Loading Conditions*, Ph.D. thesis, The Ohio State University, 2010.

[132] M.S. Shadloo, A. Zainali, S.H. Sadek, and M. Yildiz, *Improved Incompressible Smoothed Particle Hydrodynamics method for simulating flow around bluff bodies*, Computer Methods in Applied Mechanics and Engineering 200 (2011), pp. 1008–1020.

[133] D. Shepard, *A two-dimensional interpolation function for irregularly-spaced data*, in *23rd ACM National Conference*, ACM Press, New York, New York, USA, 1968, pp. 517–524.

[134] V. Shigunov, H. Söding, and Y. Zhou, *Numerical Simulation of Emergency Landing of Aircraft on a Plane Water Surfacel*, in *International Conference on High-Performance Marine Vehicles*, 3, 2001, pp. 419–430.

[135] M. Siemann and P. Groenenboom, *Pressure Evaluation at Arbitrary Locations in SPH Water Impact Simulations*, in *PARTICLES 2013*, Stuttgart, Germany, 2013, pp. 961–973.

[136] A.K. Singhal, M.M. Athavale, H. Li, and Y. Jiang, *Mathematical Basis and Validation of the Full Cavitation Model*, Journal of Fluids Engineering 124 (2002), pp. 617–624.

[137] R.F. Smiley, *An experimental study of water-pressure distributions during landings and planing of a heavily loaded rectangular flat-plate model*, Tech. Rep., NACA, Langley Field, Virginia, USA, 1951.

[138] A.G. Smith, I.W. McCaig, and W.M. Inverarity, *Maximum impact pressures on seaplane hull bottoms*, Tech. Rep. 4, 1950.

[139] A.G. Smith, C.H.E. Warren, and D.F. Wright, *Investigations of the Behaviour of Aircraft When Making a Forced Landing on Water (Ditching)*, Tech. Rep., Ministry of Supply - Aeronautical Research Council, London, UK, 1952.

[140] H. Söding, *Computation of Forces due to Slamming and in Planing, Appendix of Report Nr. 602*, Tech. Rep., Institute for Fluid Dynamics and Ship Theory, Hamburg University of Technology, Hamburg, Germany, 1999.

[141] H. Söding, *How to Integrate Free Motions of Solids in Fluids*, in *4th Numerical Towing Tank Symposium*, Hamburg, Germany, 2001.

[142] W. Sottorf, *Landing Procedures in Model Ditching Tests of Bf 109*, Tech. Rep., Washington, D. C., USA, 1949.

[143] A. Souto-Iglesias, E. Botia-Vera, and G. Bulian, *Repeatability and Two-Dimensionality of Model Scale Sloshing Impacts*, in *International Offshore and Polar Engineering Conference*, 2012.

[144] M.F. Steiner, *Accelerations and Bottom Pressures Measured on a B-24D Airplane in a Ditching Test*, Tech. Rep., NACA, Langley Field, Virginia, USA, 1944.

[145] M.F. Steiner, *Ditching behavior of military airplanes as affected by ditching aids*, Tech. Rep., NACA, Langley Field, Virginia, USA, 1945.

[146] S.M. Stubbs and M.E. Hathaway, *Effects of Bottom-Structure Flexibility on Water Landing Loads of Apollo Spacecraft Models*, Tech. Rep., NASA, Hampton, Virginia, USA, 1969.

[147] J.W. Swegle, D.L. Hicks, and S.W. Attaway, *Smoothed Particle Hydrodynamics Stability Analysis*, Journal of Computational Physics 116 (1995), pp. 123–134.

[148] P.G. Tait, *Report on some of the physical properties of fresh water and sea water*, Physics and Chemistry 2 (1888), pp. 1–76.

[149] A. Tassin, *Modelling of the oblique impact of an elongated body by a 2D + t approach*, in *IWWWFB 27*, Copenhagen, Denmark, 2012.

[150] A. Tassin, N. Jacques, A. El, M. Alaoui, A. Nême, and B. Leblé, *Assessment and comparison of several analytical models of water impact*, The International Journal of Multiphysics 4 (2010), pp. 125–140.

[151] W.L. Thomas, *Ditching investigation of a 1/20-scale model of the space shuttle orbiter*, Tech. Rep., Grumman Aerospace Corporation for NASA, Bethpage, New York, USA, 1975.

[152] W.C. Thompson, *Model Ditching Investigation pf the Boeing 707 Jet Transport*, Tech. Rep., NACA, Langley Field, Virginia, USA, 1955.

[153] W.C. Thompson, *Model Ditching Investigation of a Jet Transport Airplane with Various Engine Installations*, Tech. Rep., NACA, Langley Field, Virginia, USA, 1956.

[154] W.C. Thompson, *Rough-water ditching investigation of a model of a jet transport with the landing gear extended and with various ditching aids, NASA TN D-101*, Tech. Rep., NASA, Langley Field, Virginia, USA, 1959.

[155] W.C. Thompson, *Ditching investigation of a 1/30-scale dynamic model of a heavy jet transport airplane*, Tech. Rep., NASA, Hampton, Virginia, USA, 1972.

[156] N. Toso, *Contribution to the Modelling and Simulation of Aircraft Structures Impacting on Water*, Doctoral thesis, University of Stuttgart, 2009.

[157] R. Vacondio, *A dynamic particle coalescing and splitting scheme for SPH*, in *6th international SPHERIC workshop*, Hamburg, Germany, 2011, pp. 93–100.

[158] D. Van Nuffel, K.S. Vepa, I. De Baere, J. Degrieck, J. De Rouck, and W. Van Paepegem, *Study on the Parameters Influencing the Accuracy and Reproducibility of Dynamic Pressure Measurements at the Surface of a Rigid Body During Water Impact*, Experimental Mechanics 53 (2013), pp. 131–144.

[159] T. von Kármán, *The Impact on Seaplane Floats during Landing*, Tech. Rep., NACA, Washington DC, USA, 1929.

[160] H. Wagner, *Über Stoß- und Gleitvorgange an der Oberfläche von Flüssigkeiten*, Zeitschrift für angewandte Mathematik und Mechanik 12 (1932), pp. 193–235.

[161] M. Waimer, *Development of a Kinematics Model for the Assessment of Global Crash Scenarios of a Composite Transport Aircraft Fuselage*, Doctoral thesis, University of Stuttgart, 2013.

[162] S. Waite, *Composite Safety Issues*, in *Structures and Design Colloquium*, Stuttgart, Germany, 2014.

[163] G. Wittlin, M. Smith, A.K. Sareen, and M. Richards, *Airframe Water Impact Analysis Using a Combined MSC/DYTRAN - DRI/KRASH Approach*, in *American Helicopter Society 53rd Annual Forum*, Virginia Beach, Virginia, USA, 1997.

[164] J. Yu and G. Turk, *Reconstructing Surfaces of Particle-Based Fluids Using Anisotropic Kernels*, in *Eurographics/ ACM SIGGRAPH Symposium on Computer Animation*, Madrid, Spain, 2010.

[165] T. Zhang, S. Li, and H. Dai, *The suction force effect analysis of large civil aircraft ditching*, Science China Technological Sciences 55 (2012), pp. 2789–2797.

[166] R. Zhao and O.M. Faltinsen, *Water entry of two-dimensional bodies*, Journal of Fluid Mechanics (1993), pp. 593–612.

[167] O.C. Zienkiewicz, R.L. Fox, and D.D. Taylor, *The Finite Element Method for Solid and Structural Mechanics*, 7th ed., 2013.

Curriculum Vitae

Martin Hans SIEMANN,
born on May 28th, 1986 in Blankenburg (Harz), Germany

Education

2006 – 2011	Diplom-Ingenieur, Mechanical and Aerospace Engineering, Faculty of Mechanical Engineering, Dresden University of Technology
2013 – 2016	Doctoral Candidate, Aerospace Engineering, Faculty of Aerospace Engineering and Geodesy, University of Stuttgart

Professional Experience

since 2011	Research Scientist, Institute of Structures and Design, German Aerospace Center (DLR), Stuttgart
2011 – 2014	SMAES (Smart Aircraft in Emergency Situations)

- Development and enhancement of numerical models for the prediction of fluid loads and structural behavior during aircraft ditching
- Evaluation of experimental database to improve understanding of involved physics and for validation (guided ditching tests)

2015 – today	ADAWI (Assessment of Ditching and Water Impact)

- Continued enhancement of numerical models
- Transfer of knowledge to flexible full aircraft ditching simulation
- Establishment of routes for integration of ditching numerical simulations into design and certification process